THE UNIVERSITY *of* EDINBURGH

Utilising Stimulated Raman Scattering Microscopy to Study Intracellular Distribution of Label-Free Ponatinib in Live Cells

Kristel Sepp

Doctor of Philosophy with Integrated Study

Optical Medical Imaging with Healthcare Innovation and Entrepreneurship

The University of Edinburgh & The University of Strathclyde

2020

Declaration

This thesis is submitted in part fulfilment of the requirement for the degree of Doctor of Philosophy with Integrated Study at the University of Edinburgh. Unless otherwise stated, the work described in this thesis is original and has not been submitted previously in whole, or in part for any degree or qualification at this, or any other university. In accordance with the dissertation regulations as specified by The University of Edinburgh, this thesis does not exceed 100,000 words in length.

Kristel Sepp

September 2020

Acknowledgements

I would like to express my gratitude to supervisors Professor Alison N. Hulme and Professor Valerie G. Brunton for their continuous support and guidance. Alison, you welcomed me as a keen undergraduate student to do a summer project in 2015, and it was your infectious attitude towards research that inspired me to pursue a PhD in Raman imaging. Val, I have learned an immeasurable amount from you over the last four years – thank you for always challenging my thought-process. I am extremely grateful for all the advice that both of you have given me throughout the last four years - it has been a privilege to work with two amazing female leaders in science.

I thank the EPSRC, MRC and the OPTIMA doctoral training programme for the funding which has allowed me to undertake this interdisciplinary PhD. As part of OPTIMA, I was extremely lucky to receive bespoke training in healthcare innovation and entrepreneurship as well as an opportunity to carry out a three month internship. The training provided by OPTIMA has broadened my horizons and positively influenced my future career choices. Thank you also to everyone at Swedbank for welcoming me for an internship and introducing me to the world of banking and financial analysis.

Special thanks to the Brunton/Frame group for welcoming me to the Cancer Research UK Edinburgh Centre from day one – you helped a taught medicinal chemist become a cancer researcher. Biggest thank you goes to our resident microscopy expert Martin Lee, your support through the good and the bad times has been invaluable! I would also like to thank Henry Beetham for all the help on spheroid work, and for always being willing to discuss my research. Thank you to the ECRC lunch crew (past and present members) that turned into QuaranTea club (Martin, Henry, Robb) during the pandemic – you made my PhD experience a lot more positive!

My gratitude goes to the Gammoh group for explaining all things related to autophagy to me whenever I had questions. Jane Fraser and Agata Makar – I appreciate all the help you have given me! Joanne Simpson, you have been a beacon of light in daily lab life – thank you for always listening, giving advice and making me laugh!

I would also like to thank all the past and present members of the Hulme group for their support. I might not have done experiments in the School of Chemistry during my PhD, but I always felt included in the group. Special thanks to Marie Bluntzer for your help with the DFT calculations.

My thanks go to all support staff in the Cancer Research Centre whose hard work has made research run smoother. Thanks to Elisabeth Freyer and Stacey Riddles for helping me with FACS and Dr Jimi Wills for LC-MS.

A huge thanks to my family and friends for always supporting and encouraging me throughout this time. Thanks Mum, for being my biggest fan – I would not be writing this here today without your unconditional support. Speaking to you daily has kept me sane and got me through every hurdle on this journey. Jaanika, Margus, Kristin and Nora – thank you for helping me re-charge my batteries in Estonia whenever I needed to take a break from it all. Thank you Resa – you checked up on me daily, proofread all my chapters, and always reminded me of the light at the end of the tunnel. I can always count on you to be there for me and am forever grateful to have you in my life!

Finally, to Lindsay. You have been my rock throughout the PhD – providing a shoulder to cry on when needed, but always believing in me and encouraging me to keep going. Thank you for keeping both my caffeine and blood sugar levels high throughout the writing period, I could not have done this without you by my side!

Abstract

Despite advancements in the drug discovery process, drug attrition rate in the late stages of clinical trials still remains high. Better understanding of drug efficacy in the pre-clinical stage would potentially translate into increased clinical trial success rate and reduce the economic burden of failed trials. However, visualising intracellular drug uptake and distribution at high resolution to improve the pre-clinical drug discovery process is still a challenge for scientists.

Stimulated Raman scattering (SRS) microscopy represents a powerful imaging tool for visualising drug molecules inside cells with high resolution, without the need for additional labels, or nanoparticle sensors as used in many other optical imaging technologies. It provides Raman imaging with minimal spectral distortion and a quantitative output, allowing accurate determination of intracellular drug concentrations.

Ponatinib is a clinically approved tyrosine kinase inhibitor that targets BCR-ABL and is used to treat chronic myeloid leukaemia (CML). Drug resistance is a widespread problem in CML treatment, where ponatinib resistant patients have very limited treatment options. Ponatinib has an alkyne moiety in its structure that makes it inherently Raman active in the cellular silent region of the Raman spectrum. In this thesis, SRS microscopy was used to image intracellular ponatinib label-free with high sensitivity and specificity in live human CML cell lines, in the context of ponatinib resistance.

SRS imaging of ponatinib was optimised in Chapter 3, enabling ponatinib imaging at nanomolar treatment concentrations as well as determination of absolute ponatinib concentrations in both ponatinib sensitive and resistant CML cells. In Chapter 4, it was determined that ponatinib is sequestered into the lysosomes, with a higher lysosomal concentration found in drug resistant cells. This was associated with increased lysosome biogenesis. Target engagement studies showed that treatment with chloroquine reduced ponatinib accumulation in lysosomes, but did not re-sensitise cells to ponatinib, confirming a BCR-ABL independent resistance mechanism in this CML cell model.

To demonstrate further utility of SRS microscopy, it was applied to spheroid imaging in Chapter 5. CML cell lines formed three-dimensional (3D) cell ‘aggregates’ rather than spheroids with tight cell-cell contacts, and could not be used for SRS imaging.

However, spheroid growth was successfully optimised in a breast cancer cell line T47D; and live T47D spheroids were imaged using SRS microscopy.

Lay Abstract

Before new drugs are approved for use, they go through rigorous regulatory pathway in clinical trials, where the safety and efficacy of the new drug is tested on volunteers. This process is lengthy – an average drug takes up to ten years to get from discovery in the lab to being approved for use. Clinical trials are expensive and many drugs fail in the last phases of the process, leading to denied approval. To increase clinical trial success rate and therefore reduce the cost of drug development, it is important to gain a better understanding of drug effects in the pre-clinical phase. One way of doing so is studying drug uptake, metabolism and localisation within cancer cells. However, imaging drugs in cells with good definition is still challenging for scientists.

In this project, we demonstrate the utility of Raman microscopy for drug imaging. Raman microscopy enables visualisation of specific bonds inside molecules, and it allowed us to study ponatinib, a drug used to treat chronic myeloid leukaemia (CML). As drug resistance to ponatinib has been reported in CML patients, we imaged ponatinib in both drug sensitive and drug resistant cells. Ponatinib imaging provided insightful information on its intracellular localisation, uptake, metabolism and its resistance mechanism in CML. To demonstrate further utility of Raman microscopy, it was applied to imaging three-dimensional clusters of cells.

Contents

Chapter 1 Introduction

1.1 Drug attrition rates

Drug attrition rates in the pharmaceutical industry are an increasing problem due to the high cost and long timescales associated with the drug development process.[1-5] Despite increased investment in drug research and development (R&D) in recent decades, the annual number of drugs approved by the US Food and Drug Administration (FDA) has not increased proportionally.[6] Although significant advances have been made in the development of tools used to identify drug targets (for example computational modelling and screening) and molecules that interact with these targets (for example high-throughput target-based screening for key proteins such as G-protein coupled receptors and kinases), drug attrition rates remain challenging for the pharmaceutical industry.[4] R&D spending increases annually due to multitude of factors such as inflation, increased regulatory control as well as higher failure rates; as a result, the cost per new drug has been increasing since the 1950s at an annual rate of 13.4%. Thus pharmaceutical companies need to increase their output of new medicines in order to secure a sustainable future.[6]

It is a common occurrence that promising pre-clinical drug candidates fail to translate into clinical successes, demonstrating the ineffectiveness of current disease models used in drug discovery.[7] The major causes of attrition in late stages of the pipeline in recent years have been lack of efficacy and safety concerns (Figure 1.1a).[8] Failure due to lack of efficacy could be decreased by improving existing pre-clinical models that are used to estimate drug efficacy. The greatest attrition rates by therapeutic area are for oncology and the central nervous system (CNS) (Figure 1.1b).[8] This could be attributed to a poor understanding of the underlying mechanisms in these diseases as well as a lack of reliable and disease-relevant pre-clinical screening models.

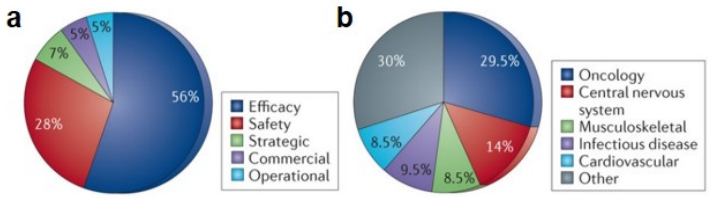

Figure 1.1 (a) Of the 148 failures between Phase II and submission in 2011 and 2012, reasons were reported for 105; the majority of failures were due to lack of efficacy. (b) The 105 reported failures broken down according to therapeutic area. Reproduced with permission,[8] copyright Springer Nature.

Standard cell-line screens and *in vivo* xenograft models fail to mimic key pathophysiological features of complex diseases such as cancer and Alzheimer's disease. Cell-based disease models still largely rely on cancer cells or immortalized cells grown in artificial environments. These cell lines have been cultured for many generations, resulting in altered genetics and lack of similarity to primary tissue cells.[9] The use of high oxygen partial pressure (approximately 20%) during experiments does not represent the true microenvironment of the diseased tissue, which fluctuates between 1% in the dermis and 14% in the arterial blood for humans.[10] Differences in culture conditions, however, can affect cell metabolism, mitochondrial function as well as cell differentiation.[11] It is hence necessary to improve pre-clinical models used to study drug efficacy in order to better understand drug uptake, distribution and metabolism prior to moving on to clinical trials. This would enable elimination of unsuitable drug candidates earlier in the pipeline, lead to safer clinical trials, and of course better use of time and financial resources.

1.2 Visualising drug localisation

In addition to lacking high quality pre-clinical models, scientists are still unable to monitor intracellular drug distribution and concentration accurately. In drug discovery and development, it is vital to analyse the drug candidates' uptake and distribution in order to evaluate their potential efficacy.

1.2.1 Currently used techniques and limitations

Drug distribution has traditionally been investigated in target cells/tissues by utilising positron emission tomography (PET)[12], magnetic resonance imaging (MRI)[13], as well as whole body autoradiography (WBA)[14]. The majority of drugs do not accumulate in tissues at high enough concentrations to be detected by MRI, so it is mostly used to study the effects of drugs on tissue morphology, physiology and biochemistry. MRI spatial resolution is about a few hundred microns and 50–60 μm for human and rodent imaging respectively.[15] PET allows drug distribution studies of radioactively labelled drugs in both animals and humans, and has been successfully used to determine the pharmacokinetics of radiolabelled cytotoxic agents, such as [^{18}F] fluorouracil in individual cancer patients, before initiating full-dose treatment.[16] However, PET has a spatial resolution in the order of 2–5 mm, which is less than MRI. WBA enables radiolabelled drug detection in whole animals.[17] Although it allows imaging with higher resolution (50-100 μm) than PET, WBA is limited by long acquisition times which

range from days to weeks.[18] The major limitation in applying MRI, PET and WBA to the study of drug uptake in tissues is the use of radioactive labels. These techniques only provide data on the concentration of radioactivity, while the actual molecular identity of the radioactivity is not known and the parent drug cannot be distinguished from metabolites.

Recently, matrix-assisted laser desorption ionization with mass spectrometry imaging (MALDI-MSI) has been applied as a label-free imaging modality to study pharmaceutical uptake and metabolism in tissue sections.[19-22] MALDI-MSI combines the resolution of WBA with the molecular specificity of mass spectrometry, enabling the detection of both the parent drug as well as its metabolites in parallel. MALDI requires matrix application on the sample to desorb and ionize compounds with a laser. Matrix selection and the method of application influence the sensitivity and spatial resolution of MALDI, and need to be optimised for each drug. Unfortunately, MALDI-MSI has a relatively low spatial resolution of approximately 20-100 µm, which prevents drug imaging at the cellular level.[23]

Secondary ion mass spectrometry imaging (SIMS-MSI) offers a complementary method to MALDI-MSI for the acquisition of higher spatial resolution images.[17] SIMS-MSI can achieve submicromolar spatial resolution reliably, and is suited to detecting small molecules with under 1000 Da molecular weight.[24] Therefore, it is unsurprising that SIMS has been used for subcellular studies of drugs such as amiodarone and boron neutron capture therapy drugs.[25,26] However, like other mass spectrometry techniques, both MALDI and SIMS are destructive imaging techniques.

Unlike MALDI and SIMS, confocal fluorescence microscopy is compatible with live cell imaging and has enabled imaging of compounds and biomolecules by attachment of a fluorescent label to the molecule of interest.[27-30] Confocal fluorescence microscopy has a spatial resolution of 150 nm, allowing subcellular imaging and detection of cellular organelles such as the nucleus, endoplasmic reticulum and Golgi apparatus.[29] This imaging technique is highly reliable, sensitive and widely used in biomedical research. The use of fluorescent labels to study drug uptake and localisation, however, is limited by the relatively large size of an average fluorophore in relation to a small molecule under investigation which can result in perturbation of the molecule's intracellular behaviour. In some cases, drug molecules are inherently fluorescent and can be detected in cells label-free.[31,32]

1.2.2 Raman scattering effect

Raman spectroscopy is a non-destructive analytical technique that is used to measure inelastic scattering of light from molecular vibrations. The Raman scattering effect was first described by C. V. Raman in 1928, who observed modified scattering of light when irradiating samples with sunlight.[33] Raman scattering is a rare phenomenon - most of the light absorbed by the molecule is elastically scattered at the same energy ($\upsilon=\upsilon_0$) (Figure 1.2a). The elastic scattering is known as Rayleigh scattering. Inelastic scattering has an extremely low probability of occurrence, only ~1 in 10^8 photons undergo Raman scattering (Stokes and anti-Stokes scattering) in comparison to Rayleigh scattering (Figure 1.2b).[34]

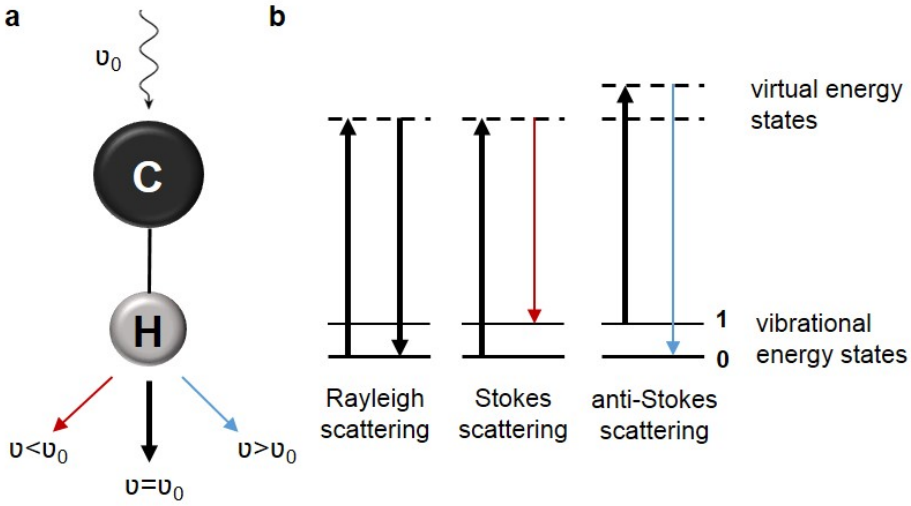

Figure 1.2 The principles of the Raman scattering effect. (a) Incident light (υ_0) is used to excite a chemical bond within a molecule (for example C-H bond). The majority of the light is scattered at the same frequency, but a small proportion is Raman scattered at a higher or lower frequency. (b) Energy level diagrams showing Rayleigh ($\upsilon=\upsilon_0$), Stokes ($\upsilon<\upsilon_0$) and anti-Stokes ($\upsilon>\upsilon_0$) scattering. Rayleigh scattering is the elastic scattering of photons during interaction with a molecular vibration. Raman scattering is the inelastic scattering of photons following interaction with a molecular vibration, and is detected as a Stokes photon, which has either lost energy (Stokes scattering) or gained energy (anti-Stokes scattering).

1.2.2.1 Spontaneous Raman spectroscopy

Spontaneous Raman spectroscopy is the original form of Raman spectroscopy. It utilises a single laser to excite all of the bonds in a molecule, producing a molecular fingerprint of the sample. In contrast to infrared (IR) spectroscopy, Raman scattering of water is very weak, making it an excellent tool for studying biological samples.[35] Figure 1.3 shows the Raman spectrum of chronic myeloid leukaemia cells. At

2850 cm^{-1} and 2953 cm^{-1} lie the CH_2 and CH_3 stretch of the cell which are indicative of cellular lipids and proteins respectively. Between 1800-2800 cm^{-1} lies the so-called 'cell-silent' region where there are surprisingly no diagnostic peaks from the cell content. In the fingerprint region, below 1700 cm^{-1}, there are a number of smaller peaks present from the cell content, including the C=O stretch from the protein backbone (1665 cm^{-1}) as well as the sharp aromatic ring peak from the amino acid phenylalanine (1001 cm^{-1}). The laser detection system for spontaneous Raman spectroscopy can be combined with a confocal microscope, enabling spectral acquisition at each pixel of the sample by raster scanning.[36] The spectral data can be used to generate a cellular distribution map of different chemical species, allowing label-free imaging.

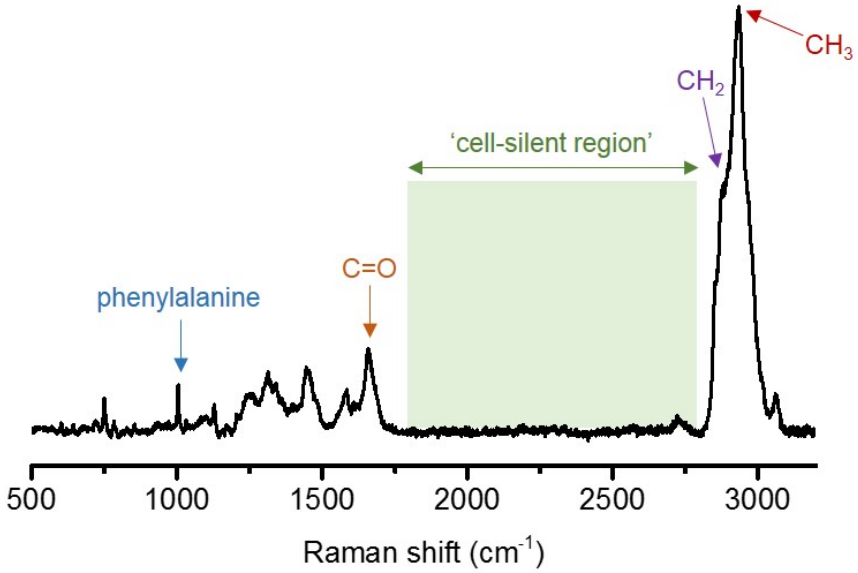

Figure 1.3 Raman spectrum of pelleted CML cells. Pelleted K562 cells were analysed by spontaneous Raman spectroscopy using λ_{ex} = 785 nm. Characteristic cellular peaks are shown: CH_3 (2953 cm^{-1}), CH_2 (2850 cm^{-1}), C=O (1655 cm^{-1}), phenylalanine (1001 cm^{-1}). The cell silent region (~1800-2800 cm^{-1}) is highlighted.

1.2.2.1.1 Raman microscopy application to drug imaging

Raman microscopy has been applied to drug imaging. A number of chemotherapeutic agents have been imaged intracellularly. Examples include studies carried out on paclitaxel, topoisomerase I inhibitor (CPT-11) as well as theraphthal and metal-carbonyl complexes.[37-42] All of these studies were carried out on label-free targets, where characteristic Raman peaks intrinsic to the molecule of interest were used to detect the molecules inside cells. Table 1.1 summarises the parameters used in each study to investigate these chemotherapeutic agents. Each of the Raman imaging

studies shown in Table 1.1 has enabled further understanding of how these molecules behave intracellularly, and hence proven that Raman spectroscopy is a valuable tool when it comes to label-free drug imaging. As Raman scattering is a very weak effect, the majority of these studies had to use drug concentrations that were in excess of clinically relevant levels for the Raman signal to be detected. More specific examples where Raman microscopy has been applied to imaging targeted cancer therapeutics are discussed later in Section 3.1.2.

Table 1.1 Comparison table of different chemotherapeutic agents that have been imaged by Raman microscopy. Summarises the parameters used for imaging as well as the cell lines that were used.

Pharmaceutical	Concentration (μM)	Treatment time (h)	Cell line	Detection vibrational bands (cm^{-1})
paclitaxel[37] (2002)	350	1	MDA-345	1000
paclitaxel[38] (2013)	~10	3, 6 & 9	MCF7	1740 (C=O)
CPT-11[42] (2009)	100	0.5, 1, 2 etc.	HeLa, MCF7, MCF7/MX	1561
theraphthal[39] (2000)	100-400	0.2 to 14	A549	Various peaks from 1000-1550
Mn-carbonyl complex[40] (2010)	2000	3	HT29	1963 for C≡O
Re-carbonyl complex[41] (2013)	25	1	MDA-MB-231	1915 and 2032

1.2.2.2 Bioorthogonal Raman labels

Bioorthogonal chemistry transformed the field of chemical biology by allowing scientists to carry out reactions within biological organisms with excellent selectivity and no toxicity or perturbation to the living system.[43] The term bioorthogonal has also been adopted to describe Raman-active tags, which vibrate in the cell-silent region of the Raman spectrum, typically at around 2100-2300 wavenumbers, enabling chemically specific imaging with minimal background.[44] Raman tags are used to enhance Raman sensitivity of the small molecule of interest. Raman-active tags need to be exogenous (i.e. cells do not have a naturally high concentration of these chemical moieties) and bioorthogonal (do not react with biomolecules intracellularly).

Two main strategies are utilised: the first is the use of bioorthogonal Raman-active groups (e.g. C≡C, C≡N, C≡O) which are either inherent to the molecule of interest, or are introduced chemically for imaging purposes.[45] The second is the use of isotopologues, which means compounds that only differ from the parent structure by isotopic substitution (e.g. C-H to C-D).[46] The advantage of using Raman tags compared their fluorescent equivalents is that they are generally smaller and show greater photostability (i.e. the intensity of the Raman signal does not decay with prolonged exposure) than their fluorescent counterparts.

The most widely studied Raman-active tag is the alkyne moiety.[44,45] Compared to other Raman tags like nitrile and deuterium, alkynes have the strongest Raman signal. In contrast to deuterium labels, which often produce multiple signals, alkynes have a narrow band width, which makes them more suitable for multiplex imaging. Figure 1.4 shows examples of Raman imaging using alkyne tags. 5'-Ethynyl-2'-deoxyuridine (EdU), an analogue of the nucleobase thymine, has been used to label cell nuclei, and can be used to visualise cell division (Figure 1.4a).[47] Hu *et al.* synthesized an alkyne tagged analogue of glucose and successfully imaged it in a number of cell and tissue types; Figure 1.4b shows uptake in mouse neurones.[48] The Raman signal of alkyne tags can be further enhanced by the addition of adjacent aromatic groups or alkynes, creating bisalkynes. Tipping *et al.* utilised this and added a bisaryldiyne (BADY) tag to the bioactive small molecule anisomycin (Figure 1.4c).[49] They successfully detected BADY-anisomycin in cells alone as well as multiplexed with EdU.

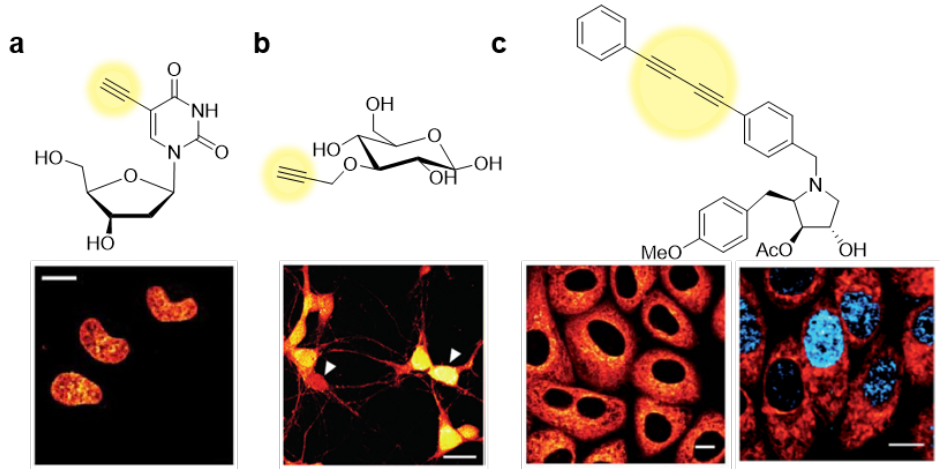

Figure 1.4 Raman imaging with bioorthogonal labels. (a) Cell nuclei labelled with EdU (100 μM) and imaged at 2125 cm^{-1} in HeLa cells. Scale bar: 10 μm. Reproduced with permission,[47] copyright Springer Nature. (b) Alkyne labelled glucose (3-*O*-propargyl-D-glucose, 3-OPG) (8 mM) imaged at 2129 cm^{-1} in primary mouse neurones. Scale bar: 20 μm. Reproduced with permission,[48] copyright John Wiley and Sons. (c) Imaging of BADY-anisomycin (10 μM, 30 min, orange) at 2219 cm^{-1} alone, and multiplexed with EdU (100 μM, 18 h, blue) at 2120 cm^{-1} in HeLa cells. Scale bars: 10 μm Reproduced with permission,[49] copyright The Royal Society of Chemistry.

Further development of Raman multiplex imaging has recently seen the application of polyynes. Polyynes are a linear chain of conjugated alkynes, which have sharp Raman peaks, a large intensity enhancement compared to terminal alkynes and natural frequency separation with increasing lengths. Hu *et al.* took advantage of the superb Raman properties of polyynes and developed a Raman multiplex imaging palette.[50] Through chain-length modulation, bond-selective isotope labelling and end-group substitutions, they achieved 20 distinct Raman colours in the cell-silent region, and named it the carbon rainbow (Carbow; Fig. 1.5a,b). Carbow dyes were applied to cellular imaging, and 15-colour tandem-fluorescence-Raman imaging in live cells was demonstrated (Figure 1.5c).

Another Raman dye palette was developed by Wei *et al.* who used triple-bond-conjugated near-infrared dyes, where each display a single peak in the cell-silent Raman spectral window.[51] In combination with available fluorescent probes, this palette provides 24 resolvable colours, with the potential for further expansion. In contrast, fluorescence microscopy can only differentiate between a maximum of six colours due to the intrinsically broad nature of fluorescence spectra.[52] The Raman

dye palettes will undoubtedly enable more complex studies in biological systems than was previously possible with fluorescence alone.

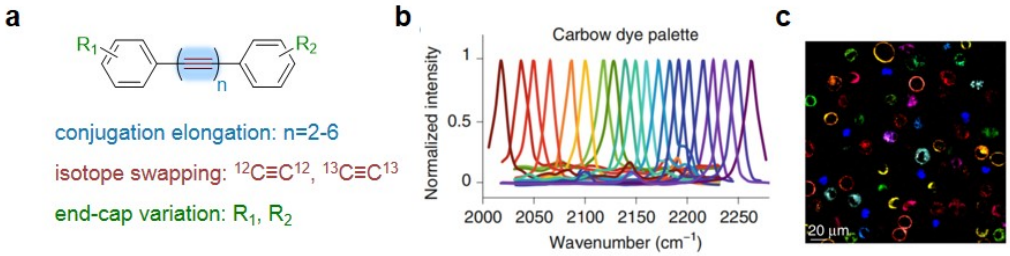

Figure 1.5 Raman multiplex imaging with the Carbow dye palette. (a) Chemical strategies for Raman-frequency expansion of polyynes: frequency modulation on the polyyne scaffold by conjugation elongation, isotope swapping and end-capping variations. (b) Carbow dye palette with 20 well-resolved Raman peaks. (c) 15-color tandem-fluorescence-Raman imaging of live HeLa cells with corresponding Carbow and fluorescent molecules. Reproduced with permission,[50] copyright Springer Nature.

1.2.2.3 Coherent Raman scattering

The use of bioorthogonal Raman tags is not the only strategy to overcome the inherently weak signal in Raman spectroscopy. Technological development has also led to the use of coherent Raman scattering techniques. Coherent Raman scattering describes non-linear techniques where two incident lasers are used to excite and image a particular vibration of interest to enhance the Raman signal. Coherent anti-Stokes Raman scattering (CARS) and stimulated Raman scattering (SRS) are both coherent Raman techniques that have found use in many biological applications.[53,54]

CARS utilises two lasers, the pump laser (ω_p) and Stokes laser (ω_s). These interact with the sample in a four-wave mixing process and generate signal at the anti-Stokes frequency, Ω ($\omega_{as} = 2\omega_p-\omega_s$) (Figure 1.6). When Ω matches a molecular vibration of interest, contrast is derived from the chemical bonds in the sample.[55] However, the process can also occur in non-resonant conditions, which leads to issues with high background noise and prevents quantitative imaging by CARS microscopy. In contrast to spontaneous Raman, CARS allows up to video-rate imaging of biological samples.[56] It is also suitable for three dimensional analysis of cells and tissues.

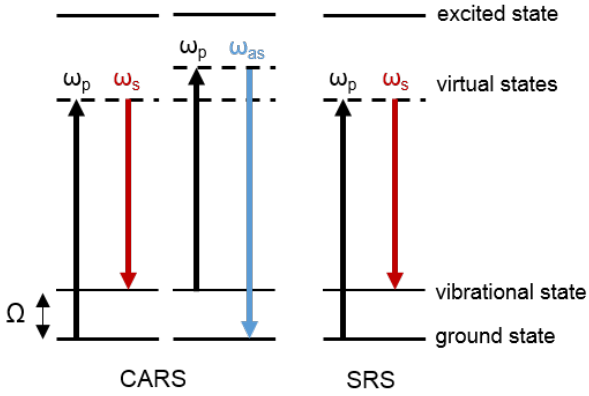

Figure 1.6 Coherent Raman scattering. Energy level diagrams showing the signal generation process of CARS and SRS. In SRS, the sample is excited with a pump and Stokes laser to create an image when Ω matches a specific molecular vibration. In CARS, a four wave mixing process is used, where Ω is tuned to the anti-Stokes frequency.

SRS signals are also generated using two lasers, the pump (ω_p) and the Stokes (ω_s) laser (Figure 1.6). The energy difference ($\Delta\omega = \omega_p - \omega_s$) between the two lasers is tuned to match a specific molecular vibration (Ω), leading to stimulated excitation of the Raman active vibrational mode. This causes an intensity loss in the pump beam (stimulated Raman loss, SRL) and an intensity gain in the Stokes beam (stimulated Raman gain, SRG). By using an acousto-optic modulator (AOM), the Stokes beam can then be modulated to enable the measurement of the change in the pump beam only by using a radio-frequency lock-in detection, which provides the contrast to generate the image. SRL and SRG do not occur when Ω does not match a molecular vibration, so there is no non-resonant background in SRS.

1.2.2.4 Stimulated Raman scattering microscopy

Stimulated Raman scattering microscopy was first described in 1962,[57] but its potential for live cell imaging was only realised in 2008 when Freudiger *et al.* developed a high-sensitivity detection system that allowed biocompatible SRS microscopy.[58] The last decade has seen the further development of SRS microscopy in order to overcome the disadvantages related to traditional Raman scattering.[59] There is a lot of interest in utilising SRS for biomedical applications and drug discovery.[60,61]

The main advantages of SRS imaging over spontaneous Raman spectroscopy include faster acquisition speeds and higher levels of vibrational excitation due to

stimulated Raman scattering, making it both a more effective and more sensitive technique for 2D/3D cell imaging.[59,60,62] It is also important to mention that SRS has a linear dependence on concentration (Figure 1.7a), like spontaneous Raman spectroscopy, and it has good data correlation with the spontaneous Raman spectrum (Figure 1.7b).[63] This makes SRS an excellent tool for quantitative imaging which is especially valuable for drug screening studies.[62] For other Raman imaging techniques, such as surface-enhanced Raman spectroscopy (SERS) and CARS, it is more complex to quantify the signal in a concentration dependent manner.[58,64,65]

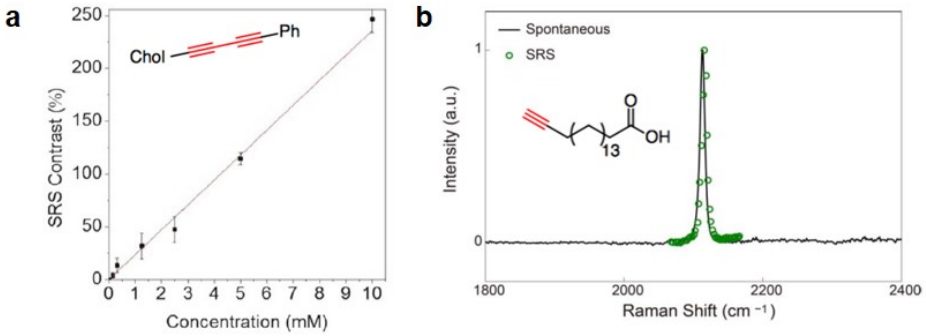

Figure 1.7 (a) SRS contrast vs concentration plot of phenyldiyne (PhDY)-Cholesterol solutions. Reproduced with permission,[66] copyright Springer Nature. (b) The non-distorted SRS spectrum intensities of Alk-16 mapped against the spontaneous Raman spectrum. Reproduced with permission,[59] copyright John Wiley and Sons.

1.2.2.4.1 SRS microscope

A schematic representation of a SRS microscope illustrates how SRS microscopy is carried out (Figure 1.8). The pump and Stokes beams are synchronised, spatially overlapped using a dichroic mirror, and co-lineated into a beam-scanning microscope. An objective lens is used to focus the beams onto a focal point in the sample, generating a stimulated Raman process at its focus. A high numerical aperture condensor is used to collect the transmitted beams, a filter then blocks out the Stokes beam, enabling the subsequent detection of the pump beam by a photo-diode. A lock-in amplifier is used to extract the SRL signal from the laser intensity, providing a 2D Raman intensity map at each pixel.

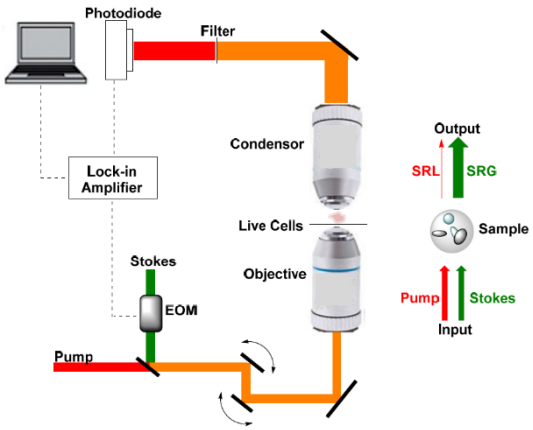

Figure 1.8 A Schematic representation of a SRS microscope. Reproduced with permission,[60] copyright The Royal Society of Chemistry.

1.2.2.4.2 SRS application to imaging pharmaceuticals

As discussed in Section 1.2, imaging pharmaceutical compounds in living systems is important to better understand their mechanism of action. SRS microscopy has been utilised for imaging pharmaceuticals using both the label-free approach as well as small Raman tags.[60]

Label-free SRS imaging has been applied to study drug formulations in tablets[67] and implants,[68] and used to study dermal drug delivery.[47,69] Liao *et al.* imaged vitamin E, a fat-soluble antioxidant widely used in skincare products, in mouse skin.[69] They imaged the α-tocopherol form of vitamin E (Figure 1.9a), using the C-H stretch of the molecule at 2911 cm^{-1} to detect its diffusion into skin. To distinguish the overlapping C-H stretch of vitamin E and the skin tissue, SRG spectra were acquired each pixel and analysed by multivariate curve resolution (MCR) analysis. The SRG image was decomposed into vitamin E (in pink), lipid (in yellow), and protein (in green) as shown in Fig. 1.9b. Vitamin E molecules were found to be enriched in the sebaceous gland (50 μm depth).

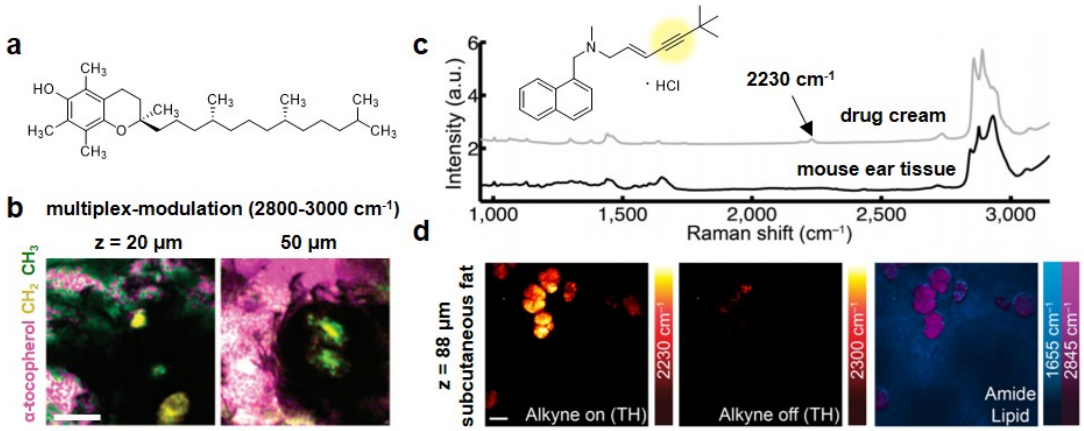

Figure 1.9 Label-free imaging of vitamin E (α-tocopherol) and terbafine hydrochloride (TH) using SRS microscopy. (a) Chemical structure of α-tocopherol. (b) MCR concentration maps of α-tocopherol (magenta), lipid (yellow) and protein (green) on anesthetized nude mouse skin after 5 min treatment at 20 µm and 50 µm depth. Scale bar: 100 µm. Reproduced with permission,[69] copyright AAAS. (c) Chemical structure of TH; Raman spectra of a drug cream (1% TH) and mouse ear skin tissue. (d) SRS imaging of mouse ear tissue (z = 88 µm). SRS images acquired from alkyne on (2230 cm^{-1}) and off-resonance (2300 cm^{-1}), protein (C=O, 1655 cm^{-1}) and lipid (CH_2, 2845 cm^{-1}) stretches. Scale bar: 20 µm. Reproduced with permission,[47] copyright Springer Nature.

Wei *et al.* imaged FDA approved antifungal skin drug terbafine hydrochloride (TH) in mouse ear tissue to a depth of about 100 µM using SRS imaging.[47] TH has an inherent alkyne with a Raman peak at 2230 cm^{-1}, which was detected in the Raman spectrum of Lamisil, a cream containing 1% TH (Figure 1.9c). SRS imaging of TH was achieved in mouse ear tissue by treating the ears with 1% TH in DMSO solution. TH was found to localise in high fat regions of the tissue (Figure 1.9d), suggesting it is penetrates into tissues through the lipid phase. This is consistent with the molecule's lipophilic nature.

When drugs do not have characteristic vibrational features, small Raman tags have been used to allow SRS imaging with improved sensitivity and specificity. Saar *et al.* used deuterium labelling to visualise the penetration of non-steroidal anti-inflammatory drug ibuprofen into mouse skin.[70] The drug was applied to the mouse ear as a propylene glycol (PG) solution, and uptake was measured over time. It was found that ibuprofen forms crystals on the tissue surface, while some drug penetration into the skin via the hair follicle was seen. Precipitation of ibuprofen was likely observed due to the faster penetration of PG into the skin, possibly coupled with some

evaporation of PG from the surface. These factors probably increased the local drug concentration above its saturation solubility. The diffusion of pharmaceutically relevant solvents into nails has also been studied via deuterium labelling.[71] SRS imaging of deuterated water (D_2O), DMSO (DMSO-d_6) and PG (PG-d_8) revealed much faster transport of water through the nail, relative to PG and DMSO.

Alkyne tags, which are more Raman active than deuterium, have also been utilised to study the intracellular distribution of small molecule inhibitors using SRS. Diyne Raman tags were applied to imaging anisomycin[49] (Figure 1.4c), antimycins[72] and ferrostatins.[73] SRS imaging of these Raman-tagged inhibitors revealed both anisomycin and antimycins localised in the endoplasmic reticulum (ER), while ferrostatin-1 accumulated in lysosomes, mitochondria and ER.

These examples demonstrate the widespread applications of SRS microscopy for studying pharmaceuticals. Additional examples, where FDA approved drugs have been imaged by Raman microscopy, are discussed in Section 3.1.2.

1.3 Chronic myeloid leukaemia (CML)

Chronic myeloid leukaemia affects approximately one individual per 100,000 population per year, accounting for 15% of all new cases of leukaemia in the Western hemisphere.[74] Although the median age at diagnosis is 53 years, all age groups, including children, are affected.[75] The common symptoms of CML patients are fatigue, anorexia, and weight loss. However, approximately 40% of patients are asymptomatic. For these patients, diagnosis is based on an abnormal blood count. The development of targeted therapy increased the 10-year survival rate for CML patients from about 20% to 80-90%. Tyrosine kinase inhibitors (TKIs) have profoundly affected the prognosis for newly diagnosed CML patients, where the overall survival rates are now only slightly lower than that of the general population.[76]

1.3.1 CML development

Chronic myeloid leukaemia (CML) is a myeloproliferative disease of hematopoietic stem cells. Over 90% of patients with CML have an abnormal Philadelphia chromosome (Ph), where chromosome 9 and chromosome 22, which contain the *ABL* (Ableson leukemia virus) and *BCR* (breakpoint cluster region) gene respectively, have translocated (Figure 1.10).[77] The Ph is found in cells from the myeloid, erythroid, megakaryocytic, and B lymphoid lineages. The Philadelphia chromosome hosts the

chimeric *BCR-ABL* oncogene that upon transcription and translation leads to the formation of cytoplasmic fusion protein BCR-ABL, which is a tyrosine kinase.[78] ATP binding activates BCR-ABL and leads to uncontrolled cell proliferation, differentiation and cell survival, which results in the CML phenotype.

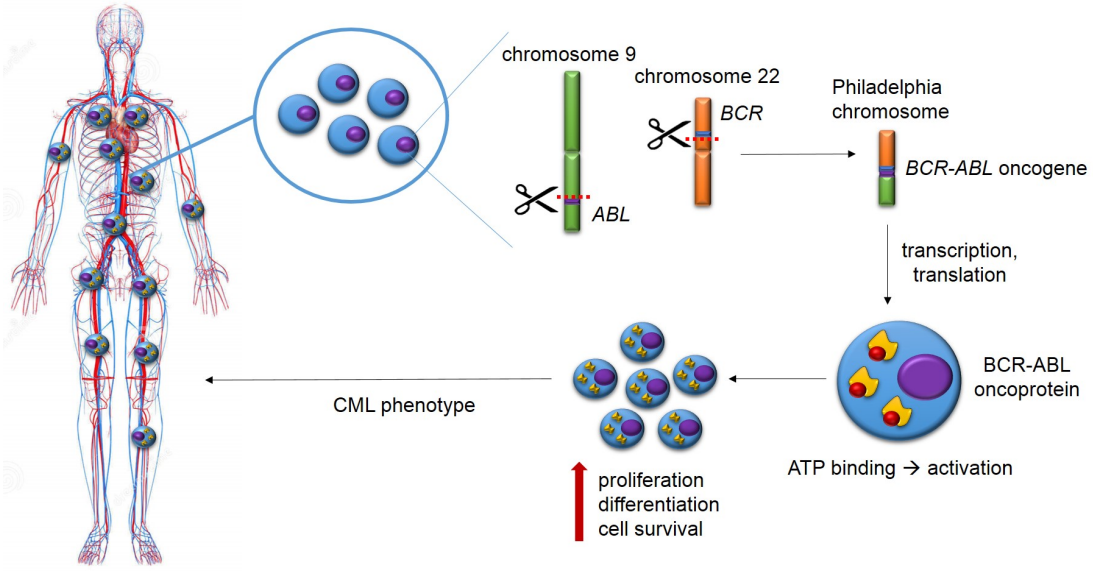

Figure 1.10 Characterisation of CML. The hallmark of CML in patients is the formation of the Philadephia chromosome upon translocation of chromosome 9 and 22. The molecular consequence of this translocation is the generation of a *BCR-ABL* oncogene, which in turn translates into BCR-ABL oncoprotein.

The majority of CML patients are in the chronic phase of the disease at the time of diagnosis.[79] Treatment in this phase of the disease gives the best prognosis for patients. Chronic phase (CP) is followed by accelerated phase (AP) and blast crisis (BC), which are characterised by additional chromosomal changes, increased BCR-ABL levels as well as increased genomic instability.[80] CML treatment during accelerated phase and blast crisis is associated with poorer outcomes. Therefore, early diagnosis and treatment is critical for patients' long-term survival.

1.3.2 Current CML therapies

CML treatment has changed dramatically over the years. Therapy was restricted to the chemotherapeutics busulphan and hydroxyurea before the 1980-s.[81] These improved patient blood count and gave symptomatic relief, but did not delay the onset of disease progression, which occurred at a median of 4–5 years after diagnosis. Allogeneic stem cell transplantation and interferon alpha became the treatments of choice during the 1980-s and 1990-s.[82,83] Compared to busulphan and hydroxyurea,

these treatments prolonged patient survival, however, interferon alpha treatment led to multiple toxicities in patients.[84] Allogeneic stem cell transplantation can be curative, but also has associated risks of morbidities and mortality.

The era of targeted therapy started in 2001 when imatinib was approved by the FDA as the first tyrosine kinase inhibitor for the treatment of CML.[85] Imatinib targets the BCR-ABL protein-tyrosine kinase, inhibits its phosphorylation and subsequently leads to inhibition of cell proliferation and the induction of apoptosis.[86] Imatinib was welcomed as a revolutionary anticancer agent in terms of its target specificity, high efficacy and low toxicity.[87] However, point mutations in the ABL kinase domain of BCR-ABL quickly led to the development of drug resistance due to impaired inhibitor binding.[88] Up to 30% of patients developed intolerance or resistance to imatinib within the first 5 years of therapy.[89]

Nilotinib was then developed as a second-line therapy for CML patients that had developed imatinib resistance.[90] Nilotinib proved to be effective against some BCR-ABL point mutations, such as E255V, M351T, and F486S, but failed against the T315I point mutation which is located at the gatekeeper region of the ATP-binding site and is crucial for drug binding. While imatinib and nilotinib both bind to the inactive BCR-ABL (type II ATP competitive inhibitors) (Figure 1.11a), dasatinib and bosutinib are two other BCR-ABL inhibitors that bind to the active BCR-ABL (type I ATP competitive inhibitor) (Figure 1.11b).[91] Unfortunately, dasatinib and bosutinib were also ineffective against the BCR-ABL^{T315I} mutant.[92,93]

The T315I point mutation is the most frequently detected mutation in patients who have developed resistance or intolerance to imatinib treatment as well as in patients with resistance to dasatinib or nilotinib.[94,95] The mutation from a small threonine to a bulky isoleucine inhibits the drugs from binding into the allosteric pocket and hence reduces the binding affinity of the aforementioned inhibitors.[91] Computational modelling has demonstrated that the T315I mutation eliminates a critical hydrogen bonding interaction necessary for high-affinity binding of all four ATP mimics.[96]

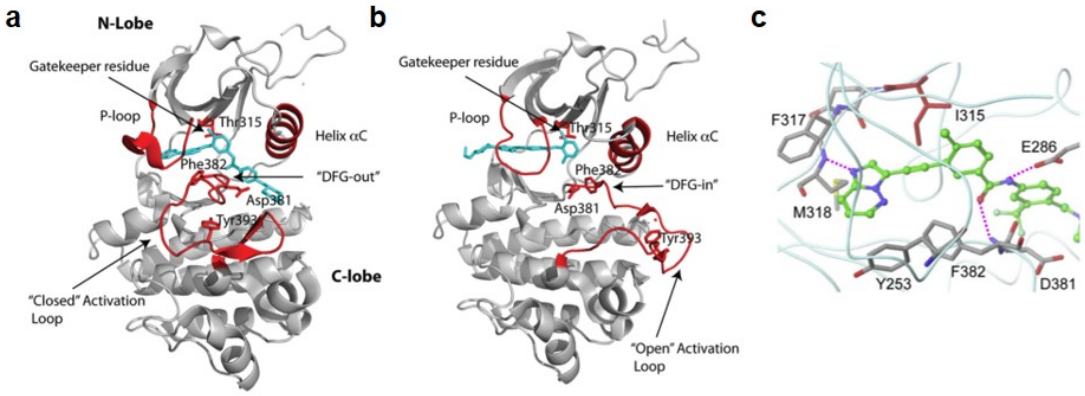

Figure 1.11 Inhibition of BCR-ABL by TKIs. (a) Imatinib (cyan) binds to the kinase domain of BCR-ABL in its inactive state where the activation loop (red) is in the "closed" conformation and the DFG motif is in the "out" conformation. (b) Dasatinib (cyan) binds to the kinase domain of BCR-ABL in its active state where the activation loon (red) is in an "open" conformation and the DFG motif is in the "in" conformation. Reproduced with permission,[97] copyright SAGE Publishing. (c) Ponatinib (green) binding to BCR-ABL^{T315I} mutant. The side chain of the mutated gatekeeper residue Ile315 is shown in red. Hydrogen bonds are highlighted with pink dashed lines. Reproduced with permission,[98] copyright Elsevier.

As a third-line treatment for CML, ponatinib was subsequently developed by O'Hare *et al.* to combat the BCR-ABL^{T315I} mutant which could not be treated with imatinib, nilotinib, dasatinib, or bosutinib.[98] These original ATP mimics all form a hydrogen bond with the side chain OH of the T315 residue in native BCR-ABL. Ponatinib was hence designed to avoid that binding mode and instead accommodates the T315I alkyl side chain by having a slim alkyne linker in the molecule, hence bypassing the additional steric hindrance found in the mutant (Figure 1.11c). While ponatinib has one less hydrogen bond with the target, it still forms five hydrogen bonds with the protein in addition to the favourable van der Waals interactions with the I315 residue. Ponatinib demonstrates high efficacy against various BCR-ABL mutants as well as the native BCR-ABL, which is why it was approved by the FDA for treatment of CML in 2011. However, the risk for serious toxicities and thrombotic events with ponatinib treatment was found to be significant post-approval. For that reason, ponatinib is now only considered as a treatment option for patients with a T315I mutation, as there are no other options for these patient. The risk of side effects is reduced when a lower ponatinib dose, 15-30 mg daily, is used instead of the standard 45 mg daily.

Research is ongoing to find better treatment options for CML patients who have developed TKI resistance to both first and second line TKIs, and possess the T315I

mutation. As of 2020, three novel third generation TKIs are in clinical trials for CML treatment, including asciminib, HQP1351 and K0706.[99] Allogeneic stem cell transplant remains an important treatment option for CML patients with AP and BP-CML, and it is considered for patients in CP-CML who have failed treatment with at least two TKIs.[99]

1.3.3 CML drug resistance mechanisms

Despite the early success associated with TKI treatment of CML, not all patients experience long-term durable responses. This is a consequence of TKI drug resistance in CML, which can either be primary, when treatment fails, or acquired, when the achieved response is lost.[100] Before a patient is declared to have TKI resistance, it is important to assess treatment compliance as well as drug-drug interactions. A lower rate of imatinib adherence to a treatment plan has been shown to correlate with poorer outcomes.[101]

Primary resistance, where treatment with TKIs does not yield desired results, affects 15% to 25% of CML patients. Mechanisms of primary resistance have two potential causes: unsuccessful BCR-ABL inhibition by the treatment (BCR-ABL dependent), inadequate number of normal hematopoietic progenitors in the bone marrow environment (BCR-ABL independent). The main causes of acquired resistance, where initial successful treatment response is followed by relapse of the disease, are BCR-ABL dependent; but a number of BCR-ABL independent resistance mechanisms have also been identified in CML.

1.3.3.1 BCR-ABL dependent resistance mechanisms

BCR-ABL dependent resistance can be caused by BCR-ABL mutations or BCR-ABL overexpression and/or amplification, which can negatively impact the effectiveness of TKI treatment in patients.[102] BCR-ABL mutations, which inhibit drug binding, are the most common cause of drug resistance (Figure 1.12a). Over 100 mutations have been identified to date. Point mutations in the ABL tyrosine kinase domain of BCR-ABL have been found in more than 50% of CML patients with clinical resistance, and are more common in patients with acquired resistance rather than primary resistance.[103] Although the majority of reported BCR-ABL mutations occur in the kinase domain, mutations outside of the kinase domain also exist. In addition, polyclonal mutations, where two or more point mutations occur in the kinase domain

of separate BCR-ABL proteins, and compound mutations, where there are two mutations within the same BCR-ABL protein, also contribute to drug resistance.[104]

Another BCR-ABL dependent drug resistance mechanism is BCR-ABL amplification as result of TKI treatment (Figure 1.12b). In this case, drug still binds to BCR-ABL, but due to higher levels of the target in the cell, not all BCR-ABL is inhibited. Both genomic amplification of *BCR-ABL* gene as well as overexpression of *BCR-ABL* transcripts have been detected in CML patients that have developed acquired drug resistance.[105]

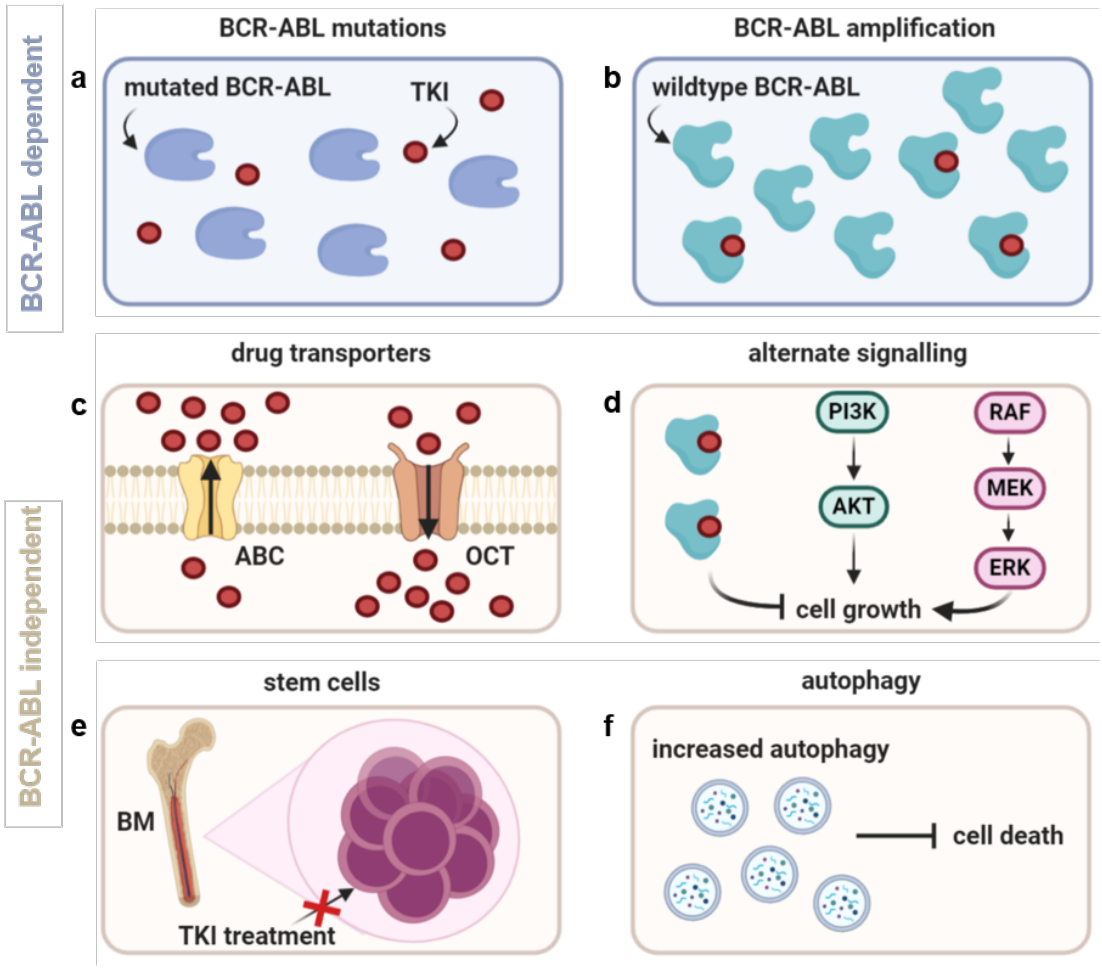

Figure 1.12 Major resistance mechanisms in CML. BCR-ABL dependent mechanism: (a) BCR-ABL mutations, (b) *BCR-ABL* amplification. BCR-ABL independent mechanisms: (c) drug transporters, (d) alternate signalling pathways, (e) CML stem cells, (f) autophagy. Image created with Biorender.

1.3.3.2 BCR-ABL independent resistance mechanisms

Although less prevalent, approximately 40% of relapsed patients have uncharacterised BCR–ABL independent mechanisms of resistance. Therefore, investigating these mechanisms for further improvement of CML therapy is crucial. BCR-ABL independent mechanisms of resistance include activation of alternate pro-survival signalling pathways, drug influx–efflux activity, inherently resistant stem cells, as well as increased autophagy.

The activation of additional pro-survival signalling mechanisms overcomes the dependence on BCR-ABL signalling in CML cells (Figure 1.12d). A number of signalling pathways have been found to be associated with BCR-ABL independent resistance mechanisms. JAK2/STAT5 and RAF/MEK/ERK signalling pathways have both been associated with BCR-ABL independent resistance in CML.[106,107] The PI3K signalling pathway was found to be upregulated by a number of independent studies.[108-110] Elevated levels of FOXO1 were found in imatinib and dasatinib dual-resistant cells, while increased mTOR was found in ponatinib resistant cells.[109] In both cases, PI3K inhibition was proposed as a novel treatment approach to overcome the BCR-ABL independent TKI resistance mechanism.

Drug transporters, which control intracellular drug levels, can also confer resistance to TKI therapy in CML (Figure 1.12c). Both membrane influx pumps, such as the human organic cation transporter 1 (OCT1), and efflux pumps, such as ATP-binding cassette (ABC) members have found to play an important role. OCT1 is required for imatinib transport into the cell, where low OCT1 levels are associated with a suboptimal treatment response, requiring a dose increase.[111] Overexpression of ABC efflux transporters P-glycoprotein (Pgp), ABCA3, ABCC2, and ABCG2 has also been found to negatively impact treatment efficacy in CML.[112,113]

CML stem cells have been found to be the cause of minimal residual disease in treated patients, hence driving relapse and disease progression.[102] Leukemic stem cells (LSC) are $CD34^+/CD38^-$ and BCR-ABL positive, only accounting for less than 1% of $CD34^+$ cells at diagnosis.[103] These cells do not require BCR-ABL activity for their survival and as a consequence are primarily resistant to TKI treatment (Figure 1.12e).[114] Leukemic stem cells possess multiple features which promote TKI resistance, including the deregulated expression of BCR-ABL and a high degree of genetic instability.[115] Targeting of CML stem cells remains an important challenge to

remove the current need for indefinite therapy with TKIs and increase the possibility of obtaining a cure for CML.

1.4 Autophagy

Autophagy is a term that describes the delivery of cytoplasmic constituents to the lysosomes for degradation.[116] Cells use autophagy to mitigate metabolic and therapeutic stresses, remove waste and manage toxic by-products of anabolism and catabolism, including reactive oxygen species (ROS).[117] As such, autophagy induction can happen under various stress conditions such as nutrient or growth factor deprivation, oxidative stress, and drug treatment. Increased autophagy has also been found to drive BCR-ABL independent resistance in CML (Figure 1.12f). The specific role of autophagy in CML is discussed further in Section 1.4.2.

The molecular mechanisms of autophagy are described in Figure 1.13. Autophagy is initiated upon inhibition of mammalian target of rapamycin (mTOR), leading to activation of Unc-51 like kinase (ULK1/2) complex which in response starts phagophore formation.[118] The class III phosphoinositide 3-kinase (PI3K-III) is critical for further expansion of phagophores. Maturation of phagophores into autophagosomes, double-membraned vesicles that are the main mediators of autophagy, is mediated by microtubule-associated protein 1 light chain 3 (LC3). LC3-I lipidation with a phosphatidylethanolamine (PE) to form LC3-II on the surface of autophagosomes is facilitated by ubiquitin-like enzymes ATG7 and ATG3. Complete autophagosomes then fuse with lysosomes to form autolysosomes. Lysosomes have an acidic lumen containing pH-sensitive digestive enzymes that can break down waste materials and cellular debris inside the autolysosome. Degradation inside autolysosome removes unwanted cellular materials such as damaged proteins, and provides the cell with new building blocks for cellular maintenance.

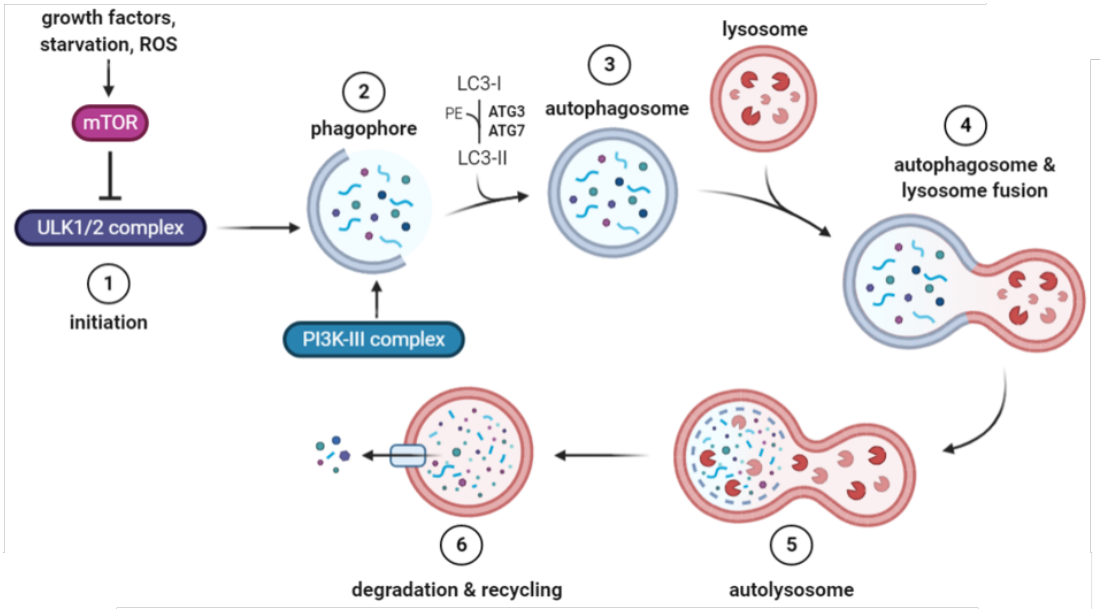

Figure 1.13 Molecular mechanisms of autophagy. 1) Autophagy initiation starts with the activation of the ULK1/2 kinase complex. 2) Phagophore formation and maturation dependent on PI3K-III complex 3) Autophagosome completion upon LC3-II incorporation into the autophagosome double membrane. 4) Autophagosome fuses with the lysosome to form autolysosome. 5) Inside the autolysosome, the inner single membrane of the autophagosomes and its cargo is lysed by lysosomal hydrolases, including cathepsins. 6) The degraded content is recycled back into the cell. Image created with Biorender.

1.4.1 Autophagy as a therapeutic target

Modulation of autophagy activity is implicated in a number of different disease areas, including neurodegeneration, infectious diseases, and cancer.[119] In neurodegenerative diseases, autophagy serves to help eliminate misfolded, toxic protein aggregates through a process called aggrephagy; and damaged mitochondria through a process called mitophagy. Pharmacological stimulation of autophagy is being investigated as a therapeutic strategy against neurodegenerative diseases.[120] Autophagy is also involved in a variety of immune functions, such as removal of intracellular bacteria, inflammatory cytokine secretion and control of inflammation. In a process called xenophagy, autophagy plays a key role in fighting off invading bacteria.[121]

The role of autophagy in cancer is multifaceted. Prior to the onset of tumorigenesis, autophagy has a cytoprotective role, where loss of autophagy is associated with a higher risk of cancer development.[122] In contrast, autophagy has also been found to provide cancer cells with metabolic plasticity, which allows them to survive under

suboptimal conditions.[123] Additionally, autophagy induction is a side effect of many cancer therapies.[124] As a result, the inhibition of autophagy has become a desirable pharmacological target, with an aim to improve the efficacy of existing therapies and to prevent resistance to treatment.[125]

There have been numerous clinical trials for cancer treatment, where the inhibition of autophagy has been used in combination with other therapeutic agents.[117] All of these studies have used chloroquine (CQ) and its derivative hydroxychloroquine (HCQ) as the autophagy inhibitors. CQ and HCQ both impair the autophagy pathway by inhibiting autophagosome and lysosome fusion in the autophagy process (Figure 1.13). These drugs have been approved for the treatment of malaria and arthritis for decades, but have limitations as autophagy inhibitors. As non-specific autophagy inhibitors, they can exert anti-tumour effects via other mechanisms than just inhibition of autophagy.[126] In that regard, it is not entirely unsurprising that clinical trials with CQ and HCQ have not delivered the required potency for effective autophagy inhibition in patients. More potent alternatives are being investigated in preclinical studies.[127]

1.4.2 Autophagy in CML drug resistance

Increasing evidence indicates that autophagy plays a critical role in CML tumorigenesis, progression, and treatment.[118] Autophagy acts as protective mechanism in CML, where imatinib treatment has been shown to increase autophagy. The induction of autophagy in response to drug treatment is associated with persistence and recovery of a subpopulation of CML cells.[128] Bellodi *et al.* found that combination treatment with imatinib and autophagy inhibitor CQ resulted in increased cell death *in vitro*, and sensitised inherently TKI-resistant CML stem cells to treatment.[129]

The efficacy of HCQ and imatinib combination treatment in previously treated CML patients with residual disease was assessed in a phase II clinical trial.[130] The results were published in 2020, concluding that combination treatment with HCQ (400-800 mg daily) and imatinib provided only modest improvement over imatinib treatment alone, and the primary end point of the study was not met. One reason for trial failure was reported to be inability to achieve adequate HCQ plasma levels to accomplish meaningful autophagy inhibition, highlighting the clinical need for more potent autophagy inhibitors.

Combined inhibition of autophagy and mTOR, as well as autophagy and the Hedgehog pathway, have also been shown to be promising approaches to successfully induce apoptosis in ponatinib-resistant and imatinib-resistant CML cells, respectively.[109,131] Both of these studies also demonstrated that specific inhibition of key autophagy proteins, autophagy-related 5 (ATG5) and ATG7, also sensitised drug resistant CML cells to treatment *in vitro*.

Although progress has been made in investigating the role of autophagy in CML, particularly in the context of drug resistance, the exact mechanisms still remain unclear; and have not yet yielded a novel therapeutic option for CML treatment.

1.5 Lysosomes

The term 'lysosome' means 'digestive body' in Greek. Lysosomes were discovered by Christian de Duve in 1955, who described the discovery as serendipitous.[132] Lysosomes are mostly known for their role as the primary degradative compartment in eukaryotic cells. They degrade both extracellular material that has been internalised by endocytosis as well as intracellular components that have been sequestered by autophagy.[133]

The defining characteristic of lysosomes is the acidic pH within the lysosomal lumen, which ranges between ~4.5 and 5.5, and provides an optimal environment for the function of pH-sensitive hydrolases. Vacuolar H^+ ATPase (v-ATPase) on the lysosome membrane is responsible for maintaining the low pH inside the lysosome by pumping in hydrogen ions (Figure 1.14).[134] Lysosome outer membrane is composed of a single phospholipid bilayer that is decorated with transmembrane proteins, including the lysosome-associated membrane protein (LAMP)1 and LAMP2, which together total 50% of lysosomal membrane proteins. Inside the acidic lumen, there are about 60 known resident acid hydrolases, which facilitate the degradation of a vast array of macromolecules and lead to the production of amino acids, monosaccharides, and free fatty acids.

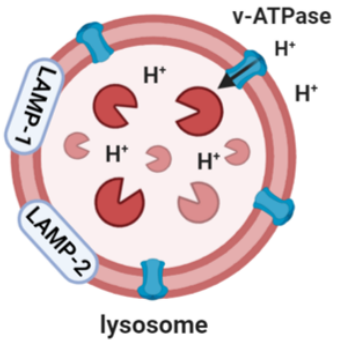

Figure 1.14 Schematic of the lysosome. Acidic pH in the lysosome lumen is achieved by the proton pump v-ATPase on the lysosome membrane. The most abundant proteins on the lysosome membranes are LAMP1 and LAMP2. Hydrolases within the lysosomal lumen are optimised to work under acidic conditions, where each hydrolase targets specific substrates for degradation. Image created with Biorender.

1.5.1 Lysosome biogenesis

There are multiple endocytic and scavenging pathways that lead to lysosome formation in the cell, starting with the transportation of endocytosed material to the early endosome (Figure 1.15). Extracellular material and pathogens are endocytosed through macropinocytosis and phagocytosis respectively, while plasma membrane–localised proteins such as signalling receptors are internalised via clathrin-mediated endocytosis.[134] Early endosomes act as the sorting centre in the cell, deciding whether internalised cargo is retained in the cell or transported back to the cell membrane for disposal. The maturation from early endosomes to late endosomes involves changes in the external protein and lipid coat by progressive acidification of the lumen. Hydrolytic enzymes and lysosomal membrane proteins are delivered to the maturing late endosome via fusion with post-Golgi vesicles transporting the cargo. Through further acidification and a series of additional steps, the lysosome is finally formed.[135] However, degradation of contents delivered to the lysosome is not the end-point of lysosomal function.

While lysosomes were originally thought to be simple cellular recycling machines, it is becoming increasingly evident that their role in cellular homeostasis is much more complex. Lysosomes are involved in a number of important biological processes, including phagocytosis, autophagy, plasma membrane repair, as well as cholesterol homeostasis.[133] Lysosomes can also trigger cell death via cathepsin release into the cell cytoplasm.

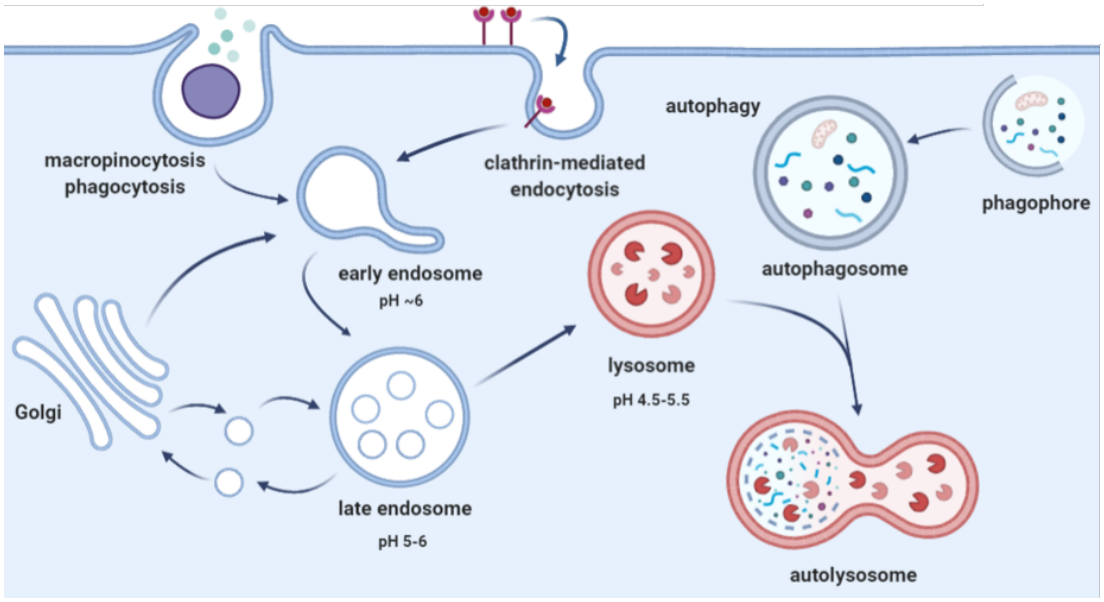

Figure 1.15 The endolysosomal system. Early endosome formation can be triggered by micropinocytosis of extracellular cargo, phagocytosis of pathogens or clathrin-mediated endocytosis of membrane-bound proteins. The Golgi-apparatus delivers hydrolases and proteins to the endosome in the form of vesicles to drive endosome maturation, acidification, and finally lysosome formation. Lysosomes are involved in a wide array of cellular processes, including autophagy. Image created with Biorender.

Lysosome biogenesis is a complex, tightly controlled cellular process. The impairment of lysosomal biogenesis pathways is implicated in a number of degenerative storage diseases, including lysosomal storage disorders and late-onset neurodegenerative diseases.[136] Transcription factor EB (TFEB) is a major regulator of lysosome biogenesis that coordinates the expression of lysosomal hydrolases, lysosomal membrane proteins, as well as autophagy proteins in response to sensing lysosomal stress.[137]

1.5.2 Lysosome biogenesis in CML

Lysosomal function plays an important role in cancer, where disease progression has been associated with changes in lysosomal volume, composition and cellular distribution.[138] Increased lysosomal drug uptake and lysosome size are also involved in cancer drug resistance.[139] Lysosomal targeting has been investigated in preclinical studies. Treatment with mefloquine, an anti-malarial agent with reported anti-cancer properties, caused lysosomal disruption and selectively induced cell death in acute myeloid leukaemia (AML) cell lines, AML stem cells, and *in vivo*.[140]

As lysosomes are involved in the autophagy process, and autophagy has been shown to be increased in CML, it is therefore unsurprising that lysosomes are also implicated in CML. Yi *et al.* investigated the effects of combination treatment using mefloquine and TKIs in stem cells derived from blast phase CML (BP-CML) patients that were resistant to TKI therapy.[141] They found that mefloquine enhanced the cytotoxicity of TKI treatment, and selectively killed drug resistant BP-CML stem cells, including ones harbouring the T315I point mutation. In addition, they showed that the mefloquine mechanism of action is biphasic – initially increasing lysosomal biogenesis and activation in CML cells, followed by oxidative stress, lysosomal lipid damage and lysosome functional impairment. This study shows that lysosomal targeting is potentially a viable option for targeting drug resistance in CML.

1.6 Spheroids

A spheroid is defined as a non-substrate-adherent, aggregated, mutually adherent population of cells adopting a spherical (-like) shape.[142] To grow spheroids, cells are cultured as aggregates with or without scaffold materials, or are embedded in gels.[143-145] Cell aggregates have many different names; ranging from mammosphere and micromass to spheroids.[146,147] In this thesis, the term spheroid is used to indicate a 3D cell aggregate (not necessarily constituting a perfect spherical shape) that does not adhere to any culture substrate (e.g. polystyrene).

Spheroids can form different morphologies depending on cell type and culture conditions (Figure 1.16).[148] When a panel of 25 breast cancer cell lines were grown in 3D on top of laminin-rich extracellular matrix (ECM) gel, four distinct 3D morphologies were identified – round, mass, grape-like and stellate. Round spheroids display organised nuclei and have robust cell-cell contacts (e.g. S1 cell line). Mass and grape-like spheroids both have disorganised nuclei, but mass spheroids form strong cell-cell contacts (e.g. BT-474 cell line) whilst grape-like spheroids form weak cell-cell contacts (e.g. SK-BR3 cell line). Stellate spheroids had distinct elongated cell bodies with disorganised nuclei (e.g. BT-549). This demonstrates heterogeneity within the 3D morphology of different cell lines, which will have an impact on drug penetration and distribution during screening. 3D morphology also influences their experimental handling - spheroids made of loosely arranged cells can be difficult to handle as they tend to disintegrate easily.

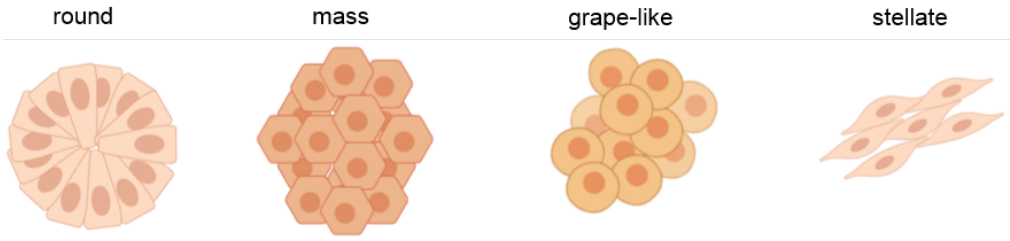

Figure 1.16 Schematic representing the various morphologies of spheroids. Spheroids adapt various shapes depending on the culture conditions and inherent nature of the cells. Image created with Biorender.

Large spheroids (~500 µm in diameter) display physicochemical gradients similar to micrometastases and small avascular tumours (0.5-1 mm^3) (Figure 1.17).[149] Limited diffusion (~150-200 µm) decreases oxygen and nutrient availability at the core of the spheroid, and causes metabolic waste accumulation at the core.[150] Oxygen deficiency induces hypoxia at the spheroid core, resulting in changed gene expression, increased aerobic glycolysis, lactic acid production and decreased pH (0.6 pH units).[151] Build-up of metabolic waste also causes both necrotic and apoptotic cell death at the hypoxic core.[152] The core is surrounded by a layer of viable quiescent cells, while the outer layer consists of proliferating cells.[153] Spheroid size and cell density greatly impacts the generation of physicochemical gradients and biological zones in the spheroid, influencing their response to drugs.

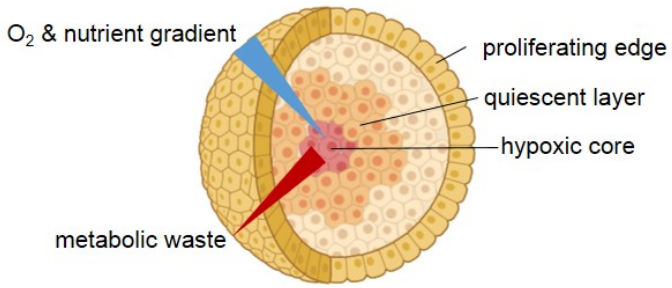

Figure 1.17 Schematic representing physicochemical gradients in a spheroid and the resulting spheroid structure. Availability of O_2 and nutrients (blue triangle) decreases with increasing depth of the spheroid. Metabolic waste accumulation (red triangle) is highest in the middle of the spheroid compared to the edge. There is a hypoxic core in the middle of the spheroid, a middle layer of quiescent cells and the peripheral layer of proliferating cells. Image created with Biorender.

1.6.1 Spheroid growth methods

Numerous different methods have been developed over the years to grow spheroids. Broadly, they can be categorised into scaffold-based or scaffold-free.[154] Scaffold-based methods make use of an external matrix, where the spheroid is grown either on top of the matrix or embedded in the matrix (Figure 1.18a). Natural matrices include hydrogels such as collagen, matrigel and gelatin. Synthetic hydrogels such as polyethylene glycol (PEG), polyglycolic acid (PGA), polylactic acid (PA) as well as peptides are also used to enhance spheroid growth. These scaffolds mimic the ECM and can provide both structural and physical support for spheroid formation, but also allow the cells to spread and migrate in 3D. However, automation of scaffold-based spheroids for use in high content screening (HCS) would be challenging as most matrices are temperature sensitive, requiring active temperature-control. In addition, variability in z-plane location of spheroids can cause problems during data collection and analysis.[155]

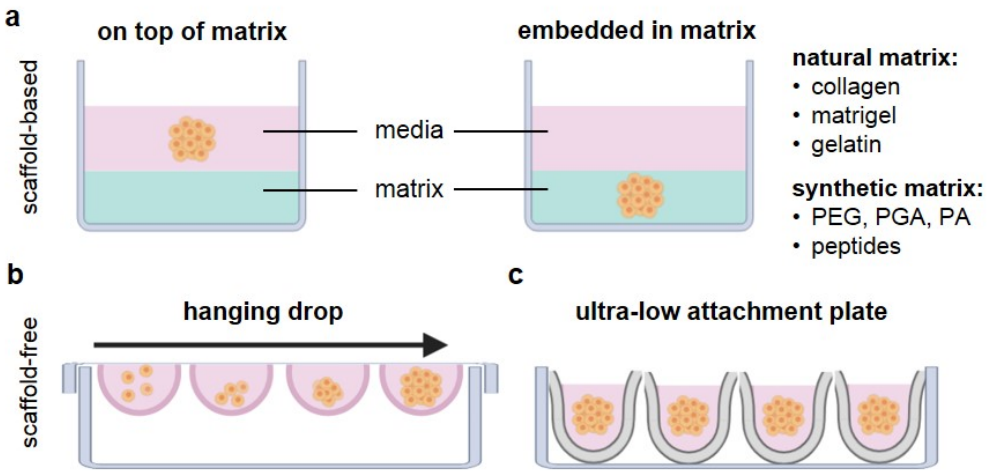

Figure 1.18 Methods for growing spheroids. (a) Scaffold-based methods involve growing a spheroid either on top of a matrix or embedded in matrix. Matrices used are either natural (e.g. collagen, matrigel, and gelatin) or synthetic (e.g. PEG, PGA, PA, peptides). Scaffold-free methods include (b) the hanging drop method (arrow indicates spheroid growth over time in the droplet) and (c) ultra-low attachment plates. Image created with Biorender.

The two most commonly used scaffold-free methods are the hanging droplet method (HDM) and the use of ultra-low attachment plates.[154] In the HDM, the cells self-aggregate in the media as there is no available surface for attachment (Figure 1.18b). Due to the limited size of the droplet, fresh culture medium needs to be added regularly to promote spheroid growth with sufficient nutrients. This makes the HDM

generally labour intensive and complex. In addition, it would be necessary to transfer the spheroids to a secondary plate for drug treatment and that is not optimal for HCS.[156]

The second scaffold-free technique for spheroid formation utilises 96- or 384-well U-shaped ultra-low attachment (ULA) plates (Figure 1.18c).[157] Like HDM, it takes advantage of self-aggregation of cells in the presence of no attachment surface. U-shaped ULA plates are often made of polystyrene and treated with hydrophilic or hydrophobic coatings like the non-adherent polymer poly(2-hydroxyethyl methacrylate) (poly-HEMA), which reduces cell attachment to the wells. It allows formation of uniform-sized spheroids within 1-3 days, where a single spheroid per well is formed.[155] This method is compatible with automation and HCS. Rotema *et al.* successfully used it to screen 633 kinase inhibitors and FDA-approved drugs on spheroids grown in ULA plates.[158] Furthermore, Madoux *et al*. developed a custom 1536-well ULA plate for high-throughput screening and used it for a pilot cytotoxicity screen of 3300 drugs.[159] Therefore, in this thesis, we also utilised U-bottom ULA plates for spheroid growth and characterisation prior to Raman imaging.

1.7 Conclusions

High drug attrition rates continue to increase the cost of drug development in the pharmaceutical industry. Pre-clinical imaging of drugs *in vitro* and *in vivo*, which could lead to improved understanding of drug uptake, retention and metabolism, remains a challenge. Raman microscopy, in particular SRS microscopy, combines high molecular specificity with excellent resolution, and shows great potential for applications in drug imaging.

Since the introduction of targeted TKI treatment in 2001, CML, a cancer of the haematopoietic stem cells, has seen a great improvement in patient survival. A significant proportion of patients, however, either have primary resistance to TKI treatment, or develop acquired resistance following TKI treatment for a number of years. Both BCR-ABL dependent and BCR-ABL independent drug resistance have been identified. Increased autophagy has been identified as a BCR-ABL independent CML drug resistance mechanism, and was targeted in a clinical trial involving combination treatment with a nonspecific autophagy inhibitor HCQ and TKI imatinib. Unfortunately, the combination treatment only marginally improved patient response compared to treatment with imatinib alone. Imaging TKIs used for CML treatment by SRS microscopy could help investigate intracellular drug localisation and its potential involvement in CML drug resistance.

1.8 Project aims

The aim of this project was to utilise SRS microscopy to study the intracellular distribution of label-free ponatinib in live CML cells. Ponatinib localisation in cells has not been reported previously. In Chapter 3, the ponatinib imaging protocol was optimised and SRS was used to determine absolute ponatinib concentrations in both drug sensitive and drug resistant CML cell lines. The sensitivity of SRS imaging was demonstrated by showing that nanomolar ponatinib treatment concentrations can be detected using this imaging technique. In Chapter 4, ponatinib accumulation in lysosomes was visualised and its significance in the context of a model of BCR-ABL independent resistance in CML was investigated. Additionally, SRS was used for target engagement studies with CQ and ponatinib combination treatment. Finally, in Chapter 5, SRS microscopy was applied to three dimensional spheroid imaging and ponatinib detection within these spheroids.

Chapter 2 Materials and Methods

2.1 Materials

2.1.1 Solutions and buffers

The composition of all the solutions and buffers used throughout the thesis are listed in Table 2.1 below.

Table 2.1 Solutions and buffers.

Solution/Buffer	Composition
1 M NaCl	58.44 g NaCl 1000 mL dH_2O
1 M Tris HCl pH 8	121.14 g Tris 1000 mL dH_2O adjust pH to 8 using 1 M HCl
0.1 M $NaHCO_3$ pH 8	8.4 g $NaHCO_3$ 1000 mL dH_2O adjust pH to 8 using 1 M HCl
6X Laemmli sample buffer	9% SDS 50% (v/v) glycerol 375 mM Tris (pH 6.8) 0.03% bromophenol blue in water. Before use, add 10% (v/v) β-mercaptoethanol
RIPA buffer	50 mM Tris HCl (pH 8) 150 mM NaCl 1% NP40 0.5% deoxycholate 0.1% SDS prepared in dH_2O
Lysis buffer – Western blot	10 mL RIPA buffer 1 tablet cOmplete™ ULTRA (Roche) 1 tablet PhosSTOP (Roche)
Tris buffered saline (TBS) 10X	200 mM Tris 1500 mM NaCl adjust pH to 7.6, prepared in dH_2O
Tris glycine SDS (TGS) buffer	25 mM Tris 192 mM glycine 0.1% (w/v) SDS

	pH 8.3, prepared in dH_2O
Blocking solution – Western blot	5% BSA (w/v) in TBST
Blocking solution – IF	1% BSA (w/v) in PBS
FACS buffer	10% FBS in PBS
Phosphate buffered saline (PBS)	1 PBS tablet 500 mL dH_2O
PBST	100 µL Triton X-100 100 mL 1X PBS
TBST	100 mL TBS (10x) 1 mL Triton X-100 900 mL dH_2O
Freezing medium	70% Media (RPMI or DMEM) 20% FBS 10% DMSO
MS extraction buffer	50% MeOH 30% MeCN 20% H_2O

2.1.2 Antibodies

2.1.2.1 Primary antibodies

The primary antibodies used in the thesis are listed in Table 2.2, with dilutions for Western blots and immunofluorescence (IF) noted. For Western blots, antibodies were diluted in 5% BSA in TBST. For IF, antibodies were diluted in 1% BSA in PBS.

Table 2.2 List of primary antibodies used.

Antibody	Host	Catalog Nr	Company	WB	IF
α-tubulin	mouse	3873	CST	1:2000	-
ATG7	rabbit	A2856	Sigma Aldrich	1:1000	-
CYP3A4	rabbit	ab135813	Abcam	1:500	-
LAMP1	rabbit	9091	CST	-	1:200
phospho-CRKL (Tyr207)	rabbit	3181	CST	1:1000	
TFEB	rabbit	PA5-65566	Invitrogen	-	1:100

2.1.2.2 Secondary antibodies

Table 2.3 List of secondary antibodies used.

Antibody	Host	Catalog Nr	Company	WB	IF
Anti-mouse IgG, HRP-linked	horse	7076	CST	1:5000	-
Anti-rabbit IgG, HRP-linked	goat	7074	CST	1:5000	-
AlexaFluor™ 488 anti-rabbit	goat	A11008	Thermo Fisher	-	1:400

2.2 Methods

2.2.1 Cell culture methods

2.2.1.1 Cell culture

The cell lines used in this thesis are listed in Table 2.4, a more detailed description of each cell line is in Table 2.5. CML cell lines and the T47D cell line were cultured in RPMI-1640 medium (Gibco) supplemented with 10% fetal bovine serum (FBS, Gibco) and 1% L-glutamine (Thermo Fisher Scientific), and maintained in a humidified atmosphere at 37 °C and 5% CO_2. Ponatinib resistant ($^{Pon\text{-}Res}$) cell lines were grown in the presence of 100 nM ponatinib. SW480 cells were cultured in Dulbecco's modified Eagle's medium (DMEM, high glucose, Sigma-Aldrich) supplemented with 10% FBS and 1% L-glutamine at 37 °C in a humidified atmosphere containing 5% CO_2. Ponatinib (Synkinase) and chloroquine (Sigma Aldrich) stock solutions were prepared in DMSO and diluted in media before addition to the cells at the indicated concentrations.

Table 2.4 Cell lines used in this thesis.

Cell line	Source	Cell line origin	Species
KCL22	Helgason group*	CML	human
KCL22$^{Pon\text{-}Res}$	Helgason group	CML	human
KCL22$^{Pon\text{-}Res}$CRISPR-Ctrl	Helgason group	CML	human
KCL22$^{Pon\text{-}Res}$CRISPR-*ATG7*	Helgason group	CML	human
BaF3-p210	Helgason group	CML	mouse
BaF3-p210$^{Pon\text{-}Res}$	Helgason group	CML	mouse
SW480	ATCC	Colon adenocarcinoma	human
T47D	ATCC	Ductal breast carcinoma	human

* All the CML cell lines were obtained from Dr Vignir Helgason's group at the University of Glasgow. CML: chronic myeloid leukaemia

Table 2.5 Summary of cell lines used in the thesis.

Cell line	Description
KCL22	Human myeloid CML cell line (phase: blast crisis) sensitive to ponatinib treatment.
KCL22$^{Pon-Res}$	Mitchell *et al.* developed a KCL22 cell line with BCR-ABL independent acquired resistance to ponatinib following exposure of KCL22 cells to increasing concentrations of ponatinib for a prolonged period. Ponatinib-resistant (KCL22$^{Pon-Res}$) clones continued to proliferate in the presence of 100 nM ponatinib.[109]
KCL22$^{Pon-Res}$CRISPR-*ATG7*	CML cell line with BCR-ABL independent acquired ponatinib resistance, where autophagy has been impaired. Mitchell *et al.* used CRISPR-Cas9 in KCL22$^{Pon-Res}$ cells to knock down *ATG7*, an essential autophagy gene required for LC3 lipidation.[109] *ATG7* knockdown inhibited LC3B-II formation and autophagy in these cells, measured by both decreased LC3B-II and increased autophagy substrate SQSTM1/p62 levels.[109]
KCL22$^{Pon-Res}$CRISPR-Ctrl	CML cell line with BCR-ABL independent acquired ponatinib resistance, with an empty CRISPR-Cas9 vector.[109]
BaF3-p210	BaF3 cells are early precursors of B lymphocytes that were established from the bone marrow of MRL/LPR, CBA/J, and BALB/c mice.[160] The p210$^{bcr-abl}$ protein is encoded by breakpoint cluster region Abelson (*BCR-ABL*) oncogene, and is the hallmark of CML in humans. p210$^{bcr-abl}$ was introduced into BaF3 cells through retroviral constructs to generate BaF3-p210 cell line.[161]
BaF3-p210$^{Pon-Res}$	BaF3-p210 cells with an acquired resistance to ponatinib. Mitchell *et al.* incubated BaF3-p210 cells with increasing concentrations of ponatinib for a prolonged period. Ponatinib-resistant (BaF3-p210$^{Pon-Res}$) clones continued to proliferate in the presence of 100 nM ponatinib.
SW480	Human colorectal cancer cell line originally isolated from a primary adenocarcinoma in the colon.[162]
T47D	Estrogen receptor positive luminal A type breast cancer cell line derived from a metastatic ductal carcinoma. When grown in 3D, T47D cells form tightly cohesive mass structures displaying robust cell–cell adhesions.[163]

2.2.1.2 Cell counting

Cell solution in media was mixed with Trypan blue dye in 1:1 ratio (50 µL cell solution + 50 µL dye). The cell mixture was pipetted into both chambers of the Tali™ cellular analysis slide (Thermo Fisher Scientific) (25 µL into each). The slide was inserted into a Tali™ Image-Based Cytometer where the cells were manually focused. An average cell concentration was recorded from 20 fields of view that were captured. The second chamber of the analysis slide was recorded in an identical manner. The average of the two cell concentrations was used to calculate a desired cell dilution for experiments.

2.2.1.2 Cryopreservation

Freshly harvested cells from a single confluent T75 flask were pelleted by centrifugation at 300 *g* (3 min) and re-suspended in freezing medium (3 mL). The cell suspension was pipetted into three cryovials (Corning, 1 mL into each). Cryovials were placed inside a Nalgene® Mr. Frosty (Sigma Aldrich) filled with isopropanol, and stored at -80 °C for 24 h to allow for 1 °C/min cooling rate. The cryovials were then transferred into liquid nitrogen for long term storage.

2.2.1.3 Liquid nitrogen recovery

Prior to retrieving cells from liquid nitrogen, media was warmed to 37 °C. Frozen cells in the cryovial were defrosted by pipetting warm media (1 mL at a time) into the cryovial and aspirating the cells to a universal tube containing warm media. The cell suspension was pelleted by centrifugation at 118 *g* (5 min). Cells were re-suspended in fresh media (10 mL), transferred into a T75 cell culture flask and cultured in a humidified atmosphere at 37 °C and 5% CO_2.

2.2.2 Alamar Blue assay

Cells were seeded onto 96 well plates on day -2 (Figure 2.1a) and incubated for 48 h at 37 °C. On day 0, Alamar Blue cell viability reagent (ThermoFisher Scientific) was added to the control plate at 1/10 concentration and incubated at 37 °C for 3 h (Figure 2.1b) prior to measuring the plate fluorescence at 590 nm using a PerkinElmer EnVisionTM 2101 Multilabel reader (Figure 2.1c). Ponatinib was added to the remaining plates at increasing concentrations (0.1 to 5000 nM) and incubated for 48 h at 37 °C (Figure 2.1d). After 48 h, Alamar Blue was added to the drug treated plates for 3 h prior to measuring the plates at 590 nm (Figure 2.1e).

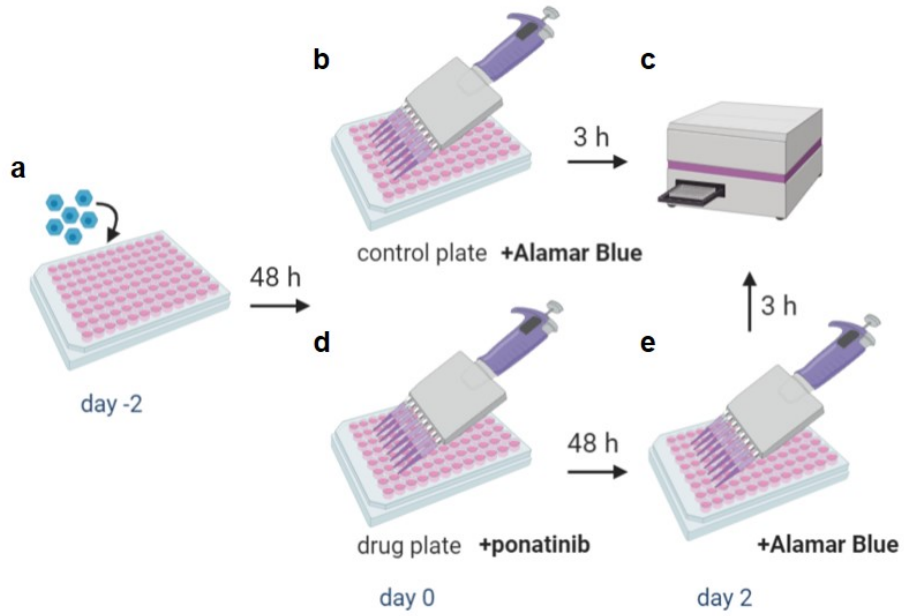

Figure 2.1 Schematic for Alamar Blue assay. (a) Cells were plated onto 96 well plates on day -2 and incubated for 48 h. (b) On day zero, Alamar Blue reagent was added to the control plate and incubated for 3 h. (c) Fluorescence was measured at 590 nm using PerkinElmer EnVisionTM 2101 Multilabel reader. (d) On day zero, ponatinib was added to drug plates and incubated for 48 h. (e) On day two, Alamar Blue reagent was added to the drug plates and incubated for 3 h prior to measuring plate fluorescence. Image created with Biorender.

2.2.2.1 GI_{50} of ponatinib in CML cell lines

Ponatinib concentration causing 50% cell growth inhibition (GI_{50}) in each CML cell line was determined using the Alamar Blue protocol described in Section 2.2.2. To analyse the data, control plate readings (day 0) were subtracted from drug treated plate readings (day 2). These absorption values from six replicate wells were normalised as a percentage of vehicle (DMSO) treated values and GI_{50} values generated using GraphPad Prism. Results presented from 3 independent experiments in Table 2.6.

Table 2.6 GI_{50} values expressed as a mean of n = 3 ± standard error of the mean (SEM) for a panel of CML cell lines.

Cell line	GI_{50} (nM ± SEM)
KCL22	2.4 ± 0.1
KCL22$^{Pon-Res}$	593 ± 88
KCL22$^{Pon-Res}$CRISPR-Ctrl	339 ± 20
KCL22$^{Pon-Res}$CRISPR-*ATG7*	702 ± 55
BaF3-p210	2.3 ± 0.1
BaF3-p210$^{Pon-Res}$	1017 ± 69

2.2.3 Immunofluorescence (IF)

2.2.3.1 Coating fluorodishes for IF

Cell-Tak™ (Corning) was diluted in 0.1 M $NaHCO_3$ (pH=8) to a final concentration of 3.5 µg/cm^2. An aliquot of diluted Cell-Tak™ was added to fluorodishes (550 µL/dish), which were left for 2 h at room temperature (RT). Fluorodishes were washed with sterile water twice, a drop of ethanol was added per fluorodish, and the dishes were left to air-dry in a sterile environment (30 min, RT). Coated dishes were stored at 4 °C and used within 7 days.

2.2.3.2 IF protocol

Cells were adhered to Cell-Tak™ coated fluorodishes (10 min, RT) prior to fixing (4% PFA in PBS, 20 min, RT) and permeabilising (0.1% Triton X-100 in PBS, (PBST), 10 min, RT). Samples were blocked with 1% BSA in PBS (30 min, RT) and incubated with primary antibody (LAMP 1, 1:200, Cell Signalling Technology; TFEB, 1:100, Invitrogen) in 1% BSA in PBS at 4 °C overnight. Samples were washed thrice with PBS, incubated with secondary antibody (AlexaFluorTM 488 goat anti-rabbit, 1:400, ThermoFisher, 1 h, RT) in 1% BSA in PBS, washed thrice with PBST and once with PBS. Finally, samples were labelled with DRAQ7 (1:60, abcam, 30 min, RT), left in PBS and stored at 4 °C before imaging.

2.2.3.3 IF image analysis

LAMP1 immunofluorescence was measured per field of view. Six fields of view were acquired for each sample and analysed on ImageJ. Background intensity was accounted for by setting the minimum intensity from 0 to 150 on each image. (image→adjust→brightness/contrast) Total pixel intensity of the image (RawIntDen)

was then measured. (analyse→measure) Number of cells on the image was obtained by measuring the number of nuclei on the corresponding DRAQ7 image, where cells on the edges were excluded. (image→adjust→threshold; analyse→analyse particles→exclude on edges) Total fluorescence intensity (TFI) per cell was then calculated by dividing the total pixel intensity of the image with the number of cells on the image. Welch's t-test was used to compare the acquired data on GraphPad Prism.

TFEB immunofluorescence was measured per nuclei in the field of view. Six fields of view were acquired for each sample and analysed on ImageJ. Background intensity was accounted for by setting the minimum intensity from 0 to 100 on each image. (image→adjust→brightness/contrast). Number of nuclei on each image was obtained from the corresponding DRAQ7 image, where cells on the edges were excluded. (image→adjust→threshold; analyse→analyse particles→size(pixels)100-infinity; circularity 0.1-1.00;exclude on edges). Mean fluorescence intensity (MFI) was measured inside individual nuclei in each field of view. The Mann-Whitney test was used to compare the acquired data on GraphPad Prism.

2.2.4 Fluorescence activated cell sorting (FACS)

Samples were stained with Lysosensor™ Green DND-189 (1 μM, 1 h, 37 °C, ThermoFisher Scientific), washed with serum free RPMI-1640 by centrifugation (300 *g*, 3 min), re-suspended in PBS +10% FBS and kept on ice prior to immediate processing. Samples were run on the BD LSRFortessa X-20 (SORP) (Becton Dickinson) and processed using BD FACSDiva software (Becton Dickinson). Data was analysed using FlowJo software (TreeStar), where geometric mean values were derived for n=3 biological repeats.

2.2.5 Protein methods

2.2.5.1 Cell lysates

Cells were plated in 10 cm dishes at 1×10^6 cells/dish, incubated for 48 h at 37 °C, and treated as indicated in the figure legends. Cells were washed with PBS (1×10 mL, 1×5 mL) and lysed in 100 μL lysis buffer for 10 min whilst kept on ice. Lysates were centrifuged at 17115 *g* (15 min, 4 °C) and the supernatant transferred to new Eppendorf tubes. Lysates were stored at -80 °C.

2.2.5.2 Protein concentration determination

Lysate protein concentration was measured using a bicinchoninic acid (BCA) assay. Micro BCA™ Protein Assay Kit (ThermoFisher Scientific) was used according to manual, with the microplate protocol used. Plate absorbance was measured at 562 nm and each lysate concentration was measured in duplicate.

2.2.5.3 Western blotting

20 µg of total protein was added to RIPA buffer mixed with 6X Laemmli sample buffer to make up a total of 15-20 µL per sample, and boiled at 95°C for 5 min to denature proteins. Samples were separated by polyacrylamide gel electrophoresis using 4-15% Mini-PROTEAN® TGX™ precast protein gels (Bio-Rad) in a BioRad Mini-PROTEAN 4 gel chamber with TGS buffer (180 V, 40 min).

Proteins were transferred to a nitrocellulose membrane (0.2 µm, Bio-Rad) using a Trans-Blot Turbo Transfer System (25 V, 2.5 A, 10 min, Bio-Rad) and blocked using Western blot blocking solution (1 h, RT). The membrane was immunoblotted with primary antibodies at 4 °C overnight, followed by washing with TBST three times. Secondary antibody was incubated with the membrane (1 h, RT) before washing with TBST thrice. Bound antibodies were visualised by chemiluminescence using Clarity ECL Substrate (Bio-Rad) and the Bio-Rad Gel Doc XRS+ System.

2.2.6 Density functional theory (DFT) calculations†

For each molecule of interest, 20 sample conformers were generated using the distance-based algorithm implemented in RDKit and a basic energy minimisation was performed using the MMFF94 forcefield. The geometry of individual structures was then further optimized at a DFT level according to Becke's three-parameter hybrid method with LYP correlation (B3LYP) using the 6-31G(d) basis set in the gaussian09 program package. Due to the large size of the molecules, Pulay's DIIS method was applied during SCF optimisation.[164] Force constants, and the resulting Raman vibrational frequencies were computed with the same DFT method and basis set. To correct for the an-harmonic nature of bonded atoms, a scaling factor of 0.96 was used to re-scale the high range frequency values.[165] The 10 structures with the lowest single point free energy were used for the data reported.

† Marie Bluntzer performed the DFT calculations.

2.2.7 Liquid chromatography mass spectrometry (LC-MS)‡

CML cells were incubated with ponatinib (5 μM, 1 h) and washed with serum free RPMI media by centrifugation (300 *g*, 3 min). The aspirated cell pellet was extracted using MS extraction buffer (1 mL). The insoluble material was pelleted (21130 *g*, 4 °C, 5 min) and the supernatant collected for analysis. Extracts were vacuum centrifuged to remove solvents before being adjusted to 0.1 % formic acid in a total volume of 50 μL. 10 μL were injected onto a Dionex BioRS using a 100 mm x 2.1 mm C18 Accucore 150 for separation over a 10 min gradient from 5% to 95% acetonitrile (with 0.1 % formic acid throughout). Eluting molecules were ionized with 3.4 kV and analysed on a Thermo Q Exactive with a scan range of 150-600 m/z and resolution 35k. Ion chromatograms were extracted using RawTraces (gitlab.com/jimiwills/rawtraces) and analysed with associated Perl scripts.

2.2.8 Spontaneous Raman spectroscopy

Spontaneous Raman spectra of solid ponatinib were acquired using a confocal Raman spectrometer (inVia™ confocal Raman microscope, Renishaw). A 297 mW 785 nm diode laser, or a 200 mW 532 nm laser excitation source was used to excite the sample through a 20× or 50× objective. CaF_2 slides were used to acquire all spectra to minimise Raman background. The recorded spectral range for grating 1200 g mm^{-1} was 100–3200 cm^{-1}, while the total data acquisition was 10 s for spectra. All spectra were background subtracted using the background correction algorithm available on the WiRE 4.4 software.

2.2.9 Stimulated Raman scattering (SRS) microscopy

2.2.9.1 SRS microscope

Images were acquired using a custom-built multi-modal microscope setup previously described.[49] Briefly: A picoEmerald (APE, Berlin, Germany) laser provided both a tuneable pump laser (720-990 nm, 7 ps, 80 MHz repetition rate) and a spatially and temporally overlapped Stokes laser (1064 nm, 5-6 ps, 80 MHz repetition rate). The output beams were inserted into the scanning unit of an Olympus FV1000MPE microscope equipped with an Olympus XLPL25XWMP N.A. 1.05 objective lens using a short-pass 690 nm dichroic mirror (Olympus). Backscattered emission signals from two-photon fluorescence were separated from scattered excitation light using a short-

‡ Dr Jimi Wills performed LC-MS injections and analysis.

pass 690 nm dichroic mirror and IR cut filter (Olympus). A series of filters and dichroic mirrors were then used to deconvolve the different emission signals onto one of 4 available photo-multiplier tubes (PMT). Lysotracker® Green and Lysotracker® Red two-photon fluorescence signals were filtered using FF552-Di02, FF483/639-Di01 and FF510/84 (Semrock).

For SRS measurements, the Stokes beam was modulated with a 20 MHz electro-optic-modulator (EoM) built into the picoEmerald laser. Forward scattered light was collected using a 20× Olympus XLUMPLFLN N.A. 1.00 objective lens and Stokes light was removed by filtering with an ET890/220m filter (Chroma). A telescope focused the light onto an APE silicon photodiode connected to an APE lock in amplifier with the time constant set to 20 µs except for fast acquisitions where it was set to 4 µs. The lock in amplifier signal was fed into an Olympus FV10-Analog unit. Laser powers after the objective were measured up to 40-70 mW for the pump laser and up to 70 mW for the Stokes laser. All images were recorded at 512 × 512 or 1024 × 1024 pixels with a pixel dwell time between 2 and 20 µs using FluoView FV10-ASW scanning software (Olympus). Where SRS signal quantification was measured, all samples were imaged under identical conditions on the same day.

2.2.9.2 SRS sample preparation

SW480 cells were plated at 5×10^4 cells in FluoroDish Cell Culture Dishes (World Precision Instruments) and incubated at 37 °C for 48 h. Adhered cells were incubated with ponatinib as indicated in the figure legends. Cells were washed with PBS (2 × 2 mL) and either imaged live or fixed with glutaraldehyde (4% in PBS, 10 min, 37 °C) or paraformaldehyde (4% in PBS, 20 min, RT). Following fixation, cells were washed with PBS (2 × 2 mL) and stored at 4 °C prior to imaging.

CML cells were plated in 10 cm dishes at 1×10^6 cells in RPMI (10% FBS, 1% L-Glutamine) for 48 h at 37 °C. Cells were incubated with ponatinib as indicated in the figure legends and washed with serum free RPMI (2 × 10 mL). The cell suspension was centrifuged (300 *g*, 3 min) to remove the media, and 3-5 µL of cell pellet (depending on coverslip size) was pipetted onto a glass slide and covered with a coverslip before live imaging by SRS microscopy.

For multi-modal imaging experiments with Lysotracker® Green or Lysotracker® Red, cells were treated with ponatinib (5 µM, 1 h) or DMSO (1:1000, 1 h) and simultaneously labelled with Lysotracker® Green (ThermoFisher Scientific) (50 nM,

1 h, 37 °C) or Lysotracker® Red (ThermoFisher Scientific) (75 nM, 1 h , 37 °C) and imaged live by SRS microscopy and two-photon fluorescence microscopy.

2.2.9.3 SRS image analysis

ImageJ[166] was used to add false colour assignments, overlays and scale bars to images. Consistent brightness settings were used throughout.

Background subtraction. For each field of view alkyne and off-resonance images were opened on ImageJ. The off-resonance image was subtracted from the alkyne image using the image calculator functionality. (process → image calculator)

Cell segmentation. A recorded cell identification macro[§] was used on ImageJ to identify individual cells. Image of interest was opened (IN_folder) and freehand selection was used to draw around an individual cell in the field of view. The selection was added to ROI manager (Ctrl+T). This was repeated for the desired number of cells. All the selections were saved in the ROIset folder by clicking OK.

(plugin→macros→run→identify_cells.ijm→IN_folder→ROIset_folder)

Cell segmentation macro was then used to individually extract all the saved cells using the ROIset saved of the image. This macro automatically saves individual cell images into a separate folder.

(plugin→macros→run→extract_cells.ijm→IN_folder→ROIset_folder→cells_extracted_folder)

2.2.9.4 Quantifying total intracellular ponatinib concentration

KCL22$^{Pon\text{-}Res}$ cells were treated with ponatinib (5 μM, 1 h), washed and imaged live to determine optimal imaging settings that would prevent pixel saturation. The final laser power settings were set to be 100 mW (the tuneable pump beam) with gain 1.

Calibration curve of ponatinib solutions in DMSO was then acquired. SRS images in the range of 2176 – 2246 cm^{-1} were obtained for each ponatinib concentration as well as DMSO alone in triplicate. The average pixel intensities of each SRS image across the range were calculated using ImageJ. The average pixel intensity values were plotted for each concentration and a Gaussian fitting was applied on Origin. The

[§] Dr Bertrand Vernay developed the ImageJ macros used in this thesis.

resulting peak was integrated, and the peak height was plotted at each concentration to give a ponatinib calibration curve.

KCL22 and KCL22$^{Pon\text{-}Res}$ cells were treated with ponatinib (5 μM, 1 h), and imaged using identical SRS settings on the same day. Z-stacks were taken for each cell line. Individual cells (n=20) were segmented from these images using ImageJ.

The data from individual cells were loaded into Matlab and processed by Dr Martin Lee. Image data were converted from software counts to a concentration using the parameters of the fitted line in excel unless the intensity fell below the y-axis intercept in which case the value was changed to zero to avoid negative concentrations. This could occur due to noise in the SRS recording but was mainly found in background areas that had been segmented from the original data.

Each pixel was used to represent a 3D volume by multiplying by pixel width, height and z-stack spacing. Using the volume and concentration from the pixel intensity a corresponding amount of ponatinib in that area scanned could be calculated. The total amount of ponatinib in the cell was calculated by summing all the data from each pixel and each image stack across all recorded images for that cell.

Cell size measurements were taken using the recorded settings for image height and the area from the manual image segmentation image to calculate the average concentration of drug across the cell.

2.2.9.5 Quantifying relative ponatinib levels at biologically relevant doses

KCL22$^{Pon\text{-}Res}$ cells were treated with ponatinib (500 nM) for either 1 h, 6 h, 24 h or 48 h. These cells were washed twice and imaged live using SRS microscopy at identical conditions (laser power 300 mW for the tuneable pump beam, gain 2). In order to maintain identical settings for all the samples in triplicate, the microscope was only used for this particular experiment over a two week period. Individual cells were segmented from a field of view (n=30) at each time point using ImageJ as described in Section 2.2.9.3. Average ponatinib Raman signal intensity (C≡C, 2221 cm^{-1}) was measured for each individual cell on ImageJ. (analyse→measure) The results were compared to the DMSO control cells using GraphPad Prism.

2.2.9.6 Quantifying relative ponatinib levels inside and outside lysosomes

CML cells were treated with ponatinib (5 μM, 1 h) and labelled with Lysotracker® Green (50 nM, 1 h) or Lysotracker® Red (75 nM, 1 h) simultaneously. The samples were washed twice with serum free media and imaged live immediately using multi-modal imaging. Optimal SRS and fluorescence settings were chosen whilst imaging the first sample of the day and kept constant throughout the day for quantitative imaging.

Images were processed and analysed on ImageJ. For every sample, the background subtraction was performed first as described in Section 2.2.9.3. Individual cells were extracted from the image as described in Section 2.2.9.3. ImageJ analysis workflow for measuring relative ponatinib intensity inside and outside lysosomes is shown in Figure 2.2. Three images that were used for the analysis included TPF (Lysotracker), ponatinib (2221 cm^{-1}) and ponatinib background subtracted. Lysosomes were highlighted in the Lysotracker image using the thresholding function. (image→adjust→threshold) This was converted into a map of lysosomes in the cell. (edit→selection→create selection) The map was transferred onto the subtracted ponatinib image. (Ctrl+shift+E) The relative Raman intensity of ponatinib inside lysosomes was measured, giving the mean and the maximum ponatinib intensities. (analyse→measure) The lysosome map was then transferred onto the ponatinib alkyne on-resonance image (2221 cm^{-1}), where the data inside the lysosomes was cleared. (Ctrl+shift+E→edit→clear) Thresholding function was used to highlight the rest of the cell aside from lysosomes, which was converted into a second map. (image→adjust→threshold→edit→selection→create selection) The cell map was transferred onto the subtracted ponatinib image. (Ctrl+shift+E) The relative ponatinib Raman intensity outside of the lysosomes was measured. (analyse→measure) This was repeated for n=30 cells from each sample.

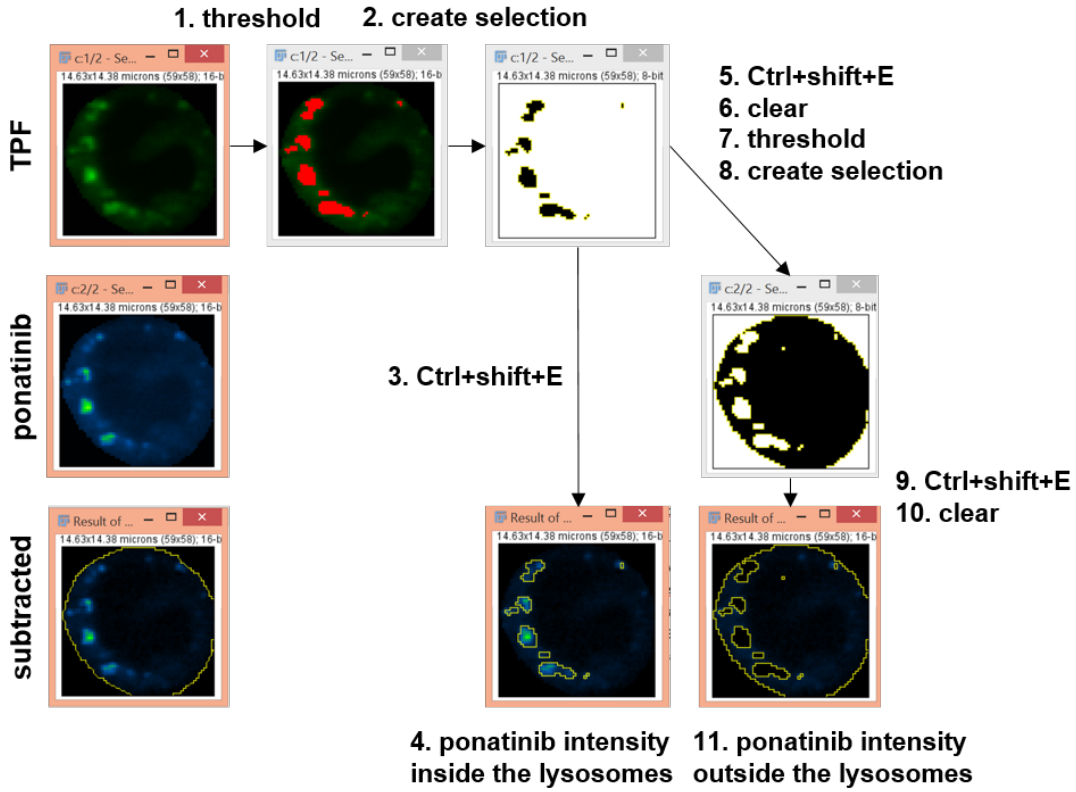

Figure 2.2 ImageJ workflow for analysing relative ponatinib intensity inside and outside lysosomes.

2.2.10 Statistical analysis

All statistical analyses were done using GraphPad Prism software. Figure 2.3 shows the workflow used to analyse the data. For each dataset, D'Agostino-Pearson normality test and Shapiro-Wilk normality test were used first to assess if the data follows Gaussian distribution. If two datasets of interest were compared and both passed the normality tests, Welch's t-test was applied. If more than two datasets were compared to each other that were normally distributed, one-way ANOVA with Tukey's multiple comparisons test was used. However, where two or more independent variables were compared two-way ANOVA with Sidak's multiple comparisons test was used. In case the data was not normally distributed, the non-parametric Mann-Whitney test was used to compare two datasets and the Kruskal-Wallis with Dunn's multiple comparisons test was used to compare three or more datasets.

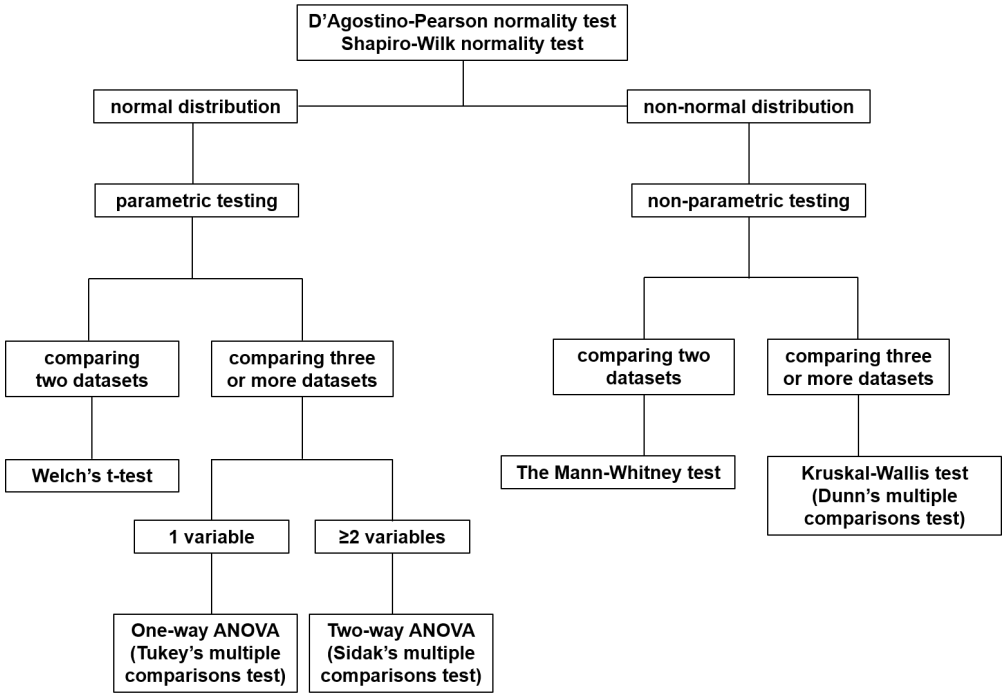

Figure 2.3 The workflow used to perform statistical testing of data on GraphPad Prism software.

2.2.11 Spheroid protocol

Spheroids were generated as previously described.[157] Briefly, cells were grown as a monolayer and seeded at 250-20,000 cells per well in an ultra-low attachment U-bottom 96-well plate (Corning). Plates were then centrifuged at 1000 *g* for 10 min. The plates were incubated under standard cell culture conditions at 37° C, 5% CO_2 in humidified incubators. Spheroid plates were imaged at time points stated in figure legends at 4× magnification in the transmitted light channel using the ImageXpress Micro XLS (Molecular Devices). On day seven post seeding the spheroids were labelled with Calcein-AM (ThermoFisher Scientific, 3.5 µM), propidium iodide ThermoFisher Scientific, 1 µM) and Hoechst 33342 (ThermoFisher Scientific, 1 µM) for 1 h in an incubator before imaging in the appropriate fluorescent channels (DAPI, FITC, Texas Red) using ImageXpress.

ImageXpress was used to create a single flattened z-stack image from an eight-step z-stack with a 50 µm step size. A 2D maximum intensity projection was used for fluorescent images and a 2D minimum intensity projection for transmitted light images. A custom CellProfiler pipeline was used to quantify the spheroid area and fluorescence intensities for each spheroid.[167]

Chapter 3 Optimisation of ponatinib imaging by SRS microscopy

3.1 Introduction

Drug imaging of protein kinase inhibitors (PKIs) by Raman microscopy is not a widely used technique, with only a few examples existing in the literature.[168-171] No PKI's have been imaged using standard SRS microscopy. As such, there are no 'standard' protocols and guidelines available to use when imaging by SRS microscopy. In this chapter, DFT calculations and LC-MS analysis were used to validate our SRS imaging approach for ponatinib, a PKI used for the treatment of CML. With the goal of imaging ponatinib in live CML cells in a quantitative manner, the SRS imaging protocol was optimised to achieve the most reliable and robust results from our custom-built microscope.[172] Part of this work has been published in a peer-reviewed journal.[173]

3.1.1 Protein kinase inhibitors

The last two decades have seen a significant increase in the development of molecularly targeted therapies in oncology, namely small molecule protein kinase inhibitors.[174] Protein kinases are involved in the pathogenesis of a number of diseases, including cancer. In 2001, imatinib was approved as the first therapeutic PKI by the FDA and since then a total of 52 PKIs have successfully passed clinical trials.[175] The majority of these (46) are oncology drugs, demonstrating that kinases are effective targets in combatting cancer. It is therefore unsurprising that they have become an important drug target in the pharmaceutical industry.[176,177] Up to 33% of drug discovery today involves protein kinases, with 175 candidates in clinical trials in 2018.[178]

3.1.2 Drug imaging of PKIs using Raman microscopy

Although recent years have seen an unprecedented number of new drugs approved by the FDA, preclinical evaluation of intracellular localisation of drug candidates remains a challenge. Raman microscopy has been applied to the visualisation of a number of PKIs since 2014, demonstrating its potential as a drug imaging tool.

3.1.2.1 Imaging by spontaneous Raman spectroscopy

El-Mashtoly *et al.* were the first to use spontaneous Raman spectroscopy to visualise a PKI.[168] It was applied to imaging erlotinib, an Epidermal Growth Factor Receptor (EGFR) inhibitor that is used as a first line treatment for non-small cell lung cancer.[179] Erlotinib has an inherent alkyne moiety in its structure conjugated with an aryl ring, giving it a comparatively strong alkyne peak in its Raman spectrum (~2100 cm^{-1}, Figure 3.1a). Intracellular erlotinib was detected in colon cancer cells (SW480), demonstrating that it localises in the cell periphery where EGFR are located (Figure 3.1b). Furthermore, using Raman spectroscopy analysis of intracellular erlotinib, they found the intracellular metabolite of erlotinib in SW480 cells to be desmethyl-erlotinib (Figure 3.1a). The human plasma concentration of erlotinib and desmethyl-erlotinib following an oral dose of 150 mg per day, however, has been measured to be 3-5 μM and 0.2-0.7 μM respectively.[180,181] These concentrations are below the detection limit of spontaneous Raman spectroscopy, which is why a higher concentration of erlotinib was used to treat cells in this study (~100 μM). Plasma concentrations, however, are not always reflective of the drug concentration inside a tumour. Patient studies have found in many cases that drug concentration in the tumour is lower than the reported plasma concentration, although the opposite also holds true.[182,183] It is unlikely that clinically relevant intra-tumour concentrations could be imaged.

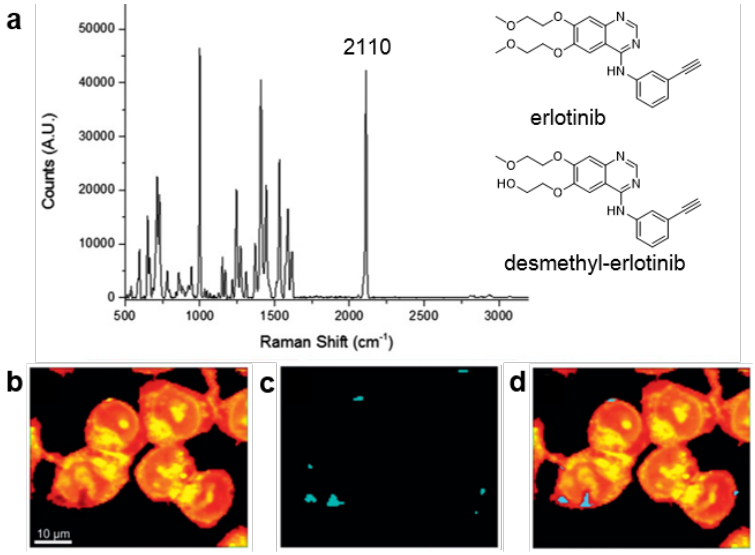

Figure 3.1 Spontaneous Raman imaging of erlotinib. (a) Raman spectrum of erlotinib, alkyne peak at 2110 cm^{-1}. (b-d) Spontaneous Raman images of SW480 cells which were treated with erlotinib (~100 μM, 12 h). (b) Raman image re-constructed from the C-H stretching intensity. (c) Raman image re-constructed from C≡C stretching intensity. (d) Overlay of panels (b) and (c). Adapted with permission,[168] copyright Royal Society of Chemistry.

Yosef *et al.* used spontaneous Raman spectroscopy to image sorafenib, a multikinase inhibitor used for the treatment of a number of cancers including kidney and liver cancer.[171,184,185] One of the targets of sorafenib are rapidly accelerated fibrosarcoma (RAF) family kinases RAF-1, B-RAF, and A-RAF including the B-RAF^{V600E} mutation, which is most often known in melanoma where RAF inhibitors are used to treat B-RAF mutant disease.[186] It has also been found to be prevalent in metastatic colon and lung cancer patients with resistance to EGFR targeted therapy.[187-189] In this study, sorafenib was used in the colon cancer cell line HT29, which harbours the B-RAF^{V600E} mutation. The structure of sorafenib lacks any specific Raman active bands in the cell-silent region. Therefore, a characteristic band from the fingerprint region was used to visualise the drug using 50 μM, 4 h treatments (Figure 3.2). Using immunofluorescence labelling alongside Raman, they showed sorafenib co-localises with the target B-RAF. The measured plasma concentration of sorafenib in metastatic patients after 400 mg dose was up to 13 μM, about 4-fold lower than the concentration required for Raman imaging in this study.[190]

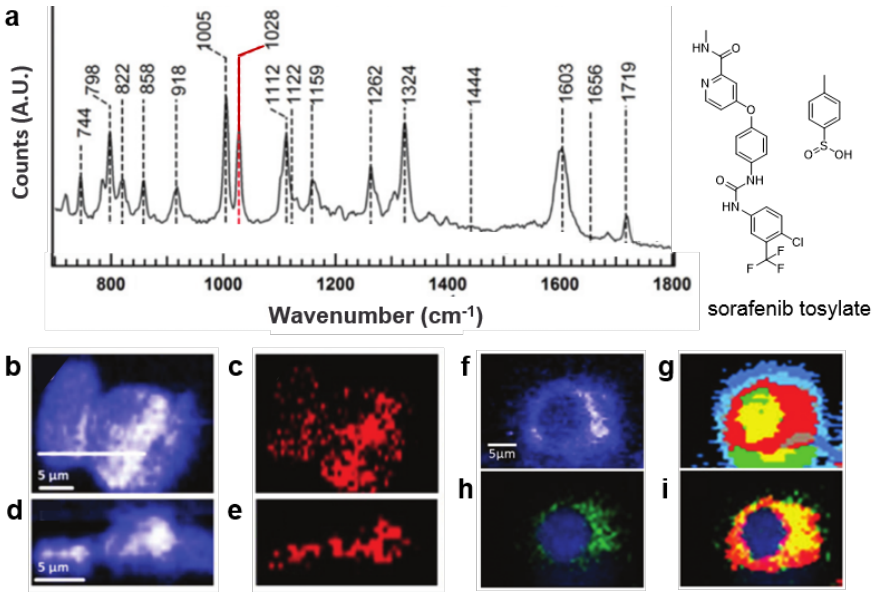

Figure 3.2 (a) Raman spectrum and chemical structure of sorafenib tosylate. (b-i) Raman imaging of HT29 cells treated with sorafenib (50 μM) for 4 h. Raman images reconstructed from (b) 1420–1470 cm^{-1} (C-H bending) and (c) 1015-1040 cm^{-1} (sorafenib without its tosylate). (d), (e) Cross-sectional Raman images along the x–z axis of the same cells. The scanning positions are indicated by the white line in (b). (f) Integrated Raman image of an HT29 cell. (g) The hierarchical clustering of the Raman data shown in (f) containing sorafenib (red). (h) Fluorescence image of the same cell showing B-RAF (green) and the nucleus (blue). (i) Overlay of sorafenib cluster from (g) (red) and (h). Sorafenib and B-RAF co-localisation in yellow. Adapted with permission,[171] copyright Royal Society of Chemistry.

Neratinib, a dual TKI inhibiting EGFR and human epidermal growth factor 2 (HER2) irreversibly, was the first PKI imaged by spontaneous Raman spectroscopy using a sub-micromolar treatment concentration.[169] Although neratinib possesses an inherently Raman active nitrile group in the cell silent region (Figure 3.3a), a strong Raman band in the fingerprint region at 1386 cm^{-1} enabled Aljakouch *et al.* to image the drug in fixed non-small cell lung cancer NCI-H1975 cells following 500 nM, 8 h treatment (Figure 3.3b-g). This is close to the measured neratinib plasma concentration (up to 257 nM).[191] In addition, Aljakouch *et al.* found that the key neratinib Raman peaks shift upon cellular metabolism, giving two different metabolite signatures: M1 (1386→1399: 2208→2217 cm^{-1}) and M2 (1386→1388/1402; 2208→2217 cm^{-1}) (Figure 4.3h). Using LC-MS, they determined the molecular weight of three major neratinib metabolites I (*M* = m/z 449.1), II (*M*=433.1) and III (*M*=461.1). DFT calculations were run to find out which metabolites determined by LC-MS could have contributed to the Raman spectra of M1 and M2. M1 was found to originate from metabolite I, whilst M2 likely originated from metabolite IIb and/or metabolite IIIb (Figure 3.3h). This work demonstrated the potential detection sensitivity of spontaneous Raman spectroscopy. The lack of ability to image drugs in live cells, however, remains, due to the slow image acquisition times of spontaneous Raman.

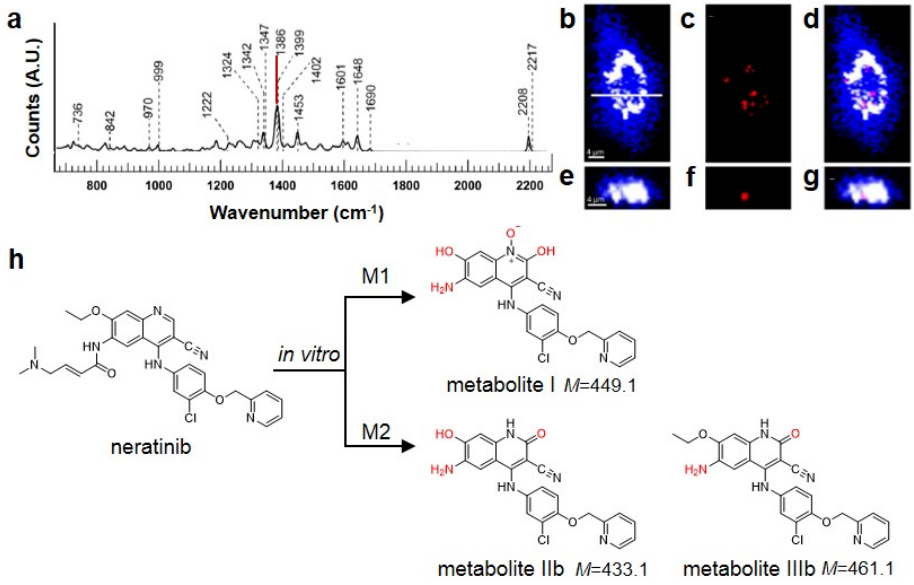

Figure 3.3 (a) Raman spectrum of free neratinib. (b-g) Raman imaging of NCI-H1975 cells treated with neratinib (500 nM, 8 h). Raman images reconstructed from the (b) C-H deformation 1425-1470 cm^{-1} and (c) neratinib 1380-1410 cm^{-1} band intensities. (d) Overlay of (b) & (c). (e-g) Cross-section Raman images along the x, z-direction of the same cell. Scanning positions indicated by the white line in (b). (h) Structures of neratinib and its intracellular metabolites M1 and M2. Adapted with permission,[169] copyright John Wiley and Sons.

3.1.2.2 Imaging by hyperspectral stimulated Raman scattering

Fu *et al.* utilised label-free hyperspectral SRS (hSRS) microscopy to study the drug uptake of imatinib and nilotinib in live CML cells (Figure 3.4).[170] Hyperspectral SRS allows imaging at multiple Raman frequencies simultaneously. The spontaneous Raman spectra of each drug were used to identify the major peaks for both imatinib and nilotinib (Figure 3.4a). The characteristic wavenumber at 1308 cm^{-1} was used to detect intracellular imatinib and nilotinib by analysing hSRS spectra following 4 h treatment with either of the drugs (20 μM) (Figure 3.4b,c). Both drugs were detected as puncta inside CML cells. Furthermore, two-photon excitation was used to measure fluorescent images alongside hSRS, and Lysotracker® Red dye was used to demonstrate drug localisation within lysosomes of the cells.

As SRS is a concentration dependent technique, they were able to measure the intracellular drug concentration of imatinib and nilotinib based on a calibration curve generated by standard drug solutions in DMSO. Interestingly, they found a 1000-fold enrichment of the drugs inside lysosomes. Lysosomal drug trapping, however, reduces cytosolic drug availability and therefore can reduce drug efficacy. It was demonstrated that combination treatment with 20 μM imatinib and 50 μM chloroquine, a non-specific autophagy inhibitor, resulted in a tenfold decrease in the lysosomal imatinib enrichment, and hence an increase in the available cytosolic imatinib. This offers a plausible explanation to why chloroquine has been shown to have a sensitising effect in imatinib-based chemotherapy.[129]

The measured plasma concentrations in CML patients treated with imatinib and nilotinib are 4 μM and 2 μM respectively.[192,193] This is still lower than the concentration used in this experiment (20 μM), highlighting the limitation of hSRS imaging when it comes to using physiologically relevant drug concentrations. Overall, Fu *et al.* showed that hSRS imaging can offer unprecedented capability in label-free drug visualisation, and could be a valuable tool in pharmacokinetic studies.

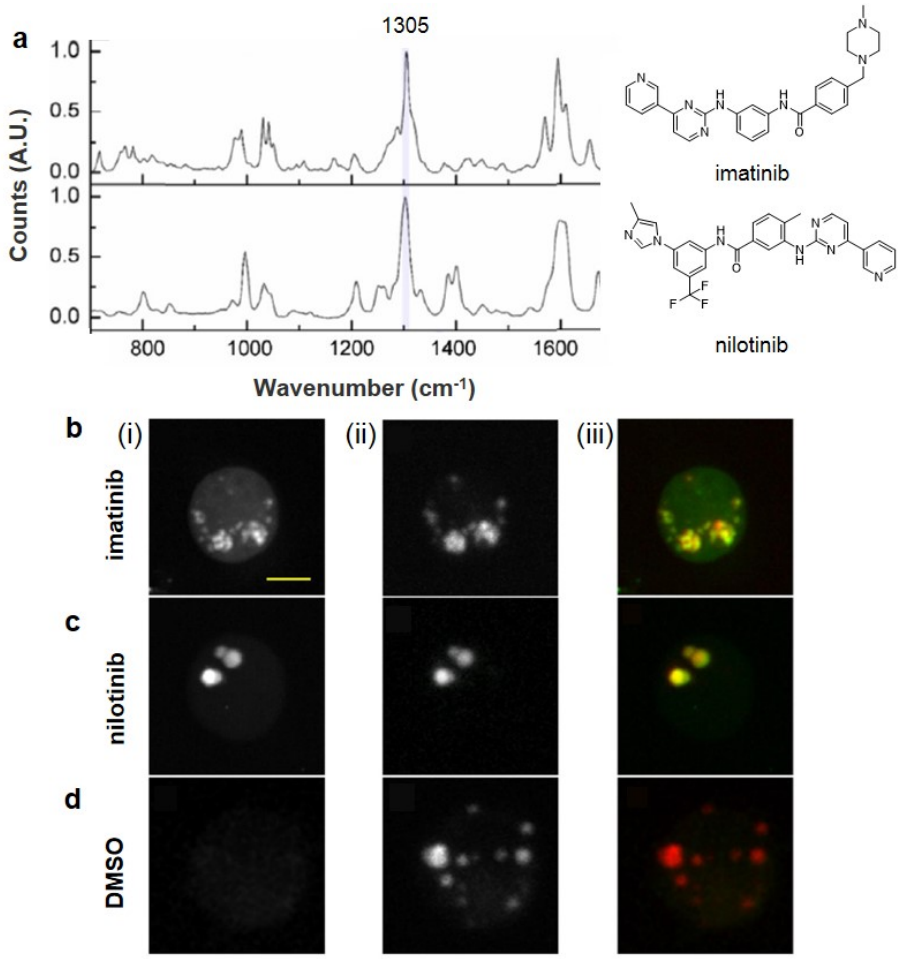

Figure 3.4 (a) Chemical structures and Raman spectra (700-1700 cm^{-1}) of imatinib and nilotinib. 1305 cm^{-1} peak marked in shaded blue used for SRS imaging of both drugs. (b-d) Two-photon fluorescence imaging of Lysotracker® Red and SRS imaging of drug accumulation. BaF3/BCR-ABL1 cells were treated with: (b) 20 μM imatinib, (c) 20 μM nilotinib or (d) DMSO for 4 h. (i) Maximum-intensity projection of 3D SRS images at 1305 cm^{-1}. (ii) Maximum-intensity projection of 3D LysoTracker® Red fluorescence images of BaF3/BCR-ABL1 cells treated with: (b) 20 μM imatinib, (c) 20 μM nilotinib and (d) DMSO only. (iii) Overlay of corresponding SRS images (green) and fluorescence images (red). Scale bar: 5 μm. Adapted with permission,[170] copyright Springer Nature.

3.2 Spontaneous Raman spectroscopy of ponatinib

The BCR-ABL TKI ponatinib (Figure 3.5a) has an inherent alkyne moiety within its structure. This can be used to image the drug's intracellular localisation without the addition of bulky tags such as fluorophores that could affect the biological activity of the drug. We therefore used this to demonstrate the utility of SRS for monitoring spatial and temporal drug distribution, using ponatinib as a model drug for the study. Initial Raman spectroscopy on powdered ponatinib enabled detection of the alkyne peak (2221 cm^{-1}) within the Raman spectrum (Figure 3.5b). This peak is in the 'cell-silent region", between 1800-2800 cm^{-1}, where no inherent cellular Raman peaks are found.[60] Imaging in this region of the Raman spectrum has the advantage of having minimal intracellular background, providing enhanced detection sensitivity.

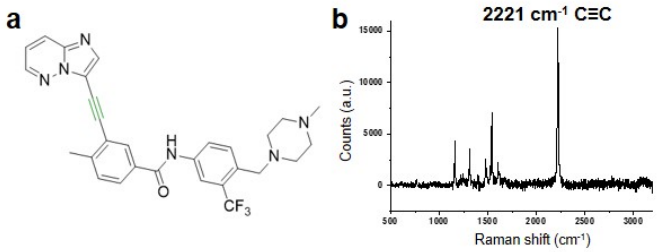

Figure 3.5 (a) Chemical structure of ponatinib. (b) Raman spectrum of solid ponatinib; C≡C peak is annotated at 2221 cm^{-1}. Raman spectra were acquired at λ_{ex} = 532 nm for 10 s using a 50× objective.

3.3 Assessing levels of ponatinib metabolism *in vitro* by LC-MS

Previous imaging of erlotinib and neratinib by Raman microscopy demonstrated that the Raman peak of interest changes upon cellular metabolism.[168,169] Hence, it was important to consider ponatinib cellular metabolism prior to SRS imaging at a single wavenumber. Small molecule drugs are known to be metabolised by cytochrome P450 (CYP) enzymes in the body.[194] CYPs are extremely versatile and catalyse a range of range of reactions, including carbon hydroxylation, heteroatom oxidation, dealkylation, epoxide formation as well as other more complex transformations.[195] In humans, the main five hepatic CYP isoforms catalysing drug metabolism are CYP3A4, CYP2D6, CYP1A2, CYP2C9, CYP2E1.[196] CYP3A4 is estimated to be responsible for the metabolism of over 50% of the drugs on the market; and it is involved in the metabolism of most TKIs.[197]

Research on ponatinib metabolism *in vivo* and in human liver microsomes found the drug is catalysed predominantly by the CYP3A4 enzyme.[198,199] The major ponatinib

metabolites identified in earlier studies include *N*-desmethyl (**2**) and *N*-oxide (**3**) forms of the drug as well as the hydroxylated (**4**) and dihydroxylated (**5**) forms (Figure 3.6).[198,200,201] Lin *et al.* also found that following hydroxylation ponatinib can further react with glutathione (GSH) to form GSH adducts **6** and **7**.[198] They suggest these GSH adducts are formed via an intermediary epoxide formation step.

Our target cell lines for SRS imaging were human CML cell lines KCL22 and the ponatinib resistant equivalent KCL22$^{Pon\text{-}Res}$ (cell lines described in Section 2.2.1.1). We used Western blot analysis to investigate CYP3A4 levels in these cell lines and found both cell lines expressed equal levels of CYP3A4 (Figure 3.7a). This indicated that intracellular metabolism of ponatinib is likely inside these CML cells. To assess the level of all the known metabolites in our human CML cell lines, we treated cells with ponatinib (5 μM, 1 h) and subsequently analysed samples by LC-MS. Ponatinib was found to be by far the most abundant species in the CML cells whilst only trace amounts of *N*-desmethyl (**2**) and dihydroxylated (**5**) metabolites were found (Figure 3.7b). Considering the concentrations of these metabolites in the CML cell lines was very low, their presence is unlikely to affect quantitative SRS imaging of ponatinib at a single wavenumber.

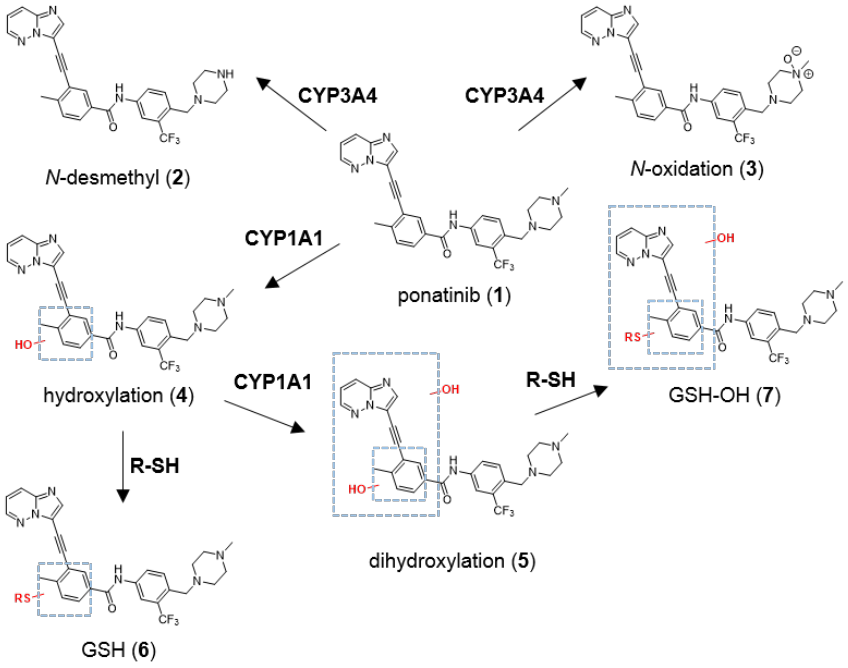

Figure 3.6 (a) Ponatinib (**1**) and its reported metabolites (**2-7**). Metabolism pathways and the major enzymes responsible for each metabolite are shown. CYP3A4 is responsible for *N*-desmethyl (**2**) and *N*-oxidation (**3**) metabolites. CYP1A1 is responsible for hydroxylation (**4**) and dihydroxylation (**5**). Hydroxylated metabolites (**4,5**) can further form adducts with glutathione to for GSH (**6**) and GSH-OH (**7**). Adapted with permission.[198]

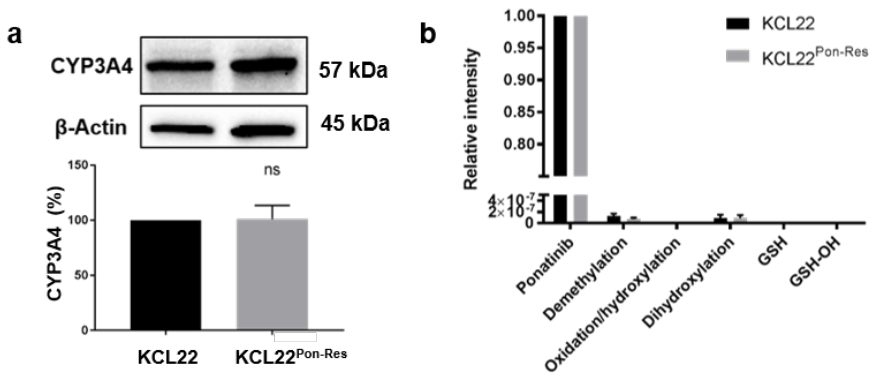

Figure 3.7 (a) Expression of CYP3A4 in lysates from KCL22 and KCL22$^{Pon\text{-}Res}$ cells. β-actin was used as a loading control. CYP3A4 levels were quantified from n=3 biological replicates and normalised to β-actin using Image Lab software. T-test was used to compare CYP3A4 levels in KCL22 and KCL22$^{Pon\text{-}Res}$ cells. (b) Ponatinib and relative ponatinib metabolite levels measured by LC-MS. Cells were treated with ponatinib (5 μM) for 1 h prior to analysis. Mean values (±SEM) from n=5 biological repeats expressed relative to ponatinib.

3.4 Predicting Raman signal intensity and frequency by DFT

In order to account for potential Raman shifts or intensity changes due to intracellular metabolism of ponatinib, DFT calculations[**] were utilised. Theoretical Raman intensities have previously been calculated by DFT and expressed as I_{Ram}.[60,202] Additionally, experimental Raman intensities have been compared to the intensity of the alkyne resonance in the nucleoside analogue ethynyl deoxyuridine (EdU) and reported as relative intensity to EdU (RIE).[45] Here, these two approaches were merged to obtain calculated RIE values (cRIE) for ponatinib as well as the metabolites we found present via LC-MS analysis (Table 3.1). DFT calculations have also been shown to predict Raman vibrational frequency shifts due to primary drug metabolism.[169] Hence, a series of DFT calculations was carried out to determine if the alkyne peak in ponatinib was likely to shift in frequency in the major metabolites; and to confirm that acquiring SRS images at a single vibrational frequency for the alkyne (Figure 1b, C≡C, 2221 cm^{-1}) would be appropriate for assessing ponatinib intracellular localisation and concentration (Table 3.1).

[**] DFT calculations performed by Marie Bluntzer.

Table 3.1. DFT calculated wavenumbers, intensities (I_{Ram}) and relative intensity to EdU values for ponatinib and its metabolites. Standard deviation for 10 lowest energy structures shown. Experimental values in brackets.††

Compound	Wavenumber[a] (cm^{-1})	I_{Ram} ($Å^4$ amu^{-1})	cRIE
EdU	2132 ± 0.74 (2120)[b]	693 ± 57	1.0
ponatinib (**1**)	2217 ± 0.5 (2221)	14649 ±1581	21.1 ± 2.3
ponatinib protonated	2217 ± 0.9	12135 ± 1059	17.5 ± 1.5
N-desmethyl ponatinib (**2**)	2218 ± 0.5	15011 ± 1194	21.7 ± 1.7
dihydroxylated ponatinib (**5**)	2218 ± 0.9	11613 ± 1136	16.8 ± 1.6
neratinib[c]	2228 ± 0.1 2238[d] (2208)[d]	819 ± 16	1.2 ± 0.1

[a] DFT calculated values ±SD with experimentally determined values in brackets. [b] Value reported by Tipping *et al.*[49] [c] C≡N rather than C≡C. [d] Values reported by Aliakouch *et al.*[169]

Ponatinib is susceptible to protonation in acidic organelles inside the cell due to the piperazine unit in its structure.[203,204] Our DFT calculation predicted both ponatinib and its protonated form would have the same alkyne Raman frequency, while the cRIE value was slightly decreased upon protonation (Table 3.1). This confirmed that SRS imaging of ponatinib at a single wavenumber would be accurate across the whole cell environment regardless of variation in subcellular pH. In our LC-MS analysis we identified trace amounts of ponatinib metabolites to be its *N*-desmethyl (**2**) equivalent alongside the dihydroxylated (**5**) form (Figure 3.7b). In *N*-desmethyl (**2**) ponatinib, the metabolism site remains distal to the alkyne, so a large shift in I_{Ram} was not expected. The DFT calculation (Table 3.1) affirmed this as a similar cRIE value was found for the parent drug and the metabolite, and minimal alkyne Raman frequency shifts were predicted. Similarly, the DFT calculation for dihydroxylated ponatinib (**5**) did not predict a big Raman frequency shift, and the calculated cRIE value was only marginally lower (Table 3.1). Hence, the DFT calculations provided further proof that ponatinib metabolism is unlikely to cause significant changes in its Raman spectrum, validating our approach to image ponatinib at a single wavenumber using SRS microscopy.

†† DFT calculations performed by Marie Bluntzer.

3.5 Imaging ponatinib *in vitro* using SRS microscopy

3.5.1 Imaging ponatinib in adherent cells

3.5.1.1 Imaging in fixed SW480 cells

As all the CML cell lines used in the model system are non-adherent, these cells could not be imaged using a traditional SRS protocol previously utilised for adherent cell lines. In order to test and optimise the ponatinib imaging protocol by SRS, an adherent colorectal carcinoma cell line (SW480) was utilised first (cell line description in Section 2.2.1.1). Fibroblast growth factor receptor 2 (FGFR2) is a member of a family of tyrosine kinase receptors (FGFR 1-4) and has been found to be amplified in a number of cancer types, including colon cancer.[205,206] In addition to being a potent BCR-ABL inhibitor, ponatinib has been shown to be a potent inhibitor of all four FGFR's with an IC_{50} value <20 nM, thus making the SW480 cell line relevant for investigating ponatinib uptake and intracellular distribution.[98,191,207]

First experiments using SW480 cells included treating the cells with ponatinib for 2 h prior to washing and fixation (Figure 3.8). The washing step was implemented after the incubation period to remove any free drug from the extracellular space that had not been taken up by the cells. The fixed cell samples were then imaged on the custom-built SRS microscope.

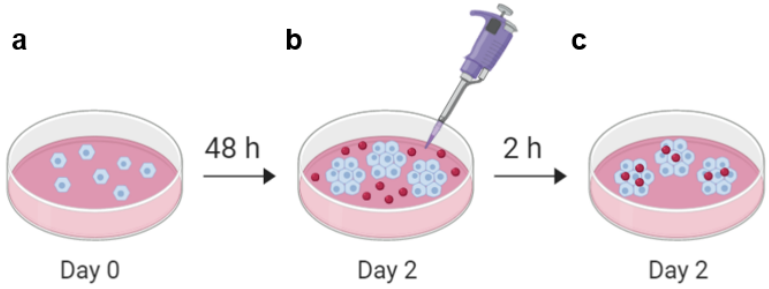

Figure 3.8 Schematic for adherent cell treatment prior to SRS imaging. (a) SW480 cells were plated onto fluorodishes on day zero and incubated for 48 h to allow them to adhere to the plates. (b) On day two SW480 cells were treated with ponatinib (concentration ranging from 25 µM to 5 µM) for 2 h before (c) washing with PBS and fixation using glutaraldehyde. Image created with Biorender.

SRS images were acquired by tuning the frequency difference between the pump and Stokes lasers to be resonant with intracellular proteins (CH_3, 2940 cm^{-1}) or ponatinib (C≡C, 2221 cm^{-1}). False colours were applied to individual Raman spectral frequencies (Figure 3.9a). This process allows cellular detection without the need for

any additional labelling. SRS images can contain background signals from competing pump-probe processes such as cross-phase modulation, transient absorption and photothermal effects.[208] Changing the pump wavelength by a few nanometres allows off-resonance images to be acquired (at a difference of 20-40 cm^{-1} from the on-resonance image), which can be used to distinguish true SRS signals from these artefacts.[208]

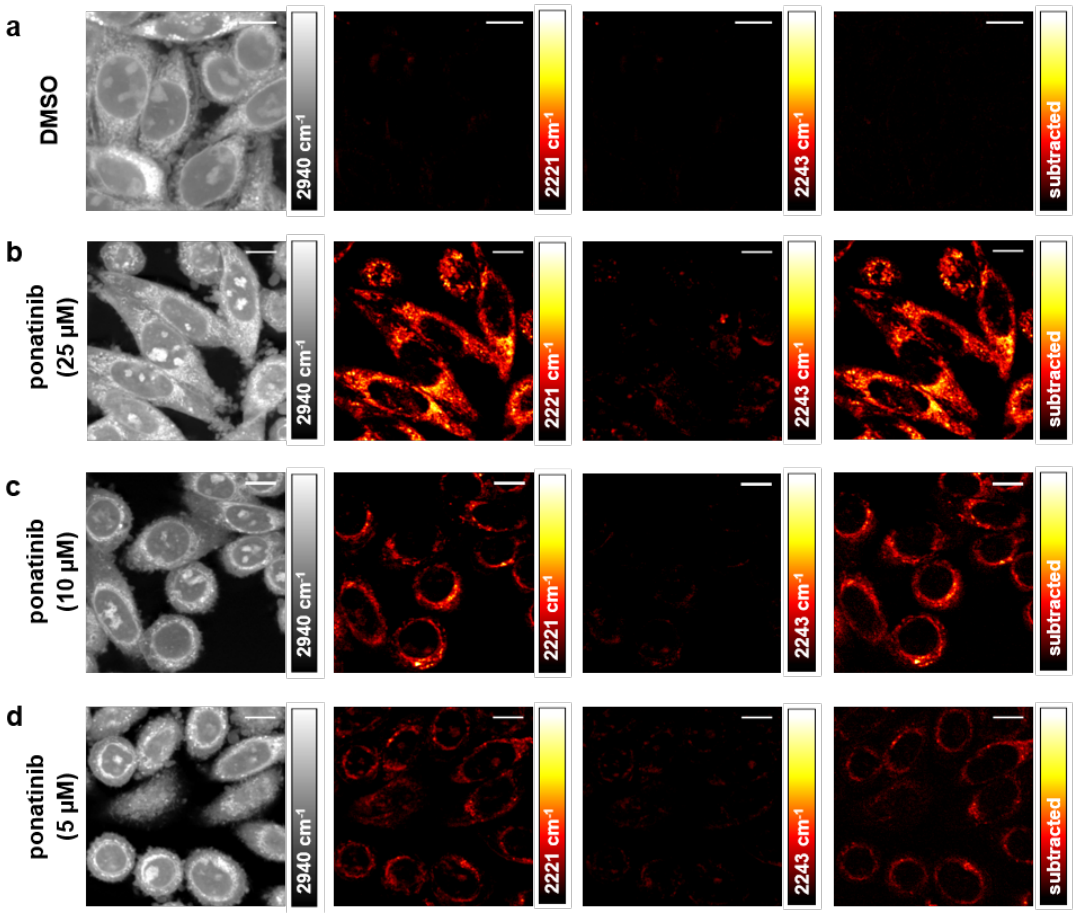

Figure 3.9 Multicolour SRS imaging of fixed SW480 cells treated with ponatinib. SW480 cells were treated with: (a) DMSO (0.0003%, v/v); (b) ponatinib (25 µM, 2 h); (c) ponatinib (10 µM, 2 h); (d) ponatinib (5 µM, 2 h) and fixed with glutaraldehyde (4%). Images were acquired in sequence from left to right: 2940 cm^{-1} (CH_3, proteins); 2221 cm^{-1} (C≡C, ponatinib); 2243 cm^{-1} (cell-silent region); 2221 cm^{-1} with background subtracted. Images acquired at 1024 × 1024 pixels, 20 µs pixel dwell time, laser power 300 mW (the tuneable pump beam) with false colours applied to different detection wavenumbers. Scale bars: 10 µm.

The DMSO control cells (Figure 3.9a) demonstrated that there was minimal SRS signal detected in the bioorthogonal region of the untreated SW480 cells at either 2221 cm^{-1} (C≡C, ponatinib on resonance) or 2243 cm^{-1} (off-resonance). SRS imaging

of SW480 cells that were treated with ponatinib (25 μM, 2 h) enabled successful detection of ponatinib (alkyne, 2221 cm^{-1}; off-resonance, 2243 cm^{-1}) which distributes throughout the cytoplasm of the cell (Figure 3.9b). Background subtracted images were created by subtracting the off-resonance image from the alkyne on resonance image (2221 cm^{-1} – 2243 cm^{-1}). In SW480 cells treated with lower ponatinib concentrations (10 μM or 5 μM, 2 h), a similar intracellular distribution of ponatinib (Figure 3.9c and 3.9d respectively) was seen compared to those treated at the higher concentration. However, as the ponatinib treatment concentration decreased, the intracellular signal also decreased, indicating reduced drug uptake by the cell, as the SRS signal is concentration dependent.[63] No drug signal (2221 cm^{-1}, C≡C, ponatinib on resonance) was detected in SW480 cells treated with ≤1 μM ponatinib (2 h). This means that at these treatment conditions ponatinib is no longer accumulating in the cells at high enough intracellular concentrations to be able to detect it by the SRS set up.

3.5.1.2 Imaging ponatinib in live SW480 cells

Once ponatinib imaging was working in fixed cells, the same protocol was tested in live cells. SW480 cells were treated as described in Figure 3.8, except this time the cells were only washed post ponatinib treatment, not fixed. Fresh media was added to the cells after washing, followed by live imaging on the SRS microscope.

Once again, control cells demonstrated minimal background signals at ponatinib on resonance (2221 cm^{-1}) and off resonance (2243 cm^{-1}) wavenumbers in the cell-silent region of the Raman spectrum (Figure 3.10a). Ponatinib was detected in the drug treated live cells (Figure 3.10b and 3.10c) when both 25 μM and 10 μM concentrations were used for 2 h before washing. In contrast to the fixed SW480 cells (Figure 3.9), where ponatinib was seen diffusely throughout the cytoplasm, it was observed that ponatinib accumulated in live SW480 cells as distinct puncta. It is possible that a proportion of internalised ponatinib was re-distributed within the cells during the washing steps of the fixation process. As cell fixation with glutaraldehyde works by cross-linking proteins via their reactive side-chains, ponatinib as a small molecule does not necessarily get fixed in the process.[209,210] This could explain why diffuse ponatinib signal was seen in fixed SW480 cells and ponatinib puncta were detected in live SW480 cells. The effect of fixing on ponatinib imaging was further investigated in different cell lines in Section 5.3.1.

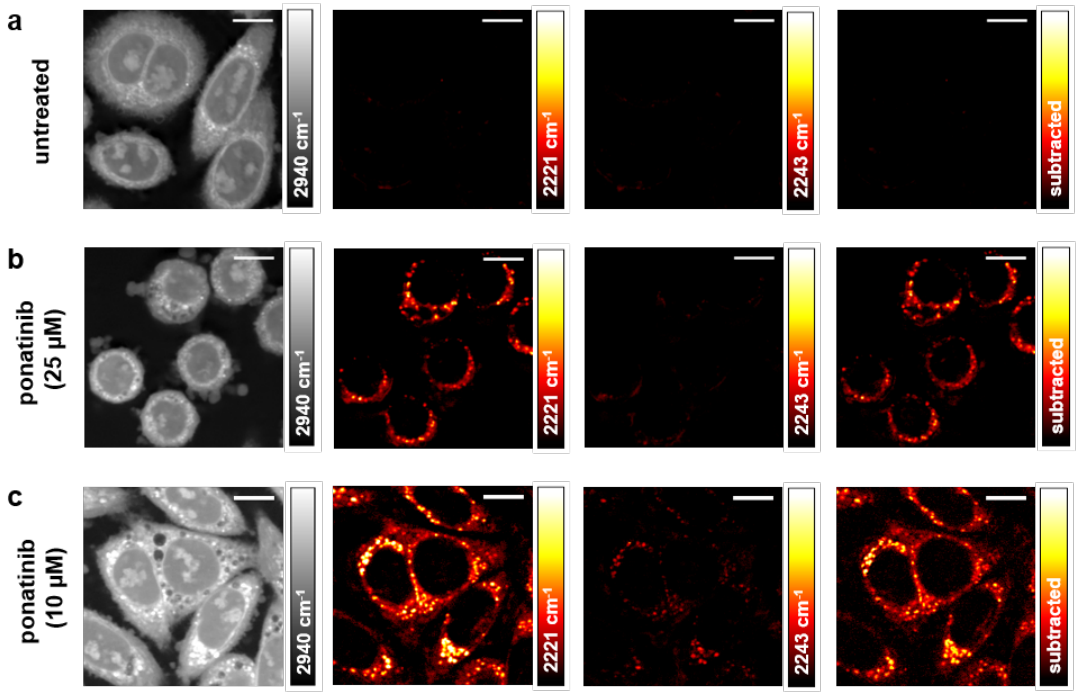

Figure 3.10 Ponatinib imaging in live SW480 cells. SW480 cells were treated with (a) DMSO (0.0003%, 2 h); (b) ponatinib (25 µM, 2 h); (c) ponatinib (10 µM, 1 h). SRS images were acquired in a sequence from left to right: 2940 cm^{-1} (CH_3, proteins); 2221 cm^{-1} (C≡C, ponatinib); 2243 cm^{-1} (off-resonance); 2221 cm^{-1} with background subtracted. Images acquired at 1024 × 1024 pixels, 20 µs pixel dwell time, laser power 300 mW (the tuneable pump beam) with false colours applied to different detection wavenumbers. Scale bars: 10 µm.

In Figure 3.10, it was also noted that the images taken of live SW480 cells treated with 10 µM ponatinib had a somewhat higher background at 2243 cm^{-1} than the fixed cells in Figure 3.9. In order to check if the off-resonance was perhaps still on the edge of the ponatinib SRS peak, a sweep of the ponatinib peak was taken between 2170–2270 cm^{-1}. Across the 100 wavenumber sweep, 26 SRS images were captured sequentially, creating a dataset where each pixel had a range of Raman intensity values. An area of ponatinib intensity within SW480 cells was then highlighted and the intensities of this area plotted across the range of wavenumbers on Fiji.

Figure 3.11 shows the SRS sweep, demonstrating that 2221 cm^{-1} is indeed the middle of the ponatinib peak inside cells. It also shows that 2243 cm^{-1} (859.0 nm on the pump laser), which was used on the microscope to take off-resonance images, is indeed still on the edge of the ponatinib peak. Taking off-resonance images at 2257 cm^{-1} (858.0 nm on the pump laser), which is further away from ponatinib peak edge, would

potentially decrease signal in the off-resonance images while still being close-by to the peak.

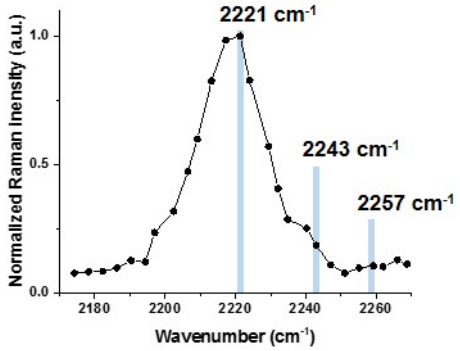

Figure 3.11 SRS sweep of ponatinib peak in SW480 cells treated with ponatinib (10 μM, 2 h). Ponatinib on resonance (2221 cm^{-1}) and off resonance (2243 cm^{-1}, 2257 cm^{-1}) peaks highlighted in blue.

3.5.2 Imaging ponatinib in non-adherent CML cells

Imaging non-adherent cells required a new experimental protocol as these cells do not attach to the plastic surface of the dishes they are grown in.

3.5.2.1 Imaging ponatinib in a panel of live mouse CML cells

CML cells were plated onto 10 cm petri dishes on day 0 and left to settle for 48 h before treatment with ponatinib (concentration ranging from 25 μM to 1 μM) for 2 h (Figure 3.12). The cells were subsequently washed with serum free media by centrifugation in Falcon tubes. Media was used for washing the cells rather than PBS as it was milder for live cells and gave better quality imaging results. Washing media was then removed from the Falcon tube, leaving a cell pellet with only a small amount of media (<500 μL). The cell pellet was then taken to the microscope room, where the pellet was gently re-suspended in the remaining media. An aliquot of live cells (2-5 μL depending on the coverslip size) was pipetted onto a microscope slide and a coverslip placed on top of the sample to form a single layer of cells. Cells were then immediately imaged on the SRS microscope.

Ponatinib imaging was first tested in BaF3 mouse CML cell lines – BaF3-p210 and BaF3 $p210^{Pon\text{-}Res}$ (cell lines described in Section 2.2.1.1). Both BaF3-p210 and BaF3-$p210^{Pon\text{-}Res}$ cells are BCR-ABL positive, meaning these cells express the main clinical target of ponatinib. However, while BaF3-p210 cells are highly sensitive to ponatinib treatment (GI_{50} – 2.3 nM), BaF3-$p210^{Pon\text{-}Res}$ are resistant to the drug with a

500-fold higher dose tolerance over 48 h treatment (GI_{50} – 1017 nM) (GI_{50} values were determined by Alamar blue assay, details in Section 2.2.2). It was hence hypothesised that imaging ponatinib in BaF3 $p210^{Pon\text{-}Res}$ cells might be easier at higher doses without affecting cell viability.

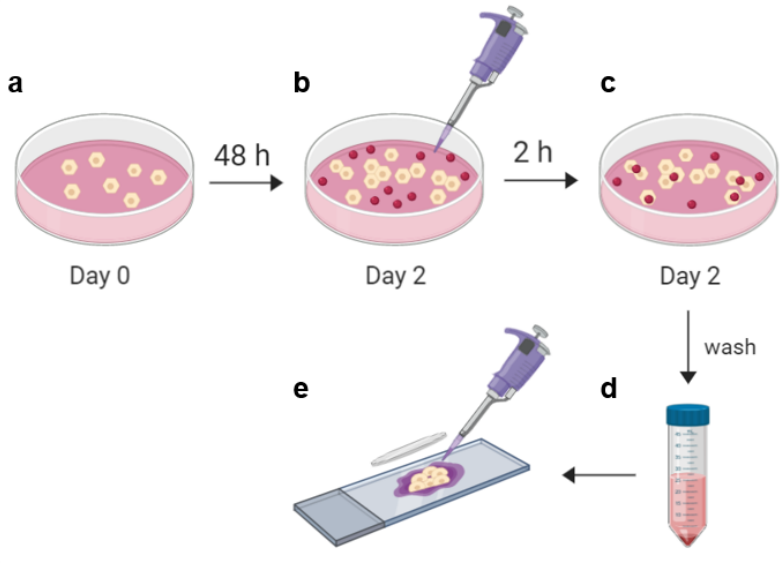

Figure 3.12 Scheme for non-adherent cell imaging using SRS microscopy. (a) CML cells were plated onto 10 cm Petri dishes on day zero and incubated for 48 h to allow them to settle. (b) On day two CML cells were treated with ponatinib (concentration ranging from 25 μM to 1 μM) for 2 h. (c) Cells were subsequently washed with drug free media and (d) centrifuged in a Falcon tube to leave a cell pellet. (e) An aliquot of the cell pellet was pipetted onto a glass microscope slide and sealed with a coverslip. Image created with Biorender.

Figure 3.13 shows sample SRS images of ponatinib in live BaF3 cells. The control BaF3 p210 cells that were treated with DMSO (2 h) showed virtually no signal in the cell silent region at 2221 cm^{-1} (C≡C, ponatinib peak) and 2096 cm^{-1} (off resonance). SRS imaging of BaF3 p210 cells that were treated with ponatinib (10 μM, 2 h) enabled successful detection of ponatinib (alkyne, 2221 cm^{-1}; off-resonance, 2096 cm^{-1}) in most of the cells in the field of view (Figure 3.13b). Ponatinib was also detected in BaF3 $p210^{Pon\text{-}Res}$ cells treated with the drug (10 μM, 2 h) (Figure 3.13c). In both cell lines, ponatinib was seen in cells as bright, very distinct puncta. This was in contrast to the SW480 cells, where ponatinib signal was also seen in the cell cytoplasm outside of the bright puncta.

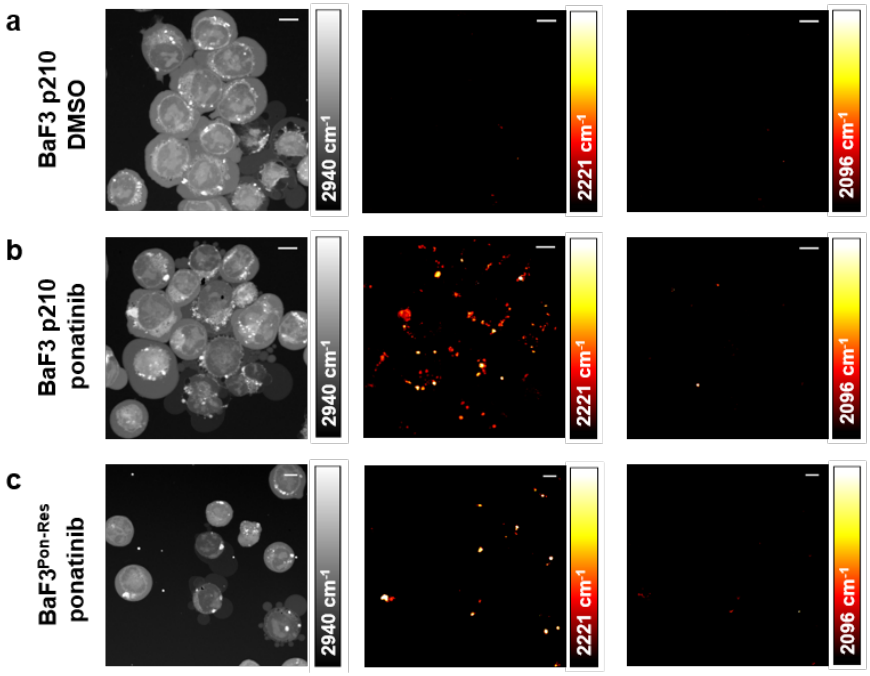

Figure 3.13 SRS imaging of live BaF3 cells treated with ponatinib. BaF3 p210 cells were treated with: (a) DMSO; (b) ponatinib (10 μM, 2 h). BaF3 $p210^{Pon\text{-}Res}$ cells were treated with (c) ponatinib (10 μM, 2 h). Images were acquired in sequence from left to right: 2940 cm^{-1} (CH_3, proteins); 2221 cm^{-1} (C≡C, ponatinib); 2096 cm^{-1} (off-resonance). Images acquired at 1024 × 1024 pixels, 20 μs pixel dwell time, laser power 300 mW (the tuneable pump beam) with false colours applied to different detection wavenumbers. Scale bars: 10 μm.

3.5.2.2 Optimising ponatinib imaging in live human CML cells

Following successful imaging in live mouse CML cells, the next challenge was repeating this in live human CML cell lines whilst also optimising the conditions. For this purpose, KCL22 cells were utilised. This cell line has a very low GI_{50} value against ponatinib (2.4 nM) as it sensitive to the drug (GI_{50} values in Section 2.2.2.1). As the long term goal of the project was to quantitatively image ponatinib in both KCL22 and $KCL22^{Pon\text{-}Res}$ cells, optimisation was carried out in the drug sensitive cell line based on the hypothesis that imaging in $KCL22^{Pon\text{-}Res}$ cells will be less challenging due to this cell line having a higher tolerance against ponatinib (GI_{50} – 593 nM).

The first optimisation step assessed the duration of ponatinib treatment in KCL22 cells. Earlier imaging experiments were performed in BaF3 cells treated with ponatinib for 2 h (Figure 3.13). The ponatinib signal was readily detected in cells after 2 h treatments (Figure 3.13), indicating high uptake of the drug in concentrated puncta. Hence, it was hypothesised that ponatinib is taken up by the cells rapidly enough to

halve the treatment time to 1 h. To test this, KCL22 cells were treated with ponatinib (10 μM, 1 h) and imaged using SRS (Figure 3.14b). Ponatinib was successfully detected in KCL22 cells following the shorter treatment - bright puncta were seen in the cytoplasm of the cells, on average 12 puncta per cell (SD±13) in n=20 cells from the field of view. Interestingly, the number of ponatinib spots ranged from 2 to 52 in different cells, demonstrating heterogeneous uptake of the drug in KCL22 cells. While the mean Raman intensity inside ponatinib spots was 1947, less concentrated diffuse ponatinib signal seen throughout the cytoplasm was 7-fold lower, 277 in n=10 cells. We considered 1 h drug treatment optimal for further live cell imaging experiments.

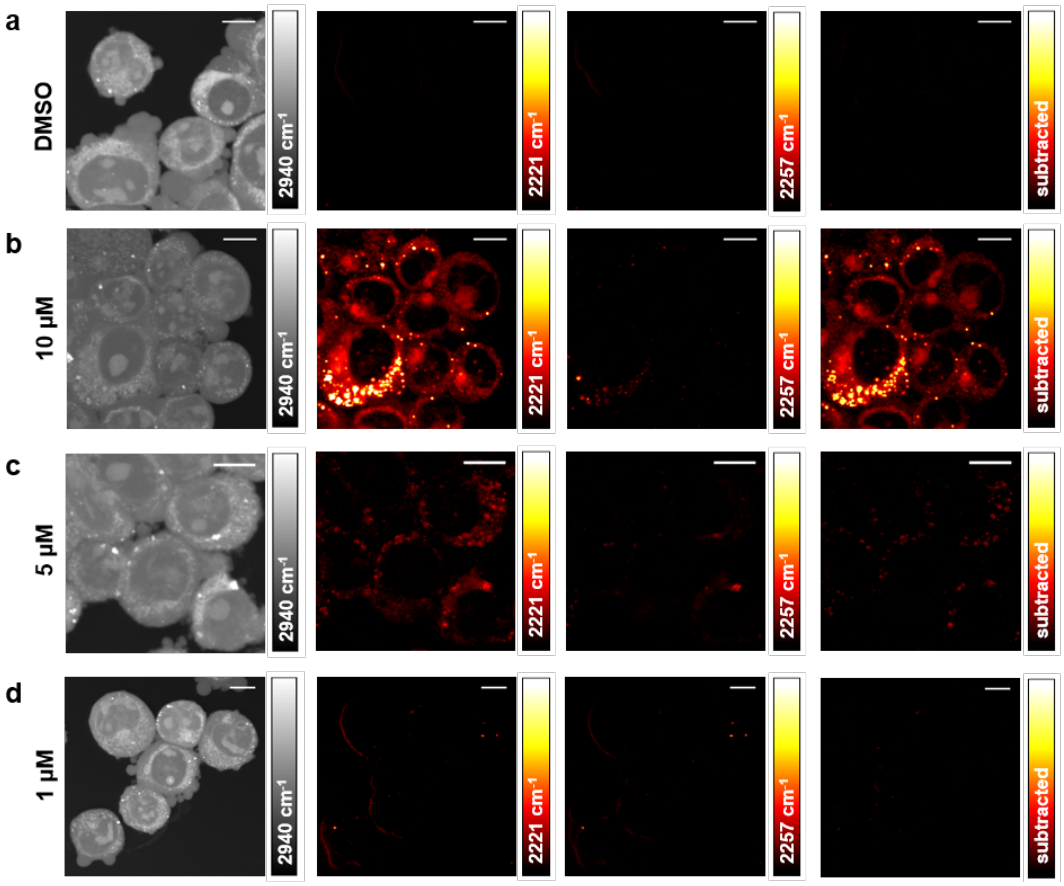

Figure 3.14 Imaging ponatinib uptake in KCL22 cells. KCL22 cells were treated with: (a) DMSO (1 h); (b) ponatinib (10 μM, 1 h); (c) ponatinib (5 μM, 1 h); (d) ponatinib (1 μM, 1 h). Images were acquired in sequence from left to right: 2940 cm^{-1} (CH_3, proteins); 2221 cm^{-1} (C≡C, ponatinib); 2257 cm^{-1} (off-resonance); 2221 cm^{-1} with background subtracted. Images acquired at 1024 × 1024 pixels, 20 μs pixel dwell time, laser power 250 mW (the tuneable pump beam) with false colours applied to different detection wavenumbers. Scale bars: 10 μm.

The second optimisation step assessed the treatment concentration in KCL22 cells. The goal was to determine the lowest ponatinib concentration at 1 h treatment where ponatinib could still be detected in live cells by SRS. KCL22 cells were treated with a range of ponatinib concentrations (10 μM to 1 μM), washed and imaged (Figure 3.14b,c,d). The most intense ponatinib Raman signal was detected in KCL22 cells treated with 10 μM ponatinib, where mean intensity in ponatinib puncta was 1947 (Figure 3.14b). This is indicative of higher uptake of ponatinib in these cells as SRS signal is concentration dependent.[63] When a sweep was taken of the ponatinib peak using SRS, we could see the alkyne peak for intracellular ponatinib (2221 cm^{-1}, Figure 3.15a). Gaussian fitting was applied to measure the peak height, giving 102.7 a.u. for KCL22 cells treated with 10 μM ponatinib.

Intracellular distribution of ponatinib could still be detected in KCL22 cells treated with a lower ponatinib concentration (5 μM, 1 h), but the Raman signal intensity in ponatinib puncta was reduced to 509, almost 4-fold lower than in cells treated with 10 μM ponatinib concentration (Figure 3.14c). When a sweep was taken of the ponatinib peak by SRS, we could see a peak corresponding to intracellular ponatinib (2221 cm^{-1}, Figure 3.15b), but the peak height was reduced to 22.2 a.u. compared to 10 μM treatment (102.7 a.u), indicative of reduced intracellular drug concentration. So the signal intensity reduction is mirrored by the reduction in peak height. As these sweeps were not obtained on the same day and under controlled conditions, the reduction in peak height is not necessarily linear. Later, in Section 3.5.3 where ponatinib SRS sweeps in DMSO solutions are obtained on the same day for the purpose of signal quantification, we show that SRS signal reduction is linear and correlates with peak height reduction.

When ponatinib concentration was reduced further (1 μM, 1 h), no ponatinib was seen inside the cells (Figure 3.14d), and a sweep of the alkyne peak gave a flat line (Figure 3.15c). This means that at these treatment conditions ponatinib is no longer accumulating in the cells at high enough intracellular concentrations to be detected by the SRS setup. Therefore, 5 μM ponatinib concentration is the lowest we can detect in KCL22 cells following short treatment, while 10 μM concentration results in higher uptake of ponatinib across the cell population.

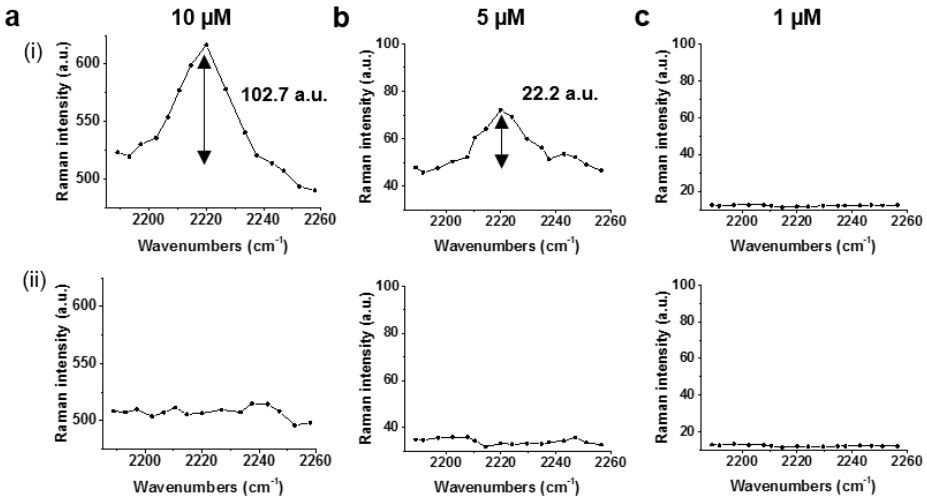

Figure 3.15 SRS sweep of ponatinib peak inside live KCL22 cells following treatment with (a) ponatinib (10 μM, 1 h), (b) ponatinib, (5 μM, 1 h), (c) ponatinib, (1 μM, 1 h) where (i) inside cells, (ii) background intensity of media. Laser power 250 mW (the tuneable pump beam).

3.5.2.3 Ponatinib uptake in CML cells

Drugs can be taken up into the cells either by passive diffusion or active transport. Passive diffusion through the cell membrane does not require cells to expend energy, whilst active transport does. In order to test if ponatinib accumulation in cells is driven by active or passive transport, KCL22 cells were incubated with the drug at either 4 °C or 37 °C and imaged subsequently (Figure 3.16). At 4 °C, all energy requiring processes are halted, meaning only passive diffusion can take place, whilst at 37 °C both active and passive transport can be utilised by cells.

The mean ponatinib Raman intensity was quantified per cell at both 37 °C and 4 °C using ImageJ (Figure 3.16b). No significant difference was found between the samples, demonstrating that KCL22 cells treated with ponatinib (5 μM, 1 h) at either 37 °C or 4 °C both had equal levels of drug uptake (Figure 3.16b). This indicates that ponatinib accumulates in KCL22 cells by passive diffusion. Previous research by Lu *et al.* used an intracellular uptake and retention (IUR) assay with ^{14}C-labeled ponatinib at 37 °C or 4 °C and found no significant difference in ponatinib IUR in CML cells, also concluding that ponatinib is passively transported into the cells.[211] Other tyrosine kinase inhibitors such as sunitinib and sorafenib, have also been reported to enter the cells via passive diffusion.[212] However, these studies did not investigate drug uptake mechanism via imaging, which we were able to do via SRS imaging.

Unlike imatinib, that is actively transported into CML cells, ponatinib transport does not depend on the drug-influx transporter organic cation transporter 1 (OCT-1) or the drug-efflux adenosine triphosphate (ATP)-binding cassette transporters (ABCB1 and ABCG2).[211,213,214] ABCB1 and ABCG2 are also involved in the efflux of dasatinib, another clinically relevant BCR-ABL TKI, but dasatinib intracellular uptake is passive and independent of OCT-1.[215,216] This highlights the heterogeneity in drug uptake and export mechanisms even when the drugs have an identical target, which in this case is BCR-ABL.

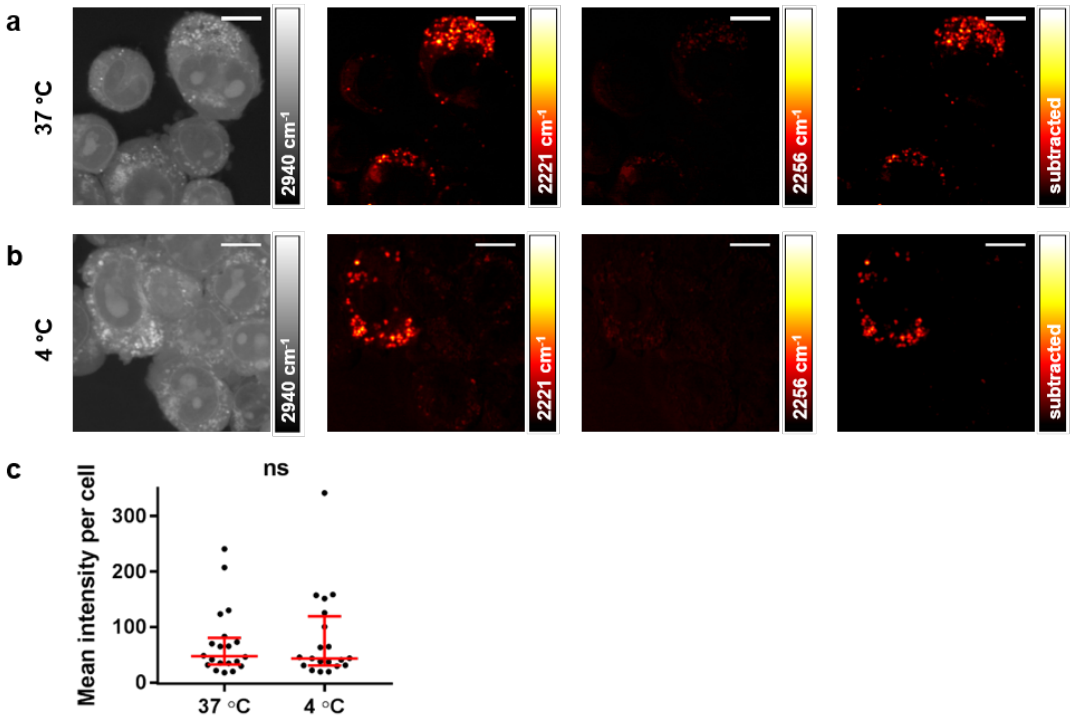

Figure 3.16 KCL22 cells were treated with ponatinib (5 μM, 1 h) at (a) 37 °C or (b) 4 °C. Images were acquired in sequence from left to right: 2940 cm^{-1} (CH_3, proteins); 2221 cm^{-1} (C≡C, ponatinib); 2257 cm^{-1} (off-resonance); 2221 cm^{-1} with background subtracted. Images acquired at 1024 × 1024 pixels, 20 μs pixel dwell time, laser power 250 mW (the tuneable pump beam) with false colours applied to different detection wavenumbers. Scale bars: 10 μm. (c) Mean ponatinib Raman intensity per cell was quantified in n=10 cells, two biological repeats using ImageJ. The Mann-Whitney test was used to compare the samples on GraphPad Prism software, p=0.9042.

3.5.3 Quantification of intracellular ponatinib concentrations using SRS

As SRS has a linear concentration dependence, determining absolute intracellular ponatinib concentration inside CML cells was one of the major goals of the project.

To determine the absolute concentrations, a calibration curve of ponatinib solutions in DMSO was first acquired. SRS images in the range of 2176–2246 cm^{-1} were acquired for each ponatinib concentration as well as DMSO alone (n=3). Subsequently, the average pixel intensities of each SRS image across the range were calculated using ImageJ. The average pixel intensities were plotted for each concentration and a Gaussian fitting was applied on Origin (Figure 3.17a). The resulting peak was integrated, and the peak height was plotted at each concentration to give a ponatinib calibration curve (Figure 3.17b).

On the same day, $KCL22^{Pon\text{-}Res}$ cells were treated with ponatinib (10 μM, 1 h), and imaged using SRS. In order to account for the noise due to day-to-day variance in the ponatinib on resonance SRS spectrum (C≡C, 2221 cm^{-1}), all the Raman intensities below the calculated Gaussian baseline in Figure 3.17a (1000 for this dataset) were subtracted from the image. The final calibrated ponatinib on resonance image (Figure 3.17c) indicates that the intracellular ponatinib concentration seen within some concentrated spots in the $KCL22^{Pon\text{-}Res}$ cells was up to 18 mM. This was an 1800-fold intracellular enrichment of ponatinib concentration compared to the extracellular concentration. Fu *et al.* have reported similar results for imatinib (933-fold) and nilotinib (2520-fold) intracellular enrichment factors in mouse CML cells using hyperspectral SRS imaging.[170] This provides an estimation of drug concentration in various single points across the image, but our goal was to determine the total concentration in a single cell.

To calculate the drug concentration inside a cell from a 3-dimensional SRS image, single cells were masked out from a z-stack of images (Figure 3.17d). Using Matlab[‡‡], each SRS intensity per pixel inside the cell was converted to a concentration measurement of ponatinib by comparing the value with that from a control curve of drug dilutions in DMSO taken at the same settings. By converting each pixel to a volume measurement using the scan parameters the concentration measurements could also be converted to an amount of drug per voxel. By summing all the values, an overall drug amount per cell could be calculated. This was repeated for a total of 10 cells. We found that $KCL22^{Pon\text{-}Res}$ cells had an average intracellular ponatinib concentration of 0.69 mM (±0.34 SD), which is 69-fold higher than the extracellular concentration used for treatment.

‡‡ Dr Martin Lee performed the Matlab analysis.

However, it was noted that using the chosen laser parameters (300 mW for the tuneable pump beam, gain 2), our cell images had exceeded the maximum measurable pixel intensities in parts of the cell images, meaning we were losing valuable data from the top end of the concentration scale. In order to rectify this, the experiment was repeated with amendments to the protocol and with a second goal of comparing absolute ponatinib concentrations in the KCL22 and KCL22$^{Pon-Res}$ cell lines.

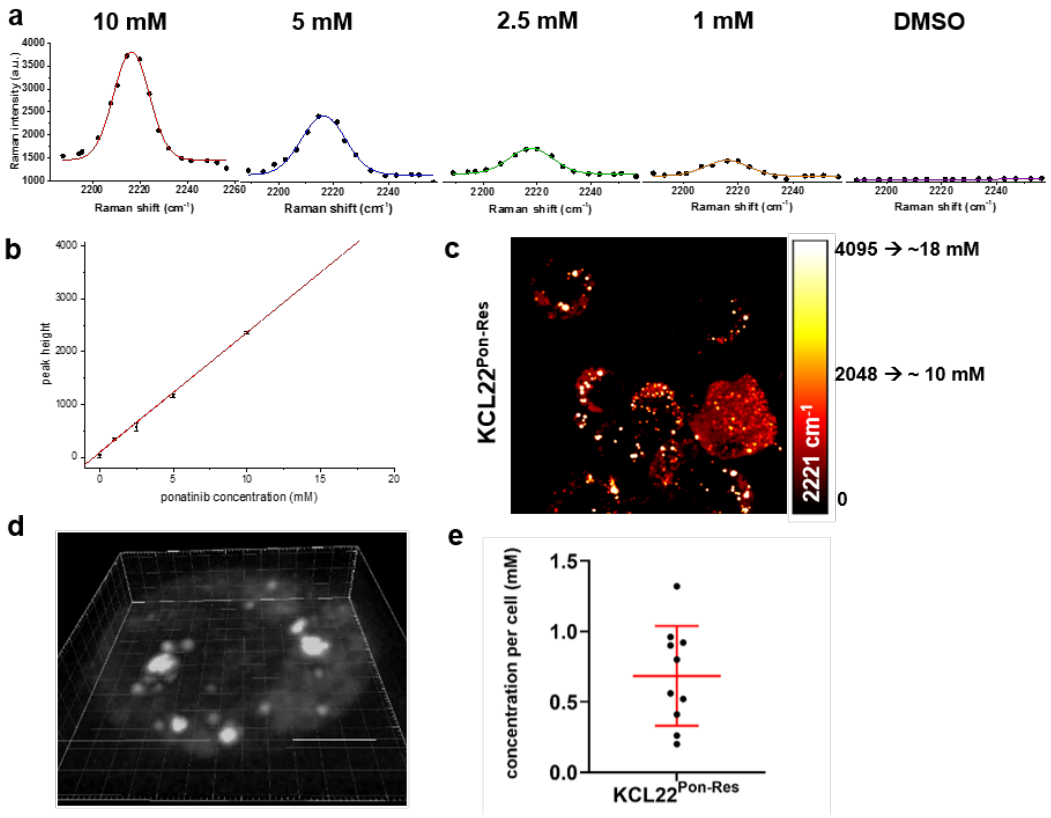

Figure 3.17 Quantitative assessment of intracellular concentration of ponatinib by SRS. (a) Detection of decreasing concentrations of ponatinib dissolved in DMSO using SRS imaging of the 2221 cm^{-1} ponatinib alkyne peak. Laser settings: 300 mW, gain 2. SRS spectra were recorded across the region 2176–2246 cm^{-1} and the average pixel intensity was calculated for each image frame. A Gaussian fitting was applied to the data. (b) Calibration curve of ponatinib in DMSO using SRS imaging. The peak heights of the SRS peaks in (a) were plotted against ponatinib concentration. A linear fitting was applied to the data. R^2 = 0.998. Error bars represent the SD across n = 3 repeats. (c) KCL22$^{Pon-Res}$ cells were treated with ponatinib (10 μM, 1 h), before SRS imaging. The colour bar corresponds to a linear ponatinib concentration range of 0-18 mM. (d) 3D z-stack image of a single KCL22$^{Pon-Res}$ cell that was selected from (c) to calculate intracellular ponatinib concentration using Matlab. (e) Quantified concentration of ponatinib in KCL22$^{Pon-Res}$ cells using SRS for n=10 cells. Error bar represents mean±SD.

In order to prevent any saturated pixels on the final cell images this time, test cells were used on the same day prior to the experiment for choosing the appropriate laser settings for the particular experiment. KCL22$^{Pon-Res}$ cells were also treated with a lower concentration of ponatinib (5 μM, 1 h) to prevent saturation of the drug in cells. The optimal laser power for the tuneable pump beam was found to be 100 mW with gain 1, whilst previously 300 mW with gain 2 was used. Thus a reduction to 33% laser power allowed the detection of ponatinib in KCL22$^{Pon-Res}$ cells without image saturation. These lower laser power settings were then used to obtain a ponatinib concentration curve in DMSO solutions ranging from 20 mM to 5 mM as well as DMSO alone (n=3). Higher concentrations of ponatinib had to be used due to the lower laser power used, resulting in lower peak heights (Figure 3.18a). As before, the resulting peaks were integrated, and the peak heights were plotted at each concentration to give a ponatinib calibration curve (Figure 3.18b).

On the same day, both KCL22 and KCL22$^{Pon-Res}$ cells were treated with ponatinib (5 μM, 1 h) and imaged using SRS (Figure 3.18c). Z-stacks were taken for each cell line. The colour bar in Figure 3.18c corresponds to a linear ponatinib concentration range of 0-153 mM that corresponds to the pixel intensity scale of 0-4095. Maximum z-projection of an individual KCL22$^{Pon-Res}$ shows two individual ponatinib puncta (Figure 3.18d). In the brighter spot, the maximum Raman intensity was found to be 4091, corresponding to approximately 150 mM ponatinib concentration. The average intensity inside that punctum was 2620 (~98 mM). This was the highest intensity ponatinib punctum seen across the two cell lines. The second, less bright punctum, had a maximum intensity of 2025 (~75 mM), with an average intensity of 1415 (~53 mM). However, these puncta only represent the parts of the cell with high concentrations of ponatinib, not the whole cell.

For calculating the concentration in whole individual cells (n=20), they were cut out from the z-stack images using ImageJ. These were used for quantifying ponatinib concentration per cell in both cell lines using Matlab[§§] (Figure 3.18e). The average ponatinib concentration was 1.67 mM (±0.37 mM) in KCL22$^{Pon-Res}$ cells, 2.4 times higher than the estimated value from the previous protocol (0.69±0.34 mM). This was expected, as in the earlier protocol there were saturated pixels on the image, which

[§§] Dr Martin Lee performed the Matlab analysis.

meant data was lost from these pixels. These results highlight the importance of using appropriate laser settings for quantification of imaging data.

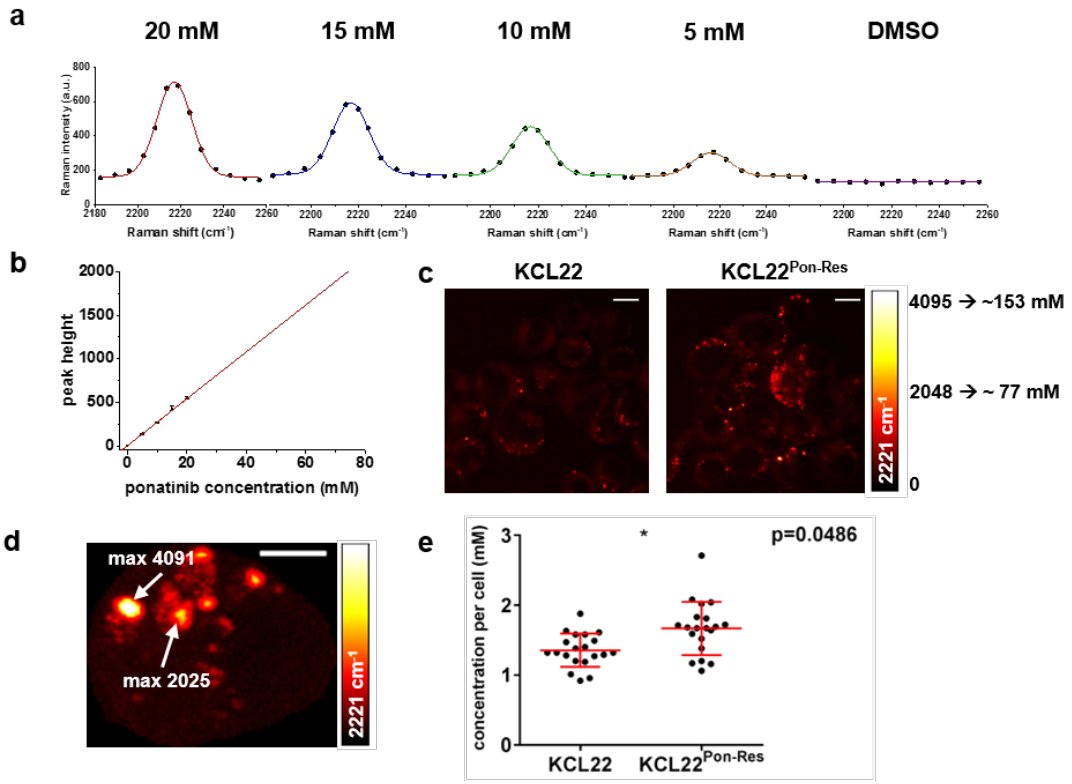

Figure 3.18 Quantitative assessment of intracellular concentration of ponatinib by SRS. (a) Detection of decreasing concentrations of ponatinib dissolved in DMSO using SRS imaging of the 2221 cm^{-1} ponatinib alkyne peak. Laser settings: 100 mW, gain 1. SRS spectra were recorded across the region 2189–2257 cm^{-1} and the average pixel intensity was calculated for each image frame. A Gaussian fitting was applied to the data. (b) Calibration curve of ponatinib in DMSO using SRS imaging. The peak heights of the SRS peaks in (a) were plotted against ponatinib concentration. A linear fitting was applied to the data. R^2 = 0.999. Error bars represent the standard deviation across n = 3 repeats. (c) KCL22 and KCL22$^{Pon\text{-}Res}$ cells treated with ponatinib (5 μM, 1 h), imaged by SRS. Scale bars: 10 μm. The colour bar corresponds to a linear ponatinib concentration range of 0-153 mM. (d) Z-stack maximum intensity projection of an individual KCL22$^{Pon\text{-}Res}$ cell showing two individual ponatinib puncta and Raman intensities inside the puncta. Scale bar: 5 μm. (e) Quantified concentration of ponatinib per cell in KCL22 and KCL22$^{Pon\text{-}Res}$ cells using SRS for n=20 cells. Concentration was quantified in 3D cells using Matlab. Statistical analysis was performed using GraphPad Prism software. Welch's t-test was used to compare the concentration between the cell lines.

KCL22 cells had an average ponatinib concentration of 1.36 mM (±0.23 SD) across the 20 cells, 19% lower than the ponatinib concentration in KCL22$^{Pon\text{-}Res}$ cells (1.67±0.37 mM). Welch's t-test was used on Graphpad Prism to compare the two cell lines. It was found KCL22$^{Pon\text{-}Res}$ cells have a significantly higher ponatinib concentration than KCL22 cells (**, p=0.004). This was counterintuitive, considering KCL22$^{Pon\text{-}Res}$ cells have a 100-fold higher GI_{50} to ponatinib compared to KCL22 cells. It is, however, consistent with reports that KCL22$^{Pon\text{-}Res}$ cells have developed a resistance mechanism that is independent of the ponatinib concentration present in cells.[109]

The methodology used here to quantify absolute intracellular ponatinib concentration is not without limitations. Firstly, a calibration curve of ponatinib solutions in DMSO was acquired. In doing so, we have made the assumption that ponatinib SRS signal intensity in DMSO solution is identical to the signal intensity inside cells, which is not necessarily the case. There are intracellular factors that could influence SRS signal intensity. Cells are made of complex biomolecules, including proteins, lipids and nucleic acids, where intracellular pH various in different cellular compartments. The presence of all these factors inside cells could have an impact on ponatinib SRS signal intensity, but this remains an area of SRS imaging that has not been explored in depth. Previous studies using SRS or Raman microscopy for concentration quantification have also generated calibration curves in DMSO solutions.[48,169,170]

In our study, we were limited by the solubility of ponatinib in DMSO, which only has a maximum solubility of 20 mM in DMSO. However, SRS detection sensitivity at optimised settings for intracellular imaging with no saturated pixels was 5 mM in DMSO, leaving a very limited window to mix the ponatinib solution with buffers to see if that would impact ponatinib SRS signal intensity. For a drug with better solubility, we believe it would be relevant to generate the calibration curve in a buffer if possible, to better represent intracellular environment.

3.5.4 Imaging ponatinib at biologically relevant concentration

Detection sensitivity remains the key limiting factor for utilising SRS for intracellular imaging as micromolar concentrations are still required to visualise target molecules.[47,49,59,66,170] However, this is often not physiologically relevant. Our goal was to image ponatinib in target cells at biologically relevant concentrations using SRS. To do so, we chose to image in KCL22$^{Pon\text{-}Res}$ CML cells, which have a high tolerance to ponatinib (GI_{50}=593 nM) (cell line described in Table 2.5, GI_{50} value in Table 2.6). For treatment, a ponatinib concentration close to the GI_{50} of the cells was chosen – 500 nM. This concentration is also close to the measured plasma concentration of ponatinib, which is 145 nM following a 45 mg oral dose.[199] We determined previously that the minimum incubation concentration that allowed intracellular detection after 1 h treatment of cells was 5 μM. Here, we were testing the hypothesis that longer incubation times would result in accumulation of higher concentrations within the cells, which would allow treatment with a lower concentration. KCL22$^{Pon\text{-}Res}$ cells were hence treated with ponatinib (500 nM) for up to 48 h before imaging the live cells using SRS microscopy (Figure 3.19). Optimal set-up resulted in acquisition times of about 45 s per image. It was necessary to use a higher laser power (300 mW for the tuneable pump beam, gain 2) to successfully acquire ponatinib images at this low concentration.

Ponatinib Raman signal intensity (C≡C, 2221 cm^{-1}) was analysed in individual cells from a field of view (n=30) at each time point using ImageJ. The results were compared to the DMSO control cells using GraphPad Prism (Figure 3.19d). It was found that there was a significant ponatinib Raman signal increase compared to the control cells at each time point. This is suggestive of intracellular accumulation of ponatinib.

The data was further analysed by looking at the number of ponatinib puncta in the cells at different time points. Familiar bright ponatinib puncta were found in the cells from the 6 h time point onwards, while the largest number of puncta was seen in cells treated with ponatinib for 24 h or 48 h (Figure 3.19e). The number of ponatinib puncta at the 1 h time point was on average only 2 per cell. At 6 h, significantly more ponatinib puncta were seen in cells, averaging at 5 per cell. Additionally, the ponatinib puncta at 6 h had higher Raman intensities compared to those seen at 1 h (green/yellow on the colour bar vs blue). This is indicative of increased ponatinib concentration in the puncta at 6 h. The number of puncta further increased at the 24 h time point (10 per

cell), but there was no significant increase at the 48 h time point (11 per cell). Interestingly, the spread of number of ponatinib puncta per cell becomes more heterogeneous at the 24 h and 48 h time points compared to the 1 h and 6 h time points, demonstrating heterogeneity within the cell population upon ponatinib treatment for prolonged periods. The same trend was seen in the relative ponatinib concentration per cell (Figure 3.19d), where at 24 h and 48 h the drug concentration per cell became more heterogeneous. This demonstrates that ponatinib uptake is not homogeneous in the target cells as some cells are able to take up and retain higher concentration of ponatinib than others.

Heterogeneous drug uptake has been reported before within tumours.[182,183,217] Ineffective drug uptake into tumours is influenced by a number of factors such as tumour microenvironment and vascularisation. However, this is not the case for heterogeneity in drug uptake *in vitro*, where intraclonal heterogeneity within the cell population has been found to influence drug uptake.[218] For example, daunorubicin, a cytotoxic chemotherapeutic, was found to be taken up heterogeneously *in vitro* in acute myeloid leukaemia (AML) patient samples.[218] This observed heterogeneity of drug uptake *in vitro* has not been studied extensively, likely due to limitations in imaging technology.

Here, for the first time, SRS has been successfully used to image a drug at a biologically relevant dose in live cells without any additional labelling or fixation. In addition, thanks to the fast acquisition speeds of SRS, it was possible to image ponatinib in live cells. This is in contrast to the study by Aljakouch *et al*., where neratinib was imaged at nanomolar concentrations in fixed cells.[169] While an average SRS image takes 45 s to image at optimised settings, spontaneous Raman microscopy is limited to fixed samples due to longer image acquisition times required (>30 min). This is a major advantage of SRS microscopy application to drug imaging.

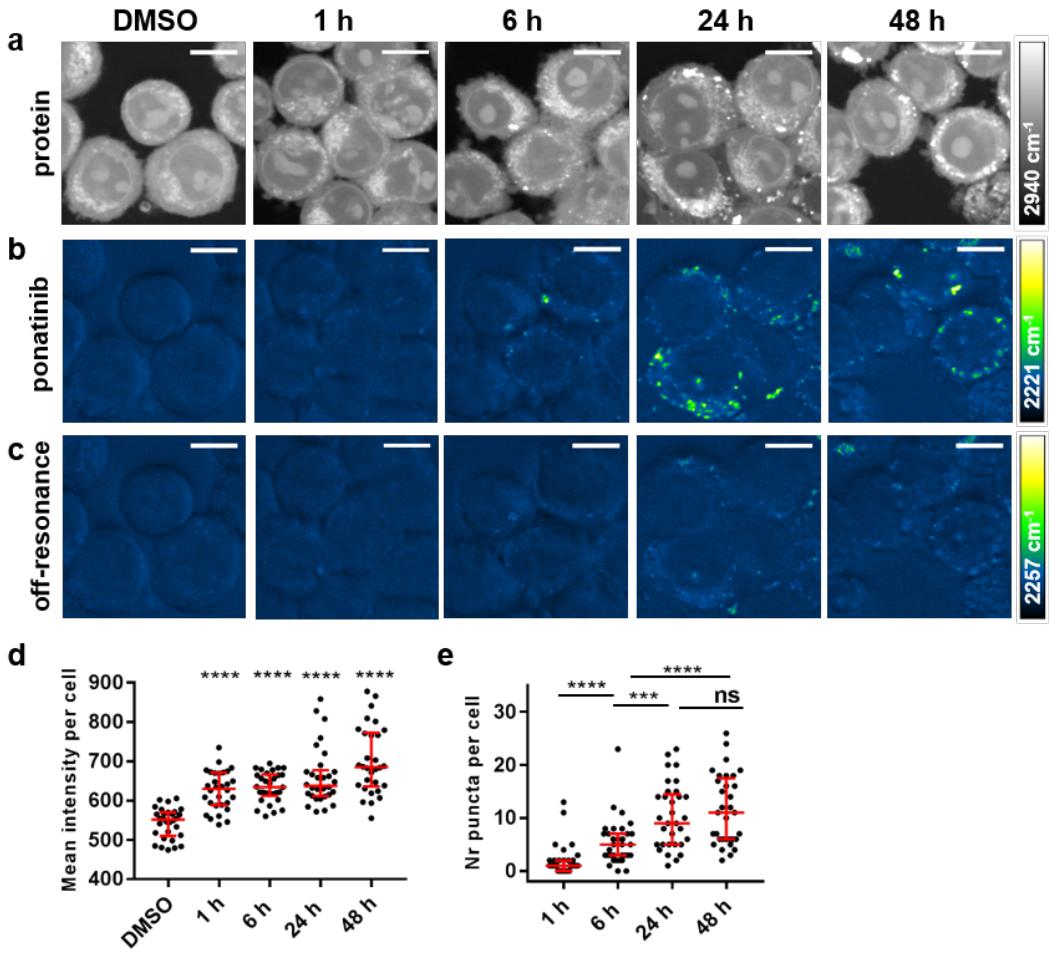

Figure 3.19 (a−c) Imaging ponatinib uptake in KCL22$^{Pon\text{-}Res}$ cells. KCL22$^{Pon\text{-}Res}$ cells were treated with DMSO (0.0003%, v/v) or ponatinib (500 nM) for 1, 6, 24, or 48 h (left to right). SRS images acquired at (a) 2940 cm^{-1} (CH_3, proteins); (b) 2221 cm^{-1} (C≡C, ponatinib); (c) 2257 cm^{-1} (off-resonance). Images acquired at 1024 × 1024 pixels, 20 µs pixel dwell time, laser power 300 mW (the tuneable pump beam), gain 2 with false colours applied to different detection wavenumbers. Scale bars: 10 µm. (d) Mean ponatinib intensity per cell quantified from 2221 cm^{-1} in n = 30 cells, three biological repeats. The Mann−Whitney test was used to compare ponatinib Raman intensity values against the DMSO control. (e) Number of ponatinib puncta per cell quantified from 2221 cm^{-1} in n=10 cells, three biological repeats. The Mann-Whitney test was used to compare number of ponatinib puncta in cells at different time points, **** p<0.0001, *** p=0.0005.

3.6 Conclusions

In this chapter, an SRS imaging approach for ponatinib in human CML cells was validated by DFT calculations and LC-MS analysis of potential ponatinib metabolites. The level of ponatinib metabolites found in CML cells was very low, while DFT calculations predicted minimal Raman shifts in their frequencies, indicating that total ponatinib concentration can be imaged by SRS at a single wavenumber.

SRS imaging of ponatinib was optimised first in adherent colon cancer cells followed by imaging in both mouse and human CML cell lines. Optimisation included testing different concentrations, treatment times and imaging at different laser powers. For 1 h treatment, it was found that the minimum ponatinib concentration required for SRS detection is 5 μM. Quantitative SRS imaging enabled determination of the absolute ponatinib concentration of both KCL22 and KCL22$^{Pon\text{-}Res}$ cells as 1.36 mM and 1.67 mM respectively, demonstrating that the drug accumulates in the cells at over 200-fold higher concentration compared to extracellular ponatinib.

SRS imaging of ponatinib was additionally achieved through incubation at biologically relevant concentrations in KCL22$^{Pon\text{-}Res}$ cells, where a 500 nM treatment was used due to its proximity to the GI_{50} value of this cell line. Longer incubation times (6 h - 48 h) were needed to detect intracellular ponatinib puncta at this concentration. However, this is the first instance where nanomolar incubation concentration of an analyte has allowed successful SRS imaging in live cells.

Chapter 4 Significance of ponatinib lysosomal accumulation in ponatinib resistant CML cells

4.1 Introduction

There is currently no available information on the intracellular localisation of ponatinib in the context of drug resistant CML. In this chapter, we used multimodal imaging, immunofluorescence (IF) and fluorescence assisted cell sorting (FACS) to demonstrate ponatinib lysosomal accumulation and its biological significance in the context of CML acquired drug resistance. A combination of SRS imaging and Western blots were used to assess the effect of lysosomal trapping on target engagement. Part of this work has been published in a peer-reviewed journal.[173]

4.1.1 Lysosomotropism

The intracellular distribution of drugs is an important consideration for drug efficacy as it can influence drug target engagement. De Duve was the first to describe the principle of selective drug partitioning inside cells based on pH.[219] He created the term lysosomotropic agents, which describes weakly basic compounds that exist in their unionised state in the cell cytosol (pH~7.4), enabling passive diffusion across the cell membrane and the lysosomal lipid bilayer (Figure 4.1a). Inside the lysosomes, which have acidic pH (~4.5), protonation of the base is favoured. Once the drug is ionised inside the lysosome, it is considered relatively membrane impermeable and cannot diffuse back out. This can reduce drug target engagement and has been associated with drug resistance.[220]

Drug localisation in cells can be heavily influenced by physicochemical properties such as pKa (acid dissociation constant). The higher the pKa, the weaker the acid and conversely the stronger the base. Duvvuri *et al.* used a series of aminoquinoline (AQ) and aminoisoquinoline (AIQ) amines to study the role of pKa in lysosomal accumulation (Figure 4.1b).[220] They showed that higher pKa correlated with increased lysosomal trapping. Compounds with pKa values near and above neutral (pKa=6.9-9.0) achieved over 50 times greater lysosomal concentrations compared to those in the cytosol, whilst compounds with pKa values 5 and below were not detected in the lysosomes. The pKa alone, however, is not responsible for lysosomal trapping.

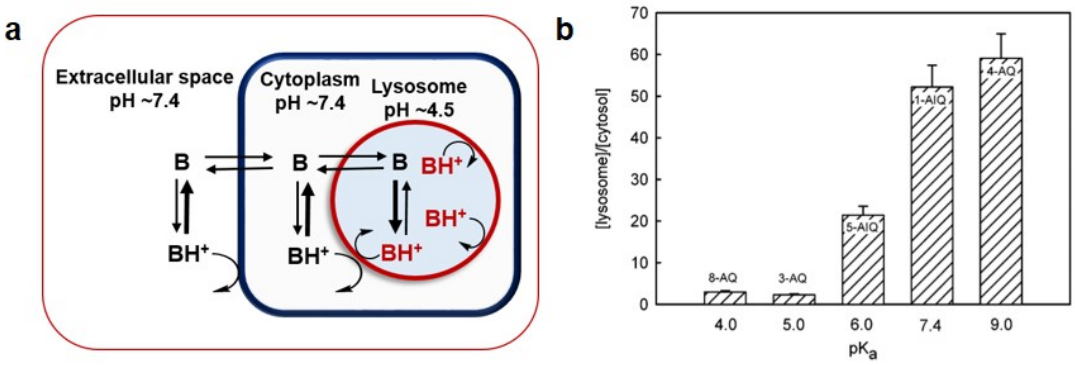

Figure 4.1 (a) Equilibrium model of lysosomotropism. Unprotonated weak base (B) can diffuse through the plasma membrane and the lysosomal membrane in its unionised form. Inside the lysosome, the majority of the drug will be protonated (BH^+) due to the low pH, rendering it membrane impermeable. (b) Lysosome to cytosol concentration ratios as a function of pKa value for model weakly basic amines in the multidrug resistant HL-60 cell line. Reproduced with permission,[220] copyright American Chemical Society.

Another physicochemical property affecting lysosomal accumulation levels of molecules in tandem with pKa is alpha (α) - it represents the lysosomal membrane permeability ratio for the drug in its ionised versus unionised form.[221] Duvvuri *et al.* demonstrated that weak bases with a low α value, such as Lysotracker Red (LTR) and Quinacrine (QNC), have a pH dependent partition coefficient (Figure 4.2). For those compounds, the ionised base (when pH < pKa) has a significantly reduced partition coefficient relative to the un-ionised base (when pH > pKa). This is due to the fact that the basic amines in LTR and QNC are localised at the distal end of the molecule, with no charge distribution. In contrast, compounds with a high α value, such as Rhodamine 123 (R123) and Rhodamine 6G (R6G) have a pH-independent partitioning coefficient. The amines in R123 and R6G are next to large aromatic networks, enabling charge delocalisation across the molecule. As such, compounds with a low α get trapped in the lysosomes (QNC, LTR), whilst compounds with high α do not (R123, R6G) (Figure 4.2b).

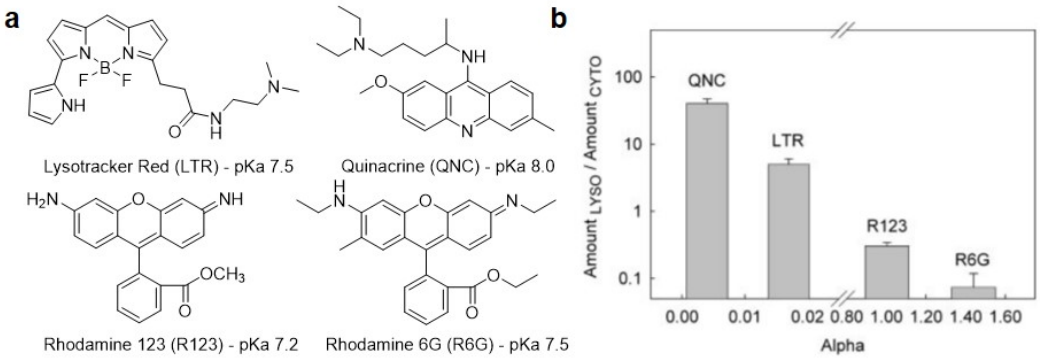

Figure 4.2 (a) Structures of fluorescent weakly basic compounds studied by Duvvuri *et al.*[221] (b) Correlation of experimental α values with the level of lysosomal accumulation. The relative amount of each compound in lysosomes ($Amount_{LYSO}$) normalised to that in cytosol ($Amount_{CYTO}$) plotted against α values. An average of three experiments ±SD. Reproduced with permission,[221] copyright American Society for Biochemistry & Molecular Biology.

4.1.2 Lysosomal drug accumulation in CML

All the TKIs approved by the FDA for CML treatment have a weakly basic amine within their structure, resulting in them having pKa values ≥6 (Table 4.1).[170,222,223] Imatinib, dasatinib, bosutinib and ponatinib all have a piperazine functional group at the tail end of the molecule with varying linker lengths (Figure 4.3). The piperazine amine makes these compounds slightly more basic than nilotinib, which has a secondary amine between two aromatic rings, reducing its basicity (Figure 4.3d). α values have not been measured for these compounds; however, considering the basic amines in these molecules are similarly to LTR and QNC located at the distal end of the molecule, they will likely have a localised charge, and are predicted have low alpha values. Therefore, these are all theoretically lysosomotropic drugs.

Table 4.1 pKa-s of drugs used for CML treatment and their association with lysosomal accumulation.[222,224-227] *n/a – not available

CML drug	pKa	Lysosomal accumulation
imatinib	8.1	√
bosutinib	8.0	√
ponatinib	7.8	n/a*
dasatinib	6.8	√
nilotinib	6.0	√

Hence, it is unsurprising that most of these compounds have been found to be associated with lysosomes by different research groups. Fu *et al.* used hSRS imaging and directly demonstrated that both imatinib and nilotinib accumulate in the lysosomes of CML cells (Figure 3.4b,c).[170] Ruzickova *et al.* used indirect LC-MS measurements, but also found that imatinib, nilotinib and dasatinib localise in lysosomes of various different cancer cells.[228] Burger *et al.* utilised the weak fluorescence properties of imatinib to show its lysosomal uptake in various cell types.[229] Bosutinib has been shown to induce cell death in melanoma cells via lysosomal membrane permeabilisation, so it likely also accumulates in lysosomes.[230] No data has been published on ponatinib intracellular localisation.

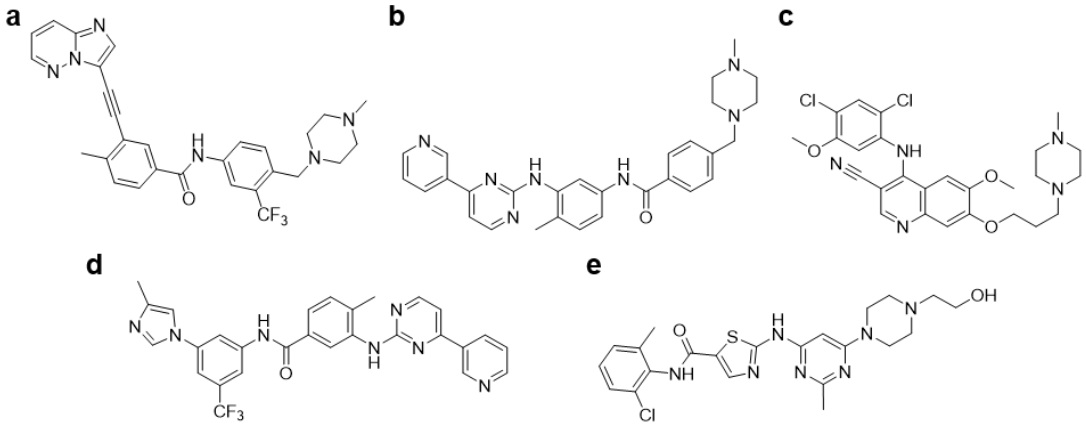

Figure 4.3 Chemical structures of TKIs used for CML treatment. (a) Ponatinib, (b) imatinib, (c) bosutinib, (d) nilotinib, (e) dasatinib.

In a systematic review of TKIs approved by the FDA between 2001 and 2015, O'Brien and Moghaddam reviewed both measured and predicted pKa values and found that 50% of the 30 TKIs had a pKa≥6 while only 3 had a pKa≥9.[223] This highlights that a large proportion of clinically used TKIs are weakly basic, and could therefore be subject to lysosomal trapping. A number of these TKIs, such as sunitinib (pKa=8.9), lapatinib (pKa=7.2), gefitinib (pKa=6.9) and neratinib (pKa=7.7) have been associated with lysosomal accumulation.[32,169,231,232] However, only sunitinib (Figure 4.4) and neratinib (Figure 3.3) accumulation in lysosomes could be imaged directly via fluorescence and Raman respectively.

4.1.3 Role of lysosomes in drug resistance

Lysosomal trapping has been associated with acquired TKI resistance.[231] Lysosomal sequestering of sunitinib, a TKI approved for the treatment of renal cell carcinoma,

was explored in the context of acquired drug resistance by Gotink *et al.* (Figure 4.4).[32] They developed sunitinib resistant cell lines through continuous exposure to sunitinib in 786-O renal cancer cells and HT-29 colon cancer cells. Using fluorescence imaging of sunitinib, they demonstrated that the drug co-localises with Lysotracker Red, where increased lysosomal accumulation was seen in drug resistant cells (Figure 4.4b).[32]

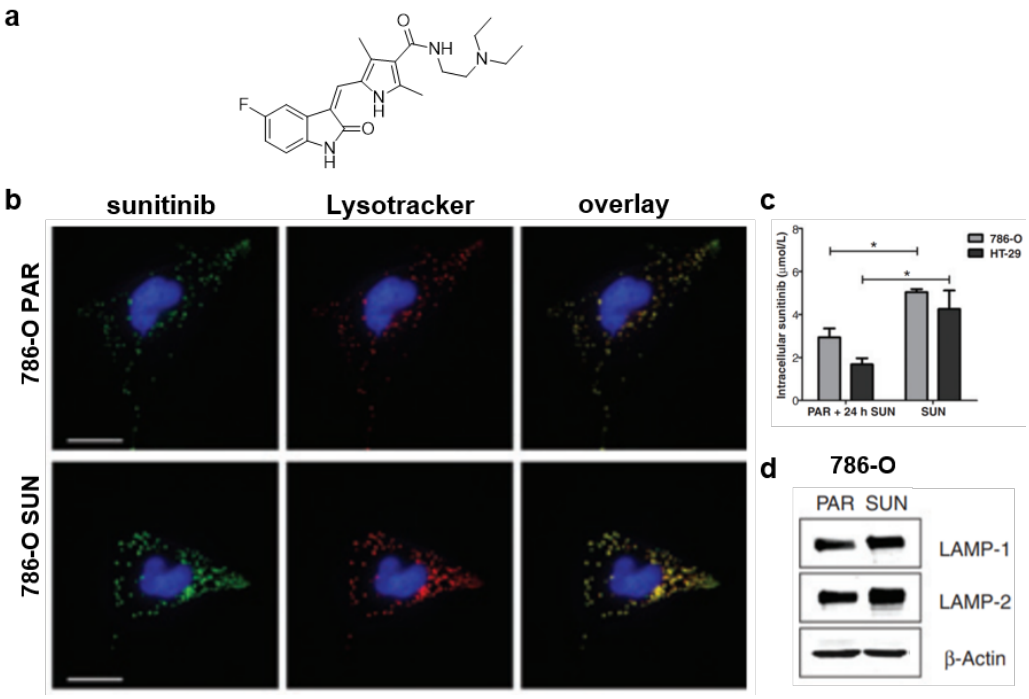

Figure 4.4 Sunitinib imaging and intracellular concentration. (a) Chemical structure of sunitinib. (b) Confocal images of 786-O parental (PAR) and sunitinib resistant (SUN) cells that were incubated with sunitinib (green) (5 μM), Lysotracker Red (red) (75 nM), and Hoechst (blue) (0.5 mg/mL) for 1 h. (c) Intracellular sunitinib concentration determined by LC-MS in 786-O and HT-29 cell lines. Parental cells were incubated with sunitinib (5 μM) for 24 h while sunitinib resistant cells were continuously incubated with sunitinib prior to analysis. (d) Western blots of LAMP1 and LAMP2 in parental and sunitinib-resistant 786-O cells. Adapted with permission,[32] copyright American Association for Cancer Research.

In addition, they found by LC-MS analysis that the total intracellular concentration of sunitinib was 1.7-2.5-fold higher in drug resistant cells, 5.04 mM and 4.25 mM in 786-O and HT-29 cells respectively compared to 2.93 mM and 1.68 mM in sunitinib sensitive cells (Figure 4.4c).[32,233] The increased sunitinib concentration in resistant cells was attributed to the increased lysosomal sequestering capacity in resistant cells, which showed increased fluorescence signal of the drug. To investigate further,

they looked at lysosomal membrane protein 1 (LAMP1) and LAMP2 levels using Western blotting. Elevated levels of both LAMP1 and LAMP2 were found in sunitinib resistant cells, which is an indication of increased lysosome number and/or size (Figure 4.4d). However, immunofluorescence imaging of LAMP1 or LAMP2 was not applied to further assess LAMP levels. Gotink *et al.* were the first to report the involvement of lysosomal sequesteration in acquired TKI resistance. The HT-29 parental and sunitinib resistant cells were further validated in an *in vivo* study, where the sunitinib resistant cells grew tumours that no longer responded to sunitinib treatment.[234]

Lysosomes have also been shown to be involved in drug resistance to imatinib, where ABC transporter A3 (ABCA3) was found to mediate lysosomal sequestration of imatinib.[235] Increased ABCA3 expression results in elevated lysosomal levels of imatinib, which has been associated with both intrinsic and acquired drug resistance in CML. P-glycoprotein (P-gp), another ABC transporter, can also mediate lysosomal sequestering, and was shown to facilitate lysosomal trapping of chemotherapeutic agent doxorubicin (pKa=8.3) in multidrug resistant cervical cancer.[236] Therefore, lysosomes play an important role in cancer drug resistance.

4.2 Lysosomal accumulation of ponatinib

In Chapter 3, we found that ponatinib localises in concentrated puncta in the cytoplasm of CML cells. It was important to consider which cellular organelles these puncta represent, as the known target of ponatinib is the cytoplasmic tyrosine kinase BCR-ABL. Ponatinib, like a large population of TKIs, is a weakly basic drug with a pKa≥7 (pKa=7.8).[224] As such, it will likely be protonated in acidic environments such as lysosomes. We hypothesised that ponatinib, like other TKIs used for CML treatment, accumulates in lysosomes or related acidic organelles inside cells. A multimodal imaging approach combining SRS and fluorescence imaging was used to investigate this.

Both parental and ponatinib resistant KCL22 cell lines were simultaneously incubated with ponatinib (5 μM, 1 h) or DMSO (vehicle control, 1 h) and Lysotracker Green (50 nM, 1 h), a cell-permeable fluorescent dye that stains acidic organelles in live cells (Figure 4.5). The control cells which were treated with DMSO and stained with Lysotracker Green (Figure 4.5a) showed no SRS signal at 2221 cm^{-1} (C≡C, ponatinib on-resonance), indicating that the presence of the fluorophore does not increase the

SRS background signal. In both KCL22 and KCL22$^{Pon\text{-}Res}$ cells treated with ponatinib (Figure 4.5b,c), we could see co-localisation between the ponatinib SRS signal at 2221 cm^{-1} and the two-photon fluorescence (TPF) signal shown in the merged images. Outside of the bright ponatinib puncta, lower levels of the drug were detected in the cytoplasm, which did not co-localise with the TPF signal. As the Raman signal of ponatinib is the highest in the puncta that co-localise with the TPF signal, it can be concluded that the majority of intracellular ponatinib is trapped within acidic organelles, most likely lysosomes, upon protonation.

4.2.1 Increased lysosomal sequestering in ponatinib resistant cells

As discussed in Section 4.1.3, there is evidence that increased lysosomal trapping plays a role in acquired resistance to TKIs.[231] To investigate if this is the case in our CML resistance model, we used the TPF signal as a map, and quantified ponatinib Raman intensity inside acidic vesicles of individual cells. Quantification results showed increased ponatinib Raman signal in the resistant KCL22$^{Pon\text{-}Res}$ cells compared to parental KCL22 cells (Figure 4.5d,e). The mean intensity of ponatinib in the acidic vesicles of KCL22$^{Pon\text{-}Res}$ cells was 1.9-fold higher compared to parental KCL22 cells (Figure 4.5d), and the maximum ponatinib signal had increased 2.5-fold (Figure 4.5e).

These results were further confirmed in an identical experiment where cells were labelled with Lysotracker Red instead of Lysotracker Green (Appendix 2, Figure S1). Using Lysotracker Red as a map for assessing ponatinib levels in lysosomes gave similar results to Lysotracker Green – both mean and maximum ponatinib intensity were increased 2-fold and 2.1-fold respectively in KCL22$^{Pon\text{-}Res}$ cells compared to drug sensitive cells. This indicates that lysosomal trapping of ponatinib in KCL22$^{Pon\text{-}Res}$ cells is increased. A similar observation has previously been made in sunitinib resistant cells, where sunitinib fluorescence signal increased in cells with acquired drug resistance.[32]

In addition, we noted the maximum ponatinib intensity inside lysosomes was very heterogeneous within the resistant cell population (Figure 4.5e). As discussed earlier in Section 3.5.4, heterogeneity of drug uptake *in vitro* has not been studied in depth. However, if drug uptake in CML patients is heterogeneous, it could have implications on treatment efficacy and drug resistance. Here, we have showed that SRS microscopy has the capacity to obtain information on drug uptake heterogeneity.

Interestingly, the ponatinib signal within the cytoplasm of the resistant cells was also significantly increased (Figure 4.5f). In contrast to common opinion, this demonstrates that lysosomal trapping in our CML drug resistance model does not lead to reduced ponatinib availability in the cytoplasm, which would reduce target inhibition. Ponatinib target inhibition is explored further in Section 4.2.3.

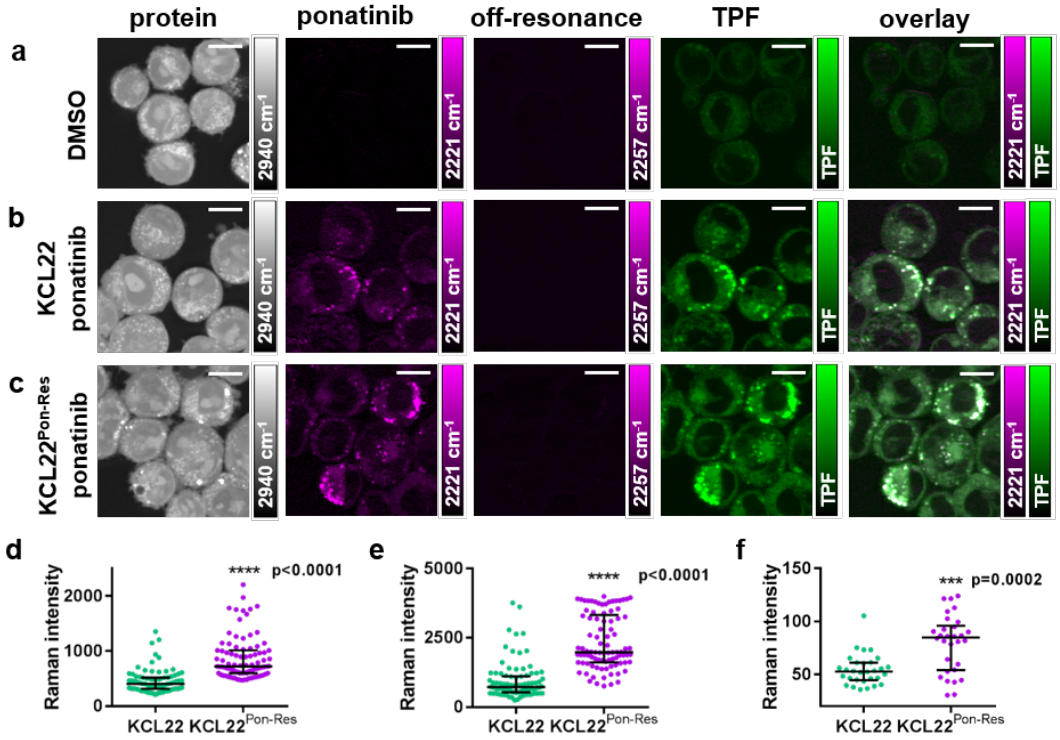

Figure 4.5 Multimodal imaging and quantitative assessment of ponatinib uptake in KCL22 and KCL22$^{Pon\text{-}Res}$ cell lines. KCL22 cells were treated with (a) DMSO (0.0003%, v/v) or (b) ponatinib (5 μM, 1 h) and labelled with Lysotracker® Green (50 nM, 1 h). (c) KCL22$^{Pon\text{-}Res}$ cells were treated with (c) ponatinib (5 μM, 1 h) labelled with Lysotracker® Green (50 nM, 1 h). SRS images acquired at (from left to right) 2940 cm^{-1} (CH_3, proteins); 2221 cm^{-1} (C≡C, ponatinib); 2257 cm^{-1} (off-resonance), TPF image acquired at 861 nm (Lysotracker® Green); overlay of ponatinib and TPF. (d) Mean ponatinib Raman intensity, and; (e) Maximum ponatinib Raman intensity inside the vesicles of each individual cell quantified for KCL22 and KCL22$^{Pon\text{-}Res}$ cells that were treated with 5 μM ponatinib for 1 h, n=30 cells, 3 biological repeats. (f) Mean ponatinib Raman intensity quantified outside of the vesicles of individual cells, n=10, 3 biological repeats. The Mann-Whitney test was used to compare ponatinib Raman intensity values. Images acquired at 1024 × 1024 pixels, 20 μs pixel dwell time, laser power 200 mW (the tuneable pump beam), gain 1 with false colours applied to different detection wavenumbers. Scale bars: 10 μm.

4.2.2 Chloroquine and ponatinib combination treatment

After finding that ponatinib lysosomal accumulation was increased in ponatinib resistant CML, we wanted to explore if altering lysosome function with another drug would reduce lysosomal trapping of ponatinib. There are two potential strategies for inhibiting lysosome function – either inhibiting drug accumulation in the lysosomes or disrupting the lysosomal membrane to release its contents.[237] Most drugs investigated for this purpose focus on inhibiting drug accumulation.

Chloroquine (CQ), another lysosomotropic agent (pKa_1=10.2, pKa_2=8.4), accumulates in the lysosomes, where it increases lysosomal pH (Figure 4.6).[170,238] When used in combination therapy, CQ has been shown to inhibit lysosomal drug uptake.[170] The precise mechanism by which CQ inhibits lysosome function, however, has not been established. Bafilomycin A1 and manzamine A both inhibit the v-ATPase proton pump on the lysosomal membrane (Figure 4.6).[127] This prevents acidification of the lysosomes, leading to increased lysosomal pH. As CQ combination treatment with imatinib, nilotinib and dasatinib has previously been shown to increase efficacy of TKIs against CML stem cells, we chose CQ for our combination treatment with ponatinib.[129]

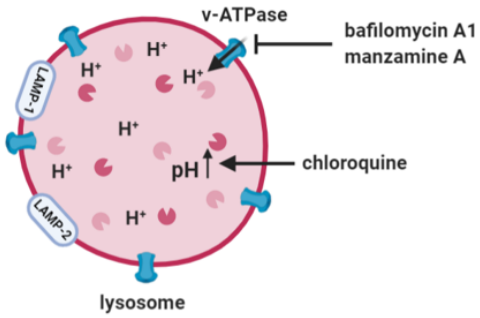

Figure 4.6 Schematic showing how CQ, bafilomycin A1 and manzamine A impair lysosomes. CQ gets protonated inside the lysosome, mopping up protons and subsequently increasing lysosomal pH. Bafilomycin A1 and manzamine A inhibit v-ATPase from pumping hydrogen ions (H^+) into the lysosomal lumen, which also increases lysosomal pH. Image created with Biorender.

It was hypothesised that combination treatment with CQ would prevent the increased lysosomal uptake of ponatinib. Prior to multimodal imaging with SRS, both KCL22 and $KCL22^{Pon\text{-}Res}$ cells were incubated with CQ (20 μM, 2 h) before treatment with ponatinib (5 μM, 1 h) and labelling with Lysotracker Green (50 nM, 1 h). CQ treatment significantly reduced the ponatinib Raman signal in both cell lines (Figure 4.7a,b; full

imaging panels shown in SI Figure S2 and Figure S3). Quantification of ponatinib signal inside lysosomes demonstrated that CQ treatment reduced mean ponatinib concentration inside the lysosomes 2.7- and 3.8-fold in the KCL22 and KCL22$^{Pon-Res}$ cells, respectively, compared to ponatinib alone (Figure 4.7c,d). Fu *et al.* reported similar results for CQ and imatinib combination treatment, which reduced lysosomal imatinib levels 5-fold in drug sensitive mouse CML cells.[170] Our results indicate that CQ combination treatment does inhibit ponatinib lysosomal trapping in both ponatinib sensitive and ponatinib resistant cells.

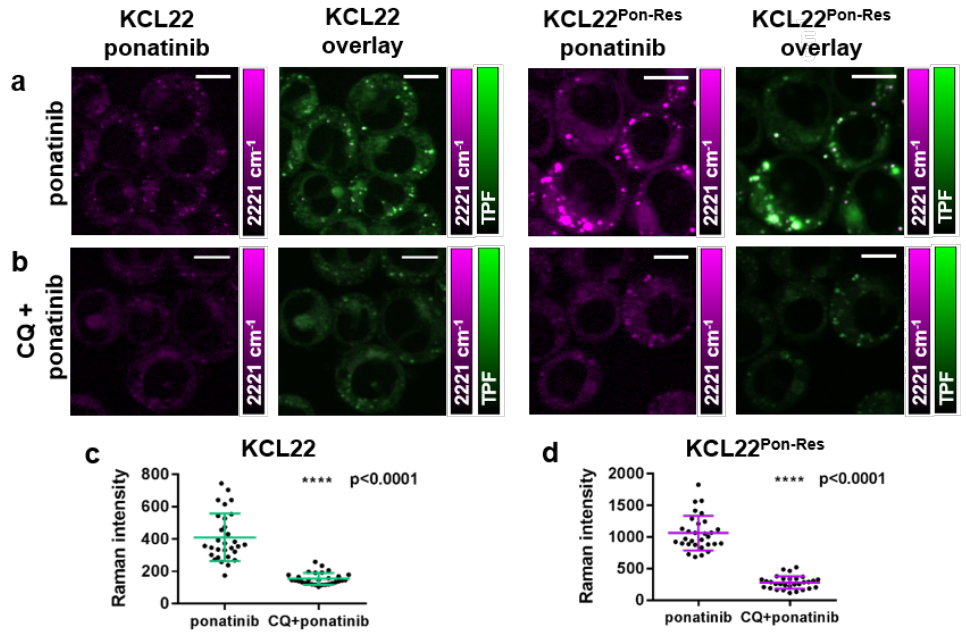

Figure 4.7 Multimodal imaging and quantitative assessment of CQ treatment on the vesicular uptake of ponatinib in KCL22 and KCL22$^{Pon-Res}$ cells. KCL22 and KCL22$^{Pon-Res}$ cells were treated with (a) ponatinib (5 μM, 1 h); (b) CQ (20 μM, 2 h) followed by combination treatment of ponatinib (5 μM, 1 h) and CQ (20 μM, 1 h). Images shown (left to right) 2221 cm^{-1} (C≡C, ponatinib); overlay TPF image at 861 nm (Lysotracker® Green) merged with 2221 cm^{-1}. (c), (d) Mean ponatinib Raman intensity inside the vesicles of each individual cell quantified in (c) KCL22 and (d) KCL22$^{Pon-Res}$ cell line, n=10 cells, 3 biological repeats. The Mann-Whitney test was used to compare ponatinib Raman intensity values. Individual data points shown with error bar as mean±SD. Images acquired at 1024 × 1024 pixels, 20 μs pixel dwell time, laser power 200 mW (the tuneable pump beam), gain 1 with false colours applied to different detection wavenumbers. Scale bars: 10 μm.

4.2.3 Ponatinib target inhibition

Lysosomal trapping is traditionally associated with decreasing drug-target engagement as it is thought to sequester the drug away from its target. Ponatinib's target in CML is the cytoplasmic BCR-ABL. We wanted to investigate the effect of ponatinib on BCR-ABL activity via Western blotting. However, BCR-ABL activity cannot be measured directly because the protein is rapidly degraded and is subject to dephosphorylation upon cell lysis.[239] CRKL is an adaptor protein that it is dependent on BCR-ABL for phosphorylation (Figure 4.8a). It has been shown that the phospho-tyrosine content of CRKL can be measured quantitatively in a dose dependent manner as a surrogate marker of BCR-ABL activity.[240] Hence, we utilised phosphorylation of CRKL as a standard readout of BCR-ABL activity.

KCL22 and KCL22$^{Pon\text{-}Res}$ cells were both treated with either DMSO (0.0003%, drug vehicle) or a range of ponatinib concentrations (10 nM - 500 nM, 1 h). The effect of ponatinib on the phosphorylation of CRKL was measured with a phospho-CRKL (p-CRKL at Tyr207) antibody (Figure 4.8b,c). A reduction in p-CRKL band intensities represents inhibition of BCR-ABL in response to drug treatment. We found that ponatinib inhibited p-CRKL, and hence BCR-ABL, to a similar degree in both drug sensitive and drug resistant cells. This demonstrates that ponatinib target engagement in KCL22$^{Pon\text{-}Res}$ cells is not reduced despite lysosomal trapping, i.e. there is sufficient cytoplasmic ponatinib to inhibit CRKL phosphorylation. It also confirms a previously reported BCR-ABL independent resistance mechanism in this cell line.[109]

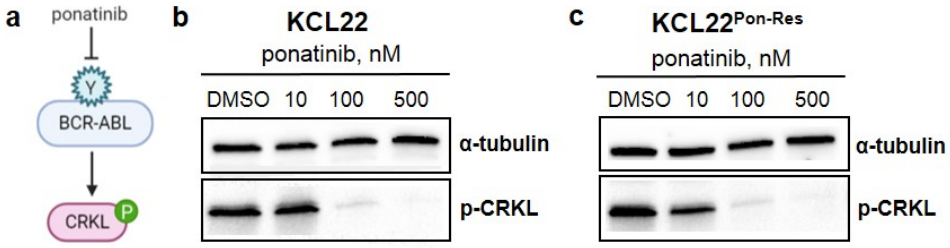

Figure 4.8 Ponatinib inhibition of p-CRKL. (a) Schematic diagram demonstrating how ponatinib inhibits BCR-ABL signalling via inhibition of the tyrosine kinase domain, which in turn prevents phosphorylation of CRKL. Created with Biorender. (b), (c) Effect of ponatinib on the phosphorylation of CRKL in KCL22 and KCL22$^{Pon\text{-}Res}$ cells. (b) KCL22 and (c) KCL22$^{Pon\text{-}Res}$ cells were treated with (left to right) either DMSO (0.0003%, v/v) or ponatinib (10 nM, 100 nM, 500 nM, 1 h). Western blot analysis was carried out with an antibody specific to phosphorylated CRKL (p-CRKLTyr207, 39 kDa). α-tubulin (50 kDa) was used as a loading control.

4.2.4 Effect of chloroquine on ponatinib target engagement

Having found that combination treatment with CQ significantly decreased lysosomal trapping of ponatinib in both cell lines (Figure 4.7), we were interested in its effect on BCR-ABL inhibition. We used Western blotting to compare the effects of CQ combination treatment with ponatinib only treatment on p-CRKL in KCL22 and KCL22$^{Pon-Res}$ cells. Both cell lines were treated with either ponatinib (10 nM – 500 nM, 1 h) or a combination of CQ (20 μM, 2 h) pre-treatment followed by ponatinib (10 nM – 500 nM, 1 h) (Figure 4.9a,b; full blots shown in Appendix 2 Figure S4 and Figure S5). To compare p-CRKL inhibition level, the bands were quantified for each lane using ImageLab software, and normalised to α-tubulin. We found that pre-treatment with CQ significantly increased p-CRKL inhibition at the lowest ponatinib dose (10 nM) for both cell lines (Figure 4.9c,d), demonstrating that reduced lysosome trapping of ponatinib in the CQ treated cells increased BCR-ABL inhibition and drug target interaction.

Interestingly, quantification of p-CRKL levels also revealed ponatinib only treatment inhibited CRKL phosphorylation more effectively in the KCL22$^{Pon-Res}$ cells compared to KCL22 ponatinib sensitive cells. This result correlates with the increased cytoplasmic levels of ponatinib in the resistant cells (Figure 4.5f) and supports a BCR-ABL independent mechanism of ponatinib resistance.[109] Hence, it is not surprising that CQ treatment does not re-sensitise KCL22$^{Pon-Res}$ cells to ponatinib (unpublished data by the Helgason group, Figure S6). It is in contrast to the BCR-ABL dependent resistance mechanism reported for other TKIs used for CML treatment, e.g. imatinib, where combination treatment with CQ and TKI increases target engagement and enhances efficacy.[129,170]

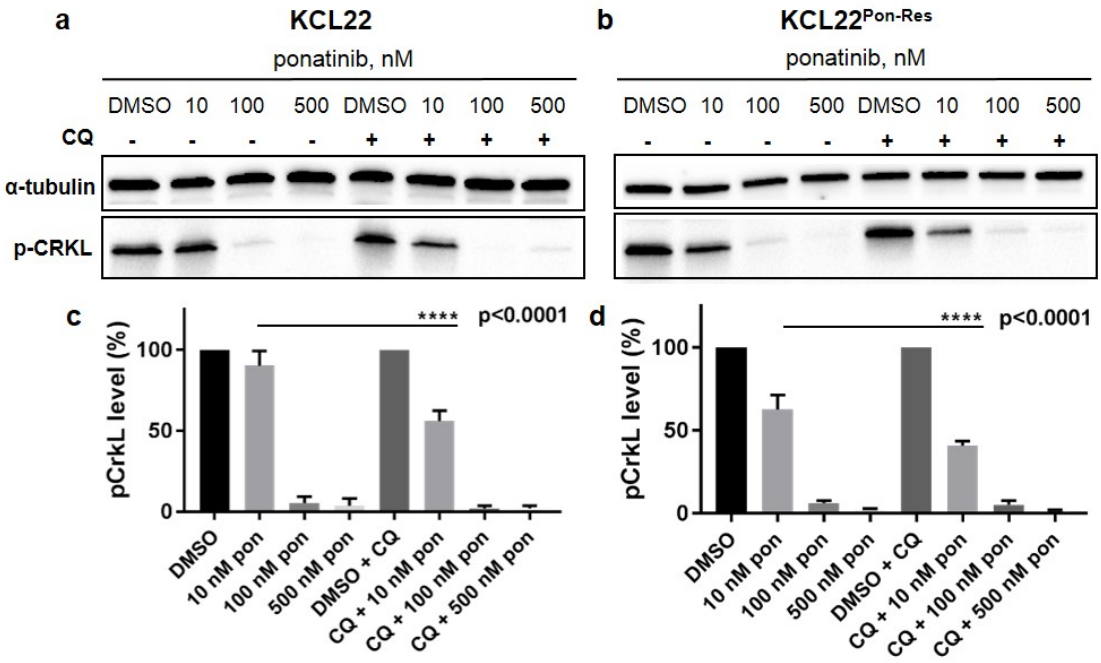

Figure 4.9 Chloroquine effect on ponatinib target engagement. (a) KCL22 and (b) KCL22$^{Pon-Res}$ cells were treated with (left to right) either DMSO (0.0003%, v/v), ponatinib (10 nM, 100 nM, 500 nM, 1 h) or a combination of CQ (20 μM, 2 h) pre-treatment and ponatinib (10 nM, 100 nM or 500 nM, 1 h). Western blot analysis was carried out with an antibody specific to phosphorylated CrkL (p-CRKLTyr207, 39 kDa). α-tubulin (50 kDa) was used as a loading control. (c), (d) p-CrkL level was normalised to α-tubulin and DMSO values from n=3 biological repeats using Image LabTM Software. One-way Anova (Tukey's multiple comparisons test) was used to compare ponatinib (10 nM) alone vs CQ combination treatment. Values shown as mean±SD.

4.3 Investigating autophagy involvement in ponatinib localisation

As discussed in Section 1.4 autophagy is a cellular degradation system that delivers cytoplasmic constituents to the lysosomes for recycling or removal. Autophagy has been shown to be implicated in CML drug resistance, but so far attempts to target autophagy in the clinic have largely failed. CQ is not just a lysosomotropic agent, it is also an indirect autophagy inhibitor. When lysosomal function is impaired by CQ, autophagy is also inhibited as lysosomes can no longer fuse with autophagosomes to form autolysosomes (Figure 4.10). To determine whether the inhibition of autophagy by CQ contributed to the reduced lysosomal accumulation of ponatinib, it was important to image ponatinib in cells where autophagy was inhibited directly. To that end, we utilised KCL22$^{Pon-Res}$ CRISPR-*ATG7* cells. Autophagy related gene 7 (ATG7), a critical component of the autophagy pathway, is essential for the lipidation of LC3

(LC3-II) (Figure 4.10).[241,242] LC3-II attaches to the phagophore membrane, which is necessary for autophagosome formation. *ATG7* knockdown inhibits LC3-II formation and subsequently also inhibits autophagy. Mitchell *et al.* have previously shown that LC3-II levels are decreased in KCL22$^{Pon\text{-}Res}$ CRISPR-*ATG7* cells compared to KCL22$^{Pon\text{-}Res}$ CRISPR-Control cells, demonstrating that this cell line has a defect in its autophagy pathway.[109]

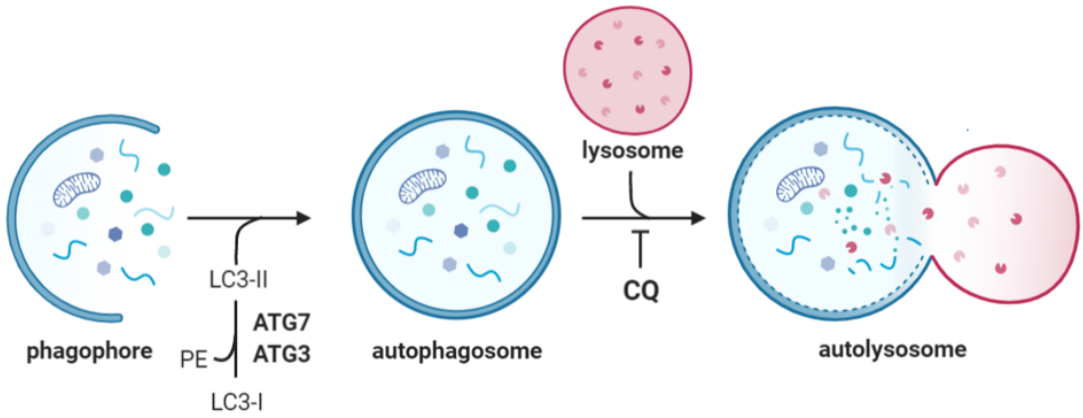

Figure 4.10 Schematic representation of autophagy demonstrating both ATG7 involvement in LC3-I lipidation to LC3-II and CQ inhibition of autolysosome formation. PE-phophatidylethylamine. Image created with Biorender.

4.3.1 Imaging ponatinib in ATG7 knockdown CML cells

Prior to imaging, we confirmed by Western blotting that ATG7 was knocked down in KCL22$^{Pon\text{-}Res}$ CRISPR-*ATG7* cells (Figure 4.11a), and checked that both KCL22$^{Pon\text{-}Res}$ CRISPR-*ATG7* (GI_{50}=702 nM) and KCL22$^{Pon\text{-}Res}$ CRISPR-Control (GI_{50}=339 nM) cells still retained ponatinib resistance (Table 2.6).

For multimodal imaging, KCL22$^{Pon\text{-}Res}$ CRISPR-*ATG7* and KCL22$^{Pon\text{-}Res}$ CRISPR-Control cells were simultaneously treated with ponatinib (5 μM, 1 h) and labelled with Lysotracker Green (50 nM, 1 h) (Figure 4.11b,c). As previously, the TPF signal was used as a map to quantify relative Raman signal of ponatinib in acidic organelles of individual cells in both cell lines. No significant difference between the two cell lines was found, demonstrating that autophagy does not play a role in ponatinib accumulation in lysosomes (Figure 4.11d). It is therefore likely that the reduction of ponatinib concentration in lysosomes upon CQ combination treatment was due to the lysosomotropic properties of CQ, which decreased the lysosomal trapping capacity of ponatinib.

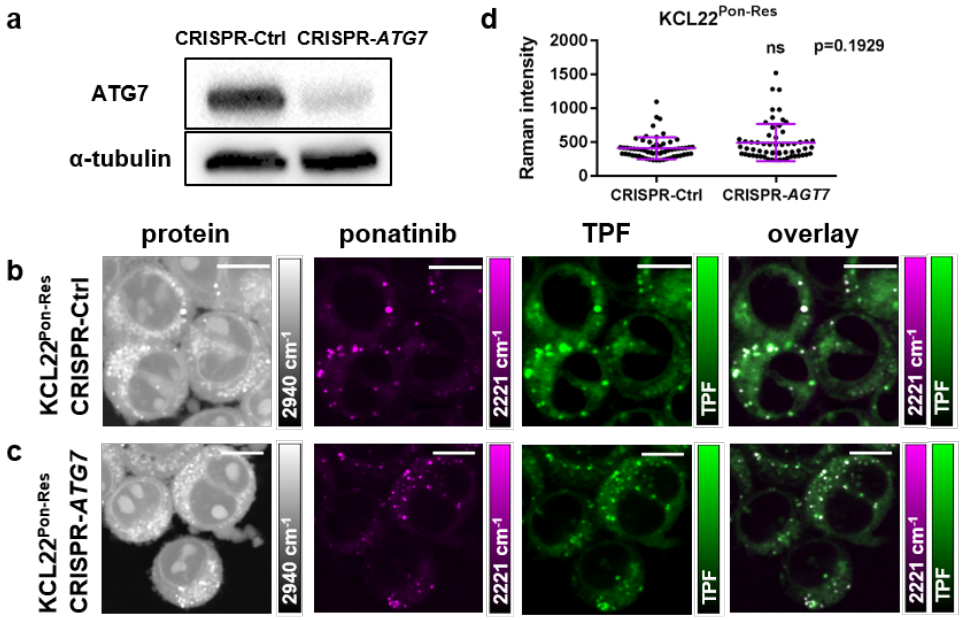

Figure 4.11 Multimodal imaging and quantitative assessment of ponatinib uptake in KCL22$^{Pon-Res}$ CRISPR cell lines. (a) ATG7 (75 kDa) protein expression in KCL22$^{Pon-Res}$ CRISPR cell lines. α-tubulin (50 kDa) was used as a loading control. (b) KCL22$^{Pon-Res}$ CRISPR-Ctrl and (c) KCL22$^{Pon-Res}$ CRISPR-*ATG7* cell lines that were treated with ponatinib (5 μM, 1 h) and labelled with Lysotracker Green (50 nM, 1 h) simultaneously. SRS images acquired at (from left to right) 2940 cm^{-1} (CH_3, proteins); 2221 cm^{-1} (C≡C, ponatinib); TPF image acquired at 861 nm (Lysotracker® Green); overlay of ponatinib and TPF. Scale bars: 10 μm. (d) Mean ponatinib Raman intensity at 2221 cm^{-1} inside the vesicles of each individual cell quantified for KCL22$^{Pon-Res}$ CRISPR-Ctrl and KCL22$^{Pon-Res}$ CRISPR-*ATG7* cells treated with 5 μM ponatinib for 1 h, n=20 cells, 3 biological repeats. The Mann-Whitney test was used to compare ponatinib Raman intensity values. Individual data points shown with error bar as mean±SD. Images acquired at 1024 × 1024 pixels, 20 μs pixel dwell time, laser power 100 mW (the tuneable pump beam), gain 1 with false colours applied to different detection wavenumbers. Scale bars: 10 μm.

4.4 Lysosome biogenesis increased in ponatinib resistant CML

After it was determined that autophagy was not involved in increased lysosomal accumulation of ponatinib in KCL22$^{Pon-Res}$ cells, it was necessary to further investigate the potential reasons for this increased uptake in the context of acquired drug resistance. Lysosomes have an important role in the cell and have previously been implicated in TKI drug resistance.[32,231] Therefore, we decided to explore the importance of lysosomes in our drug resistance model.

4.4.1 Number of lysosomes in ponatinib resistant CML

First, we decided to investigate the number of lysosomes in both KCL22 and KCL22$^{Pon-Res}$ cells. To do so, we used the Lysotracker Green and Lysotracker Red data, which had been generated during multimodal imaging of ponatinib in lysosomes (Section 4.2). The number of acidic vesicles was quantified from fluorescence images in 30 individual cells per sample for both cell lines (Figure 4.12a,b). We found the number of acidic vesicles was significantly increased in KCL22$^{Pon-Res}$ cells compared to drug sensitive cells using both Lysotracker Green and Lysotracker Red labelling (Figure 4.12c,d). This was a first indication that the number of lysosomes is increased in ponatinib resistant cells upon drug treatment. However, as Lysotracker dyes label acidic organelles, this data did not give us a direct measure of the number of lysosomes.

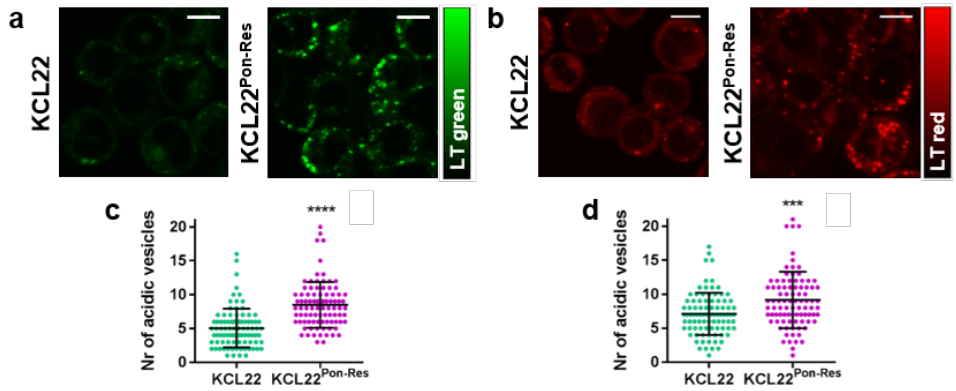

Figure 4.12 Assessing lysosome number in CML cells using Lysotracker Green and Lysotracker Red. (a), (b) Representative fluorescence image of KCL22 and KCL22$^{Pon-Res}$ cells treated with ponatinib (5 µM, 1 h) and labelled with either (a) Lysotracker® Green (50 nM, 1 h) or (b) Lysotracker® Red (75 nM, 1 h). Scale bars: 10 µm. (c), (d) Number of acidic vesicles per cell quantified for both KCL22 and KCL22$^{Pon-Res}$ cells from the fluorescence images in n=30 cells, 3 biological repeats. The Mann Whitney test was used to compare the number or acidic vesicles, **** ($p<0.0001$), *** ($p=0.0003$). Individual data points shown with error bar as mean±SD.

4.4.2 LAMP1 levels in ponatinib resistant CML

To investigate the number of lysosomes more directly, we used immunofluorescence to measure LAMP1 levels in our cell lines. LAMP1 and LAMP2 are the most abundant lysosomal transmembrane proteins, which together account for about 50% of total lysosomal membrane proteins.[134] Therefore, measuring LAMP1 levels gives a more direct indication of lysosome numbers than Lysotracker labelling.

We imaged LAMP1 in both untreated (DMSO, 0.0003%, 1 h) and drug treated (ponatinib, 5 μM, 1 h) cells stained with LAMP1 antibody, where cell nuclei were labelled with DRAQ7 nuclear dye (Figure 4.13a,b). LAMP1 fluorescence intensity was quantified per cell in both KCL22 and KCL22$^{Pon\text{-}Res}$ cell lines (Figure 4.13c). Both ponatinib treated and untreated KCL22$^{Pon\text{-}Res}$ cells were found to have significantly higher levels of LAMP1 than KCL22 cells. Ponatinib treatment did not increase LAMP1 levels significantly in either cell line when compared to the DMSO control. Elevated LAMP1 levels are associated with increased lysosome number or lysosome size. Hence, our results indicate that ponatinib resistant CML cells have increased number of lysosomes and or lysosome size. Gotink *et al.* also reported increased levels of LAMP1 and LAMP2 in sunitinib resistant cell lines (Figure 4.4d).[32] We interpreted the increased LAMP1 level as a potential indicator of increased lysosome biogenesis. IF images of LAMP1 could also be used to quantify the lysosome number and size. However, we originally set up the experiment to measure total fluorescence intensity per image, and the images acquired do not have high enough resolution to allow lysosome number to be quantified.

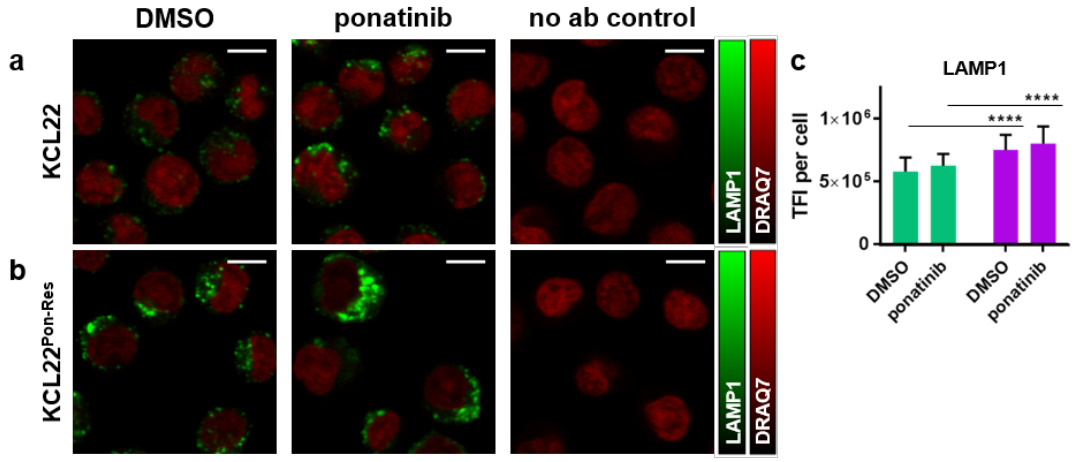

Figure 4.13 Immunofluorescence imaging of LAMP1 in CML cells. (a) KCL22 and (b) KCL22$^{Pon\text{-}Res}$ cells were treated with either DMSO (0.0003%, v/v) or ponatinib (5 μM) for 1 h, fixed and stained with LAMP1 (green). Nuclei were stained with DRAQ7 (red). No antibody (ab) control cells were treated with DMSO (0.0003%, v/v) and stained with DRAQ7, but not stained with LAMP1. (c) Immunofluorescence of LAMP1 quantified in KCL22 (green) and KCL22$^{Pon\text{-}Res}$ (purple) cells. Total fluorescence intensity (TFI) of LAMP1 in individual cells of n=6 fields of view was quantified from 3 biological repeats. Welch's t-test was used to compare LAMP1 levels. Values shown as mean±SD, **** ($p<0.0001$). Images acquired at 1024 × 1024 pixels, 4 μs pixel dwell time, laser power 200 mW (the tuneable pump beam), gain 1. Scale bars: 10 μm.

4.4.3 TFEB levels in ponatinib resistant CML

Finding increased LAMP1 levels in ponatinib resistant cells prompted us to look into lysosome biogenesis in our CML model. Nuclear TFEB is a master regulator of lysosome biogenesis (Figure 4.14).[243] TFEB positively regulates the transcription of genes involved in all steps of lysosome biogenesis, including lysosomal proliferation, acidification, and exocytosis. TFEB also regulates genes involved in autophagy pathways. Overall, TFEB modulates processes that promote clearance of lysosomal substrates within cells.

Under normal conditions, TFEB is localised in the cell cytoplasm, where it is phosphorylated by mTOR complex 1 (mTORC1) on the lysosomal surface.[137] Phosphorylated TFEB binds to 14-3-3 proteins which promotes its cytoplasmic retention. In contrast, nutrient starvation or lysosomal stress leads to TFEB dephosphorylation by calcineurin, which is activated by lysosomal Ca^{2+} release via muculipin 1 (MCOLN1) receptor on the lysosome surface.[244] In the nucleus, TFEB activates coordinated lysosomal expression and regulation (CLEAR) genes, which triggers lysosome biogenesis (Figure 4.14).[137] High nuclear TFEB localisation is implicated in a number of lysosome storage disorders.

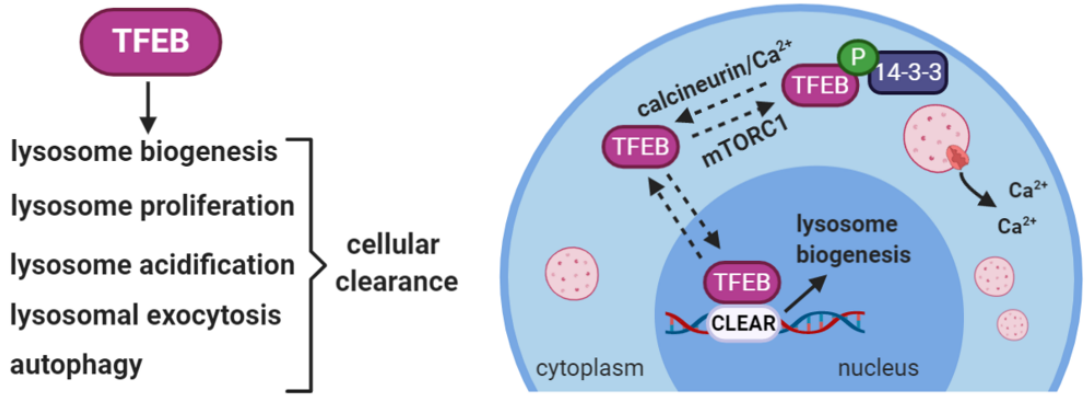

Figure 4.14 TFEB regulated processes. TFEB positively regulates the transcription of genes related to lysosome biogenesis (CLEAR). When TFEB is phosphorylated by mTORC1 it stays in the cytoplasm where it is sequestered by 14-3-3 proteins. Calcineurin, which is activated by the release of Ca^{2+} from the lysosomes can dephosphorylate TFEB, which drives its translocation into the nucleus, where it activates the transcription of genes that lead to increased lysosomal biogenesis and various other processes that promote cellular clearance. Image created with Biorender.

To establish whether lysosome biogenesis was differentially regulated in the resistant CML cells, we measured TFEB levels via immunofluorescence labelling. Both KCL22 and KCL22$^{Pon-Res}$ cells were treated with DMSO (0.0003%, 1 h) or ponatinib (5 μM, 1 h) and stained with TFEB antibody. Nuclei were stained with DRAQ7. Immunofluorescence imaging revealed that the majority of TFEB co-localised with DRAQ7 in both drug sensitive and drug resistant cells (Figure 4.15, Figure S7 for no antibody control images). This result indicates that both CML cell lines have high TFEB activity and possibly elevated levels of lysosome biogenesis. The nuclear localisation of TFEB in KCL22 cells shows that even drug sensitive CML cells have upregulated TFEB activity.

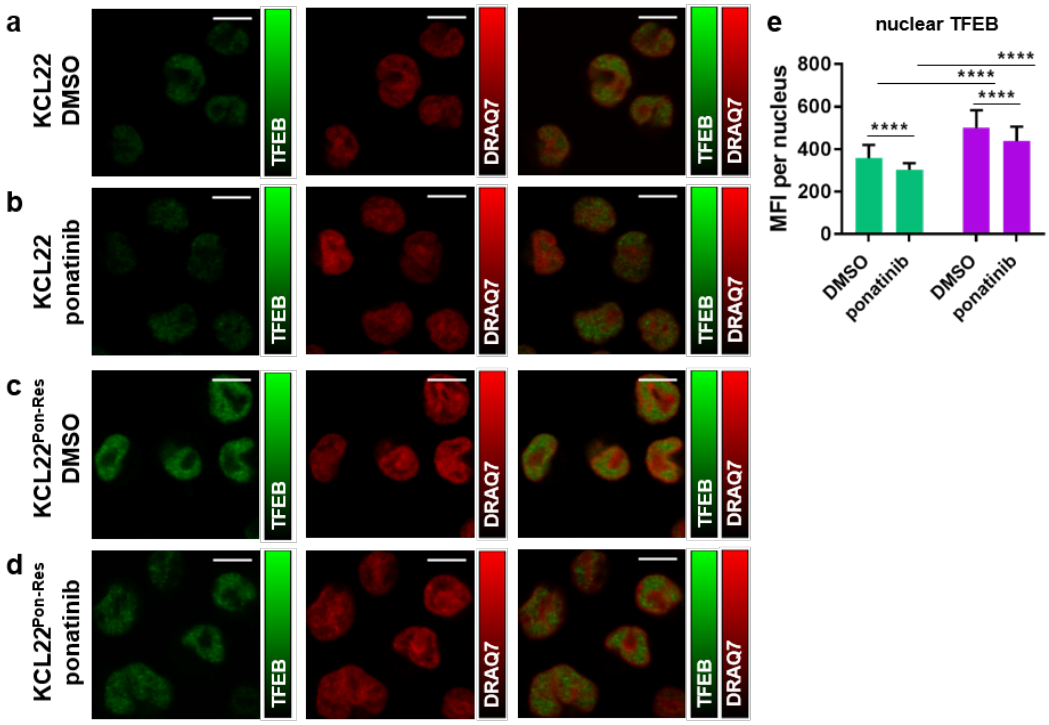

Figure 4.15 Immunofluorescence imaging of nuclear TFEB in CML cells. (a), (b) KCL22 and (c), (d) KCL22$^{Pon-Res}$ cells were treated with either (a), (c) DMSO (0.0003%, v/v) or (b), (d) ponatinib (5 μM) for 1 h, fixed and stained with TFEB (green). Nuclei were stained with DRAQ7 (red). (e) Immunofluorescence of nuclear TFEB quantified in KCL22 (green) and KCL22$^{Pon-Res}$ (purple) cells. Mean fluorescence intensity (MFI) in individual nuclei of n=6 fields of view was quantified from 3 biological repeats. The Mann-Whitney test was used to compare TFEB levels. Values shown as mean±SD, **** ($p<0.0001$). Images acquired at 1024 × 1024 pixels, 4 μs pixel dwell time, laser power 200 mW (the tuneable pump beam), gain 1. Scale bars: 10 μm.

Quantification of nuclear TFEB in individual cells demonstrated that KCL22$^{Pon-Res}$ cells had increased TFEB levels compared to KCL22 cells (Figure 4.15e), indicative of increased lysosome biogenesis in the resistant cells. Previous research by Mitchell *et al.* established that KCL22$^{Pon-Res}$ cells have increased mTORC1 levels compared to ponatinib sensitive KCL22 cells.[109] Therefore, an mTORC1 related reduction in TFEB phosphorylation cannot be responsible for the increased TFEB levels in the nuclei of KCL22$^{Pon-Res}$ cells. As mentioned above, TFEB can be dephosphorylated by calcineurin, a serine/threonine phosphatase. Calcineurin is activated upon starvation, lysosomal stress or oxidative stress (Figure 4.16).[245] Activation of calcineurin is dependent on lysosomal release of Ca^{2+} through MCOLN1 on the lysosome surface.[244] Our results show increased basal level of LAMP1 (Figure 4.13c) as well as elevated nuclear TFEB in KCL22$^{Pon-Res}$ cells. It is therefore possible that lysosomal MCOLN1 mediated Ca^{2+} release is increased in ponatinib resistant cells, leading to elevated calcineurin dependent dephosphorylation of TFEB, which results in higher nuclear TFEB levels that promote lysosome biogenesis. Additional experiments would be required to prove this theory. This would involve exploring MCOLN1 levels, Ca^{2+} lysosomal release as well as calcineurin activity within both cell lines.

Additionally, we found that ponatinib treatment actually decreased nuclear TFEB levels in both KCL22 and KCL22$^{Pon-Res}$ cells (Figure 4.15e). Medina *et al.* showed previously that treatment with a lysosomotropic agent, glycyl-*L*-phenylalanine 2-naphthylamide (GPN), reduced Ca^{2+} release from lysosomes.[244] As we have established, ponatinib is also a lysosomotropic agent, and localises in the lysosomes (Figure 4.5). It is plausible that ponatinib accumulation in lysosomes decreases Ca^{2+} release from lysosomes, leading to reduced calcineurin activity and consequently decreased TFEB nuclear localisation, which is what we saw upon ponatinib treatment in our cells (Figure 4.16). However, further investigation would be required to make a definite conclusion.

The main take-away message from the immunofluorescence imaging of TFEB in CML cells was that both drug sensitive and ponatinib resistant cells KCL22$^{Pon-Res}$ cells had higher levels of nuclear TFEB compared to KCL22 cells, indicative of increased lysosome biogenesis. Sardiello *et al.* have shown that TFEB overexpression results in higher cellular LAMP1 levels as well as increased number of lysosomes per cell.[137] Sung *et al.* recently demonstrated that increased TFEB activation in glioblastoma is a cause of drug resistance and inhibits apoptosis.[246] They showed that combination

treatment with melatonin and vorinostat decreased TFEB expression, increased apoptosis and decreased glioma stem cell tumour-sphere formation and size. TFEB association with drug resistance has also been shown for both ovarian cancer and non-small cell lung cancer.[247,248] These studies positively correlate with our findings, and could reflect an adaptation in our ponatinib resistant CML model, which allows these cells to survive in the presence of ponatinib. To further assess the significance of elevated TFEB levels in our CML resistance model, a TFEB CRISPR knockout cell line could be created to determine if that would re-sensitise resistant CML cells to ponatinib. Additionally, transcriptome analysis could be used to investigate TFEB levels in drug responsive and drug resistant CML patients, as well as levels of known gene targets of TFEB.

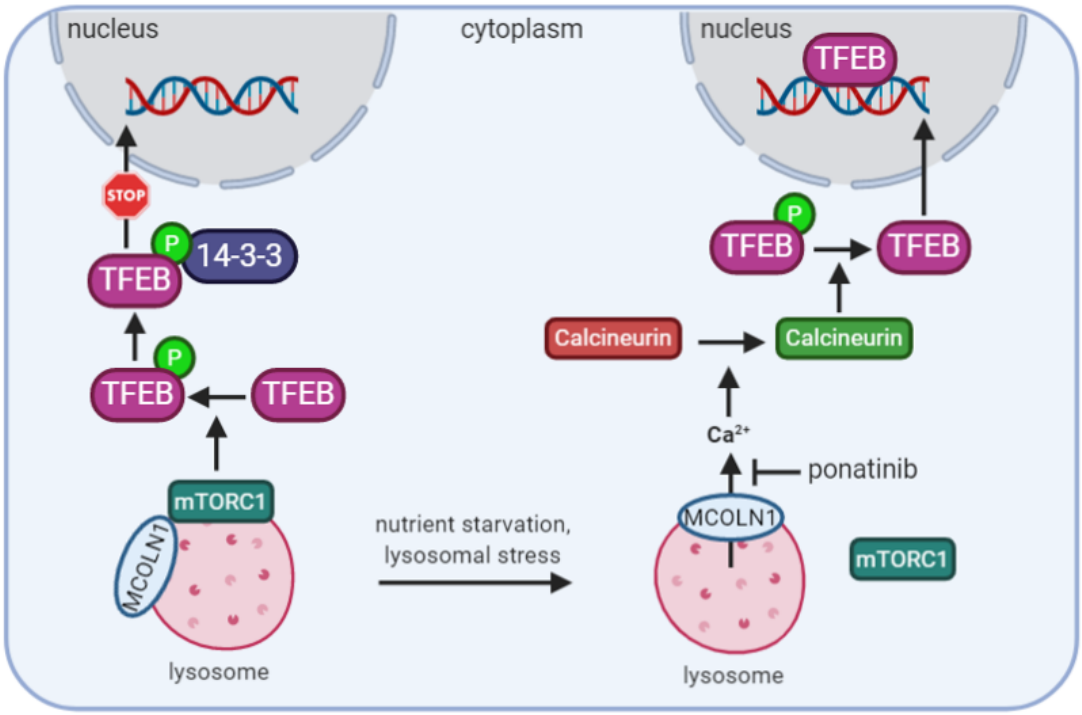

Figure 4.16 Model of lysosomal Ca^{2+} mediated regulation of TFEB. Under normal conditions, TFEB is phosphorylated by mTORC1 on the lysosomal surface, interacts with the 14-3-3 proteins and remains in the cytoplasm. During nutrient starvation, lysosomal stress or oxidative stress, Ca^{2+} is released from the lysosome through the MCOLN1 receptor, establishing increased Ca^{2+} levels in the vicinity of the lysosome. Ca^{2+} leads to local calcineurin activation and TFEB dephosphorylation. Dephosphorylated TFEB translocates to the nucleus where it promotes transcription of lysosomal genes. Ponatinib lysosomal trapping potentially decreases Ca^{2+} release from the lysosomes. Image created with Biorender.

4.4.4 Lysosomal pH in ponatinib resistant CML

Although the elevated LAMP1 and TFEB levels in ponatinib resistant CML cells were indicative of increased lysosome biogenesis, we still did not know how that related to the increased concentration of ponatinib in the lysosomes of resistant cells (Figure 4.5d,e). TFEB has also been reported to modulate the expression of genes involved in lysosomal acidification.[243,245] As lysosomal pH influences the equilibrium involved in ponatinib lysosomal accumulation, we decided to investigate the pH levels in our CML cell lines. To do so, we utilised Lysosensor Green, a dye whose fluorescence increases in acidic environments.

Both KCL22 and KCL22$^{Pon\text{-}Res}$ cells were treated with DMSO (0.0003%, 1 h) or ponatinib (5 μM, 1 h) and simultaneously labelled with Lysosensor Green (1 μM, 1 h). The live cells were immediately analysed by FACS, where Lysosensor Green fluorescence was measured within the cell population. We found no difference in Lysosensor Green fluorescence in DMSO treated samples, indicating that lysosomal pH is equal in KCL22 and KCL22$^{Pon\text{-}res}$ cells (Figure 4.17a). However, in ponatinib treated samples, Lysosensor Green fluorescence was increased in KCL22$^{Pon\text{-}Res}$ cells compared to KCL22 cells (Figure 4.17b). Geometric (GEO) mean values calculated from the histograms of three individual samples confirmed these observations (Figure 4.17c).

These results suggest ponatinib treatment decreases lysosomal pH in both cell lines, but more significantly in the drug resistant KCL22$^{Pon\text{-}Res}$ cells. It is possible that v-ATPase activity on the lysosomal membrane is increased upon ponatinib treatment, leading to reduced pH. If lysosomal pH is more acidic in the KCL22$^{Pon\text{-}Res}$ cells upon ponatinib treatment, it may explain why these cells have higher levels of lysosomal ponatinib accumulation. A lower pH likely shifts the equilibrium of ponatinib uptake towards increased lysosomal uptake, and increases lysosomal H^+ availability. This would lead to increased protonation of ponatinib and trap it within the lysosomal lumen, resulting in increased ponatinib concentration in the lysosomes of KCL22$^{Pon\text{-}Res}$ cells.

The impact of low pH on drug uptake into acidic vesicles has been associated with cancer drug resistance by previous research.[249,250] Overexpression of v-ATPase that is responsible for lysosome acidification has been found before in drug resistant cell lines.[251] Inhibition of the v-ATPase by bafilomycin A1 re-sensitised drug resistant renal cancer cells to daunomycin, doxorubicin and epirubicin.[252] In these drug resistance

models it is assumed that lysosomal trapping leads to insufficient drug target engagement and consequent cell survival. In contrast, we have shown in our CML resistance model that increased lysosomal trapping in ponatinib resistant cells (Figure 4.5) does not lead to reduced target engagement (Figure 4.9). Therefore, the acidic pH and increased lysosomal trapping of ponatinib in our CML resistance model are more likely to be a 'side-effect' of drug resistance rather than the cause of it.

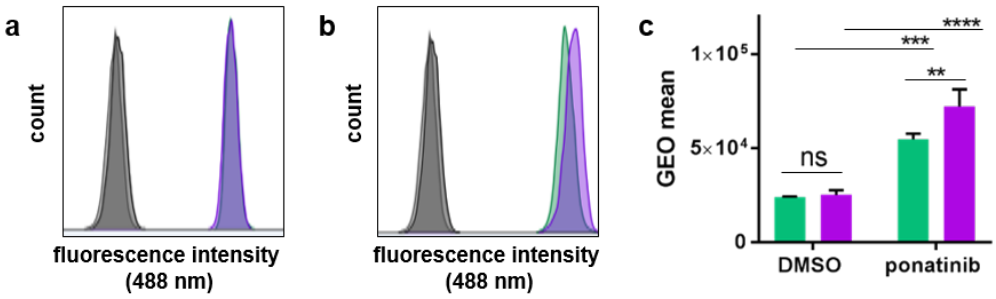

Figure 4.17 Estimating lysosomal pH in CML cells labelled with Lysosensor Green. (a), (b) Representative FACS histograms of KCL22 (green) and KCL22$^{Pon\text{-}Res}$ (purple) cells that were treated with (a) DMSO (0.0003%, v/v) or (b) ponatinib (5 μM, 1 h) and labelled with Lysosensor™ Green DND-189 (1 μM, 1 h). Grey and Black lines represent unlabelled KCL22 and KCL22$^{Pon\text{-}Res}$ control cells respectively. (c) Geometric mean values derived from n=3 biological repeats of FACS data using FlowJo software. One-way Anova (Tukey's multiple comparisons test) was used to compare the GEO means. Values shown as mean±SD, **** ($p<0.0001$), *** ($p=0.0002$), ** ($p=0.0096$), ns ($p>0.9999$).

4.5 Investigating ponatinib retention in the lysosomes

We then asked whether ponatinib trapping in lysosomes also results in retention of ponatinib in lysosomes following removal of the drug from media after treatment. It was hypothesised that ponatinib will be retained in the lysosomes following washout.

4.5.1 Ponatinib imaging by SRS following washout

KCL22 and KCL22$^{Pon\text{-}Res}$ cells were treated with ponatinib (5 μM, 1 h), washed, and re-incubated in drug free media for either 0, 1, 2 or 4 h post wash before live cell imaging using SRS (Figure 4.18). All the samples were labelled with Lysotracker (50 nM, 1 h) before live cell imaging. The SRS signal of ponatinib prior to wash-out showed ponatinib distribution in both lysosomes and the cytoplasm of the cells (Figure 4.18b,d, 0 h). Surprisingly, there was a rapid reduction in signal in both the KCL22 and KCL22$^{Pon\text{-}Res}$ cells 1 h post wash-out (Figure 4.18b,d). Ponatinib signal inside the

lysosomes of individual cells (n=10) was further quantified at each time point and showed a significant decrease in ponatinib signal in both parental and resistant cells after 1 h, with a small but significant signal remaining up to 4 h post wash-out (Figure 4.18e,f). A comparison of relative ponatinib concentrations within lysosomes between KCL22 and KCL22$^{Pon\text{-}Res}$ cells at the respective time-points showed a similar loss of signal in both cell lines, although the initial ponatinib signal was higher in the KCL22$^{Pon\text{-}Res}$ cells as shown previously (Figure 4.18g).

These results demonstrated clearly that ponatinib is not retained in the lysosomes as we hypothesised. As we did not see major metabolism of ponatinib in either KCL22 or KCL22$^{Pon\text{-}Res}$ cells from the LC-MS analysis (Figure 3.7b), however, it is unlikely that the rapid loss of ponatinib SRS signal following washout is due to drug metabolism within the lysosomes.

TFEB is a known regulator of lysosomal exocytosis, a process during which lysosomes fuse with the cell membrane and release their contents into the extracellular environment.[245,253] Zhitomirsky and Assaraf showed that lysosomal accumulation of a number of drugs, including sunitinib, triggered lysosomal translocation from the perinuclear region to the cell membrane, where lysosomal content, including lysosomal enzymes, were secreted into the extracellular milieu via lysosomal exocytosis.[254] We know that TFEB is localised in the nucleus in both KCL22 and KCL22$^{Pon\text{-}Res}$ cells, indicating they have activated lysosomal biogenesis and exocytosis pathways (Figure 4.15). Therefore, it is indirect evidence that lysosomal exocytosis potentially plays a role in the rapid loss of ponatinib signal in CML cells following treatment and drug washout. To gain more direct proof, it would be necessary to image lysosomal movement in CML cells both during and after treatment using either Lysotracker or LAMP1 labelling. Unfortunately, the CML cells are small in size (10-15 μm diameter) and have very large nuclei in proportion to the rest of the cell. For that reason, we decided it was not feasible to differentiate between lysosome localisation near the perinuclear region and the cell membrane.

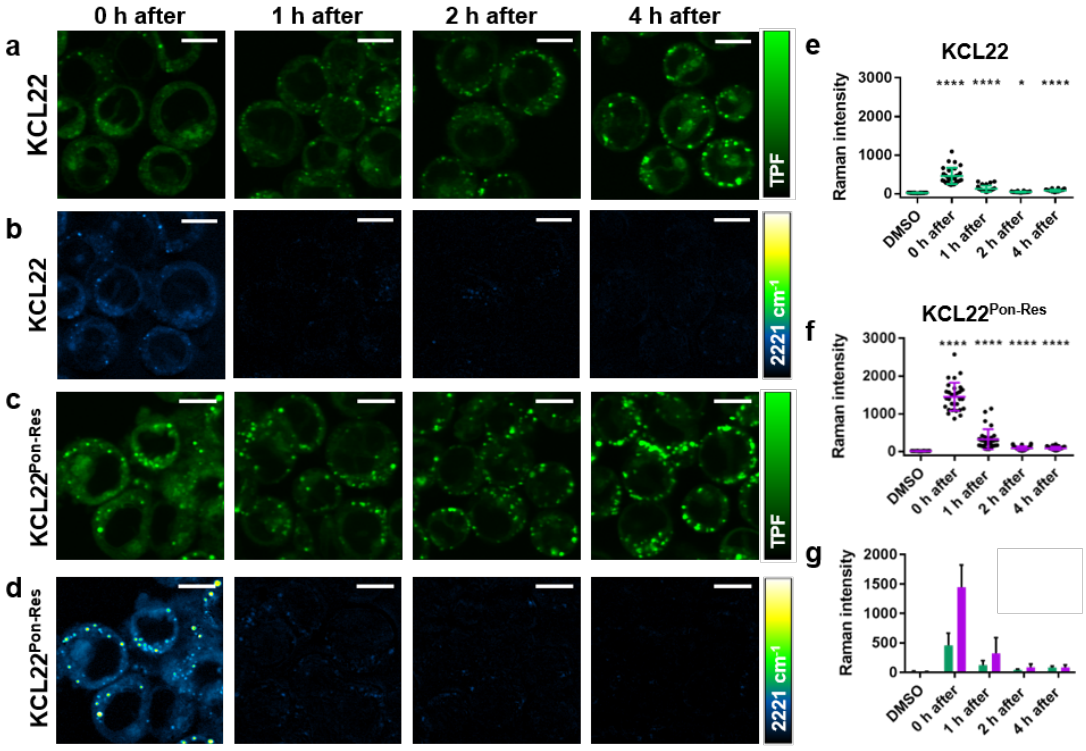

Figure 4.18 Multimodal imaging and quantitative assessment of ponatinib retention in lysosomes. KCL22 and KCL22$^{Pon\text{-}Res}$ cells were treated with ponatinib (5 μM, 1 h) labelled with Lysotracker® Green (50 nM, 1 h). The cells were imaged at (from left to right) 0 h, 1 h, 2 h or 4 h after wash out. (a), (c) TPF images acquired at 861 nm (Lysotracker® Green). (b), (d) SRS images acquired at 2221 cm^{-1} (C≡C, ponatinib). (e), (f) Mean ponatinib Raman intensity inside the vesicles of each individual cell quantified for (e) KCL22 and (f) KCL22$^{Pon\text{-}Res}$ cells at each time point post treatment, n=10 cells, 3 biological repeats. The Kruskal-Wallis test with Dunn's multiple comparisons test was used to compare ponatinib Raman intensity values against the DMSO control, **** ($p<0.0001$), * ($p=0.0107$). Individual data points shown with error bar as mean±SD. (g) Ponatinib Raman signal quantification for KCL22 (green) and KCL22$^{Pon\text{-}Res}$ (purple) cells at each time point. Images acquired at 1024 × 1024 pixels, 20 μs pixel dwell time, laser power 200 mW (the tuneable pump beam), gain 1 with false colours applied to different detection wavenumbers. Scale bars: 10 μm.

An additional factor that may contribute to ponatinib signal loss from the lysosomes is ponatinib diffusion out of the lysosomes following washout (Figure 4.19). Removing ponatinib from the media after drug treatment changes the drug uptake equilibrium in the cell. Although we believe ponatinib is trapped in the lysosomes in its protonated form, we do not know what proportion of the drug is protonated within the lysosomes. It is possible that at these very high local concentrations of ponatinib the v-ATPase proton pumps can get saturated, where not all of lysosomal ponatinib will get

protonated. In this case, following washout, the deprotonated drug would be able to diffuse back out of the lysosome, into the cytoplasm, and out of the cell as the new drug uptake equilibrium is reached.

Although we did not determine the exact mechanism of ponatinib transport out of the CML cells following washout, SRS imaging showed that it is a dynamic process where lysosomes play an important role. SRS has the temporal imaging capability to allow live cell visualisation in real time to study drug uptake and efflux. Tipping has demonstrated this previously using SRS imaging for Raman-tagged anisomycin, where following washout anisomycin Raman signal disappearance was seen in real time.[255] Alternatively, drug uptake and efflux can be monitored by fluorescence microscopy. In contrast to Raman tags, photostability is a concern for the majority of fluorophores, and has made it challenging to apply fluorescence microscopy for quantitative temporal drug imaging.[256,257] In the current study, we were limited by the fact that CML cells are non-adherent, which experimentally prevented us from using SRS imaging to further study ponatinib lysosomal uptake and transport in real time.

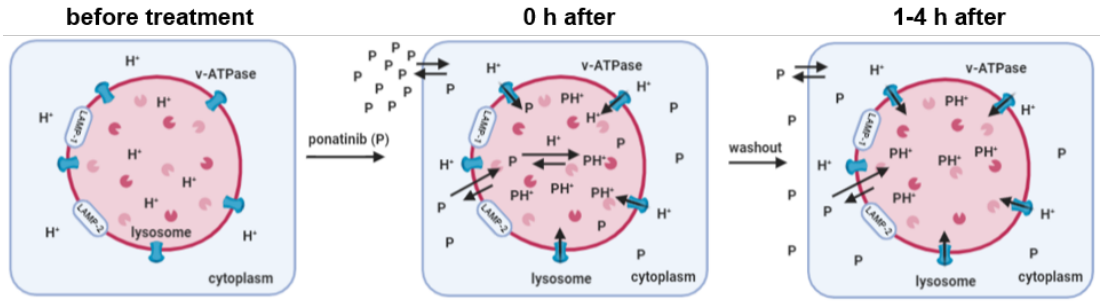

Figure 4.19 Schematic representation of ponatinib (P) accumulation in the cell via passive diffusion. Ponatinib treatment actives v-ATPase pumps, forcing more protons into the lysosomal lumen to enable lysosomal trapping of ponatinib (PH^+). However, after washout (1-4 h after), external ponatinib is removed from the media, causing intracellular ponatinib to diffuse back out of the cytoplasm as well as the lysosome of the cell to reach a new equilibrium.

4.6 Conclusions

In this chapter, SRS imaging was applied to determine ponatinib intracellular localisation and explore its biological significance in the context of ponatinib resistant CML. We demonstrated that ponatinib localises in the lysosomes of both parental and drug resistant CML cells, while both ponatinib lysosomal and cytoplasmic accumulation were found to be increased in ponatinib resistant cells. In addition, lysosome number was found to be elevated in ponatinib resistant cells by Lysotracker

imaging, and further confirmed by LAMP1 immunofluorescence measurements. In untreated cells, lysosomal pH was equal in both ponatinib sensitive and resistant cell lines, but ponatinib treatment increased lysosomal acidity more in drug resistant cells. Together, these results demonstrate that lysosomal uptake of ponatinib is differentially regulated in our ponatinib resistant CML model. Subsequently to publishing our findings, Englinger *et al.* reported ponatinib localisation in lipid droplets within lung cancer cells using ponatinib fluorescence to visualise the drug.[258] Considering they used a completely different cell model compared to us, it is possible that ponatinib intracellular localisation differs in lung cancer cells. As ponatinib is not a highly fluorescent molecule, intracellular visualisation required the use of 10 μM concentrations, which is higher than we used for SRS imaging.

Interestingly, we did not find ponatinib retention in the lysosomes following drug washout. This is postulated to be a result of lysosomal exocytosis and or diffusion of ponatinib out of the lysosomes to re-establish equilibrium after drug removal from the media. Further experiments would be required to prove this using real time SRS imaging.

Combination treatment with chloroquine, a nonspecific autophagy inhibitor that acts as a lysosomotropic agent, decreased ponatinib lysosomal sequestering significantly in both cell lines, and consequently increased target engagement. Using an autophagy knockdown cell line, we found that autophagy does not play a role in ponatinib lysosomal trapping. Therefore, CQ likely reduces lysosomal uptake of ponatinib due to its lysosomotropic properties, which decrease the ability of ponatinib to accumulate in the lysosomes. However, CQ combination treatment does not re-sensitise cells to ponatinib due to BCR-ABL independent resistance mechanism in this CML model. These results highlight that although lysosomal trapping can influence drug uptake and target engagement, it does not always have an effect on cell viability. This is an important consideration for other BCR-ABL independent resistance mechanisms where target inhibition is no longer sufficient to induce cell death. In addition, it applies to other cancers where TKI independent resistance mechanisms occur, such as non-small cell lung cancer where treatment with EGFR targeted therapy leads to EGFR independent acquired resistance.[259] To improve future treatment of cancers with target independent resistance mechanisms, it is important to identify the underlying causes of these resistance mechanisms, and target them with new treatments.

While investigating lysosome biogenesis in our CML model, we found a significant increase in nuclear TFEB, a master regulator of lysosome biogenesis and autophagy, in the ponatinib resistant cells. Recently, Sung *et al.* demonstrated that elevated TFEB activation in glioblastoma is a cause of drug resistance and inhibits apoptosis, where TFEB targeting increased cell death.[246] This is potentially something that could also be investigated in the context of ponatinib resistant CML. Mitchell *et al.* have shown that mTORC1 is overexpressed in ponatinib resistant CML and mTORC inhibition with NVP-BEZ235, an inhibitor of mTORC1, mTORC2 and all PI3K isoforms, was effective in inducing cell death *in vitro*, *in vivo* and in TKI-resistant primary CML cells.[109] The relationship between TFEB and mTOR in CML has not been extensively studied and how both TFEB and mTOR can be constitutively activated in ponatinib resistant CML is unknown. Recent reports in other cell models, however, have identified TFEB mediated endocytosis as a critical process leading to activation of mTORC1 and autophagic function.[260,261] Therefore, further exploration of TFEB role in ponatinib resistant CML would potentially be interesting to determine if TFEB could be a potential drug target in CML.

In summary, we determined intracellular localisation of ponatinib for the first time using SRS, demonstrating that acquired drug resistance can influence drug uptake and localisation in CML, which in turn has an effect on target engagement. However, lysosomal accumulation of ponatinib did not influence cell viability in this BCR-ABL independent CML model. We therefore propose that lysosomal uptake of ponatinib in drug resistant CML is rather a side effect of drug resistance than the primary cause.

Chapter 5 Spheroid imaging

5.1 Introduction

Previous chapters focused on applying SRS drug imaging in two dimensions using a monolayer of cells. However, many cancers form solid tumours in patients. It is therefore also important to study drug efficacy in three-dimensional (3D) cancer models. Most such research has traditionally been done *in vivo* using animal models, but more recently cancer spheroids have emerged as an additional option for pre-clinical drug evaluation. In this chapter, SRS utility is tested for drug imaging in cancer spheroids.

5.1.1 Use of spheroids in drug development

Conventional drug discovery screens utilise 2D cell culture where adherent cells are grown in monolayers.[262] Although it provides a simple and effective tool for pre-clinical drug screens, 2D cell culture fails to mimic the complex physiology of the *in vivo* tumour microenvironment (TME), lacking cell–cell and cell–matrix interactions that are present in tumours.[150] In contrast, 3D cell culture systems exhibit physiologically relevant cell-cell and cell-matrix interactions, gene expression, heterogeneity as well as structural complexity characteristic to tumours (Table 5.1).[142] Compared to 2D culture, spheroids represent a more accurate *in vitro* model for pre-clinical drug testing.

To progress from the pre-clinical drug screening phase to the clinical phase, drug activity has to be shown *in vivo* first. However, *in vivo* models have drawbacks including ethical considerations, high cost, and they are not high throughput. In addition, there are physiological differences between animals and humans, which sometimes fail to accurately represent human disease and can later lead to issues such as drug toxicity in clinical trials. 3D spheroids possess close to all the important characteristics of *in vivo* tumours (Table 5.1), but due to lack of vasculature in spheroids, drug penetration in spheroids is not exactly similar to *in vivo* tumours. Therefore, spheroids likely cannot replace the use of *in vivo* models, but they can help reduce the number of animals used by trialling active compounds that are then tested *in vivo*, and represent an important tool that can be used alongside 2D and *in vivo* models during pre-clinical drug evaluation.

Drug screens comparing 2D and 3D cultures have shown drastic differences in sensitivity.[263,264] Spheroids are typically more resistant to drug treatment compared to 2D culture.[265] More importantly, 3D cultures have now been shown to accurately predict patient responses to chemotherapy, and mimic intra- and interpatient heterogeneity to drug response.[266,267] This highlights the importance of using 3D models in pre-clinical drug screening.

Table 5.1 Key features of 2D cell culture, spheroids and *in vivo* tumours. Adapted with permission,[150] copyright Elsevier.

Feature	2D	Spheroid	*In vivo* tumour
Spatial restriction of cells	✓	×	×
Concentration gradient of O_2, nutrients, metabolic waste	×	✓	✓
Hypoxic core	×	✓	✓
Proliferative, quiescent & necrotic zones	×	✓	✓
Heterogeneous clonal subpopulations	✓	✓	✓
Cancer stem cell niche	×	✓	✓
Gene expression profile	Different	Similar	Similar

5.1.2 Drug imaging in spheroids

Spheroids are not only useful for drug sensitivity studies; they can also be used to better understand uptake, penetration and metabolism of drugs in 3D. However, the biggest challenge for drug imaging in 3D is penetration depth of imaging techniques. Confocal fluorescence microscopy has been applied to imaging doxorubicin, an inherently fluorescent cytotoxic drug routinely used for the treatment of both solid tumours and haematological malignancies, but it was only able to detect the fluorescence up to 50 μm in depth (Figure 5.1a).[31,268,269] At 100 μm depth, the real degree of doxorubicin penetration could no longer be determined.[31] In confocal microscopy, the same lens is used to excite the sample and to collect the emitted photons from the sample, where the pinhole system removes out-of-focus light and enables optical sectioning.[270] However, the light scattering from the sample degrades fluorescence signal and leads to exponential decay in emitted photons from the sample with increasing imaging depth.

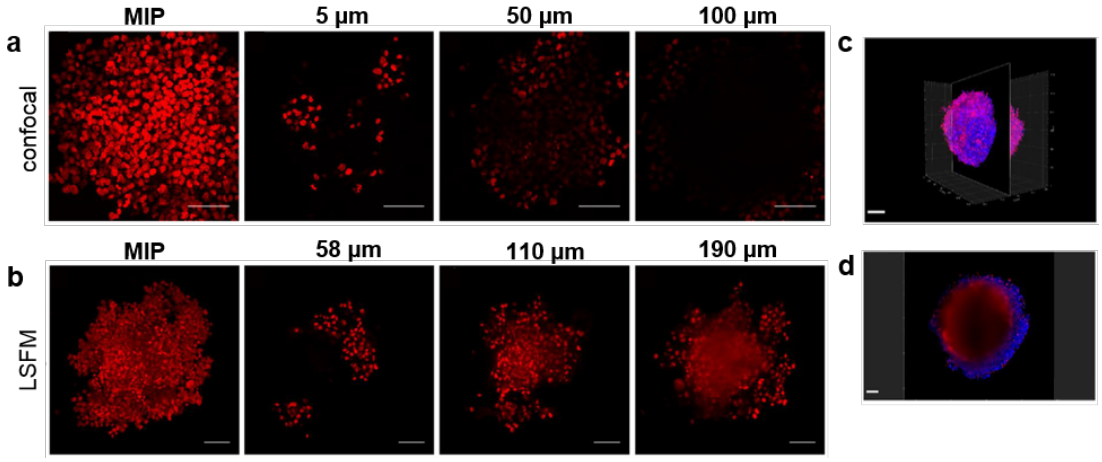

Figure 5.1 Comparison of confocal imaging and LSFM imaging of doxorubicin in a pancreatic tumour spheroid. (a) Confocal imaging of spheroid with a diameter of ~600 µm that was incubated with doxorubicin (20 µM, 3 h) prior to imaging. Images from left to right: Maximum intensity projection (MIP) of the z-stack; spheroid section at ~5 µm depth; spheroid section ~50 µm depth and optical section at ~100 µm depth. (b) LSFM imaging of spheroid with a diameter of ~600 µm that was incubated with doxorubicin (20 µM, 3 h) prior to imaging. Images acquired from left to right: MIP of the z-stack; spheroid sections at ~58 µm; ~110 µm and ~190 µm (middle of spheroid). (c), (d) LSFM imaging of spheroid (diameter ~1 mm) that was incubated with doxorubicin (20 µM, 4 h) (red) and labelled with Hoechst 33342 (blue). (d) Spheroid section at 403 µm depth. Scale bars: 100 µm. Reproduced with permission.[31]

In contrast, light sheet fluorescence microscopy (LSFM) uses a separate illumination lens and detection lens, which are placed perpendicular to each other. As no pinhole is used, more photons from the sample are detected. This gives LSFM superior imaging depth compared to confocal fluorescence microscopy.[31] Lazzari *et al.* demonstrated that LSFM can be used to image doxorubicin uptake in spheroids with a diameter of 600 µm, where doxorubicin was successfully detected at up 190 µm depth (Figure 5.1b).[31] To further demonstrate the imaging depth and 3D reconstruction of LSFM, they imaged doxorubicin in 1 mm diameter spheroids (Figure 5.1c). Diffuse doxorubicin signal could be detected in the middle of the spheroid at 403 µm depth (Figure 5.1d), but clear distinction of doxorubicin in the cell nuclei was not possible as a consequence of strong scattering phenomena this deep in the spheroid.

MALDI imaging mass spectrometry (MALDI-IMS) has also been applied to imaging drug uptake in spheroids.[271] In contrast to fluorescence, MALDI imaging is done on sections through the spheroid to allow penetration of the drug to be measured, not on

the whole spheroid at once. Although MALDI-IMS has become a widely used tool in pre-clinical drug screening,[272] especially for tissue imaging, it is limited by low spatial resolution of approximately 20 μm. Hence, to gain meaningful information about drug uptake and metabolism in different spheroid sections, large spheroids (ideally ≥ 500 μm in diameter) have to be imaged. In addition, MALDI-IMS protocol is relatively complex, requiring sectioning of frozen spheroids prior to imaging as well as choosing an appropriate matrix for detecting the small molecule of interest.[153,273,274]

LaBonia *et al.* successfully imaged irinotecan and its active metabolite in colon cancer spheroids using MALDI-IMS.[275] Irinotecan is a prodrug that is metabolised by carboxylesterase in the body into its active metabolite SN-38, which is a topoisomerase I inhibitor (Figure 5.2a).[276] It is widely used to treat colon, pancreatic and lung cancer.[277] LaBonia *et al.* used a novel 3D printed fluidic device that provided a continuous drug flow of irinotecan (50 μM) over 24-h treatment period. This drug treatment method was applied to large spheroids with a diameter of approximately 1 mm. Subsequent MALDI-IMS imaging revealed the prodrug of irinotecan localised in the centre of the tumour spheroid, while the active metabolite SN-38 primarily localised on the edge of the spheroid (Figure 5.2b). As the outer rim of the spheroid contains the proliferating cells, the metabolism of the prodrug into the active metabolite was likely in that area of the spheroid. This study perfectly illustrates the relevance of imaging drugs in spheroids by giving spatial information on both the drug and its metabolite distribution, and highlights the heterogeneity in their respective distributions.

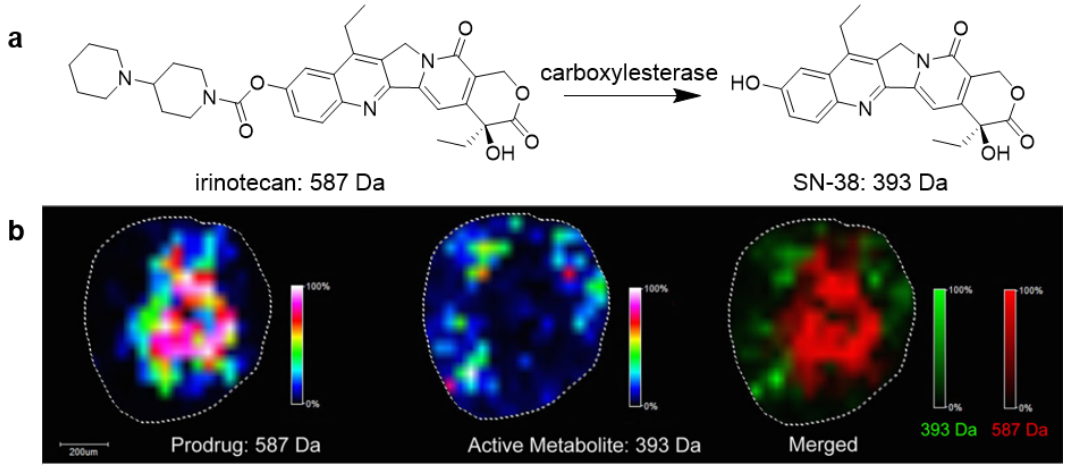

Figure 5.2 MALDI-IMS imaging of irinotecan in HCT-116 spheroids. (a) Metabolic reaction of irinotecan prodrug into its active metabolite, SN-38. (b) Imaging of irinotecan (left) and SN-38 (center). Merged image (right) shows that the active metabolite (SN-38) is localised to the periphery of the spheroid while the prodrug (irinotecan) localises to the core. Reproduced with permission,[275] copyright John Wiley & Sons.

5.2 Optimising spheroid growth

Unlike in previous chapters, where human CML cell lines KCL22 and KCL22$^{Pon\text{-}Res}$ were successfully used to image ponatinib in 2D, the goal in this chapter was to use SRS to image in 3D. In order to do that, we needed to optimise spheroid growth using these cell lines.

5.2.1 Growing spheroids from CML non-adherent cells

Not all leukaemia cell lines form spheroids and they are not routinely grown in 3D. However, a few examples exist where acute myeloid leukaemia (AML) and acute lymphoblastic leukaemia (ALL) cells have been shown to form spheroids.[278,279] As discussed in Section 1.6.1 the U-bottom ULA plate method has been shown to allow rapid formation of consistently sized uniform spheroids and is amenable to HTS.[280] Therefore, we also chose to utilise this method for spheroid growth optimisation.[157]

KCL22 and KCL22$^{Pon\text{-}Res}$ cell lines were seeded onto a U-bottom ULA 96-well plate at various seeding densities (250 to 6,000 cells per well in 200 µL media). The spheroid formation was initiated by centrifugation of the plates at 1000 *g* for 10 min. Spheroids were grown for seven days and imaged using the ImageXpress. Example of the ULA

96-well plate with CML spheroids on day 7 is shown in Figure 5.3, demonstrating that a single spheroid per well is generated using this method.

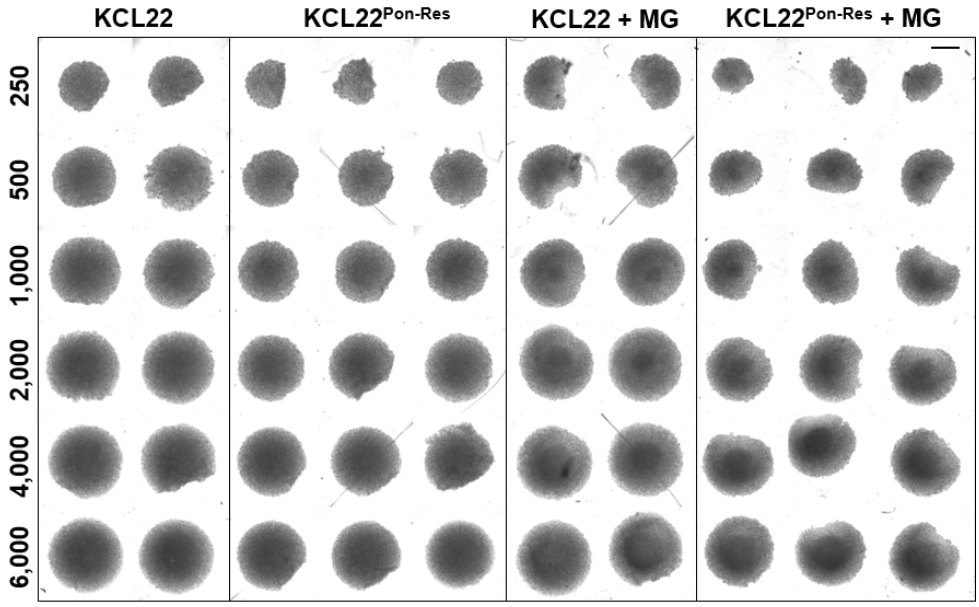

Figure 5.3 U-bottom ULA 96-well plate with CML spheroids. KCL22 and KCL22$^{Pon\text{-}Res}$ cells were seeded at various densities (250-6,000 cells) on day 0 with or without matrigel (MG). Phase contrast image of the plate was recorded on day 7 post seeding using ImageXpress. Scale bar: 1 mm.

Transmitted light images were acquired on ImageXpress for each well on day 2, day 4 and day 7 post seeding to measure spheroid growth over time (Figure 5.4a,b). Both KCL22 and KCL22$^{Pon\text{-}Res}$ spheroids grew over seven days. Spheroid size was measured based on the spheroid area using Cellprofiler. On day 2 and day 4 post seeding it is visible that seeding density is proportional to spheroid size, but by day 7 the spheroids at higher seeding density (2,000-6,000 cells per well) have reached a plateau and are almost equal in size (Figure 5.4c,d). However, when looking at each seeding density separately, all the spheroids grew visibly between day 2 and day 4 as well as day 4 and day 7 (Figure 5.4 e,f). These trends were similar in both KCL22 and KCL22$^{Pon\text{-}Res}$ spheroids.

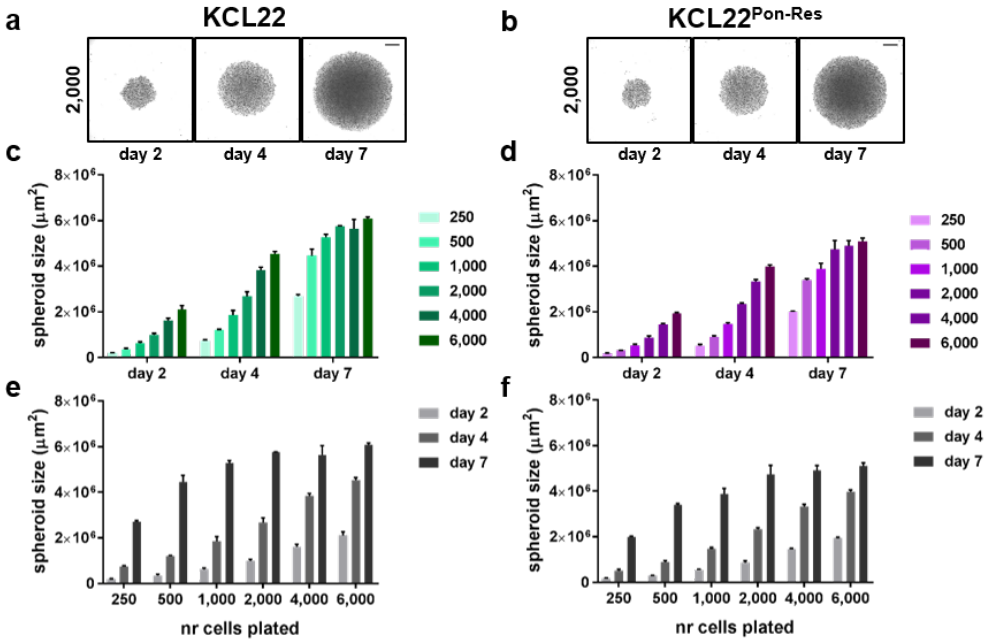

Figure 5.4 CML spheroid growth. KCL22 and KCL22$^{Pon\text{-}Res}$ cells were seeded at various densities on day 0 (250-6,000 cells per well) and imaged using ImageXpress on day 2, day 4 and day 7. Sample spheroid images of (a) KCL22 and (b) KCL22$^{Pon\text{-}Res}$ shown for 2,000 cells per well. Scale bars: 500 µm. (c), (e) KCL22 and (d), (f) KCL22$^{Pon\text{-}Res}$ spheroid sizes (µm^2) measured from n=2-8 spheroids per seeding density. Values shown as mean±SD.

Next, spheroid size between KCL22 and KCL22$^{Pon\text{-}Res}$ cells was compared using the imaging data from day 7 (Figure 5.5a). Morphologically, both KCL22 and KCL22$^{Pon\text{-}Res}$ spheroids look relatively similar, but the KCL22$^{Pon\text{-}Res}$ cell line formed significantly smaller spheroids than KCL22 cell line at each seeding density (Figure 5.5b). This could indicate that KCL22$^{Pon\text{-}Res}$ cells proliferate slower in 3D. Although proliferation rates were never directly compared between the cell lines in 2D, it was observed during passaging of cells that KCL22 cells proliferated faster. This could explain the smaller spheroid size in 3D as well, since identical number of cells were seeded for both cell lines. However, sometimes spheroid size can be smaller due to more tightly packed cells; and does not necessarily reflect the cell number.

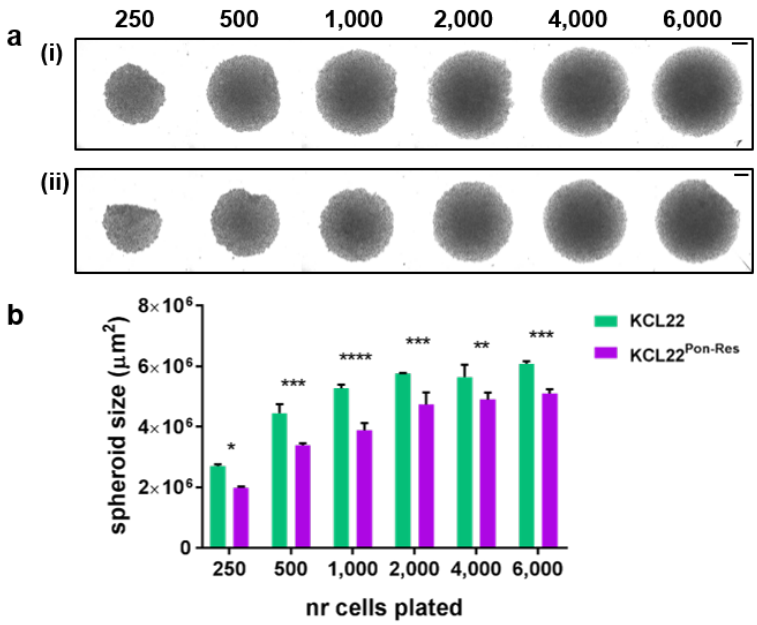

Figure 5.5 Comparison of spheroid size between KCL22 and KCL22$^{Pon-Res}$ cell lines. (a) Representative spheroid images taken on day 7 after seeding for (i) KCL22 and (ii) KCL22$^{Pon-Res}$ cell line at various seeding densities (250-6,000 cells per well). Scale bars: 500 µm. (b) Spheroid size measured from ImageXpress images using CellProfiler on day 7. Two-way ANOVA (Sidak's multiple comparisons test) was used to compare spheroid sizes from n=2-8 spheroids per seeding density. Values shown as mean±SD, **** ($p<0.0001$), *** ($p=0.0003$), ** ($p=0.0094$), * ($p=0.0133$).

To characterise the spheroids further, on day 7 after seeding, the spheroids were labelled with Hoechst (blue), Calcein AM (green) and propidium iodide (PI, red). Hoechst labels cell nuclei by binding to the minor groove of DNA.[281] Calcein-acetoxymethylester (Calcein-AM) is a non-fluorescent cell permeable compound that is used as a live cell marker.[282] Inside live cells, esterases convert Calcein AM into Calcein, which is fluorescent. Propidium iodide (PI) is a dead cell dye that binds to the DNA of dead cells.[283] As it is membrane impermeable, PI does not label the DNA of live cells.

The spheroids were labelled with all three fluorophores simultaneously and single images per well were acquired in each channel on the ImageXpress Micro (IXM) automated HCS platform subsequently. Sample images of Calcein AM and PI labelled KCL22 and KCL22$^{Pon-Res}$ spheroids at different seeding densities are shown in Figure 5.6a-d. Using the Hoechst fluorescent signal as a whole spheroid map (images not shown), Calcein AM and PI MFI was quantified in individual spheroids (Figure 5.6e,f). Calcein fluorescence slightly decreased with increasing spheroid size in both cell

lines, indicating that although the spheroid size is increasing the number of viable cells is not increasing proportionally. There was no significant difference between the KCL22 and KCL22$^{Pon-Res}$ cell lines. PI staining was normalised to spheroid size to account for the difference in KCL22 and KCL22$^{Pon-Res}$ measured spheroid sizes. PI staining increased with increasing spheroid size, indicative of the increasing size of the dead cell core in the spheroids, which can also be seen from the images (Figure 5.6c,d,f). In the larger spheroids (2,000-6,000 cells per well at seeding) the area of dead cells is taking up the majority of the spheroid volume. PI staining was lower in KCL22$^{Pon-Res}$ spheroids compared to KCL22 spheroids at most seeding densities, reflective of the smaller dead cell core in these spheroids.

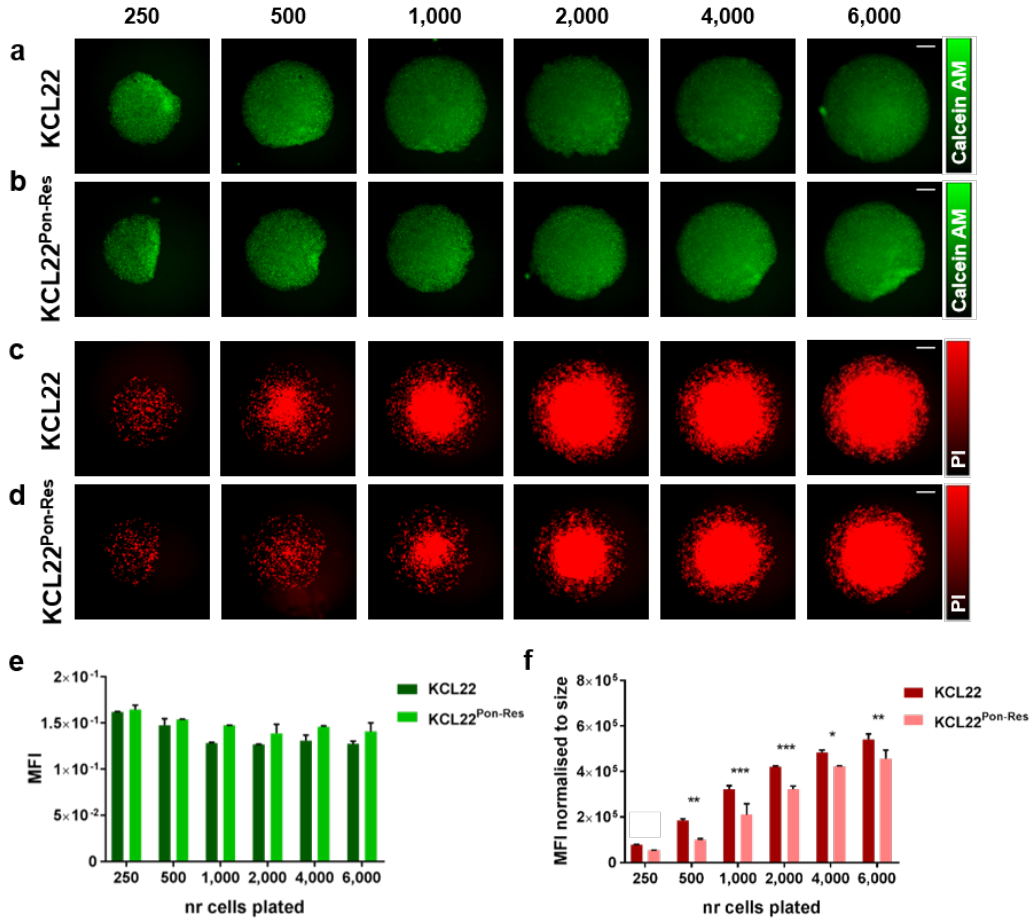

Figure 5.6 Propidium iodide (PI) and Calcein AM staining in CML spheroids. KCL22 and KCL22$^{Pon-Res}$ cells seeded at various densities on day 0 were grown for seven days to form spheroids. Spheroids were labelled with (a), (b) Calcein AM and (c), (d) PI for 1 h on day 7. Scale bars: 500 µm. MFI of (e) Calcein AM and (f) PI was measured for each spheroid and PI intensity was normalised to spheroid size. Two-way ANOVA (Sidak's multiple comparisons test) was used to compare fluorescence intensity from a minimum of n=2-8 spheroids per seeding density. Values shown as mean±SD, *** (p=0.0004), ** (p=0.0033), * (p=0.0176).

The effect of matrigel on CML spheroid growth was also tested during the optimisation stage. Matrigel is a gelatinous protein mixture derived from mouse tumour cells and commercialised as Matrigel.[284-286] It is a sterile reconstituted basement membrane preparation that primarily consists of laminin, collagen IV, entactin as well as various proteases, growth factors and proteins; and forms a 3D gel at 37 °C.[285] Matrigel mimics the ECM of tumours and is routinely used for a variety of *in vitro*, *in vivo* and *ex vivo* experiments, where it promotes cell morphogenesis, differentiation and tumour growth. It has also been shown to aid spheroid formation in 3D cell culture.[157,280]

KCL22 and KCL22$^{Pon\text{-}Res}$ cells were seeded in the presence or absence of matrigel and grown for seven days. Spheroids were imaged on day 2, day 4 and day 7 post seeding and the spheroid size was measured on each day. It was noted that on day 2 and day 4 both KCL22 and KCL22$^{Pon\text{-}Res}$ spheroids grown in the presence of matrigel were more compact and smaller in size (Figure 5.7a,b). Ivascu and Kubbies reported a similar case, where matrigel enabled tighter spheroid formation in a breast cancer cell line MDA-MB-231, which otherwise did not form spheroids at all.[157] However, in our experiment, by day 7 the CML spheroids grown with no matrigel were the same size as the spheroids grown in matrigel, and upon visual observation both displayed similar morphology.

For SRS imaging, it was a requirement to be able to move the spheroids out of the U-bottom well of the ULA plate as the plate cannot be imaged directly. This type of spheroid transfer is usually done by careful pipetting. Spheroid transfer was tested both on day 4 and day 7. Unfortunately, when the CML spheroid transfer was attempted for either cell line grown with or without matrigel, the spheroid structure fell apart. Therefore, the KCL22 and KCL22$^{Pon\text{-}Res}$ cell lines had formed cell aggregates in 3D rather than true spheroids. This is not unusual and been reported for a number other cell lines grown in ULA plates.[157,280] In addition, CML cells do not normally form cell-cell contacts. It is possible that matrigel did have some effect on CML spheroid formation in the first few days and acted to physically compact the spheroids, but this effect did not result in actual spheroid formation over seven days.

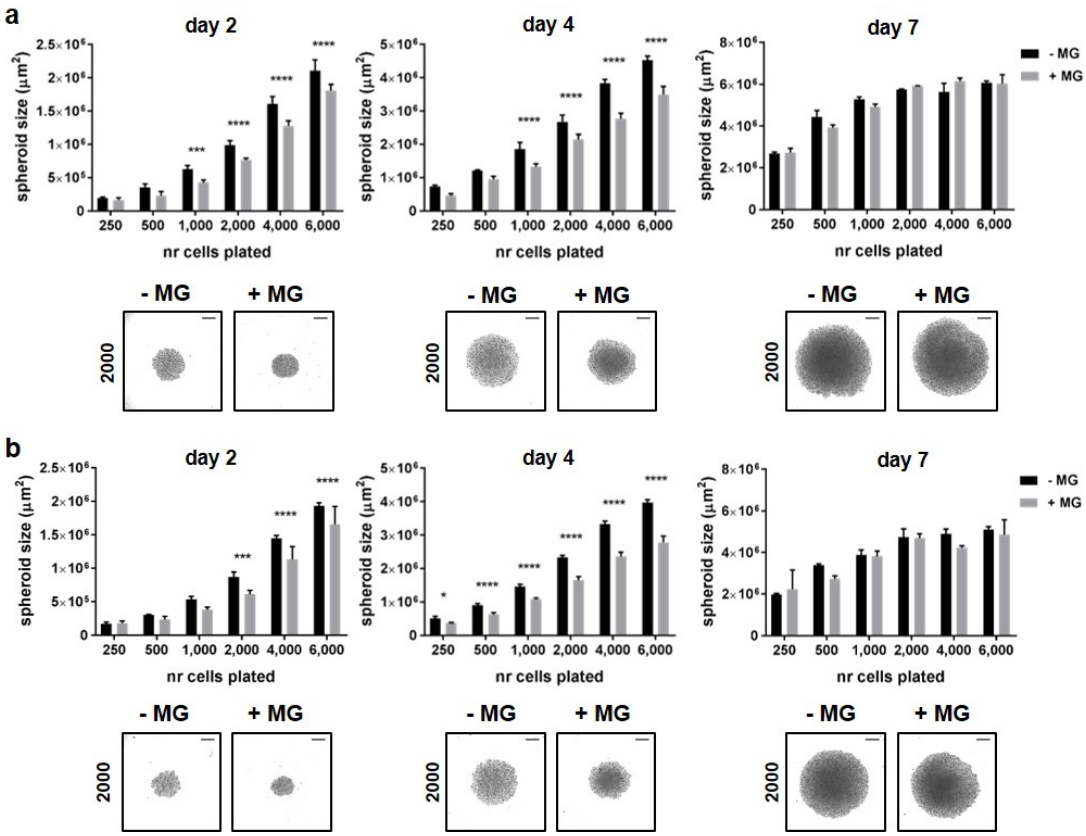

Figure 5.7 Matrigel (MG) effect on CML spheroid size. (a) KCL22 and (b) KCL22$^{Pon\text{-}Res}$ spheroids were seeded with 2.5% MG or without MG on day 0 at various densities (250-6,000 cells per well) and spheroid size was measured on day 2, day 4 and day 7 post seeding. Representative spheroid images shown at 2,000 cells per well seeding density for both (a) KCL22 and (b) KCL22$^{Pon\text{-}Res}$ on day 2, day 4 and day 7. Scale bars: 500 µm. Two-way ANOVA (Sidak's multiple comparisons test) was used to compare spheroid sizes from a minimum of n=2-8 spheroids per seeding density. Values shown as mean±SD, **** ($p<0.0001$), *** ($p=0.0002$). * ($p=0.0146$).

5.2.2 Growing spheroids from T47D adherent cells

As the goal of this chapter was utilisation of SRS imaging on spheroids and the CML cell lines of interest did not form tight spheroids, another cell line was chosen for 3D imaging purposes. T47D, an adherent breast cancer cell line that is known to form tight spheroids in ULA plates, was picked as an alternative.[148,157,163]

5.2.2.1 Testing spheroid growth conditions

T47D cells were initially seeded at 2,000 cells per well with or without matrigel and grown for seven days. Spheroid growth was imaged on day 2, day 4 and day 7 using the ImageXpress (Figure 5.8a,b). The transmitted light images clearly show that T47D spheroids only formed when there was no added matrigel in the wells. Spheroid size was measured on each day the spheroids were imaged, and showed that T47D spheroids grow in size between both day 2 and day 4 as well as day 4 and day 7 (Figure 5.8c). The average spheroid diameter on day 7 was estimated to be 530 µm. To confirm the T47D spheroids have tight cell-cell contacts they were transferred onto an imaging slide by pipetting, after which the spheroid structure remained intact.

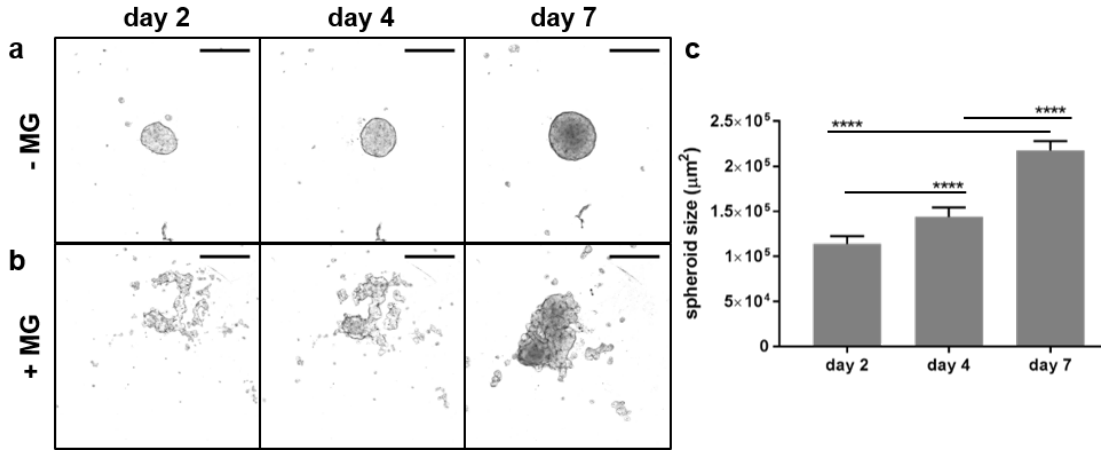

Figure 5.8 Matrigel (MG) effect on T47D spheroid growth. T47D cells were seeded at 2,000 cells per well on day 0 (a) without MG or (b) with 2.5% MG and the spheroid formation was imaged on day 2, day 4 and day 7. Scale bars: 500 µm (b) T47D cells did not form spheroids in the presence of MG. (c) T47D spheroid size was measured on day 2, day 4 and day 7 from (a). One-way ANOVA (Tukey's multiple comparisons test) was used to compare spheroid size on different days from n=31 spheroids. Values shown as mean±SD, **** ($p<0.0001$).

5.2.2.2 Optimising spheroid size

The effect of seeding density on T47D spheroid size and composition was tested next. T47D cells were seeded at different seeding densities (2,000-6,000 cells per well) on day 0, grown for seven days to forms spheroids, and labelled with Hoechst, Calcein AM and PI on day 7 before imaging on the ImageXpress. Spheroid size increased with increasing seeding density (Figure 5.9a-d). The average diameters of spheroids seeded at 2,000, 4,000 and 6,000 cells per well were estimated to be 540 µm, 590 µm and 650 µm respectively. Calcein AM staining slightly decreased with spheroid size for T47D cells, demonstrating that larger spheroids don't necessarily have higher

number of viable cells (Figure 5.9e). In contrast to the CML cell aggregates, where the Calcein AM staining was equal throughout the spheroid, T47D spheroids have a clear viable edge with higher intensity Calcein AM fluorescence. This is more distinct in the larger spheroids (4,000 and 6,000 cells per well).

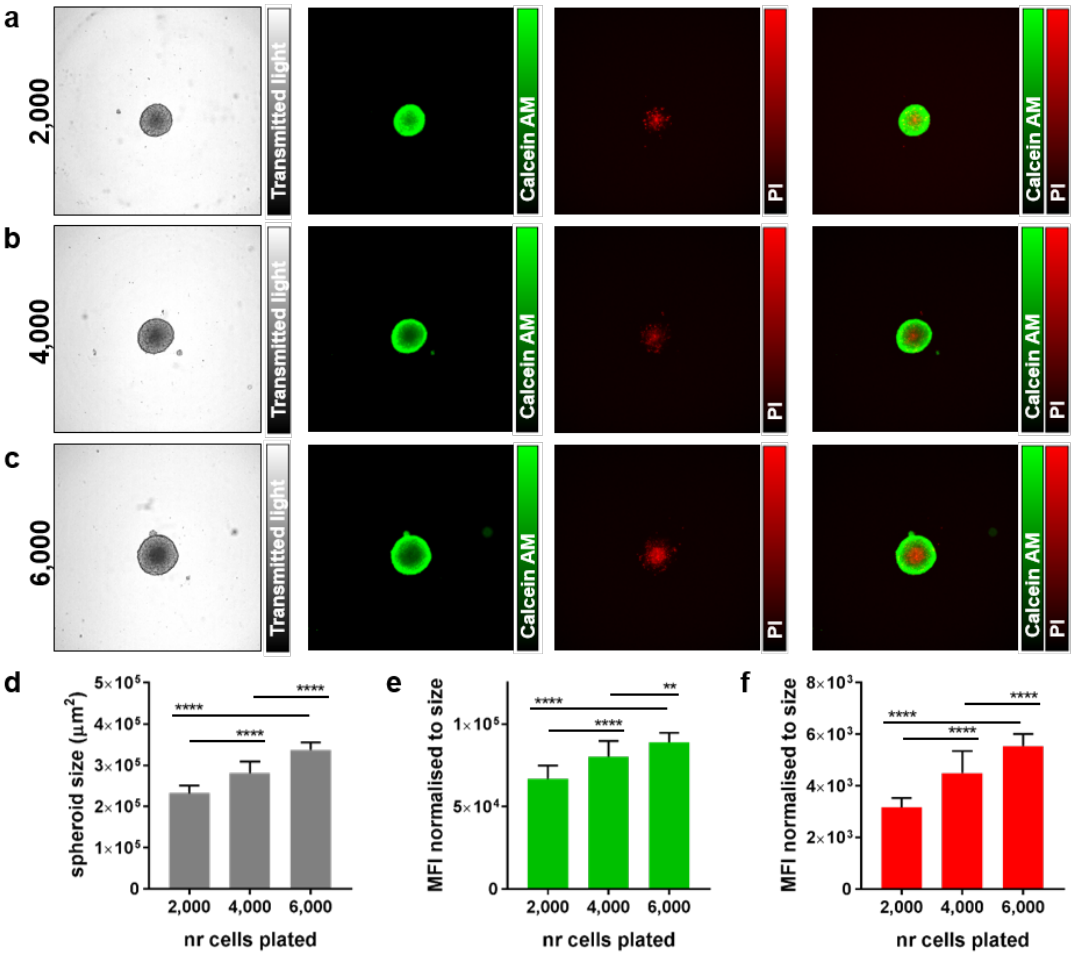

Figure 5.9 Seeding density effect on T47D spheroid size and composition. T47D cells were seeded at (a) 2,000 (b) 4000 or (c) 6,000 cells per well on day 0 and grown for seven days to form spheroids. Spheroids were labelled with Calcein AM (3.5 µM) and PI (1 µM) for 1 h on day 7 and imaged on the ImageXpress. Scale bars: 500 µm. (d) Spheroid size was measured from the phase contrast images for a minimum of n=18 spheroids per seeding density. (e) MFI from Calcein AM images. (f) MFI from PI images normalised to spheroid size. Minimum of n=16 spheroids per seeding density were analysed. One-way ANOVA (Tukey's multiple comparisons test) was used to compare spheroid size, Calcein AM and PI fluorescence from n=16-24 spheroids per seeding density. Values shown as mean±SD, **** ($p<0.0001$), *** ($p=0.0003$), ** ($p=0.0022$).

PI staining showed that the dead cells are concentrated within the core of these spheroids (Figure 5.9a-c). PI fluorescence intensity increased with spheroid size, indicative of an increasing dead cell core size in spheroids with larger diameter (Figure 5.9f). Overall, the labelling confirmed that T47D cells have formed spheroids with a distinct viable outer layer and a dead cell core. This is consistent with previously reported data, where T47D spheroids were shown to have a hypoxic core by labelling with an anti-pimonidazole antibody, which is a hypoxia marker.[287] In addition, it has been demonstrated previously that T47D spheroids have up-regulated hypoxia and low-nutrition related genes in 3D culture compared to 2D.

In an attempt to see if we can grow larger T47D spheroids, which would be compatible for comparison imaging with MALDI, and up to 1 mm diameter, another experiment was conducted with higher seeding densities. T47D cells were seeded at 6,000, 10,000 and 20,000 cells per well on day zero, grown for seven days, and labelled with Hoechst, Calcein AM and PI before imaging on the ImageXpress. As seen earlier, spheroid size measurements demonstrated that increasing seeding density resulted in increased size (Figure 5.10a-d). The average diameters of spheroids seeded at 6,000, 10,000 and 20,000 cells per well were estimated to be 660 µm, 810 µm and 960 µm respectively.

In correlation with previous imaging, Calcein AM staining slightly decreased with increasing spheroid size while PI staining intensity increased in line with spheroid size (Figure 5.10e,f). However, at 20,000 cells per well seeding density, the spheroid no longer consisted of just a simple viable edge and a dead core (Figure 5.10c). It now appeared to have an outer proliferating edge as well as an inner ring of live cells as well as two separate dead cell regions within the spheroid core. This demonstrates that although it is possible to grow T47D spheroids with close to 1 mm diameter, the internal spheroid structure at that size becomes more complex and needs to be considered when using these spheroids for drug imaging and/or screening.

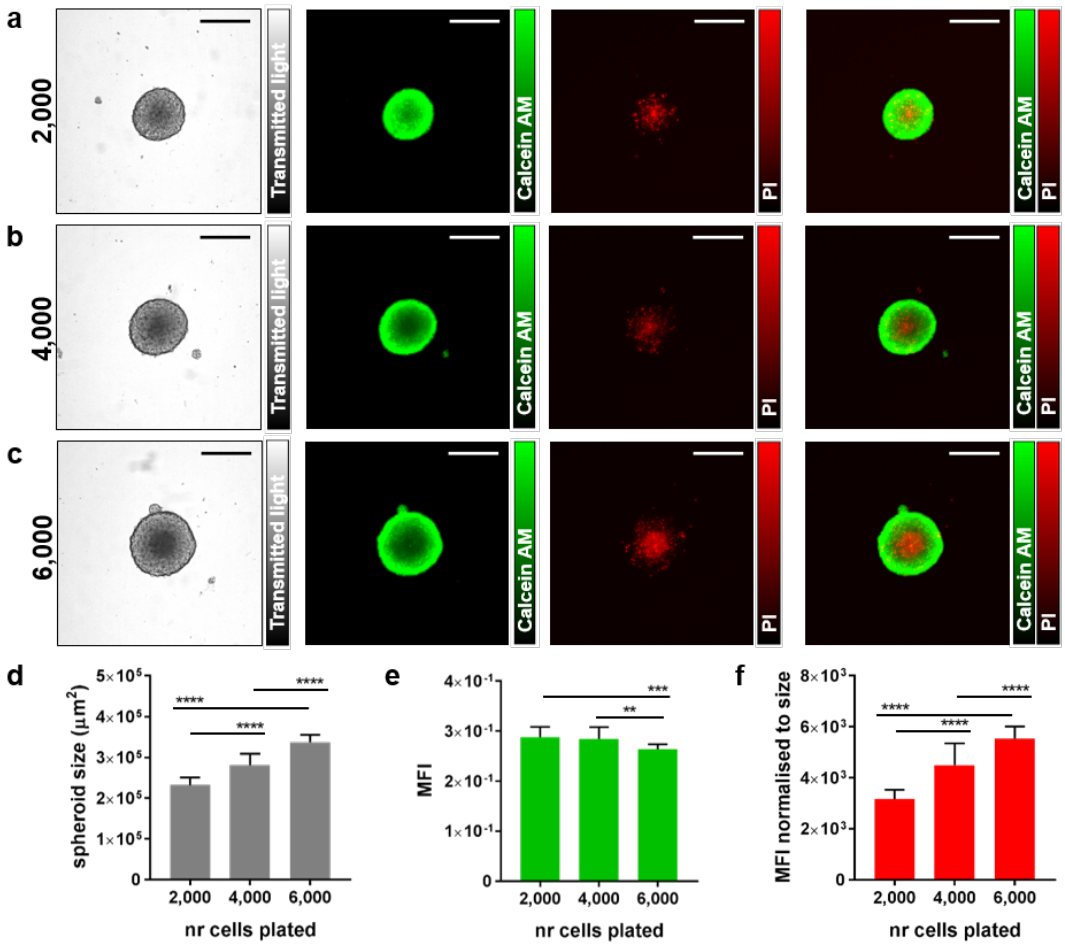

Figure 5.10 Growing larger T47D spheroids. T47D cells were seeded at (a) 6,000 (b) 10,000 or (c) 20,000 cells per well on day 0 and grown for seven days to form spheroids. Spheroids were labelled with Calcein AM (3.5 µM) and PI (1 µM) for 1 h on day 7 and imaged on the ImageXpress. Scale bars: 500 µm. (d) Spheroid size was measured from the phase contrast images for a minimum of n=18 spheroids per seeding density. (e) MFI from Calcein AM images normalised to spheroid size. (f) MFI from PI images normalised to spheroid size. Minimum of n=16 spheroids per seeding density were analysed. One-way ANOVA (Tukey's multiple comparisons test) was used to compare spheroid size, Calcein AM fluorescence and PI fluorescence from n=16-23 spheroids per seeding density. Values shown as mean±SD, **** ($p<0.0001$).

During T47D spheroid growth, spheroid contraction between day 0 and the first few days of spheroid growth was noticed when observing the ULA plate on a benchtop microscope. To investigate this further, transmitted light images of T47D spheroids plated at different seeding densities (6,000, 10,000, 20,000 cells per well) were acquired on day 1, 2, 3, 6 and 7 post seeding (Figure 5.11a-c). Spheroid size was quantified on each day at the three different seeding densities (Figure 5.11d).

Between day 1 and day 2 (24 h – 48 h post seeding) the spheroid size decreased for all three seeding densities, confirming the spheroid contraction effect seen on the benchtop microscope. Between day 2 and day 3 (48 h – 72 h post seeding) spheroid size remained constant for the smallest seeding density (6,000 cells per well), while the spheroids size continued to decrease for spheroids with larger seeding density (10,000 and 20,000 cells per well). During those first three days, the spheroids contracted, resulting in spheroid size decreasing. It is possible that during that time strong cell-cell contacts were formed. To prove this, it would be necessary to fix and stain the spheroids with a cell-cell adhesion marker such as E-cadherin, and to measure the strength of the adhesions.

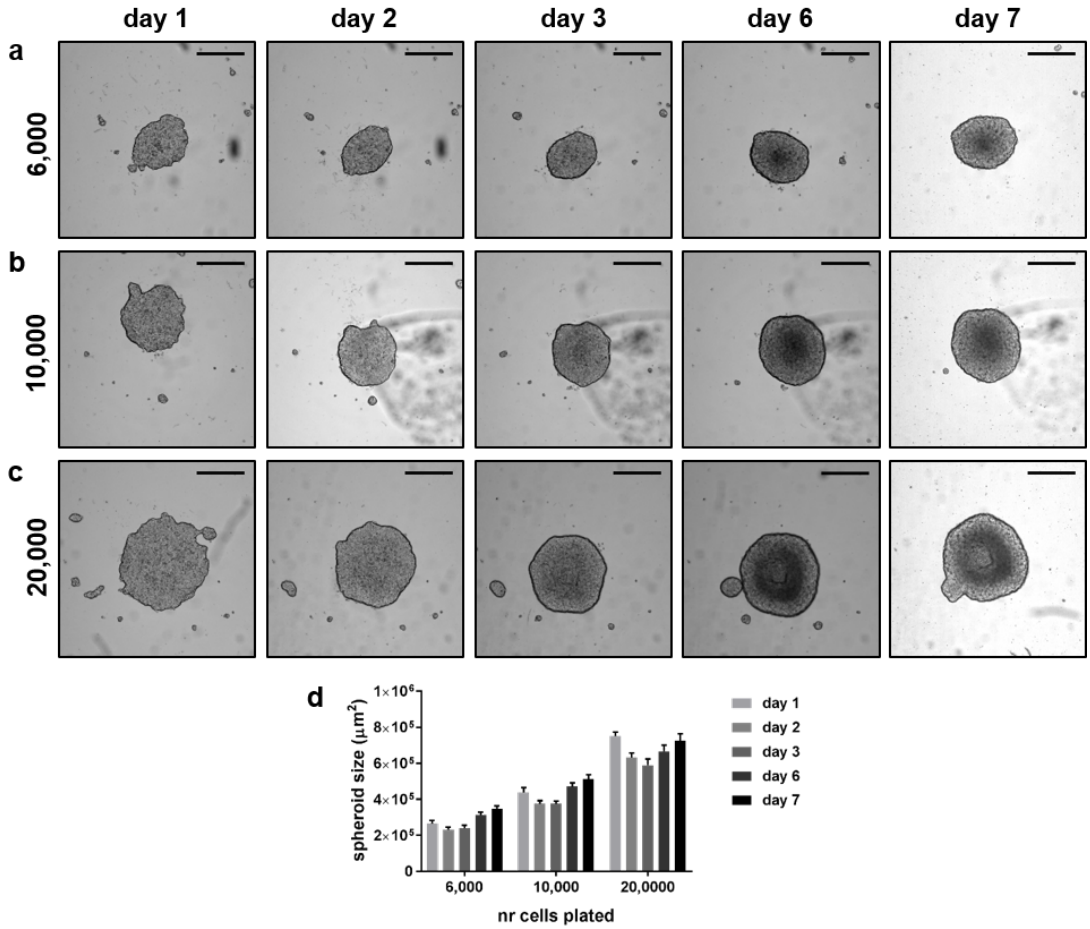

Figure 5.11 T47D spheroid size changes between day 1 and day 7. T47D cells were seeded at (a) 6,000, (b) 10,000 or (c) 20,000 cells per well on day 0 and the spheroid formation was imaged between day 1 and day 7 using the ImageXpress. Scale bars: 500 µm. (d) Spheroid size was measured from the phase contrast images for a minimum of n=17-23 spheroids per seeding density. Values shown as mean±SD.

Between day 3 and day 6 spheroid size increased for all the seeding densities and the same was true between day 6 and day 7. These results demonstrate that while higher seeding density leads to larger spheroid size, it also takes longer for the spheroids to form and compact. From a drug screen perspective, if inhibitors were added to the spheroids, these should be added after day 3 when the spheroids have fully formed. Wenzel *et al.* used T47D spheroids for a HCS of 1120 drug molecules and they chose to drug the spheroids on day 4 post seeding.[287]

5.3 Imaging ponatinib in 2D T47D cells

Before SRS imaging could be attempted in the T47D spheroids, it was necessary to check that ponatinib can be imaged in T47D cells in 2D cell culture first. T47D cells were treated with DMSO or ponatinib, washed and imaged live using SRS microscopy as described earlier in Section 3.5.1. Control cells showed close to no background signals at ponatinib on resonance (2221 cm^{-1}) and off resonance (2257 cm^{-1}) wavenumbers in the cell-silent region of the Raman spectrum (Figure 5.12a). Ponatinib was detected in the drug treated live cells (Figure 5.12b) where 5 μM ponatinib was added for 1 h before washing. Both diffuse cytoplasmic signal of ponatinib as well as ponatinib puncta were clearly visible.

An SRS sweep of the ponatinib peak was taken as described in Section 3.5.1.2. Across the sweep between 2189 – 2257 cm^{-1} wavenumbers, 17 SRS images were captured sequentially for both the control cells and the ponatinib treated cells. The SRS sweep of the control cells showed that there was no peak present when cells were not treated with ponatinib (Figure 5.12c), while a ponatinib peak can be detected in the SRS sweep of T47D cells that were treated with the drug (Figure 5.12d). This experiment confirmed ponatinib can be successfully imaged in live T47D cells in 2D.

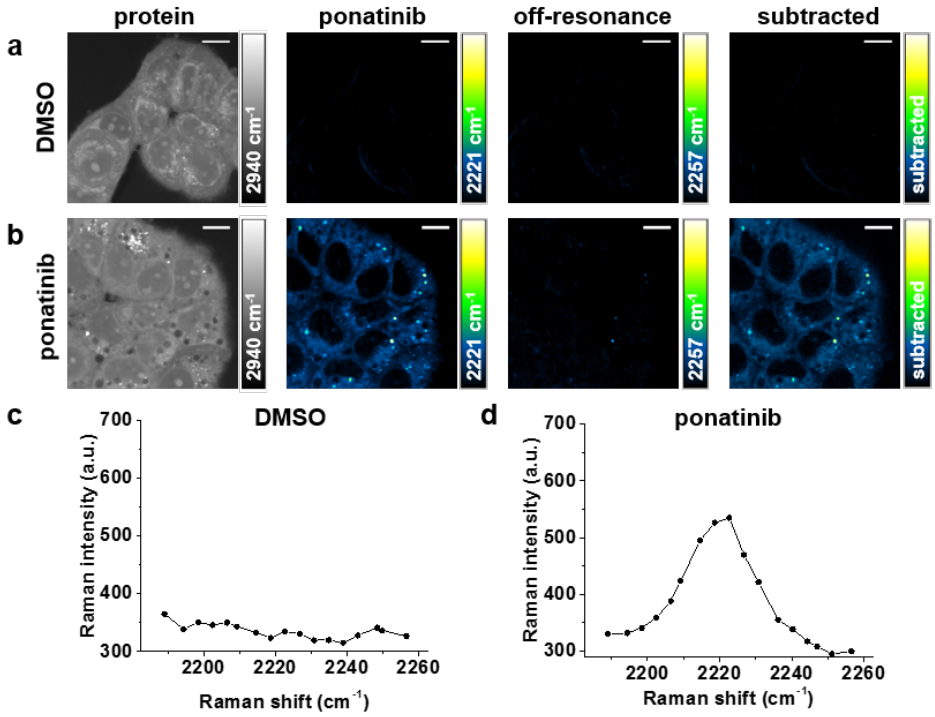

Figure 5.12 Ponatinib imaging in live T47D cells. T47D cells were treated with (a) DMSO (0.0003%, 2 h); (b) ponatinib (5 μM, 1 h). SRS images were acquired in a sequence from left to right: 2940 cm^{-1} (CH_3, proteins); 2221 cm^{-1} (C≡C, ponatinib); 2257 cm^{-1} (off-resonance); 2221 cm^{-1} with background subtracted. Images acquired at 1024 × 1024 pixels, 20 μs pixel dwell time, laser power 250 mW (the tuneable pump beam), gain 1 with false colours applied to different detection wavenumbers. Scale bars: 10 μm. (c), (d) SRS sweep of ponatinib peak in T47D cells treated with (c) DMSO (0.0003%, 2 h); (d) ponatinib (5 μM, 1 h).

5.3.1 The influence of fixing on imaging ponatinib in T47D cells

When ponatinib was imaged in SW480 cells in Chapter 3 (Section 3.5.1), we noticed that fixing of cells after drug treatment negatively influenced ponatinib imaging using SRS. In fixed cells, only a diffuse cytoplasmic ponatinib signal was seen in comparison to bright ponatinib puncta in live SW480 cells. To look into this further, we compared live imaging and two different fixing agents, paraformaldehyde (PFA) and glutaraldehyde (GA), in T47D cells (Figure 5.13). In live T47D cells ponatinib puncta, which are likely localised in acidic organelles such as lysosomes, are clearly visible by SRS imaging (Figure 5.13a). When the cells were treated under identical conditions, but fixed with PFA, no ponatinib puncta were detected in the cells, and only a faint cytoplasmic signal could be seen (Figure 5.13b). The same results were obtained when a different fixative, GA, was used (Figure 5.13c).

To gain further proof that significant proportion of ponatinib is washed out of the cell during the fixing protocol, the same experiment was conducted in an ovarian cell line, ES2. As expected, ponatinib puncta were visible in live ES2 cells (Figure 5.14a) while no puncta were seen in fixed ES2 cells (Figure 5.14b). These results are consistent with the SRS imaging data obtained for the SW480 cell line previously. Similarly, ponatinib signal was never detected in CML cell lines when they were fixed (data not shown). These results illustrate that fixing influences ponatinib cellular localisation. It is therefore an important consideration to think about the impact of fixation when looking at drug distribution using other imaging modalities as well. Most clinical tissue specimens are stored as formalin-fixed paraffin-embedded (FFPE) samples, which have a long lifetime and can be stored at room temperature.[288] However, MALDI imaging of drugs generally requires frozen, rather that fixed tissue sections.[275,289,290] It is thought drug molecules are likely to be washed away, at least in part, during the traditional fixation process.[288] Our results indicate that the same principle applies for SRS imaging. Hence, spheroid imaging is carried out on live samples.

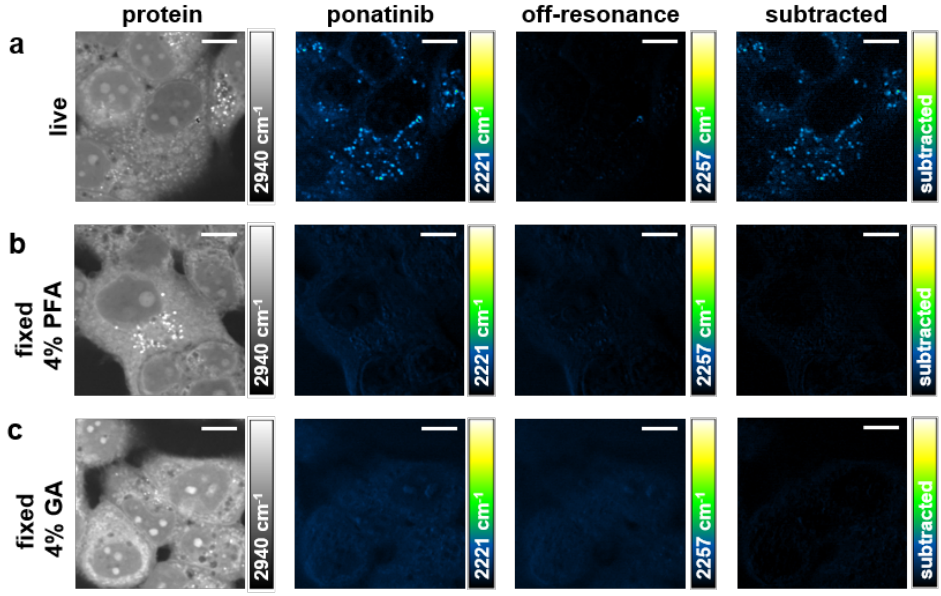

Figure 5.13 The effect of fixing on ponatinib SRS imaging in T47D cells. T47D cells were treated with ponatinib (5 μM, 1 h) and (a) imaged live or (b) fixed with PFA (4%); (c) fixed with glutaraldehyde (4%) and imaged subsequently. SRS images were acquired in a sequence from left to right: 2940 cm^{-1} (CH_3, proteins); 2221 cm^{-1} (C≡C, ponatinib); 2257 cm^{-1} (off-resonance); 2221 cm^{-1} with background subtracted. Images acquired at 1024 × 1024 pixels, 20 μs pixel dwell time, laser power 250 mW (the tuneable pump beam), gain 1 with false colours applied to different detection wavenumbers. Scale bars: 10 μm.

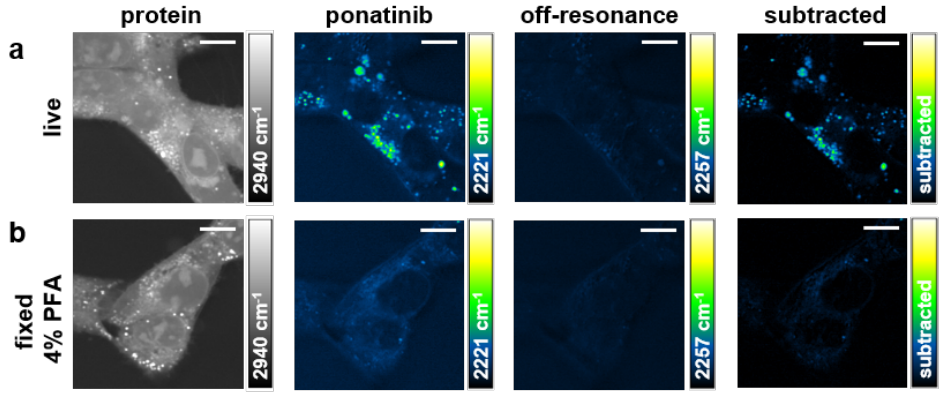

Figure 5.14 The effect of fixing on ponatinib SRS imaging in ES2 cells. ES2 cells were treated with ponatinib (5 μM, 1 h) and (a) imaged live or (b) fixed with PFA (4%) and imaged subsequently. SRS images were acquired in a sequence from left to right: 2940 cm^{-1} (CH_3, proteins); 2221 cm^{-1} (C≡C, ponatinib); 2257 cm^{-1} (off-resonance); 2221 cm^{-1} with background subtracted. Images acquired at 1024 × 1024 pixels, 20 μs pixel dwell time, laser power 250 mW (the tuneable pump beam) with false colours applied to different detection wavenumbers. Scale bars: 10 μm.

5.4 SRS imaging of live T47D spheroids

Initial SRS imaging of live T47D spheroids was carried out to assess imaging depth capabilities of our SRS microscope. A T47D spheroid established from seeding 6,000 cells per well, was labelled after seven days with Hoechst, Calcein AM and PI, and visualised using multimodal imaging (Figure 5.15). This T47D spheroid had an estimated diameter of about 650 μm. Images were acquired at 5 μm, 18 μm, 37μm, 100 μm and 200 μm depth from the top of the spheroid (Figure 5.15a-d). SRS images were taken at the protein stretch (CH_3, 2940 cm^{-1}). Fluorescence images of cell nuclei (Hoechst, blue), live cells (Calcein AM, green) and dead cells (PI, red) were recorded simultaneously.

SRS images taken at 5 μm and 18 μm depth show bright signal within the spheroid, where all the cells throughout the field of view can clearly be seen (Figure 5.15a,b) SRS signal loss was already seen at 37 μm depth as the middle of the spheroid looked darker, and the signal almost completely disappeared at 100 μm depth (Figure 5.15c,d). The next image was acquired at 200 μm depth (image not shown), where no SRS signal was detected. These results are in agreement with the literature where Weia *et al.* previously imaged spheroids using SRS and reported an imaging depth of 120 μm in tumour spheroids without tissue clearing.[291]

Calcein AM staining from 18 µm depth onwards was only bright around the edge of the spheroid, similar to the images acquired on the ImageXpress. However, the multiphoton microscope is giving much better image resolution, enabling visualisation of individual cells within the spheroid.

Unfortunately, the Calcein AM green fluorescence was bleeding through into the red channel on the multiphoton microscope. Hence, the red channel also appears to have an intensely stained outer edge, but that is not true PI fluorescence. Actual PI staining is visible on the images acquired deeper inside the spheroid at 37 µm and 100 µm depth, where the dead cell core is clearly stained (Figure 5.15c,d). This demonstrates that although SRS signal and Hoechst fluorescence signal are reduced at 100 µm due to depth penetration limitations, cells are still present in the core of the spheroid.

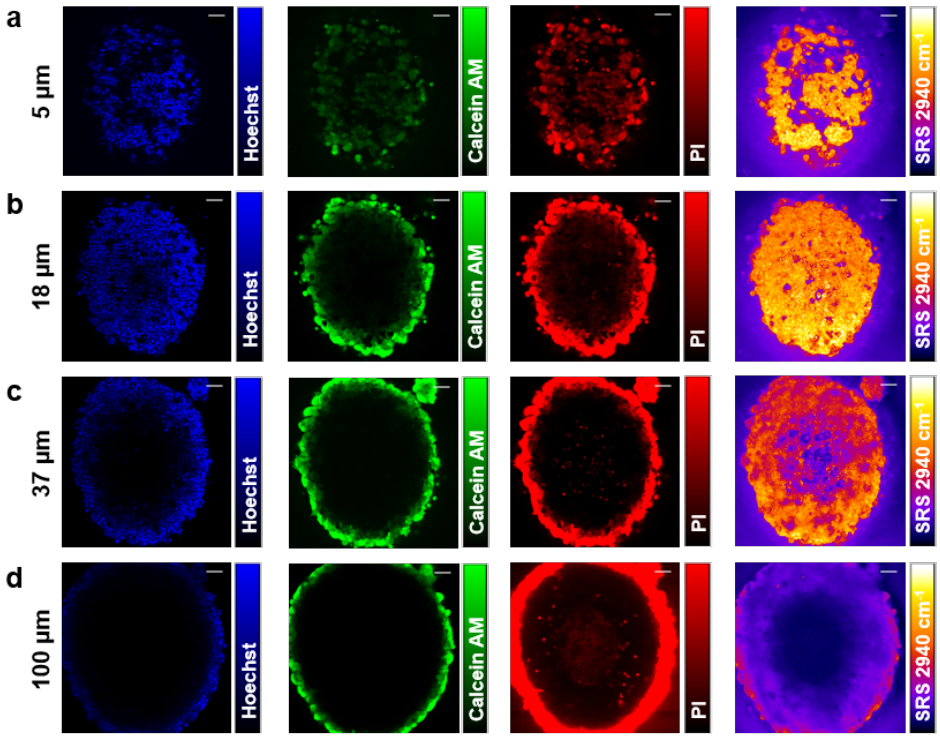

Figure 5.15 Multimodal imaging of T47D spheroid. T47D cells were seeded at 6,000 cells per well and grown for seven days to form a spheroid. On day 7 the spheroid was labelled with Hoechst (1 µM), Calcein AM (3.5 µM), PI (1 µM) for 1 h and imaged live at various depths (a) 5 µm; (b) 18 µm; (c) 37 µm; (d) 100 µm. Images were acquired from left to right: Hoechst; Calcein AM; PI; SRS 2940 cm^{-1} (CH_3, protein). Images acquired at 1024 × 1024 pixels, 20 µs pixel dwell time, laser power 250 mW (the tuneable pump beam) with false colours applied to different detection wavenumbers. Scale bars: 50 µm.

To test reproducibility of both spheroid formation and SRS imaging depth, another T47D spheroid at 6,000 cells per well seeding density was formed over seven days, labelled with aforementioned fluorescent dyes and imaged using the multiphoton microscope (Figure 5.16). The estimated diameter of the spheroid was 660 μm, which is only 10 μm (±2%) larger than the diameter of the previous T47D spheroid seeded at 6,000 cells per well; proving that our spheroid growth protocol produces spheroids with consistent sizing from independent experiments.

For this T47D spheroid, smaller step-sizes were taken for the z-stack during multimodal imaging to better estimate the SRS imaging depth. Images were acquired at 15 μm, 30 μm, 60 μm, 100 μm, 130 μm and 200 μm depth from the top of the spheroid (Figure 5.16a-e). As before, the SRS signal was significantly reduced by 100 μm depth, but some protein signal was still detected at 130 μm depth (Figure 5.18d,e). No signal was detected at 200 μm depth (image not shown).

Both 6,000 cells per well spheroids from independent experiments looked similar in size on the multiphoton images. These spheroids filled the whole field of view of the microscope, with only edges of the spheroid slightly out of the field of view (Figure 5.16 & Figure 5.16). If the goal is to image the whole spheroid in one field of view, 4,000 well seeding density should be used in the future with seven day spheroid growth as it generates spheroids with about 10% smaller diameter (590 μm vs 650 μm).

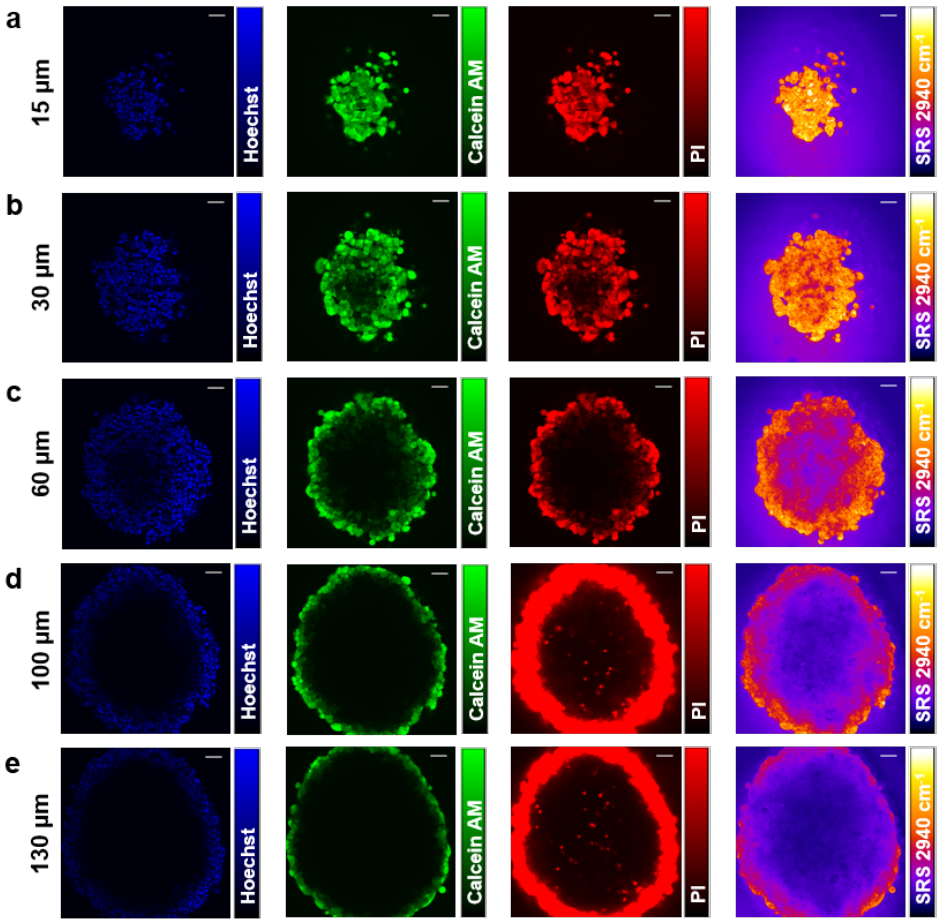

Figure 5.16 Multimodal imaging of T47D spheroid. T47D cells were seeded at 6,000 cells per well and grown for seven days to form a spheroid. On day 7 the spheroid was labelled with Hoechst (1 µM), Calcein AM (3.5 µM), PI (1 µM) for 1 h and imaged live at various depths (a) 15 µm; (b) 30 µm; (c) 60 µm; (d) 100 µm; (e) 130 µm. Images were acquired from left to right: Hoechst; Calcein AM; PI; SRS 2940 cm^{-1} (CH_3, protein). Images acquired at 1024 × 1024 pixels, 20 µs pixel dwell time, laser power 250 mW (the tuneable pump beam) with false colours applied to different detection wavenumbers. Scale bars: 50 µm.

As we saw from the ImageXpress images, seeding 10,000 cells per well generated T47D spheroids with close to 1 mm diameter (~960 µm) and a more complex internal structure (Figure 5.10c). One of these larger spheroids was imaged on the multiphoton to compare and contrast it to the smaller (~650-660 µm) T47D spheroids (Figure 5.15 & Figure 5.16). Images were acquired at 15 µm, 30 µm, 60 µm, 100 µm, 130 µm and 200 µm depth from the top of the spheroid (Figure 5.17a-e). It was clear from the images that this spheroid did not fit into a single field of view on the multiphoton microscope due to its larger size. It would be necessary to acquire multiple images at each depth to obtain a full spheroid picture, increasing imaging

time per spheroid as well as making image analysis more complex. In terms of imaging depth, SRS signal intensity was similar to the spheroids imaged earlier, where we could detect the spheroid protein signal up to 130 µm depth (Figure 5.17e). PI staining demonstrated that the bigger T47D spheroid (~960 µm diameter) had more dead cells in the core compared to the smaller T47D spheroids (~650-660 µm diameter), indicative of higher level of dead cells (Figure 5.17c-e vs Figure 5.16c-e).

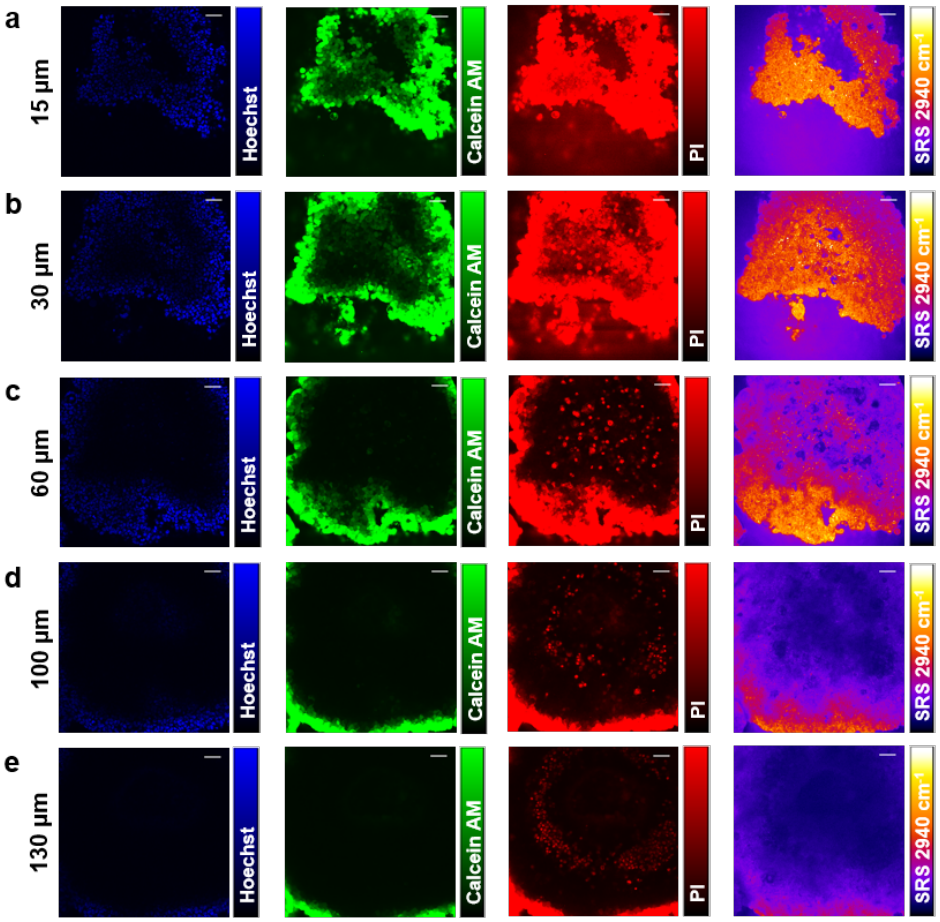

Figure 5.17 Multimodal imaging of T47D spheroid. T47D cells were seeded at 20,000 cells per well and grown for seven days to form a spheroid. On day 7 the spheroid was labelled with Hoechst (1 µM), Calcein AM (3.5 µM), PI (1 µM) for 1 h and imaged live at various depths (a) 15 µm; (b) 30 µm; (c) 60 µm; (d) 100 µm; (e) 130 µm. Images were acquired from left to right: Hoechst; Calcein AM; PI; SRS 2940 cm^{-1} (CH_3, protein). Images acquired at 1024 × 1024 pixels, 20 µs pixel dwell time, laser power 250 mW (the tuneable pump beam) with false colours applied to different detection wavenumbers. Scale bars: 50 µm.

To get a better view of the whole spheroid, z-stacks of each of the T47D spheroids were obtained using SRS imaging (Figure 5.18). Between a 103 and 133 SRS images were acquired and used to reconstruct 3D images of each spheroid (Figure 5.18a-c). It is possible to see that the two spheroids seeded at 6,000 cells per well fit into the field of view, while the spheroid seeded at 20,000 cells per well does not. As a result, we can see the morphology of the smaller spheroids much more clearly with protruding bumps of cells visible on the surface. High-resolution images of the superficial morphology of spheroids are usually taken using scanning electron microscopy (SEM).[150,268,292] However, SEM requires samples to be fixed and dehydrated with or without gold coating prior to imaging. In contrast, SRS imaging allowed us to image spheroids live with no extensive sample preparation protocol.

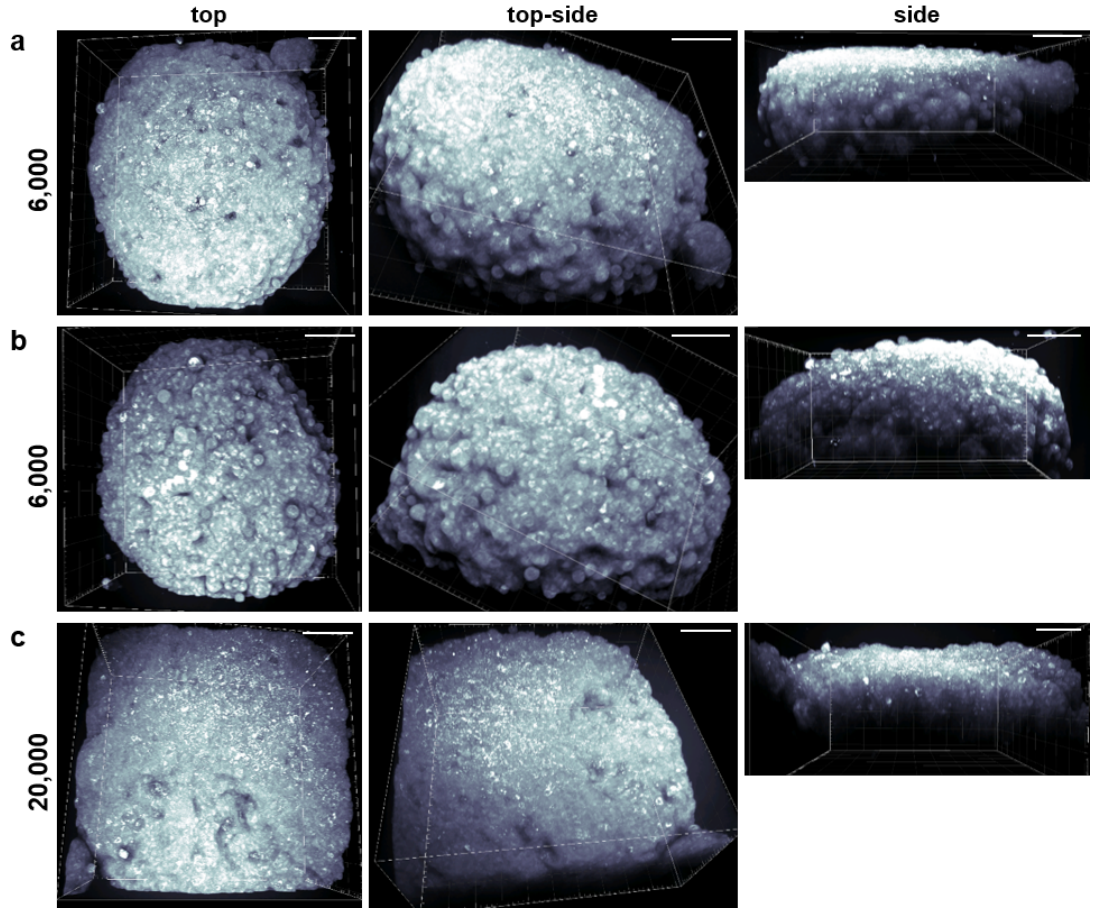

Figure 5.18 3D SRS imaging of live T47D spheroids. T47D cells were seeded at (a), (b) 6,000 or (c) 20,000 cells per well and grown for seven days to form spheroids. Z-stack images of live T47D spheroids were acquired using SRS at 2940 cm^{-1} (CH_3, proteins). (a) 103 images acquired at 2 µm step size. (b) 130 images acquired at 2 µm step size. (c) 133 images acquired at 2 µm step size. All the images acquired at 512 × 512 pixels, (a) 4 µs pixel dwell time (b), (c) 10 µs pixel dwell time, laser power 250 mW (the tuneable pump beam). Scale bars: 100 µm.

These initial SRS images acquired in spheroids highlight that depth penetration is a major limitation for SRS imaging just as it is for fluorescence based imaging. For both fluorescence and SRS imaging the imaging depth depends on the attenuation coefficient of the tissue, which has two major contributing factors, the amount of scattering and the amount of absorbance from the sample.[293] Scattering is mostly a product of the tissue itself and varies with tissue type - lung tissue is subject to high level of scattering while skin is not. In addition, scattering is wavelength dependent, where higher wavelength light scatters less and is generally better for imaging deeper into the sample. Absorption of light by the sample, however, also influences imaging depth. As absorption is a function of all the different chromophores in the tissue, including water, haemoglobin, melanin and fat amongst others, it is a complicated factor to predict. These properties of tissues vary from tissue to tissue, person to person and even time to time. Therefore, defining absolute imaging depths for either fluorescence or SRS imaging would not be accurate.

Here, we used two-photon fluorescence microscopy to visualise the fluorophores within the spheroid. Two-photon excitation generates fluorescence from both the focal plane and from outside the focal plane, where out-of-focus fluorescence increases as the focus is pushed deeper into the sample.[294] The depth limit of two-photon excitation is generally limited by the amount of background fluorescence produced from outside the focal plane. Takasaki *et al.* recently explored TPF depth penetration in mouse brain cortex using GCaMP6 green fluorescence.[294] They found that two photon depth limit was approximately 450 μm in the mouse cortex. Depth penetration in tissue can be increased using red-shifted fluorophores, which allows for longer wavelength excitation light to be used. This helps to reduce both scattering and absorbance of the excitation and emission light. Tischbirek *et al.* have shown that TPF imaging with a red fluorophore enabled mouse brain cortex imaging up to 900 μm in depth.[295]

In SRS imaging, the depth penetration is dependent on additional factors, which reduce imaging depth in comparison to TPF. For SRS to occur two different wavelength lasers need to be focussed by an objective at the same point in the tissue and the photons that arrive need to be overlapped both spatially and temporally. This will be complicated by both the optical properties of the tissue which vary with wavelength, as well as due to chromatic aberrations within the optical elements of the microscope itself. Another limiting factor in SRS is that it is a homodyne technique, where the signal is carried at the same wavelength as the excitation wavelength,

meaning that it is necessary to collect both the stimulated photons as well as the normal photons to allow for a measurement to be taken. Therefore, it us unsurprising that the maximum depth penetration for mouse brain tissue using SRS has been measured as 205 μm, significantly less than TPF.[296]

The fact that SRS imaging in 3D is limited by depth penetration, is clearly visible on the side view images of the spheroids, where the signal intensity decreases exponentially deeper inside the spheroid and eventually disappears completely (Figure 5.18a-c). In addition, it appears that SRS imaging depth is lower in the larger, thicker spheroid (Figure 5.18c) compared to the smaller, thinner spheroids (Figure 5.18a,b). Others have previously also applied SRS imaging to tissue. Wei *et al.* detected terbafine in mouse ear tissue at about 100 μm depth and Saar *et al.* imaged deuterated ibuprofen at about 15 μm depth.[47,70] Additionally, Chiu *et al.* imaged deuterated solvent penetration into human nail plate using SRS, and detected deuterated water up to 100 μm depth.[71] They also investigated the effect of tissue thickness on SRS penetration depth using three nails samples from three different individuals with varying thickness, where signal was normalised to CH_2 intensity on the nail surface. The CH_2 signal profile across the nail was found to be similar for the three samples examined. More recently, however, Hill *et al.* investigated SRS penetration depth in brain tissue slices with varying thickness (250 μm - 2 mm).[296] They found that maximum imaging depth was reduced in thicker samples, where the maximum imaging depth for 250 μm sample was 205 μm, while for 2 mm sample it was 130 μm. These were the reported depth limits using transmissive imaging mode, which we also used for the spheroid imaging. In contrast, when Hill *et al.* used epi detection, slightly improved signal to noise ratio and imaging depth were achieved in the thicker, 2 mm samples. Overall, our early data on SRS application to imaging spheroids is in good agreement with previously published data on tissues and spheroids.

To enhance the depth penetration when using SRS, tissue clearing protocols have also been developed. Weia *et al.* used 8 M urea with 0.2% Triton X-100 for spheroid and tissue clearing, reporting 10-fold increase in SRS depth-penetration upon clearing the samples.[291] However, this protocol requires days to weeks to complete depending on the sample type. Li *et al.* tested a number of tissue clearing agents on brain tissue samples to improve the clearing protocol and found that using formamide solutions at gradient concentrations for 30 min in total yielded the best results, increasing SRS

imaging depth up to 500 μm.[297] As we have shown that the ponatinib SRS signal in 2D cell culture disappears upon cell fixation (Section 5.3.1), we believe a tissue clearing protocol would likely have similar effects when imaging ponatinib in spheroids.

5.4.1 SRS imaging of ponatinib in live T47D spheroids

Initial ponatinib imaging in a live T47D spheroid was attempted using SRS microscopy. A T47D spheroid was seeded at 6,000 cells per well and grown for seven days. At this time the mature spheroid was treated with ponatinib (10 μM, 1 h) in the U-bottom ULA plate. Following treatment, SRS images of the live spheroid were acquired immediately after transferring the spheroid to a slide. Ponatinib was detected at both 20 μm and 70 μm depth, but the off-resonance images showed significantly higher background than we have previously seen during 2D SRS imaging of ponatinib (Figure 5.19a,b). The three-dimensional spheroid sample has overall more 'bulk' than a 2D sample, leading to increased background signals from competing pump-probe processes such as cross-phase modulation, transient absorption and photothermal effects.[63] Background subtraction does indicate that ponatinib is present in the spheroid – at 20 μm depth ponatinib uptake appears homogeneous across the section (Figure 5.19a). In contrast, at 70 μm depth on the subtracted image, the ponatinib signal only appears on the edges of the spheroid. However, at 70 μm depth the same is also seen on the protein image due to SRS signal loss as a result of light scattering deeper in the spheroid.

To look at ponatinib uptake in the spheroid in more detail, we zoomed into an area of the spheroid at both imaging depths (Figure 5.19c,d). At 20 μm depth, a few ponatinib puncta were identified from the on resonance image (2221 cm^{-1}) where the corresponding off-resonance image did not have puncta present (Figure 5.19c). Upon close examination it was also possible to point out individual ponatinib puncta with low background signal at 70 μm depth (Figure 5.19d). These early results show that despite higher background in the off-resonance area in 3D imaging, it is still possible to detect ponatinib uptake in spheroids. However, it certainly makes it harder to confidently distinguish between true ponatinib signal and background artefacts. It is noteworthy, that much higher laser power was required to detect ponatinib in 3D (350 mW at 20 μm, 500 mW at 70 μm) compared to 2D imaging (200-250 mW).

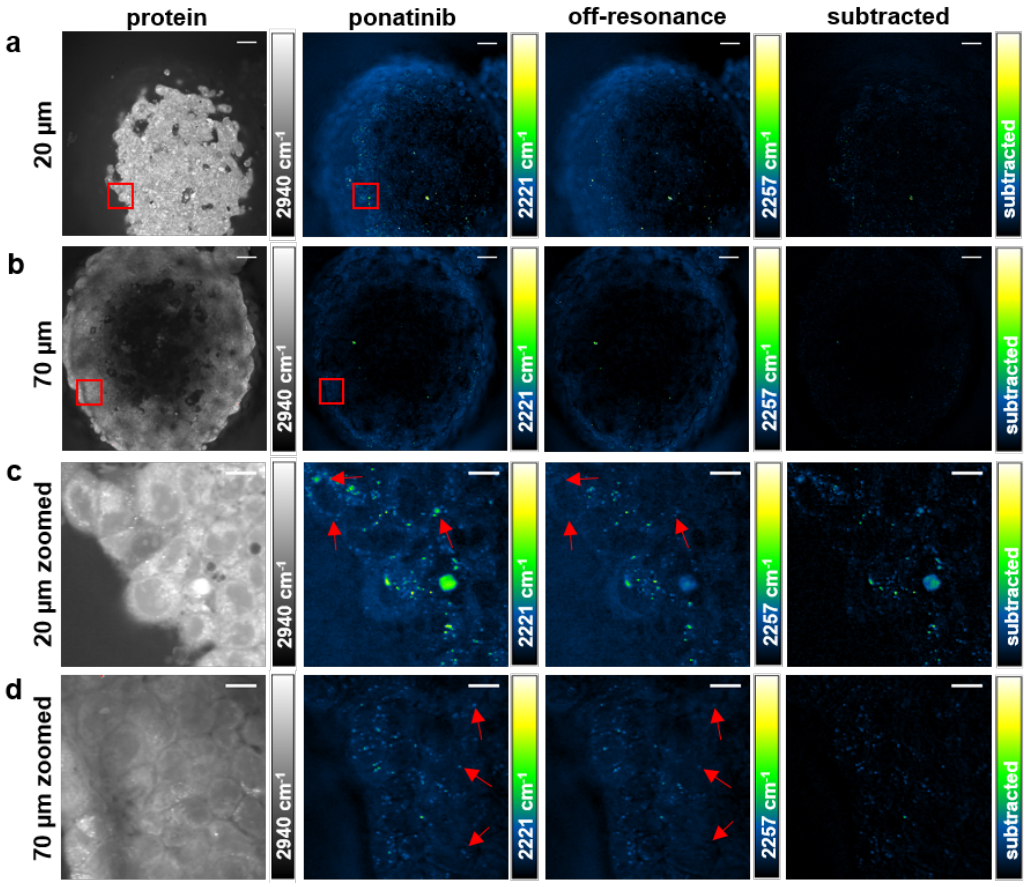

Figure 5.19 SRS imaging of ponatinib in a live T47D spheroid. T47D spheroid was seeded at 6,000 cells per well, grown for seven days, and incubated with ponatinib (10 µM, 1 h) on day 7. SRS images of the spheroid acquired at (a) 20 µm and (b) 70 µm depth (from left to right) 2940 cm^{-1} (CH_3, proteins); 2221 cm^{-1} (C≡C, ponatinib); 2257 cm^{-1} (off-resonance); 2221 cm^{-1} with background subtracted. (c) Zoomed in to the red square from (a), red arrows pointing at ponatinib spots with low background. (d) Zoomed in to the red square from (b), red arrows pointing at ponatinib spots with low background. Images acquired at 1024 × 1024 pixels, 20 µs pixel dwell time, laser power 250 mW (the tuneable pump beam) for CH_3, 350 mW for ponatinib in (a) and 500 mW for ponatinib in (b). False colours applied to different detection wavenumbers. Scale bars: (a), (b) 50 µm; (c), (d) 10 µm.

5.5 Conclusions

In this chapter, spheroid growth was optimised using a U-shaped ULA plate method. We found that CML cell lines KCL22 and KCL22$^{Pon\text{-}Res}$ only form cell aggregates in ULA plates. In contrast, the breast cancer cell line T47D formed tight spheroids with strong cell-cell contacts. T47D spheroids were characterised by size as well as live and dead cell dyes, demonstrating that they have a proliferative edge and a dead cell core after seven days of growing.

Prior to SRS imaging of spheroids, ponatinib was imaged in 2D cell culture using T47D cells. Ponatinib could successfully be detected in live T47D cells, but when cells were fixed ponatinib signal disappeared inside cells. We believe this is likely due to the drug being washed out of the cell during the fixing protocol since ponatinib is not covalently bound to its target. As we have shown the majority of ponatinib localises within acidic organelles – fixing can influence organelle pH, and subsequently lead to re-distribution of ponatinib during fixing and the associated wash steps.

The T47D spheroids were imaged using the multiphoton microscope. It was determined that the SRS imaging depth penetration is around 130 µm on our microscope. Initial SRS images of ponatinib in a T47D spheroid were also acquired, where ponatinib puncta were detected at 20 µm depth and 70 µm depth inside the spheroid. However, it was clear that SRS off-resonance background is a lot higher when imaging at depth, reducing the signal-to-noise ratio and making it more difficult to differentiate true ponatinib signal from background artefacts. For this type of drug imaging hSRS would be a more advantageous technique, as it would allow imaging on and off the ponatinib SRS peak significantly faster. An alternative option for reducing background signal would be the use of frequency modulated SRS (FM-SRS).[208] In contrast to normal SRS, where amplitude modulation is used with on-and-off laser, FM-SRS modulates the laser frequency from on-resonance to off-resonance, and gives a final image where wavelength independent competing background processes have already been removed. Rigneault *et al.* have also explored other avenues for reducing SRS background signals, such as using stimulated Raman gain and opposite loss detection (SRGOLD), where SRG and SRL are both measured.[298] Theoretically, SRGOLD can double the signal intensity acquired as SRG and SRL signal are added up, without increasing background signals.[299] Unfortunately, unsymmetric parasitic background signals cannot be removed by SRGOLD imaging. These advanced SRS imaging techniques could be

applied to drug imaging to improve signal to noise ratio, which is especially prominent in 3D SRS imaging.

Although others have used clearing techniques to improve SRS imaging depth, we believe this would not be the best option for drug imaging in 3D. We found that fixing protocol washes away significant proportion of ponatinib from the cell, reducing detectable drug signal with SRS, and altering drug localisation. Clearing protocol would likely have a similar effect on ponatinib as well as other drugs. Therefore, using clearing techniques for drug imaging with SRS in 3D is probably not the best approach for improving imaging depth. A more suitable option would be sectioning of frozen spheroids, as is done for MALDI imaging of drugs. Imaging serial sections of drug treated spheroids rather than the whole spheroid would help overcome the depth penetration issues for SRS imaging. Additionally, it would hopefully improve SNR for imaging ponatinib in spheroids, giving less background off resonance. It is not known, however, if freezing the sample will influence the SRS signal – this would have to be investigated.

In summary, preliminary data was acquired in this chapter to take drug imaging with SRS microscopy from 2D to 3D. Although drug signal was successfully detected in a spheroid for the first time using SRS microscopy, it was accompanied by high background signal. The two major limitations for SRS drug imaging in 3D were found to be depth penetration and significant level of background signals from competing pump-probe processes.

Chapter 6 Future perspectives

In this thesis SRS was successfully used for label-free imaging of ponatinib in 2D and 3D. A wide range of SRS applications that are beneficial for improving our understanding of intracellular drug behaviour were demonstrated throughout the chapters. While visualising intracellular drug uptake and distribution to improve the pre-clinical drug discovery process is still a challenge for scientists, SRS imaging provides a potential solution that allows quantitative drug imaging at sub-cellular resolution in live cells.

We explored ponatinib localisation in a BCR-ABL independent CML resistance model, where increased lysosomal uptake of ponatinib was found in ponatinib resistant cells compared to drug sensitive cells. Lysosomal uptake was not, however, found to be the cause of drug resistance. Unlike imatinib resistance, which has been studied extensively, not much is published on ponatinib resistance mechanisms. In contrast to CML resistance to 1st and 2nd generation TKIs, where BCR-ABL mutations are prevalent in patients, mutations are rarely the cause of ponatinib resistance.[300] Certain compound mutations, where multiple mutations occur within the same BCR-ABL clone, have been found to decrease sensitivity to ponatinib.[301] Deininger *et al.*, however, used next generation sequencing on 267 heavily pre-treated CP-CML patients, and found that compound mutations do not confer primary and/or secondary resistance to ponatinib in CML patients.[302] Instead, BCR-ABL independent resistance mechanisms seem to be the cause of ponatinib resistance. Research on BCR-ABL independent ponatinib resistance models has identified mTOR and Axl as potential new drug targets.[109,303] Therefore, both our results and literature on ponatinib resistance are in agreement that BCR-ABL independent resistance mechanisms warrant novel treatment approaches to be investigated to improve the treatment of CML patients who have become resistant to BCR-ABL inhibition.

Although in this project we focused ponatinib imaging on drug resistant CML, as a multikinase inhibitor, it has various other cellular targets in addition to BCR-ABL. As such, ponatinib has been explored as a treatment option for other cancers in various clinical trials, including lung cancer, gastrointestinal tumours, glioblastoma as well as other haematological malignancies.[304] In these trials, ponatinib targets have included FGFRs, RET, KIT and FLT3 amongst others. So far these trials have not led to successful approval of ponatinib use in non-haematological cancers, but many are

still ongoing. This presents additional opportunities for studying ponatinib localisation in other cancer types using SRS imaging with our established protocols.

Our work on ponatinib imaging demonstrated the quantitative nature of SRS imaging and allowed us to quantify the absolute ponatinib concentration within individual cells for the first time. The methodology for using SRS for absolute drug concentration determination, however, could be improved further in the future. First of all, more biologically relevant solvent could be used for acquiring the concentration curve. Additionally, the potential influence of varying pH on SRS signal intensity could be explored experimentally. This would help ensure that when drugs localise in acidic compartments inside cells it does not affect their Raman signal.

Investigating intracellular drug metabolism by SRS alone is not very efficient, because Raman shifts are not easily observable in SRS. Hyperspectral SRS would be a more sensitive technique for detecting Raman shifts. As we did not have access to hSRS, we used DFT measurements to assess the likelihood of Raman shifts and intensity changes of known ponatinib metabolites, and measured ponatinib metabolite levels in our cell lines of interest using LC-MS. We demonstrated that the combined use of DFT, LC-MS and SRS enables drug metabolism to be investigated alongside drug localisation inside cells, which cannot be achieved by mass spectrometry techniques alone.

Although MALDI is the gold standard for label-free drug imaging and investigating drug metabolism simultaneously, it is limited by its poor resolution, which is 20-100 µm.[23] In contrast, SRS has a spatial resolution of about 300 nm and allows drug imaging with subcellular resolution.[61] For both techniques, the detection sensitivity varies from drug to drug.[23,305] MALDI is the more powerful tool for detecting drug metabolites while SRS has superior resolution. As such, we envisage that combining MALDI and SRS, especially for drug imaging in spheroids and tumours, would enable superior information on drug metabolism and cellular localisation to be captured compared to using either technique alone. Randall *et al.* have recently demonstrated the utility of MALDI and SRS tandem imaging in a in a patient-derived xenograft model of glioblastoma, where tumour slices with 12 µm thickness were imaged.[289] MALDI was used for erlotinib detection and SRS for protein, lipid and heme imaging alongside standard histology staining. They found that SRS imaging provided detailed spatial and chemical information that could not be provided by standard histology. This could

be taken a step further by using SRS for drug imaging in tumours, which so far has not been reported.

SRS, like all imaging modalities, has its limitations, including detection sensitivity, depth penetration as well as parasitic background signals. Although we successfully managed to image ponatinib in CML cells following 500 nM treatment concentration, it still required accumulation of the drug at approximately 1 mM local concentration inside the cell. Hyperspectral SRS would allow detection of on and off resonance images simultaneously. This would increase image acquisition speeds and would likely improve detection sensitivity. Previous research by Fu *et al.* reported the detection sensitivity of hSRS as 1-2 mM, however, they were imaging drugs within the fingerprint region of the Raman spectrum.[170] Imaging in the 'cell silent' region would likely improve the detection sensitivity of hSRS. More recently, Zong *et al.* showed that SRS detection sensitivity can also be increased by plasmon-enhanced SRS (PESRS), where single molecule detection of adenine on gold nanoparticles was demonstrated.[306]

SRS detection sensitivity can be enhanced by the addition of Raman active tags as well. As ponatinib was inherently Raman active it did not require labelling, but not all drugs have a Raman active moiety within the 'cell silent' region. To allow wider application of SRS imaging to other drugs, addition of Raman active tags could be considered. This has been demonstrated before by Tipping *et al.*, where BADY tag was successfully incorporated in a small molecule anisomycin, enabling its intracellular visualisation.[49] However, addition of a Raman tag to a drug could perturb the molecules' bioactivity, and care must be taken to prevent that from happening. Traditional Raman tags that significantly increase the Raman activity of the molecule of interest such as BADY are usually very lipophilic. Hence, Raman tags could influence the logP of the drug molecule and affect the molecule's localisation within the cell. Future development of Raman tags for drug imaging purposes will therefore likely focus on the synthesis of Raman active tags with more drug-like physicochemical properties.

The other major limitation of SRS imaging is depth penetration. We found that depth penetration in spheroids was approximately 130 μm when visualising the protein stretch. Our results are in agreement with previous SRS spheroid imaging by Weia *et al.*, who also reported 120 μm depth penetration with SRS.[291] Depth penetration is dependent on both tissue type and sample thickness. When SRS imaging was

compared for 1 mm thick samples, Hill *et al.* found that depth penetration for brain, kidney, liver and lung were 185 µm, 165 µm, 170 µm and 70 µm respectively.[296] It is therefore unsurprising that most small molecule detection using SRS imaging in 3D, including spheroids, tissue slices, nail and *in vivo* imaging, has been done around or below 100 µm depth.[46,70,71] Same holds true for CARS imaging of deuterated compounds in skin.[307,308] Although we could detect ponatinib puncta at 70 µm depth in spheroids using SRS, imaging in 3D significantly increased SRS background signals, which made it more difficult to differentiate true ponatinib signal from background artefacts. This highlights that drug imaging *in vivo* using SRS is going to be challenging. We think in the near future, 3D drug imaging using SRS will be more likely achievable in spheroid and/or tissue slices similarly to MALDI, which will remove depth penetration issues whilst still allowing heterogeneity in drug uptake to be visualised with superior resolution in comparison to MALDI.

Application of advanced SRS modalities, such as FM-SRS and SRGOLD to drug imaging, could improve depth penetration and reduce SRS background, but has yet to be explored. Depth penetration could also be improved by advanced data processing. Hill *et al.* showed 24% (40 µm) increase in SRS depth penetration by using a convolution neural networks based denoising algorithm.[296] It is hence still possible that *in vivo* drug imaging using SRS microscopy will be feasible in the future.

References

1. Tagle, D. A. The NIH microphysiological systems program: developing *in vitro* tools for safety and efficacy in drug development. *Curr. Opin. Pharmacol.* **2019,** 48, 146-154.

2. Kola, I.; Landis, J. Can the pharmaceutical industry reduce attrition rates? *Nat. Rev. Drug Discov.* **2004,** 3, 711-715.

3. DiMasi, J. A.; Grabowski, H. G. Economics of new oncology drug development. *J. Clin. Oncol.* **2007,** 25, 209-16.

4. Swinney, D. C.; Anthony, J. How were new medicines discovered? *Nat. Rev. Drug Discov.* **2011,** 10, 507-19.

5. Moreno, L.; Pearson, A. D. How can attrition rates be reduced in cancer drug discovery? *Expert Opin. Drug Discov.* **2013,** 8, 363-8.

6. Munos, B. Lessons from 60 years of pharmaceutical innovation. *Nat. Rev. Drug Discov.* **2009,** 8, 959-68.

7. Horvath, P.; Aulner, N.; Bickle, M.; Davies, A. M.; Nery, E. D.; Ebner, D.; Montoya, M. C.; Ostling, P.; Pietiainen, V.; Price, L. S.; Shorte, S. L.; Turcatti, G.; Schantz, C. v.; Carragher, N. O. Screening out irrelevant cell-based models of disease. *Nat. Rev. Drug Discov.* **2016,** 15, 751-769.

8. Arrowsmith, J.; Miller, P. Trial watch: phase II and phase III attrition rates 2011-2012. *Nat. Rev. Drug Discov.* **2013,** 12, 569.

9. Nestor, C. E.; Ottaviano, R.; Reinhardt, D.; Cruickshanks, H. A.; Mjoseng, H. K.; McPherson, R. C.; Lentini, A.; Thomson, J. P.; Dunican, D. S.; Pennings, S.; Anderton, S. M.; Benson, M.; Meehan, R. R. Rapid reprogramming of epigenetic and transcriptional profiles in mammalian culture systems. *Genome Biol.* **2015,** 16, 11.

10. Carreau, A.; Hafny-Rahbi, B. E.; Matejuk, A.; Grillon, C.; Kieda, C. Why is the partial oxygen pressure of human tissues a crucial parameter? Small molecules and hypoxia. *J. Cell. Mol. Med.* **2011,** 15, 1239-1253.

11. Tiede, L. M.; Cook, E. A.; Morsey, B.; Fox, H. S. Oxygen matters: tissue culture oxygen levels affect mitochondrial function and structure as well as responses to HIV viroproteins. *Cell Death Dis.* **2011,** 2, e246.

12. Su, H.; Bodenstein, C.; Dumont, R. A.; Seimbille, Y.; Dubinett, S.; Phelps, M. E.; Herschman, H.; Czernin, J.; Weber, W. Monitoring tumor glucose utilization by positron emission tomography for the prediction of treatment response to epidermal growth factor receptor kinase inhibitors. *Clin Cancer Res* **2006,** 12, 5659-67.

13. Ponce, A. M.; Viglianti, B. L.; Yu, D.; Yarmolenko, P. S.; Michelich, C. R.; Woo, J.; Bally, M. B.; Dewhirst, M. W. Magnetic resonance imaging of temperature-sensitive liposome release: drug dose painting and antitumor effects. *J. Natl. Cancer Inst.* **2007,** 99, 53 – 63.

14. Solon, E. G.; Balani, S. K.; Lee, F. W. Whole-body autoradiography in drug discovery. *Curr. Drug Metab.* **2002,** 3, 451-462.

15. Beckmann, N.; Laurent, D.; Tigani, B.; Panizzutti, R.; Rudin, M. Magnetic resonance imaging in drug discovery: lessons from disease areas. *Drug Discov. Today* **2004,** 9, 35-42.

16. Wagner, C. C.; Langer, O. Approaches using molecular imaging technology — use of PET in clinical microdose studies. *Adv. Drug Deliv. Rev.* **2011,** 63, 539-546.

17. Solon, E. G.; Schweitzer, A.; Stoeckli, M.; Prideaux, B. Autoradiography, MALDI-MS, and SIMS-MS imaging in pharmaceutical discovery and development. *AAPS J.* **2010,** 12, 11-26.

18. Solon, E. G. Autoradiography: high-resolution molecular imaging in pharmaceutical discovery and development. *Expert Opin. Drug Discov.* **2007,** 2, 503-514.

19. Caprioli, R. M.; Farmer, T. B.; Gile, J. Molecular imaging of biological samples: Localization of peptides and proteins using MALDI-TOF MS. *Anal. Chem.* **1997,** 69, 4751-4760.

20. Signor, L.; Varesio, E.; Staack, R. F.; Starke, V.; Richter, W. F.; Hopfgartner, G. Analysis of erlotinib and its metabolites in rat tissue sections by MALDI quadrupole time-of-flight mass spectrometry. *J. Mass Spectrom.* **2007,** 42, 900-909.

21. Troendle, F. J.; Reddick, C. D.; Yost, R. A. Detection of pharmaceutical compounds in tissue by matrix-assisted laser desorption/ionization and laser desorption/chemical ionization tandem mass spectrometry with a quadrupole ion trap. *J. Am. Soc. Mass Spectrom.* **1990,** 10, 1315-1321.

22. Marko-Varga, G.; Fehniger, T. E.; Rezeli, M.; Dome, B.; Laurell, T.; Vegvari, A. Drug localization in different lung cancer phenotypes by MALDI mass spectrometry imaging. *J. Proteomics* **2011,** 74, 982-92.

23. Greer, T.; Sturm, R.; Li, L. Mass spectrometry imaging for drugs and metabolites. *J. Proteomics* **2011,** 74, 2617 – 2631.

24. Lietz, C. B.; Gemperline, E.; Li, L. Qualitative and quantitative mass spectrometry imaging of drugs and metabolites. *Adv. Drug Deliv. Rev.* **2013,** 65, 1074-1085.

25. Agui-Gonzalez, P.; Jahne, S.; Phan, N. T. N. SIMS imaging in neurobiology and cell biology. *J. Anal. At. Spectrom.* **2019,** 34, 1355-1368.

26. Chandra, S.; Ahmad, T.; Barth, R. F.; Kabalka, G. W. Quantitative evaluation of boron neutron capture therapy (BNCT) drugs for boron delivery and retention at subcellular-scale resolution in human glioblastoma cells with imaging secondary ion mass spectrometry (SIMS). *J. Microsc.* **2014,** 254, 146-156.

27. Stephens, D. J.; Allan., V. J. Light microscopy techniques for live cell imaging. *Science* **2003,** 300, 82-86.

28. Prescher, J. A.; Bertozzi, C. R. Chemistry in living systems. *Nat. Chem. Biol.* **2005,** 1, 13-21.

29. Fernández-Suárez, M.; Ting, A. Y. Fluorescent probes for super-resolution imaging in living cells. *Nat. Rev. Mol. Cell Biol.* **2009,** 9, 929-943.

30. Sletten, E. M.; Bertozzi, C. R. Bioorthogonal chemistry: Fishing for selectivity in a sea of functionality. *Angew. Chem. Int. Ed.* **2009,** 48, 6974-6998.

31. Lazzari, G.; Vinciguerra, D.; Balasso, A.; Nicolas, V.; Goudin, N.; Garfa-Traore, M.; Fehér, A.; Dinnyés, A.; Nicolas, J.; Couvreur, P.; Mura, S. Light sheet fluorescence microscopy versus confocal microscopy: in quest of a suitable tool to assess drug and nanomedicine penetration into multicellular tumor spheroids. *Eur. J. Pharm. Biopharm.* **2019,** 142, 195–203.

32. Gotink, K. J.; Broxterman, H. J.; Labots, M.; Haas, R. R. d.; Dekker, H.; Honeywell, R. J.; Rudek, M. A.; Beerepoot, L. V.; Musters, R. J.; Jansen, G.; Griffioen, A. W.; Assaraf, Y. G.; Pili, R.; Peters, G. J.; Verheul, H. M. W. Lysosomal sequestration of sunitinib: a novel mechanism of drug resistance. *Clin. Cancer Res.* **2011,** 17.

33. Raman, C. V.; Krishnan, K. S. A new type of secondary radiation. *Nature* **1928,** 121, 501–502.

34. Butler, H. J.; Ashton, L.; Bird, B.; Cinque, G.; Curtis, K.; Dorney, J.; Esmonde-White, K.; Fullwood, N. J.; Gardner, B.; Martin-Hirsch, P. L.; Walsh, M. J.; McAinsh, M. R.; Stone, N.; Martin, F. L. Using Raman spectroscopy to characterise biological materials. *Nat. Protocols* **2016,** 11, 664-687.

35. Amrania, H.; McCrow, A. P.; Matthews, M. R.; Kazarian, S. G.; Kuimova, M. K.; Phillips, C. C. Ultrafast infrared chemical imaging of live cells. *Chem. Sci.* **2011,** 2, 107-111.

36. Costa, S. G. d.; Richter, A.; Schmidt, U.; Breuninger, S.; Hollricher, O. Confocal Raman microscopy in life sciences. *Morphologie* **2019,** 103, 11-16.

37. Ling, J.; Weitman, S. D.; Miller, M. A.; Moore, R. V.; Bovik, A. C. Direct Raman imaging techniques for study of the subcellular distribution of a drug. *Appl Opt* **2002,** 41, 6006-6017.

38. Salehi, H.; Derely, L.; Vegh, A. G.; Durand, J. C.; Gergely, C.; Larroque, C.; Fauroux, M. A.; Cuisinier, F. J. G. Label-free detection of anticancer drug paclitaxel in living cells by confocal Raman microscopy. *Applied Physics Letters* **2013,** 102, 113701.

39. Feofanov, A. V.; Grichine, A. I.; Shitova, L. A.; Karmakova, T. A.; Yakubovskaya, R. I.; Egret-Charlier, M.; Vigny, P. Confocal Raman Microspectroscopy and Imaging Study of Theraphthal in Living Cancer Cells. *Biophys J* **2000,** 78, 499-512.

40. Meister, K.; Niesel, J.; Schatzschneider, U.; Metzler-Nolte, N.; Schmidt, D. A.; Havenith, M. Label-free imaging of metal-carbonyl complexes in live cells by Raman microspectroscopy. *Angew Chem Int Ed Engl* **2010,** 49, 3310-2.

41. Clede, S.; Lambert, F.; Sandt, C.; Kascakova, S.; Unger, M.; Harte, E.; Plamont, M. A.; Saint-Fort, R.; Deniset-Besseau, A.; Gueroui, Z.; Hirschmugl, C.; Lecomte, S.; Dazzi, A.; Vessieres, A.; Policar, C. Detection of an estrogen derivative in two breast cancer cell lines using a single core multimodal probe for imaging (SCoMPI) imaged by a panel of luminescent and vibrational techniques. *Analyst* **2013,** 138, 5627-38.

42. Harada, Y.; Dai, P.; Yamaoka, Y.; Ogawa, M.; Tanaka, H.; Nosaka, K.; Akaji, K.; Takamatsu, T. Intracellular dynamics of topoisomerase I inhibitor, CPT-11, by slit-scanning confocal Raman microscopy. *Histochem Cell Biol* **2009,** 132, 39-46.

43. Devaraj, N. K. The future of bioorthogonal chemistry. *ACS Cent. Sci.* **2018,** 4, 952−959.

44. Yamakoshi, H.; Dodo, K.; Okada, M.; Ando, J.; Palonpon, A.; Fujita, K.; Kawata, S.; Sodeoka, M. Imaging of EdU, an alkyne-tagged cell proliferation probe, by Raman microscopy. *J Am Chem Soc* **2011,** 133, 6102-5.

45. Yamakoshi, H.; Dodo, K.; Palonpon, A.; Ando, J.; Fujita, K.; Kawata, S.; Sodeoka, M. Alkyne-tag Raman imaging for visualization of mobile small molecules in live cells. *J. Am. Chem. Soc.* **2012,** 134, 20681-9.

46. Wei, L.; Yu, Y.; Shen, Y.; Wang, M. C.; Min, W. Vibrational imaging of newly synthesized proteins in live cells by stimulated Raman scattering microscopy. *PNAS* **2013,** 110, 11226-11231.

47. Wei, L.; Hu, F.; Shen, Y.; Chen, Z.; Yu, Y.; Lin, C.-C.; Wang, M. C.; Min, W. Live-cell imaging of alkyne-tagged small biomolecules by stimulated Raman scattering. *Nat. Methods* **2014,** 4, 410-412.

48. Hu, F.; Chen, Z.; Zhang, L.; Shen, Y.; Wei, L.; Min, W. Vibrational imaging of glucose uptake activity in live cells and tissues by stimulated Raman scattering. *Angew. Chem. Int. Ed. Engl.* **2015,** 54, 9821 –9825.

49. Tipping, W. J.; Lee, M.; Serrels, A.; Brunton, V. G.; Hulme, A. N. Imaging drug uptake by bioorthogonal stimulated Raman scattering microscopy. *Chem. Sci.* **2017,** 8, 5606-5615.

50. Hu, F.; Zeng, C.; Long, R.; Miao, Y.; Wei, L.; Xu, Q.; Min, W. Supermultiplexed optical imaging and barcoding with engineered polyynes. *Nat. Methods* **2018,** 15, 194-200.

51. Wei, L.; Chen, Z.; Shi, L.; Long, R.; Anzalone, A. V.; Zhang, L.; Hu, F.; Yuste, R.; Cornish, V. W.; Min, W. Super-multiplex vibrational imaging. *Nature* **2017,** 544, 465–470.

52. Valm, A. M.; Cohen, S.; Legant, W. R.; Melunis, J.; Hershberg, U.; Wait, E.; Cohen, A. R.; Davidson, M. W.; Betzig, E.; Lippincott-Schwartz, J. Applying systems-level spectral imaging and analysis to reveal the organelle interactome. *Nature* **2017,** 546, 162-167.

53. Zhang, C.; Zhang, D.; J.-X. Cheng. Coherent Raman scattering microscopy in biology and medicine. *Annu. Rev. Biomed. Eng.* **2015,** 17, 415-445.

54. Cheng, J.-X.; Xie, S. X. Vibrational spectroscopic imaging of living systems: An emerging platform for biology and medicine. *Science* **2015,** 350, aaa8870.

55. Evans, C. L.; Xie, X. S. Coherent anti-Stokes Raman scattering microscopy: Chemical imaging for biology and medicine. *Annu. Rev. Anal. Chem.* **2008,** 1, 883–909.

56. Evans, C. L.; Potma, E. O.; Puoris'haag, M.; Cote, D.; Lin, C. P.; Xie, X. S. Chemical imaging of tissue *in vivo* with video-rate coherent anti-Stokes Raman scattering microscopy. *Proc. Natl. Acad. Sci.* **2005,** 102, 16807–16812.

57. Woodbury, E. J.; Ng, W. K. Ruby Laser Operation in the Near IR. *Proc. IRE* **1962,** 50, 2367-2368.

58. Freudiger, C. W.; Min, W.; Saar, B. G.; Lu, S.; Holtom, G. R.; He, C.; Tsai, J. C.; Kang, J. X.; Xie, X. S. Label-free biomedical imaging with high sensitivity by stimulated Raman scattering microscopy. *Science* **2008,** 322, 1857-1861.

59. Hong, S.; Chen, T.; Zhu, Y.; Li, A.; Huang, Y.; Chen, X. Live-cell stimulated Raman scattering imaging of alkyne-tagged biomolecules. *Angew. Chem. Int. Ed. Engl.* **2014,** 53, 5827-5831.

60. Tipping, W. J.; Lee, M.; Serrels, A.; Brunton, V. G.; Hulme, A. N. Stimulated Raman scattering microscopy: an emerging tool for drug discovery. *Chem. Soc. Rev.* **2016,** 45, 2075-2089.

61. Hu, F.; Shi, L.; Min, W. Biological imaging of chemical bonds by stimulated Raman scattering microscopy. *Nat. Methods* **2019,** 16, 830-842.

62. Fu, D.; Lu, F.-K.; Zhang, X.; Freudiger, C.; Pernik, D. R.; Holtom, G.; Xie, X. S. Quantitative chemical imaging with multiplex stimulated Raman scattering microscopy. *J. Am. Chem. Soc.* **2012,** 134, 3623-3626.

63. Zhang, D.; Wang, P.; Slipchenko, M. N.; Cheng, J.-X. Fast vibrational imaging of single cells and tissues by stimulated Raman scattering microscopy. *Acc. Chem. Res.* **2014,** 47, 2282−2290.

64. Kneipp, K.; Kneipp, H.; Itzkan, I.; Dasari, R. R.; Feld, M. S. Surface-enhanced Raman scattering and biophysics. *J. Phys. Condens. Matter* **2002,** 14, R597-R624.

65. Weeks, T.; Schie, I.; Hartigh, L. J. d.; Rutledge, J. C.; Huser, T. Lipid-cell interactions in human monocytes investigated by doubly-resonant coherent anti-Stokes Raman scattering microscopy. *J. Biomed. Opt.* **2011,** 16, 021117.

66. Lee, H. J.; Zhang, W.; Zhang, D.; Yang, Y.; Liu, B.; Barker, E. L.; Buhman, K. K.; Slipchenko, L. V.; Dai, M.; Cheng, J.-X. Assessing cholesterol storage in live cells and C. elegans by stimulated Raman scattering imaging of phenyl-diyne cholesterol. *Sci. Rep.* **2015,** 5, 7930.

67. Slipchenko, M. N.; Chen, H.; Ely, D. R.; Jung, Y.; Carvajal, M. T.; Cheng, J.-X. Vibrational imaging of tablets by epi-detected stimulated Raman scattering microscopy. *Analyst* **2010,** 135, 2613–2619.

68. Francis, A. T.; Nguyen, T. T.; Lamm, M. S.; Teller, R.; Forster, S. P.; Xu, W.; Rhodes, T.; Smith, R. L.; Kuiper, J.; Su, Y.; Fu, D. In situ stimulated Raman scattering (SRS) microscopy study of the dissolution of sustained-release implant formulation. *Mol. Pharma.* **2018,** 15, 5793–5801.

69. Liao, C.-S.; Wang, P.; Wang, P.; Li, J.; Lee, H. J.; Eakins, G.; Cheng, J.-X. Spectrometer-free vibrational imaging by retrieving stimulated Raman signal from highly scattered photons. *Sci. Adv.* **2015,** 1, e1500738.

70. Saar, B. G.; Contreras-Rojas, L. R.; Xie, X. S.; Guy, R. H. Imaging drug delivery to skin with stimulated Raman scattering microscopy. *Mol. Pharmaceutics* **2011,** 8, 969–975.

71. Chiu, W. S.; Belsey, N. A.; Garrett, N. L.; Moger, J.; M. B. Delgado-Charro; Guy, R. H. Molecular diffusion in the human nail measured by stimulated Raman scattering microscopy. *Proc. Natl. Acad. Sci. U.S.A.* **2015,** 112, 7725–7730.

72. Seidel, J.; Miao, Y.; Porterfield, W.; Cai, W.; Zhu, X.; Kim, S.-J.; Hu, F.; Bhattarai-Kline, S.; Min, W.; Zhang, W. Structure-activity-distribution relationship study of anti-cancer antimycin-type depsipeptides. *Chem. Commun.* **2019,** 55, 9379–9382.

73. Gaschler, M. M.; Hu, F.; Feng, H.; Linkermann, A.; Min, W.; Stockwell, B. R. Determination of the subcellular localization and mechanism of action of ferrostatins in suppressing ferroptosis. *ACS Chem. Biol.* **2018,** 13, 1013–1020.

74. Apperley, J. F. Chronic myeloid leukaemia. *Lancet* **2015,** 385, 1447–1459.

75. Sawyers, C. L. Chronic myeloid leukemia. *N. Engl. J. Med.* **1999,** 340, 1330-1340.

76. SasakI, K.; Strom, S. S.; O'Brien, S.; Jabbour, E.; Ravandi, F.; Konopleva, M.; Borthakur, G.; Pemmaraju, N.; Daver, N.; Jain, P.; Pierce, S.; Kantarjian, H.; Cortes, J. E. Prospective analysis: Relative survival in patients with chronic myeloid leukemia in phronic phase in the era of tyrosine kinase inhibitors. *Lancet Haematol.* **2015,** 2, e186–e193.

77. Nowell, P.; Hungerford, D. A minute chromosome in human chronic granulocytic leukemia. *Science* **1960,** 132, 1497.

78. Salesse, S.; Verfaillie, C. M. BCR/ABL: from molecular mechanisms of leukemia induction to treatment of chronic myelogenous leukemia. *Oncogene* **2002,** 21, 8547-8559.

79. Mitra, D.; Trask, P. C.; Iyer, S.; Candrilli, S. D.; Kaye, J. A. Patient characteristics and treatment patterns in chronic myeloid leukemia: evidence from a multi-country retrospective medical record chart review study. *Int. J. Hematol.* **2012,** 95, 263-273.

80. Radich, J. P. The biology of CML blast crisis. *Hematology Am. Soc. Hematol. Educ. Program* **2007,** 2007, 385-391.

81. Bower, H.; Bjorkholm, M.; Dickman, P. W.; Hoglund, M.; Lambert, P. C.; Andersson, T. M.-L. Life excpectancy of patients with chronic myeloid leukemia approaches the life expectancy of the general population. *J. Clin. Oncol.* **2016,** 34, 2851-2857.

82. Goldman, J. M. Allogeneic bone marrow transplantation: State of the art and future directions *Bone Marrow Transplant.* **1989,** 4, 133-134.

83. O'Brien, S.; Kantarjian, H.; Talpaz, M. Practical guidelines for the management of chronic myelogenous leukemia with interferon alpha. *Leuk. Lymphoma* **1996,** 23, 247-252.

84. Silver, R. T.; Woolf, S. H.; Hehlmann, R.; Appelbaum, F. R.; Anderson, J.; Bennett, C.; Goldman, J. M.; Guilhot, F.; Kantarjian, H. M.; Lichtin, A. E.; Talpaz, M.; Tura, S. An evidence-based analysis of the effect of busulfan, hydroxyurea, interferon, and allogeneic bone marrow transplantation in treating the chronic phase of chronic myeloid leukemia: developed for the American Society of Hematology. *Blood* **1999,** 95, 1517-1536.

85. Cohen, M. H.; Williams, G.; Johnson, J. R.; J. Duan, J. G.; Rahman, A.; Benson, K.; Leighton, J.; Kim, S. K.; Wood, R.; Rothmann, M.; Chen, G.; U, K. M.; Staten, A. M.; Pazdur, R. Approval summary for imatinib mesylate capsules in the treatment of chronic myelogenous leukemia. *Clin. Cancer. Res.* **2002,** 8, 935-942.

86. Druker, B. J.; Talpaz, M.; Resta, D. J.; Peng, B.; Buchdunger, E.; Ford, J. M.; Lydon, N. B.; Kantarjian, H.; Capdeville, R.; Ohno-Jones, S.; Sawyers, C. L. Efficacy and safety of a specific inhibitor of the BCR-ABL tyrosine kinase in chronic myeloid leukemia. *N. Eng. J. Med.* **2001,** 344, 1031-1037.

87. Lamontanara, A. J.; Gencer, E. B.; Kuzyk, O.; Hantschel, O. Mechanisms of resistance to BCR-ABL and other kinase inhibitors. *Biochim. Biophys. Acta* **2013,** 1834, 1449-1459.

88. Hughes, T.; Deininger, M.; Hochhaus, A.; Branford, S.; Radich, J.; Kaeda, J.; Baccarani, M.; Cortes, J.; Cross, N. C. P.; Druker, B. J.; Gabert, J.; Grimwade, D.; Hehlmann, R.; Kamel-Reid, S.; Lipton, J. H.; Longtine, J.; Martinelli, G.; Saglio, G.; Soverini, S.; Stock, W.; Goldman, J. M. Monitoring CML patients responding to treatment with tyrosine kinase inhibitors: review and recommendations for harmonizing current methodology for detecting BCR-ABL transcripts and kinase domain mutations and for expressing results. *Blood* **2006,** 108, 28-37.

89. Druker, B. J.; Guilhot, F.; O'Brien, S. G.; Gathmann, I.; Kantarjian, H.; Gattermann, N.; Deininger, M. W. N.; Silver, R. T.; Goldman, J. M.; Stone, R. M.; Cervantes, F.; Hochhaus, A.; Powell, B. L.; Gabrilove, J. L.; Rousselot, P.; Reiffers, J.; Cornelissen, J. J.; Hughes, T.; Agis, H.; Fischer, T.; Verhoef, G.; Shepherd, J.; Saglio, G.; Gratwohl, A.; Nielsen, J. L.; Radich, J. P.; Simonsson, B.; Taylor, K.; Baccarani, M.; So, C.; Letvak, L.; Larson, R. A. Five-year follow-up of patients receiving imatinib for chronic myeloid leukemia. *N. Engl. J. Med.* **2006,** 355, 2408-2417.

90. Kantarjian, H.; Giles, F.; Wunderle, L.; Bhalla, K.; O'Brien, S.; Wassmann, B.; Tanaka, C.; Manley, P.; Rae, P.; Mietlowski, W.; Bochinski, K.; Hochhaus, A.; Griffin, J. D.; Hoelzer, D.; Albitar, M.; Dugan, M.; Cortes, J.; Alland, L.; Ottmann, O. G. Nilotinib in imatinib-resistant CML and Philadelphia chromosome–positive ALL. *N. Eng. J. Med.* **2006,** 354, 2542-2551.

91. Wu, P.; Nielsen, T. E.; Clausen, M. H. FDA-approved small-molecule kinase inhibitors. *Trends Pharmacol Sci* **2015,** 36, 422-39.

92. M. Talpaz; N. P. Shah; H. Kantarjian; N. Donato; J. Nicoll; R. Paquette; J. Cortes; S. O'Brien; C. Nicaise; E. Bleickardt; M. A. Blackwood-Chirchir; V. Iyer; T.-T.

Chen; F. Huang; A. P. Decillis; C. L. Sawyers. Dasatinib in imatinib-resistant Philadelphia chromosome–positive leukemias. *The new england journal of medicine* **2006,** 354, 2531-2541.

93. Levinson, N. M.; Boxer, S. G. Structural and spectroscopic analysis of the kinase inhibitor bosutinib and an isomer of bosutinib binding to the Abl tyrosine kinase domain. *PLoS One* **2012,** 7, e29828.

94. Kim, S. H.; Kim, D.; Kim, D. W.; Goh, H. G.; Jang, S. E.; Lee, J.; Kim, W. S.; Kweon, I. Y.; Park, S. H. Analysis of Bcr-Abl kinase domain mutations in Korean chronic myeloid leukaemia patients: poor clinical outcome of P-loop and T315I mutation is disease phase dependent. *Hematol. Oncol.* **2009,** 27, 190-197.

95. Kim, W. S.; Kim, D.; Kim, D. W.; Kweon, I. Y.; Kim, S. H.; Goh, H. G.; Park, S. H.; Lee, J. Dynamic change of T315I BCR-ABL kinase domain mutation in Korean chronic myeloid leukaemia patients during treatment with Abl tyrosine kinase inhibitors. *Hematol. Oncol.* **2010,** 28, 82-88.

96. Tokarski, J. S.; Newitt, J. A.; Chang, C. Y. J.; Cheng, J. D.; Wittekind, M.; Kiefer, S. E.; Kish, K.; Lee, F. Y. F.; Borzillerri, R.; Lombardo, L. J.; Xie, D.; Zhang, Y.; Klei, H. E. The structure of dasatinib (BMS-354825) bound to activated ABL kinase domain elucidates its inhibitory activity against imatinib-resistant ABL mutants. *Cancer Res.* **2006,** 66, 5790-5797.

97. Reddy, E. P.; Aggarwal, A. K. The ins and outs of Bcr-Abl inhibition. *Genes & Cancer* **2012,** 3, 447-454.

98. O'Hare, T.; Shakespeare, W. C.; Zhu, X.; Eide, C. A.; Rivera, V. M.; Wang, F.; Adrian, L. T.; Zhou, T.; Huang, W.-S.; Xu, Q.; III, C. A. M.; Tyner, J. W.; Loriaux, M. M.; Corbin, A. S.; Wardwell, S.; Ning, Y.; Keats, J. A.; Wang, Y.; Sundaramoorthi, R.; Deiniger, M. W. N.; Druker, B. J.; Clackson, T. AP24534, a pan-BCR-ABL inhibitor for chronic myeloid leukemia, potently inhibits the T315I mutant and overcomes mutation-based resistance. *Cancer Cell* **2009,** 16, 401-412.

99. Jabbour, E.; Kantarjian, H. Chronic myeloid leukemia: 2020 update on diagnosis, therapy and monitoring. *Am. J. Hematol.* **2020,** 95, 691–709.

100. Shah, N. P. Medical management of CML. *Hematology Am. Soc. Hematol. Educ. Program* **2007,** 2007, 371-375.

101. Darkow, T.; Henk, H. J.; Thomas, S. K.; Feng, W.; Baladi, J.-F.; Goldberg, G. A.; Hatfield, A.; Cortes, J. Treatment interruptions and non-adherence with imatinib and associated healthcare costs: a retrospective analysis among managed care patients with chronic myelogenous leukaemia. *Pharmacoeconomics* **2007,** 25, 481-496.

102. Sundaram, D. N. M.; Jiang, X.; Brandwein, J. M.; Valencia-Serna, J.; Remant, K. C.; Uludag, H. Current outlook on drug resistance in chronic myeloid leukemia (CML) and potential therapeutic options. *Drug Discov. Today* **2019,** 24, 1355-1369.

103. Lussana, F.; Intermesoli, T.; Stefanoni, P.; Rambaldi, A. *Mechanisms of resistance to targeted therapies in chronic myeloid leukemia*. Springer, Cham: 2018; Vol. 249.

104. Kimura, S.; Ando, T.; Kojima, K. BCR-ABL point mutations and TKI treatment in CML patients. *J. Hematol. Transfus.* **2014,** 2, 1022.

105. Gorre, M. E.; Mohammed, M.; Ellwood, K.; Hsu, N.; Paquette, R.; Rao, P. N.; Sawyers, C. L. Clinical resistance to STI-571 cancer therapy caused by BCR-ABL gene mutation or amplification. *Science* **2001,** 293, 876–880.

106. Wang, Y.; Cai, D.; Brendel, C.; Barett, C.; Erben, P.; Manley, P. W.; Hochhaus, A.; Neubauer, A.; Burchert, A. Adaptive secretion of granulocyte-macrophage colony stimulating factor (GM-CSF) mediates imatinib and nilotinib resistance in BCR/ABL+ progenitors via JAK-2/STAT-5 pathway activation. . *Blood* **2007,** 109, 2147–2155.

107. Ma, L.; Shan, Y.; Bai, R.; Xue, L.; Eide, C. A.; Ou, J.; Zhu, L. J.; Hutchinson, L.; Cerny, J.; Khoury, H. J.; Sheng, Z.; Druker, B. J.; Li, S.; Green, M. R. A therapeutically targetable mechanism of BCR-ABL–independent imatinib resistance in chronic myeloid leukemia. *Sci. Transl. Med.* **2014,** 6, 252ra121.

108. Wagle, M.; Eiring, A. M.; Wongchenko, M.; Lu, S.; Guan, Y.; Wang, Y.; Lackner, M.; Amler, L.; Hampton, G.; Deininger, M. W.; O'Hare, T.; Yan, Y. A role for FOXO1 in BCR–ABL1-independent tyrosine kinase inhibitor resistance in chronic myeloid leukemia. *Leukemia* **2016,** 30, 1493–1501.

109. Mitchell, R.; Hopcroft, L. E. M.; Baquero, P.; Allan, E. K.; Hewit, K.; James, D.; Hamilton, G.; Mukhopadhyay, A.; O'Prey, J.; Hair, A.; Melo, J. V.; Chan, E.; Ryan, K. M.; Maguer-Satta, V.; Druker, J. B.; Clark, R. E.; Mitra, S.; Herzyk, P.; Nicolini, F. E.; Salomoni, P.; Shanks, E.; Calabretta, B.; Holyoake, T. L.; Helgason, V. G. Targeting BCR-ABL-independent TKI resistance in chronic myeloid leukemia by mTOR and autophagy inhibition. *J. Natl. Cancer Inst.* **2018,** 110, 467-478.

110. Burchert, A.; Wang, Y.; Cai, D.; Bubnoff, N. v.; Paschka, P.; Müller-Brüsselbach, S.; Ottmann, O. G.; Duyster, J.; Hochhaus, A.; Neubauer, A. Compensatory PI3-kinase/Akt/mTor activation regulates imatinib resistance development. *Leukemia* **2005,** 19, 1774–1782.

111. White, D. L.; Saunders, V. A.; Dang, P.; Engler, J.; Hughes, T. P. OCT-1 activity measurement provides a superior imatinib response predictor than screening for single-nucleotide polymorphisms of OCT-1. *Leukemia* **2010,** 24, 1962–1965.

112. Dulucq, S.; Bouchet, S.; Turcq, B.; Lippert, E.; Etienne, G.; Reiffers, J.; Molimard, M.; Krajinovic, M.; Mahon, F.-X. Multidrug resistance gene (MDR1)

polymorphisms are associated with major molecular responses to standard-dose imatinib in chronic myeloid leukemia. *Blood* **2008,** 112, 2024–2027.

113. Eadie, L. N.; Hughes, T. P.; White, D. L. Patients with low OCT-1 activity and high ABCB1 fold rise have poor long-term outcomes in response to tyrosine kinase inhibitor therapy. *Leukemia* **2018,** 32, 2288–2291.

114. Hamilton, A.; Helgason, G. V.; Schemionek, M.; Zhang, B.; Myssina, S.; Allan, E. K.; Nicolini, F. E.; Müller-Tidow, C.; Bhatia, R.; Brunton, V. G.; Koschmieder, S.; Holyoake, T. L. Chronic myeloid leukemia stem cells are not dependent on Bcr-Abl kinase activity for their survival. *Blood* **2012,** 119, 1501–1510.

115. Jiang, X.; Zhao, Y.; Smith, C.; Gasparetto, M.; Turhan, A.; Eaves, A.; Eaves, C. Chronic myeloid leukemia stem cells possess multiple unique features of resistance to BCR-ABL targeted therapies. *Leukemia* **2007,** 21, 926–935.

116. Mizushima, N. Autophagy: process and function. *Genes Devel.* **2007,** 21, 2861–2873.

117. Rebecca, V. W.; K.Amaravadi, R. Emerging strategies to effectively target autophagy in cancer. *Oncogene* **2016,** 35, 1-11.

118. Helgason, G. V.; Karvela, M.; Holyoake, T. L. Kill one bird with two stones: potential efficacy of BCR-ABL and autophagy inhibition in CML. *Blood* **2011,** 118, 2035–2043.

119. Dikic, I.; Elazar, Z. Mechanism and medical implications of mammalian autophagy. *Nat. Rev. Mol. Cell Biol.* **2018,** 19, 349-364.

120. Nah, J.; Yuan, J.; Jung, Y.-K. Autophagy in neurodegenerative diseases: From mechanism to therapeutic approach. *Mol. Cells* **2015,** 38, 381-389.

121. Gomes, L. C.; Dikic, I. Autophagy in Antimicrobial Immunity. *Mol. Cell* **2014,** 54, 224–233.

122. Liang, X. H.; Jackson, S.; Seaman, M.; Brown, K.; Kempkes, B.; Hibshoosh, H.; Levine, B. Induction of autophagy and inhibition of tumorigenesis by beclin 1. *Nature* **1999,** 402, 672–676.

123. Kimmelman, A. C.; White, E. Autophagy and tumor metabolism. *Cell Metab.* **2017,** 25, 1037–1043.

124. Zou, Z.; Yuan, Z.; Zhang, Q.; Long, Z.; Chen, J.; Tang, Z.; Zhu, Y.; Chen, S.; Xu, J.; Yan, M.; Wang, J.; Liu, Q. Aurora kinase A inhibition-induced autophagy triggers drug resistance in breast cancer cells. *Autophagy* **2012,** 8, 1798–1810.

125. Towers, C. G.; Thorburn, A. Therapeutic targeting of autophagy. *EBioMedicine* **2016,** 14, 15–23.

126. Eng, C. H.; Wang, Z.; Tkach, D.; Toral-Barza, L.; Ugwonali, S.; Liu, S.; Fitzgerald, S. L.; George, E.; Frias, E.; Cochran, N.; de Jesus, R.; Mcallister, G.; Hoffman, G. R.; Bray, K.; Lemon, L.; Lucas, J.; Fantin, V. R.; Abraham, R. T.; Murphy, L. O.; Nyfeler, B. Macroautophagy is dispensable for growth of KRAS mutant tumors and chloroquine efficacy. *Proc. Natl. Acad. Sci.* **2016,** 113, 182–187.

127. Piao, S.; Amaravadi, R. K. Targeting the lysosome in cancer. *Ann. N.Y. Acad. Sci.* **2016,** 1371, 45-54.

128. Crowley, L. C.; Elzinga, B. M.; O'Sullivan, G. C.; McKenna, S. L. Autophagy induction by Bcr-Abl-expressing cells facilitates their recovery from a targeted or nontargeted treatment. *Am. J. Hematol.* **2011,** 86, 38–47.

129. Bellodi, C.; Lidonnici, M. R.; Hamilton, A.; Helgason, G. V.; Soliera, A. R.; Ronchetti, M.; Galavotti, S.; Young, K. W.; Selmi, T.; Yacobi, R.; Etten, R. A. V.; Donato, N.; Hunter, A.; Dinsdale, D.; Tirrò, E.; Vigneri, P.; Nicotera, P.; Dyer, M. J.; Holyoake, T.; Salomoni, P.; Calabretta, B. Targeting autophagy potentiates tyrosine kinase inhibitor–induced cell death in Philadelphia chromosome–positive cells, including primary CML stem cells. *J. Clin. Invest.* **2009,** 119, 1109–1123.

130. Horne, G. A.; Stobo, J.; Kelly, C.; Mukhopadhyay, A.; Latif, A. L.; Dixon-Hughes, J.; McMahon, L.; Cony-Makhoul, P.; Byrne, J.; Smith, G.; Koschmieder, S.; BrÜmmendorf, T. H.; Schafhausen, P.; Gallipoli, P.; Thomson, F.; Cong, W.; Clark, R. E.; Milojkovic, D.; Helgason, G. V.; Foroni, L.; Nicolini, F. E.; Holyoake, T. L.; Copland, M. A randomised phase II trial of hydroxychloroquine and imatinib versus imatinib alone for patients with chronic myeloid leukaemia in major cytogenetic response with residual disease. *Leukemia* **2020,** 34, 1775–1786.

131. Zeng, X.; Zhao, H.; Li, Y.; Fan, J.; Sun, Y.; Wang, S.; Wang, Z.; Song, P.; Ju, D. Targeting Hedgehog signaling pathway and autophagy overcomes drug resistance of BCR-ABL positive chronic myeloid leukemia. *Autophagy* **2015,** 11, 355–372.

132. Duve, C. d.; Pressman, B. C.; Gianetto, R.; Wattiaux, R.; Appelmans, F. Tissue fractionation studies. 6. Intracellular distribution patterns of enzymes in rat-liver tissue. *Biochem. J.* **1955,** 60, 604–617.

133. Saftig, P.; Klumperman, J. Lysosome biogenesis and lysosomal membrane proteins: trafficking meets function. *Nat. Rev. Mol. Cell Biol.* **2009,** 10, 623-635.

134. Perera, R. M.; Zoncu, R. The lysosome as a regulatory hub. *Annu. Rev. Cell Dev. Biol.* **2016,** 32, 223-253.

135. Vacca, F.; Scott, C.; Gruenberg, J. The late endosome. In *Encyclopedia of Cell Biology*, Bradshaw, R. A.; Stahl, P. D., Eds. Elsevier: USA, 2016; Vol. 2, pp 201-210.

136. Bajaj, L.; Lotfi, P.; Pal, R.; Ronza, A. d.; Sharma, J.; Sardiello, M. Lysosome biogenesis in health and disease. *J. Neurochem.* **2019,** 148, 573-589.

137. Sardiello, M.; Palmieri, M.; Ronza, A. d.; Medina, D. L.; Valenza, M.; Gennarino, V. A.; Malta, C. D.; Donaudy, F.; Embrione, V.; Polishchuk, R. S.; Banfi, S.; Parenti, G.; Cattaneo, E.; Ballabio, A. A gene network regulating lysosomal biogenesis and function. *Science* **2009,** 325, 473-476.

138. Kallunki, T.; Olsen, O. D.; Jäättela, M. Cancer-associated lysosomal changes: friends or foes? *Oncogene* **2013,** 32, 1995-2004.

139. Colombo, F.; Trombetta, E.; Cetrangolo, P.; Maggioni, M.; Razini, P.; Santis, F. D.; Torrente, Y.; Prati, D.; Torresani, E.; Porretti, L. Giant lysosomes as a chemotherapy resistance mechanism in hepatocellular carcinoma cells. *PLoS One* **2014,** 9, e114787.

140. Sukhai, M. A.; Prabha, S.; Hurren, R.; Rutledge, A. C.; Lee, A. Y.; Sriskanthadevan, S.; Sun, H.; Wang, X.; Skrtic, M.; Seneviratne, A.; Cusimano, M.; Jhas, B.; Gronda, M.; MacLean, N.; Cho, E. E.; Spagnuolo, P. A.; Sharmeen, S.; Gebbia, M.; Urbanus, M.; Eppert, K.; Dissanayake, D.; Jonet, A.; Dassonville-Klimpt, A.; Li, X.; Datti, A.; Ohashi, P. S.; Wrana, J.; Rogers, I.; Sonnet, P.; Ellis, W. Y.; Corey, S. J.; Eaves, C.; Minden, M. D.; Wang, J. C. Y.; Dick, J. E.; Nislow, C.; Giaever, G.; Schimmer, A. D. Lysosomal disruption preferentially targets acute myeloid leukemia cells and progenitors. *J. Clin. Invest.* **2013,** 123.

141. Yi, H. L.; Than, H.; Sng, C.; Cheong, M. A.; Chuah, C.; Xiang, W. Lysosome inhibition by mefloquine preferentially enhances the cytotoxic effects of tyrosine kinase inhibitors in blast phase chronic myeloid leukemia. *Transl. Oncol.* **2019,** 12, 1221–1228.

142. Fennema, E.; Rivron, N.; Rouwkena, J.; Blitterswijk, C. v.; Boer, J. D. Spheroid culture as a tool for creating 3D complex tissues. *Trends Biotechnol.* **2013,** 31, 108-115.

143. Chang, R.-Z. L. H.-Y. Recent advances in three-dimensional multicellular spheroid culture for biomedical research. *Biotechnol. J.* **2008,** 3, 1172–1184.

144. Moroni, L.; Wijn, J. R. d.; Blitterswijk, C. A. v. Integrating novel technologies to fabricate smart scaffolds. *J. Biomater. Sci. Polym. Ed.* **2008,** 19, 543–572.

145. Chaudhuri, O. Viscoelastic hydrogels for 3D cell culture. *Biomat. Sci.* **2017,** 5, 1480-1490.

146. Klopp, A. H.; Lacerda, L.; Gupta, A.; Debeb, B. G.; Solley, T.; Li, L.; Spaeth, E.; Xu, W.; Zhang, X.; Lewis, M. T.; Reuben, J. M.; Krishnamurthy, S.; Ferrari, M.; Gaspar, R.; Buchholz, T. A.; Cristofanilli, M.; Marini, F.; Andreeff, M.; Woodward, W. A. Mesenchymal stem cells promote mammosphere formation and decrease E-cadherin in normal and malignant breast cells. *PLoS ONE* **2010,** 5, e12180.

147. Greco, K. V.; Iqbal, A. J.; Rattazzi, L.; Nalesso, G.; Moradi-Bidhendi, N.; Moore, A. R.; Goldring, M. B.; Dell'Accio, F.; Perretti, M. High density micromass cultures of a human chondrocyte cell line: A reliable assay system to reveal the modulatory functions of pharmacological agents. *Biochem. Pharmacol.* **2011,** 82, 1919–1929.

148. Kenny, P. A.; Lee, G. Y.; Myers, C. A.; Neve, R. M.; Semeiks, J. R.; Spellman, P. T.; Lorenz, K.; Lee, E. H.; Barcellos-Hoff, M. H.; Petersen, O. W.; Gray, J. W.; Bissell, M. J. The morphologies of breast cancer cell lines in three-dimensional assays correlate with their profiles of gene expression. *Mol. Oncol.* **2007,** 1, 84-96.

149. Mehta, G.; Hsiao, A. Y.; Ingram, M.; Luker, G. D.; Takayama, S. Opportunities and challenges for use of tumor spheroids as models to test drug delivery and efficacy. *J. Control. Release* **2012,** 164, 192–204.

150. Nath, S.; Devi, G. R. Three-dimensional culture systems in cancer research: Focus on tumor spheroid model. *Pharmacol. Therapeut.* **2016,** 163, 94-108.

151. Alvarez-Pérez, J.; P. Ballesteros, P.; Cerdán, S. Microscopic images of intraspheroidal pH by ^{1}H magnetic resonance chemical shift imaging of pH sensitive indicators. *Magma* **2005,** 18, 293–301.

152. Hirschhaeuser, F.; Menne, H.; Dittfeld, C.; West, J.; Mueller-Klieser, W.; Kunz-Schughart, L. A. Multicellular tumor spheroids: An underestimated tool is catching up again. *J. Biotechnol.* **2010,** 148, 3-15.

153. Li, H.; Hummon, A. B. Imaging mass spectrometry of three-dimensional cell culture systems. *Anal. Chem.* **2011,** 83, 8794–8801.

154. Langhans, S. A. Three-dimensional in vitro cell culture models in drug discovery and drug repositioning. *Front. Pharmacol.* **2018,** 9, 1-14.

155. Sant, S.; Johnston, P. A. The production of 3D tumor spheroids for cancer drug discovery. *Drug Discov. Today Technol.* **2017,** 23, 27-36.

156. Friedrich, J.; Seidel, C.; Ebner, R.; Kunz-Schughart, L. A. Spheroid-based drug screen: considerations and practical approach. *Nat. Protoc.* **2009,** 4, 309.

157. Ivascu, A.; Kubbies, M. Rapid generation of single-tumor spheroids for high-throughput cell function and toxicity analysis. *J. Biomol. Screen.* **2006,** 11, 922-932.

158. Rotema, A.; Janzer, A.; Izar, B.; Ji, Z.; Doench, J. G.; Garraway, L. A.; Struhl, K. Alternative to the soft-agar assay that permits high-throughput drug and genetic screens for cellular transformation. *Proc. Natl. Acad. Sci. U.S.A.* **2015,** 112, 5708-5713.

159. Madoux, F.; Tanner, A.; Vessels, M.; Willetts, L.; Hou, S.; Scampavia, L.; Spicer, T. P. A 1536-well 3D viability assay to assess the cytotoxic effect of drugs on spheroids. *SLAS Discov.* **2017,** 22, 516–524.

160. Palacios, R.; Steinmetz, M. IL3-dependent mouse clones that express B-220 surface antigen, contain Ig genes in germ-line configuration, and generate B Lymphocytes in vivo. *Cell* **1985,** 41, 727-734.

161. Daley, G. Q.; Baltimore, D. Transformation of an interleukin 3-dependent hematopoietic cell line by the chronic myelogenous leukemia-specific P210bcr/abl protein. . *Proc. Natl. Acad. Sci. USA* **1988,** 85, 9312-9316.

162. Leibovitz, A.; Stlnson, J. C.; 3rd, W. B. M.; McCoy, C. E.; Mazur, K. C.; Mabry, N. D. Classification of human colorectal adenocarcinoma cell lines. *Cancer Res.* **1976,** 36, 4562-4569.

163. Holliday, D. L.; Speirs, V. Choosing the right cell line for breast cancer research. *Breast Cancer Res.* **2011,** 13, 215.

164. Pulay, P. Improved SCF convergence acceleration. *J. Comp. Chem.* **1982,** 3, 556-560.

165. Laury, M. L.; Carlson, J. M.; Wilson, A. K. Vibrational frequency scale factors for density functional theory and the polarization consistent basis sets. *J. Comp. Chem.* **2012,** 33, 2380–2387.

166. Schindelin, J.; Arganda-Carreras, I.; E. Frise, E.; Kaynig, V.; Longair, M.; Pietzsch, T.; Preibisch, S.; Rueden, C.; Saalfeld, S.; Schmid, B.; Tinevez, J. Y.; White, D. J.; Hartenstein, V.; Eliceiri, K.; Tomancak, T.; Cardona, A. Fiji: an open-source platform for biological-image analysis. *Nat. Methods* **2012,** 9, 676–682.

167. Carpenter, A. E.; Jones, T. R.; Lamprecht, M. R.; Clarke, C.; Kang, I. H.; Friman, O.; Guertin, D. A.; Chang, J. H.; Lindquist, R. A.; Moffat, J.; Golland, P.; Sabatini, D. M. CellProfiler: image analysis software for identifying and quantifying cell phenotypes. *Genome Biol.* **2006,** 7, R100.

168. El-Mashtoly, S. F.; Petersen, D.; Yosef, H. K.; Mosig, A.; Reinacher-Schick, A.; Kotting, C.; Gerwert, K. Label-free imaging of drug distribution and metabolism in colon cancer cells by Raman microscopy. *Analyst* **2014,** 139, 1155-61.

169. Aljakouch, K.; Lechtonen, T.; Yosef, H. K.; Hammoud, M. K.; Alsaidi, W.; Kotting, C.; Mugge, C.; Kourist, R.; El-Mashtoly, S. F.; Gerwert, K. Raman microspectroscopic evidence for the metabolism of a tyrosine kinase inhibitor, neratinib, in cancer cells *Angew. Chem. Int. e* **2018,** 57, 7250-7254.

170. Fu, D.; Zhou, J.; Zhu, W. S.; Manley, P. W.; Wang, Y. K.; Hood, T.; Wylie, A.; Xie, X. S. Imaging the intracellular distribution of tyrosine kinase inhibitors in living

cells with quantitative hyperspectral stimulated Raman scattering. *Nat Chem* **2014,** 6, 614-22.

171. Yosef, H. K.; Frick, T.; Hammoud, M. K.; Maghnouj, A.; Hahn, S.; Gerwert, K.; El-Mashtoly, S. F. Exploring the efficacy and cellular uptake of sorafenib in colon cancer cells by Raman micro-spectroscopy. *Analyst* **2018,** 143, 6069-6078.

172. Lee, M.; Downes, A.; Chau, Y.-Y.; Serrels, B.; Hastie, N.; Elfick, A.; Brunton, V. G.; Frame, M. C.; Serrels, A. In vivo imaging of the tumor and its associated microenvironment using combined CARS / 2-photon microscopy. *IntraVital* **2015,** 4.

173. Sepp, K.; Lee, M.; Bluntzer, M. T. J.; Helgason, G. V.; Hulme, A. N.; Brunton, V. G. Utilising stimulated Raman scattering microscopy to study intracellular distribution of label-free ponatinib in live cells. *J. Med. Chem.* **2020,** 63, 2028-2034.

174. Shawver, L. K.; Slamon, D.; Ullrich, A. Smart drugs:Tyrosine kinase inhibitors in cancer therapy. *Cancer Cell* **2002,** 1, 117-123.

175. Roskoski, R. Properties of FDA-approved small molecule protein kinase inhibitors: A 2020 update. *Pharmacol. Res.* **2020,** 152, 104609.

176. Cohen, P. Protein kinases — the major drug targets of the twenty-first century? *Nat. Rev. Drug Discov.* **2002,** 1, 309-315.

177. Kinch, M. S. An analysis of FDA-approved drugs for oncology. *Drug Discov Today* **2014,** 19, 1831-5.

178. Carles, F.; Bourg, S.; Meyer, C.; Bonnet, P. PKIDB: A curated, annotated and updated database of protein kinase inhibitors in clinical trials. *Molecules* **2018,** 23, 908.

179. Johnson, J. R.; Cohen, M.; Sridhara, R.; Chen, Y. F.; Williams, G. M.; Duan, J.; Gobburu, J.; Booth, B.; Benson, K.; Leighton, J.; Hsieh, L. S.; Chidambaram, N.; Zimmerman, P.; Pazdur, R. Approval summary for erlotinib for treatment of patients with locally advanced or metastatic non-small cell lung cancer after failure of at least one prior chemotherapy regimen. *Clin Cancer Res* **2005,** 11, 6414-21.

180. M. Hidalgo; L. L. Siu; J. Nemunaitis; J. Rizzo; L. A. Hammond; C. Takimoto; S. G. Eckhardt; A. Tolcher; C. D. Britten; L. Denis; K. Ferrante; D. D. Von Hoff; S. Silberman; Rowinsky, E. K. Phase I and Pharmacologic Study of OSI-774, an Epidermal Growth Factor Receptor Tyrosine Kinase Inhibitor, in Patients With Advanced Solid Malignancies. *J Clin Oncol* **2001,** 19, 3267-3279.

181. Masters, A. R.; Sweeney, C. J.; Jones, D. R. The quantification of erlotinib (OSI-774) and OSI-420 in human plasma by liquid chromatography-tandem mass spectrometry. *J Chromatogr B Analyt Technol Biomed Life Sci* **2007,** 848, 379-83.

182. Morosi, L.; Zucchetti, M.; D'Incalci, M.; Davoli, E. Imaging mass spectrometry: challenges in visualization of drug distribution in solid tumors. *Curr. Opin. Pharmacol.* **2013,** 13, 807–812.

183. Nerini, I. F.; Morosi, L.; Zucchetti, M.; Ballerini, A.; Giavazzi, R.; D'Incalci, M. Intratumor heterogeneity and its impact on drug distribution and sensitivity. *Clin. Pharmacol. & Therapeut.* **2014,** 96, 224-238.

184. Larkin, J. M. G.; Eisen, T. Renal cell carcinoma and the use of sorafenib. *Clin. Risk Manag.* **2006,** 2, 87-98.

185. Kane, R. C.; Farrell, A. T.; Madabushi, R.; Booth, B.; Chattopadhyay, S.; Sridhara, R.; Justice, R.; Pazdur, R. Sorafenib for the treatment of unresectable hepatocellular carcinoma. *Oncologist* **2009,** 14, 95-100.

186. Sun, C.; Wang, L.; Huang, S.; Heynen, G. J. J. E.; Prahallad, A.; Robert, C.; Haanen, J.; Blank, C.; Wesseling, J.; Willems, S. M.; Zecchin, D.; Hobor, S.; Bajpe, P. K.; Lieftink, C.; Mateus, C.; Vagner, S.; Grernrum, W.; Hofland, I.; Schlicker, A.; Wessels, L. F. A.; Beijersbergen, R. L.; Bardelli, A.; Nicolantonio, F. D.; Eggermont, A. M. M.; Bernards, R. Reversible and adaptive resistance to BRAF(V600E) inhibition in melanoma. *Nature* **2014,** 508, 118-122.

187. Hsu, H.-C.; Thiam, T. K.; Lu, Y.-J.; Yeh, C. Y.; Tsai, W.-S.; You, J. F.; Hung, H. Y.; Tsai, C.-N.; Hsu, A.; Chen, H.-C.; Chen, S.-J.; Yang, T.-S. Mutations of KRAS/NRAS/BRAF predict cetuximab resistance in metastatic colorectal cancer patients. *Oncotarget* **2016,** 7, 22257-22270.

188. Ohashi, K.; Sequist, L. V.; Arcila, M. E.; T., M.; Chmielecki, J.; Lin, Y.-L.; Pan, Y.; Wang, L.; Stanchina, E. D.; Shien, K.; Aoe, K.; Toyooka, S.; Kiura, K.; Fernandez-Cuesta, L.; Fidias, P.; Yang, J. C.-H.; Miller, V. A.; Riely, G. J.; Kris, M. G.; Engelman, J. A.; Vnencak-Jones, C. L.; Dias-Santagata, D.; Ladanyi, M.; Pao, W. Lung cancers with acquired resistance to EGFR inhibitors occasionally harbor BRAF gene mutations but lack mutations in KRAS, NRAS, or MEK1. *Proc. Natl. Acad. Sci. USA* **2012,** 109, E2127–E2133.

189. Maurer, G.; Tarkowski, B.; Baccarini, M. Raf kinases in cancer–roles and therapeutic opportunities. *Oncogene* **2011,** 30, 3477-3488.

190. Vaishampayan, U. N.; Burger, A. M.; Sausville, E. A.; Heilbrun, L. K.; Li, J.; Horiba, N.; Egorin, M. J.; Ivy, P.; Pacey, S.; Lorusso, P. M. Safety, efficacy, pharmacokinetics and pharmacodynamics of the combination of sorafenib and tanespimycin. *Clin. Cancer Res.* **2010,** 16, 3795-3804.

191. Gozgit, J. M.; Wong, M. J.; Moran, L.; Wardwell, S.; Mohemmad, Q. K.; Narasimhan, N. I.; Shakespeare, W. C.; Wang, F.; Clackson, T.; Rivera, V. M. Ponatinib (AP24534), a multitargeted pan-FGFR inhibitor with activity in multiple FGFR-amplified or mutated cancer models. *Mol. Cancer Ther.* **2012,** 11, 690-699.

192. Larson, R. A.; Druker, B. J.; Guilhot, F.; O'Brien, S. G.; Riviere, G. J.; Krahnke, T.; Gathmann, I.; Wang, Y. Imatinib pharmacokinetics and its correlation with response and safety in chronic-phase chronic myeloid leukemia: a subanalysis of the IRIS study. . *Blood* **2008,** 111, 4022-4028.

193. Deininger, M. D. Nilotinib. *Clin. Cancer. Res.* **2008,** 14, 4027-4031.

194. Zhang, Z.; Tang, W. Drug metabolism in drug discovery and development. . *Acta Pharm. Sin. B.* **2018,** 8, 721-732.

195. Isin, E. M.; Guengerich, F. P. Complex reactions catalyzed by cytochrome P450 enzymes. *Biochim. Biophys. Acta* **2007,** 1770, 314-329.

196. Bertz, J. R.; Granneman, G. R. Use of in vitro and in vivo data to estimate the likelihood of metabolic pharmacokinetic interactions. *Clin. Pharmacokinet.* **1997,** 32, 210-258.

197. Teo, Y. L.; Ho, H. K.; Chan, A. Metabolism-related pharmacokinetic drug−drug interactions with tyrosine kinase inhibitors: current understanding, challenges and recommendations. *Br. J. Clin. Pharmacol.* **2015,** 79, 241-253.

198. Lin, D.; Kostov, R.; Huang, J. T.-J.; Henderson, C. J.; Wolf, C. R. Novel pathways of ponatinib disposition catalyzed by CYP1A1 involving generation of potentially toxic metabolites. *J. Pharmacol. Exp. Ther.* **2017,** 363, 12-19.

199. Narasimhan, N. I.; Dorer, D. J.; Niland, K.; Haluska, F.; Sonnichsen, D. Effects of ketoconazole on the pharmacokinetics of ponatinib in healthy subjects. *J. Clin. Pharmacol.* **2013,** 53, 974-981.

200. Attwa, M. W.; Kadi, A. A.; Darwish, H. W.; Amer, S. M.; Alrabiah, H. L. C-ESI-MS/MS identification and characterization of ponatinib in vivo phase I and phase II metabolites. *Clin. Chim. Acta.* **2018,** 485, 144-151.

201. Kadi, A. A.; Darwish, H. W.; Attwa, M. W.; Amer, S. M. Detection and characterization of ponatinib reactive metabolites by liquid chromatography tandem mass spectrometry and elucidation of bioactivation pathways. *RSC Adv.* **2016,** 6, 72575-72585.

202. Zhao, Z.; Shen, Y.; Hu, F.; Min, W. Applications of vibrational tags in biological imaging by Raman microscopy. *Analyst* **2017,** 142, 4018-4029.

203. Klein, T.; Vajpai, N.; Phillips, J. J.; Davies, G.; Holdgate, G. A.; Phillips, C.; Tucker, J. A.; Norman, R. A.; Scott, A. D.; Higazi, D. R.; Lowe, D.; Thompson, G. S.; Breeze, A. L. Structural and dynamic insights into the energetics of activation loop rearrangement in FGFR1 kinase. *Nat. Commun.* **2015,** 6, 7877.

204. Ye, Y. E.; Woodward, C. N.; Narasimhan, I. N. Absorption, metabolism, and excretion of [^{14}C]ponatinib after a single oral dose in humans. *Cancer Chemother. Pharmacol.* **2017,** 79, 507-518.

205. Mathur, A.; Ware, C.; Davis, L.; Gazdar, A.; Pan, B.-S.; Lutterbach, B. FGFR2 is amplified in the NCI-H716 colorectal cancer cell line and is required for growth and survival. *PLoS One* **2014,** 9, e98515.

206. Hung, J.-S.; Huang, J.; Lin, Y.-C.; Huang, M.-J.; Lee, P.-H.; Lai, H.-S.; Liang, J.-T.; Huang, M.-C. C1GALT1 overexpression promotes the invasive behavior of colon cancer cells through modifying O-glycosylation of FGFR2. *Oncotarget* **2014,** 5, 2096-2106.

207. Tan, F. H.; Putoczki, T. L.; Stylli, S. S.; Luwor, R. B. Ponatinib: a novel multi-tyrosine kinase inhibitor against human malignancies. *OncoTargets Ther.* **2019,** 12, 635-644.

208. Zhang, D.; Slipchenko, M. N.; Leaird, D. E.; Weiner, A. M.; Cheng, J.-X. Spectrally modulated stimulated Raman scattering imaging with an angle-to-wavelength pulse shaper *Opt. Express* **2013,** 21, 13864–13874.

209. Eltoum, I.; Fredenburgh, J.; Grizzle, W. E. Advanced concepts in fixation: 1. Effects of fixation on immunohistochemistry, reversibility of fixation and recovery of proteins, nucleic acids, and other molecules from fixed and processed tissues. 2. Developmental methods of fixation. . *J. Histotechnol.* **2001,** 24, 201-210.

210. Eltoum, I.; Fredenburgh, J.; Myers, R. B.; Grizzle, W. E. Introduction to the theory and practice of fixation of tissues. *J. Histotechnol.* **2001,** 24, 173-190.

211. Lu, L.; Saunders, V. A.; Leclercq, T. M.; Hughes, T. P.; White, D. L. Ponatinib is not transported by ABCB1, ABCG2 or OCT-1 in CML cells. *Leukemia* **2015,** 29, 1792-1794.

212. Hu, S.; Chen, Z.; Franke, R.; Orwick, S.; Zhao, M.; Rudek, M. A.; Sparreboom, A.; Baker, S. D. Interaction of the multikinase inhibitors sorafenib and sunitinib with solute carriers and ATP-binding cassette transporters. *Clin. Cancer Res.* **2009,** 15, 6062–6069.

213. Thomas, J.; Wang, L.; Clark, R. E.; Pirmohamed, M. Active transport of imatinib into and out of cells: implications for drug resistance. *Blood* **2004,** 104, 3739–3745.

214. Burger, H.; Tol, H.; Brok, M.; Wiemer, E. A. C.; de Bruijn, E. A.; Guetens, G.; de Boeck, G.; Sparreboom, A.; Verweij, J.; Nooter, K. Chronic imatinib mesylate exposure leads to reduced intracellular drug accumulation by induction of the ABCG2 (BCRP) and ABCB1 (MDR1) drug transport pumps. *Cancer Biol. Ther.* **2005,** 4, 747–752.

215. Hiwase, D. K.; Saunders, V.; Hewett, D.; Frede, A.; Zrim, S.; Dang, P.; Eadie, L.; To, L. B.; Melo, J.; Kumar, S.; Hughes, T. P.; White, D. L. Dasatinib cellular uptake and efflux in chronic myeloid leukemia cells: therapeutic implications. *Clin. Cancer Res.* **2008,** 14, 3881–3888.

216. Giannoudis, A.; Davies, A.; Lucas, C. M.; Harris, R. J.; Pirmohamed, M.; Clark, R. E. Effective dasatinib uptake may occur without human organic cation transporter 1 (hOCT1): implications for the treatment of imatinib-resistant chronic myeloid leukemia. *Blood* **2008,** 112, 3348-3354.

217. Giordano, S.; Morosi, L.; Veglianese, P.; Licandro, S. A.; Frapolli, R.; Zucchetti, M.; Cappelletti, G.; Falciola, L.; Pifferi, V.; Visentin, S.; D'Incalci, M.; Davoli, E. 3D Mass Spectrometry Imaging reveals a Very Heterogeneous drug distribution in tumors. *Sci. Rep.* **2016,** 6, 37027.

218. Palucka, K. A.; Knaust, E.; Xu, D.; Macnamara, B.; Porwit-MacDonald, A.; Gruber, A.; Peterson, C.; Björkholm, M.; Pisa, P. Intraclonal heterogeneity in the in vitro daunorubicin-induced apoptosis in acute myeloid leukemia. *Leuk. Lymphoma* **1999,** 32, 309-316.

219. Duve, C. d.; Barsy, T. d.; Poole, B.; A. Trouet; Tulkens, P.; Hoof, F. V. Lysosomotropic agents. *Biochem. Pharmacol.* **1974,** 23, 2495-2531.

220. Duvvuri, M.; Konkar, S.; Funk, R. S.; Krise, J. M.; Krise, J. P. A chemical strategy to manipulate the intracellular localization of drugs in resistant cancer cells. *Biochemistry* **2005,** 44, 15743-15749.

221. Duvvuri, M.; Gong, Y.; Chatterji, D.; Krise, J. P. Weak base permeability characteristics influence the intracellular sequestration site in the multidrug-resistant human leukemic cell line HL-60. *J. Biol. Chem.* **2004,** 279, 32367–32372.

222. Dasatinib (Sprycel), Application number: 21-986 & 22-072. https://www.accessdata.fda.gov/drugsatfda_docs/nda/2006/021986s000_Sprycel__ClinPharmR.pdf (05.06.2020).

223. O'Brien, Z.; Moghaddam, M. F. A systematic analysis of physicochemical and ADME properties of all small molecule kinase inhibitors approved by US FDA from January 2001 to October 2015. *Curr. Med. Chem.* **2017,** 24, 3159-3184.

224. Ponatinib (Iclusig), Application number: 203469Orig1s000. https://www.accessdata.fda.gov/drugsatfda_docs/nda/2012/203469Orig1s000ClinPharmR.pdf (05.06.2020).

225. Imatinib (Gleevec), Application number: NDA 21-335. https://www.accessdata.fda.gov/drugsatfda_docs/nda/2001/21-335_Gleevec_biopharmr_P1.pdf

226. Nilotinib (Tasigna), Application number: 22-068, . https://www.accessdata.fda.gov/drugsatfda_docs/nda/2007/022068s000_ClinPharmR.pdf (05.06.2020).

227. Bosutinib (Bosulif), Application number: 2033410Orig1s000. (05.06.2020).

228. Ruzickova, E.; Skoupa, N.; Dolezel, P.; Smith, D. A.; Mlejnek, P. The lysosomal sequestration of tyrosine kinase inhibitors and drug resistance. *Biomolecules* **2019,** 9, 675.

229. Burger, H.; Dekker, A. T. d.; Segeletz, S.; Boersma, A. W. M.; Bruijn, P. d.; Debiec-Rychter, M.; Taguchi, T.; Sleijfer, S.; Sparreboom, A.; Mathijssen, R. H. J.; Wiemer, E. A. C. Lysosomal sequestration determines intracellular imatinib levels. *Mol. Pharmacol.* **2015,** 88, 477–487.

230. Noguchi, S.; Shibutani, S.; Fukushima, K.; Mori, T.; Igase, M.; Mizuno, T. Bosutinib, an SRC inhibitor, induces caspase-independent cell death associated with permeabilization of lysosomal membranes in melanoma cells. *Vet. Comp. Oncol.* **2018,** 16, 69-76.

231. Zhitomirsky, B.; Assaraf, Y. G. Lysosomes as mediators of drug resistance in cancer. *Drug Resist. Updates* **2016,** 24, 23-33.

232. Kazmi, F.; Hensley, T.; Pope, C.; Funk, R. S.; Loewen, G. J.; Buckley, D. B.; Parkinson, A. Lysosomal sequestration (trapping) of lipophilic amine (cationic amphiphilic) drugs in immortalized human hepatocytes (Fa2N-4 cells). *Drug Metab. Dispos.* **2013,** 41, 897-905.

233. Honeywell, R.; Yarzadah, K.; Giovannetti, E.; Losekoot, N.; E. F. Smit; Walravena, M.; Lind, J. S. W.; Tibaldic, C.; Verheula, H. M.; Peters, G. J. Simple and selective method for the determination of various tyrosine kinase inhibitors used in the clinical setting by liquid chromatography tandem mass spectrometry. *J. Chromatogr. B* **2010,** 878, 1059–1068.

234. Gotink, K. J.; Haas, R. R. d.; Peters, G. J.; Broxterman, H. J.; Miles, K. M.; Pili, R.; Honeywell, R. J.; Dekker, H.; Adelaiye, R.; Griffioen, A. W.; Peters, G. J.; Pili, R.; Verheul, H. M. W. Acquired tumor cell resistance to sunitinib causes resistance in a HT-29 human colon cancer xenograft mouse model without affecting sunitinib biodistribution or the tumor microvasculature. *Oncoscience* **2014,** 1, 844-853.

235. Chapuy, B.; Panse, M.; Radunski, U.; Koch, R.; Wenzel, D.; Inagaki, N.; Haase, D.; Truemper, L.; Wulf, G. G. ABC transporter A3 facilitates lysosomal sequestration of imatinib and modulates susceptibility of chronic myeloid leukemia cell lines to this drug. *Haematologica* **2009,** 94, 1528-1536.

236. Yamagishi, T.; Sahni, S.; Sharp, D. M.; Arvind, A.; Jansson, P. J.; Richardson, D. R. P-glycoprotein mediates drug resistance via a novel mechanism involving lysosomal sequestration. *J. Biol. Chem.* **2013,** 288, 31761-31771.

237. Klerk, D. J. d.; Honeywell, R. J.; Jansen, G.; Peters, G. J. Transporter and lysosomal mediated (multi)drug resistance to tyrosine kinase inhibitors and potential strategies to overcome resistance. *Cancers* **2018,** 10, 503.

238. Warhurst, D. C.; Steele, J. C. P.; Adagu, I. S.; Craig, J. C.; Cullander, C. Hydroxychloroquine is much less active than chloroquine against chloroquine-resistant *Plasmodium falciparum*, in agreement with its physicochemical properties. *J. Antimicrob. Chemother.* **2003,** 52, 188–193.

239. Gorre, M. E.; Mohammed, M.; Ellwood, K.; Hsu, N.; Paquette, R.; Rao, P. N.; Sawyers, C. L. Clinical resistance to STI-571 cancer therapy caused by BCR-ABL gene mutation or amplification. *Science* **2001,** 293, 876-880.

240. Hoeve, J. t.; Arlinghaus, R. B.; Guo, J. Q.; Heisterkamp, N.; Groffen, J. Tyrosine phosphorylation of CRKL in Philadelphia+ leukemia. *Blood* **1994,** 84, 1731-1736.

241. Yang, Z.; Klionsky, D. J. Mammalian autophagy: core molecular machinery and signaling regulation. *Curr. Opin. Cell Biol.* **2010,** 22, 124-131.

242. Glick, D.; Barth, S.; Macleod, K. F. Autophagy: cellular and molecular mechanisms. *J. Pathol.* **2010,** 221, 3-12.

243. Sardiello, M. Transcription factor EB: from master coordinator of lysosomal pathways to candidate therapeutic target in degenerative storage diseases. *Ann. N.Y. Acad. Sci.* **2016,** 1371, 3-14.

244. Medina, D. L.; Paola, S. D.; Peluso, I.; Armani, A.; Stefani, D. D.; Venditti, R.; Montefusco, S.; Scotto-Rosato, A.; Prezioso, C.; Forrester, A.; Settembre, C.; Wang, W.; Gao, Q.; Xu, H.; Sandri, M.; Rizzuto, R.; Matteis, M. A. D.; Ballabio, A. Lysosomal calcium signalling regulates autophagy through calcineurin and TFEB. *Nat. Cell Biol.* **2015,** 17, 288-299.

245. Napolitano, G.; Ballabio, A. TFEB at a glance. *J. Cell Sci.* **2016,** 129, 2475-2481.

246. Sung, G. J.; Kim, S. H.; Kwak, S.; Park, S. H.; Song, J. H.; Jung, J. H.; Kim, H.; Choi, K. C. Inhibition of TFEB oligomerization by co-treatment of melatonin with vorinostat promotes the therapeutic sensitivity in glioblastoma and glioma stem cells. *J. Pineal. Res.* **2019,** 66, e12556.

247. Kim, Y. R.; Park, M. S.; Eum, K. H.; Kim, J.; Lee, J. W.; Bae, T.; Lee, D. H.; Choi, J. W. Transcriptome analysis indicates TFEB1 and YEATS4 as regulatory transcription factors for drug resistance of ovarian cancer. *Oncotarget* **2015,** 6, 31031-31038.

248. Giatromanolaki, A.; Kalamida, D.; Sivridis, E.; Karagounis, I. V.; Gatter, K. C.; Harris, A. L.; Koukourakis, M. I. Increased expression of transcription factor EB

(TFEB) is associated with autophagy, migratory phenotype and poor prognosis in non-small cell lung cancer. *Lung Cancer* **2015,** 90, 98-105.

249. Raghunand, N.; Gillies, R. J. pH and drug resistance in tumors. *Drug Resist. Updates* **2000,** 3, 39-47.

250. Ma, L.; Center, M. S. The gene encoding vacuolar H^+-ATPase subunit C is overexpressed in multidrug-resistant HL60 cells. *Biochem. Biophys. Res. Commun.* **1992,** 182, 675-681.

251. Martinez-Zaguilan, R.; Raghunand, N.; Lynch, R. M.; Bellamy, W.; Martinez, G. M.; Rojas, B.; Smith, D.; Dalton, W. S.; Gillies, R. J. pH and drug resistance. I. Functional expression of plasmalemmal V-type H^+-ATPase in drug-resistant human breast carcinoma cell lines. *Biochem. Pharmacol.* **1999,** 57, 1037-1046.

252. Ouar, Z.; Bens, M.; Vignes, C.; Paulais, M.; Pringel, C.; Fleury, J.; Cluzeaud, F.; Lacave, R.; Vandewalle, A. Inhibitors of vacuolar H^+-ATPase impair the preferential accumulation of daunomycin in lysosomes and reverse the resistance to anthracyclines in drug-resistant renal epithelial cells. *Biochem. J.* **2003,** 370, 185-193.

253. Xu, H.; Ren, D. Lysosomal physiology. *Annu. Rev. Physiol.* **2015,** 77, 57-80.

254. Zhitomirsky, B.; Assaraf, Y. G. Lysosomal accumulation of anticancer drugs triggers lysosomal exocytosis. *Oncotarget* **2017,** 8, 45117-45132.

255. Tipping, W. J. Spectroscopically bioorthogonal Raman imaging approaches for intracellular visualisation. The University of Edinburgh, Edinburgh, 2017.

256. Yang, S. K.; Shi, X.; Park, S.; Ha, T.; Zimmerman, S. C. A dendritic single-molecule fluorescent probe that is monovalent, photostable and minimally blinking. *Nat. Chem.* **2013,** 5, 692-697.

257. Liu, Y.; Tseng, Y.; Huang, L. Biodistribution studies of nanoparticles using fluorescence imaging: a qualitative or quantitative method? *Pharm. Res.* **2012,** 29, 3273–3277.

258. Englinger, B.; Laemmerer, A.; Moser, P.; Kallus, S.; Röhrl, C.; Pirker, C.; Baier, D.; Mohr, T.; Niederstaetter, L.; Meier-Menches, S. M.; Gerner, C.; Gabler, L.; Gojo, J.; Timelthaler, G.; Senkiv, J.; Jäger, W.; Kowol, C. R.; Heffeter, P.; Berger, W. Lipid droplet-mediated scavenging as novel intrinsic and adaptive resistance factor against the multikinase inhibitor ponatinib. *Int. J. Cancer* **2020,** 147, 1680–1693.

259. Liu, Q.; Yu, S.; Zhao, W.; Qin, S.; Chu, Q.; Wu, K. EGFR-TKIs resistance via EGFR-independent signaling pathways. *Mol. Cancer* **2018,** 17, 53.

260. Nnah, I. C.; Wang, B.; Saqcena, C.; Weber, G. F.; Bonder, E. M.; Bagley, D.; Cegli, R. D.; Napolitano, G.; Medina, D. L.; Ballabio, A.; Dobrowolski, R. TFEB-driven

endocytosis coordinates MTORC1 signaling and autophagy. *Autophagy* **2019,** 15, 151-164.

261. Malta, C. D.; Siciliano, D.; Calcagni, A.; Monfregola, J.; Punzi, S.; Pastore, N.; Eastes, A. N.; Davis, O.; Cegli, R. D.; Zampelli, A.; Giovannantonio, L. G. D.; Nusco, E.; Platt, N.; Guida, A.; Ogmundsdottir, M. H.; Lanfrancone, L.; Perera, R. M.; Zoncu, R.; Pelicci, P. G.; Settembre, C.; Ballabio, A. Transcriptional activation of RagD GTPase controls mTORC1 and promotes cancer growth. *Science* **2017,** 356, 1188–1192.

262. Breslin, S.; O'Driscoll, L. Three-dimensional cell culture: the missing link in drug discovery. *Drug Discov. Today* **2013,** 18, 240-249.

263. Torisawa, Y.-S.; Takagi, A.; Shiku, H.; Yasukawa, T.; Matsue, T. A multicellular spheroid-based drug sensitivity test by scanning electrochemical microscopy. *Oncol. Rep.* **2005,** 13, 1107-1112.

264. Tung, Y.-C.; Hsiao, A. Y.; Allen, S. G.; Torisawa, Y.-S.; Hoc, M.; Takayama, S. High-throughput 3D spheroid culture and drug testing using a 384 hanging drop array. *Analyst* **2011,** 136, 473–478.

265. Lovitt, C. J.; Shelper, T. B.; Avery, V. M. Evaluation of chemotherapeutics in a three-dimensional breast cancer model. *J. Cancer Res. Clin. Oncol.* **2015,** 141, 951–959.

266. Ooft, S. N.; Weeber, F.; Dijkstra, K. K.; McLean, C. M.; Kaing, S.; Werkhoven, E. v.; Schipper, L.; Hoes, L.; Vis, D. J.; Haar, J. v. d.; Prevoo, W.; Snaebjornsson, P.; Velden, D. v. d.; Klein, M.; Chalabi, M.; Boot, H.; Leerdam, M. v.; Bloemendal, H. J.; Beerepoot, L. V.; Wessels, L.; Cuppen, E.; Clevers, H.; Voest, E. E. Patient-derived organoids can predict response to chemotherapy in metastatic colorectal cancer patients. *Sci. Transl. Med.* **2019,** 11, eaay2574.

267. Witte, C. J. d.; Valle-Inclan, J. E.; Hami, N.; Lohmussaar, K.; Kopper, O.; Vreuls, C. P. H.; Jonges, G. N.; Diest, P. v.; Nguyen, L.; Clevers, H.; Kloosterman, W. P.; Cuppen, E.; Snippert, H. J. G.; Zweemer, R. P.; Witteveen, P. O.; Stelloo, E. Patient-derived ovarian cancer organoids mimic clinical response and exhibit heterogeneous inter-and intrapatient drug responses. *Cell Rep.* **2020,** 31, 107762.

268. Ma, H.; Jiang, Q.; Han, S.; Wu, Y.; Tomshine, J. C.; Wang, D.; Gan, Y.; Zou, G.; Liang, X.-J. Multicellular tumor spheroids as an in vivo–like Tumor model for three-dimensional imaging of chemotherapeutic and nano material cellular penetration. *Mol. Imaging* **2012,** 11, 487–498.

269. Cortes-Funes, H.; Coronado, C. Role of anthracyclines in the era of targeted therapy. *Cardiovasc. Toxicol.* **2007,** 7, 56–60.

270. Pampaloni, F.; Ansari, N.; Stelzer, E. H. K. High-resolution deep imaging of live cellular spheroids with light-sheet-based fluorescence microscopy. *Cell Tissue Res.* **2013,** 352, 161-177.

271. Liu, X.; Weaver, E. M.; Hummon, A. B. Evaluation of therapeutics in three-dimensional cell culture systems by MALDI imaging mass spectrometry. *Anal. Chem.* **2013,** 85, 6295−6302.

272. Swales, J. G.; Hamm, G.; Clench, M. R.; Goodwin, R. J. A. Mass spectrometry imaging and its application in pharmaceutical research and development: A concise review. *Int. J. Mass Spectrom.* **2019,** 437, 99-112.

273. Sleno, L.; Volmer, D. A. Some fundamental and technical aspects of the quantitative analysis of pharmaceutical drugs by matrix-assisted laser desorption/ionization mass spectrometry. *Rapid Commun. Mass Spectrom.* **2005,** 19, 1928–1936.

274. Bocklitz, T. W.; Crecelius, A. C.; Matthäus, C.; Tarcea, N.; Eggeling, F. v.; Schmitt, M.; Schubert, U. S.; Popp, J. Deeper understanding of biological tissue: Quantitative correlation of MALDI-TOF and Raman imaging. *Anal. Chem.* **2013,** 85, 10829−10834.

275. LaBonia, G. J.; Lockwood, S. Y.; Heller, A. A.; Spence, D. M.; Hummon, A. B. Drug penetration and metabolism in 3D cell cultures treated in a 3D printed fluidic device: assessment of irinotecan via MALDI imaging mass spectrometry. *Proteomics* **2016,** 16, 1814-1821.

276. Vanhoefer, U.; Harstrick, A.; Achterrath, W.; Cao, S.; Seeber, S.; Rustum, Y. M. Irinotecan in the treatment of colorectal cancer: clinical overview. *J. Clin. Oncol.* **2001,** 19, 1501-1518.

277. Man, F. M. d.; Goey, A. K. L.; Schaik, R. H. N. v.; Mathijssen, R. H. J.; Bins, S. Individualization of irinotecan treatment: A review of pharmacokinetics, pharmacodynamics, and pharmacogenetics. *Clin. Pharmacokinet.* **2018,** 57, 1229–1254.

278. Nair, R. R.; Piktel, D.; Hathaway, Q. A.; Rellick, S. L.; Thomas, P.; Saralkar, P.; Martin, K. H.; Geldenhuys, W. J.; Hollander, J. M.; Gibson, L. F. Pyrvinium pamoate use in a B cell acute lymphoblastic leukemia model of the mone tumor microenvironment. *Pharm. Res. (2020) 37: 43* **2020,** 37, 43.

279. Bray, L. J.; Binner, M.; Körner, Y.; Bonin, M. v.; Bornhäuser, M.; Werner, C. A three-dimensional ex vivo tri-culture model mimics cell-cell interactions between acute myeloid leukemia and the vascular niche. *Haematologica* **2017,** 102, 1215-1226.

280. Vinci, M.; Gowan, S.; Boxall, F.; Patterson, L.; Zimmermann, M.; Court, W.; Lomas, C.; Mendiola, M.; Hardisson, D.; Eccles, S. A. Advances in establishment and

analysis of three-dimensional tumor spheroid-based functional assays for target validation and drug evaluation. *BMC Biol.* **2012,** 10, 29.

281. Harapanhalli, R. S.; McLaughlin, L. W.; Howell, R. W.; Rao, D. V.; Adelstein, S. J.; Kassis, A. I. [^{125}I/^{127}I]IodoHoechst 33342: Synthesis, DNA binding, and biodistribution. *J. Med. Chem.* **1996,** 39, 4804-4809.

282. Uggeri, J.; Gatti, R.; Belletti, S.; Scandroglio, R.; Corradini, R.; Rotoli, B. M.; Orlandini, G. Calcein-AM is a detector of intracellular oxidative activity. *Histochem. Cell Biol.* **2004,** 122, 499–505.

283. Hudson, B.; Upholt, W. B.; Devinny, J.; Vinograd, J. The use of an ethidium analogue in the dye-buoyant density procedure for the isolation of closed circular DNA: the variation of the superhelix density of mitochondrial DNA. *Proc. Natl. Acad. Sci. U.S.A.* **1969,** 62, 813-820.

284. Hughes, C. S.; Postovit, L. M.; Lajoie, G. A. Matrigel: A complex protein mixture required for optimal growth of cell culture. *Proteomics* **2010,** 10, 1886–1890.

285. Kleinman, H. K.; Martin, G. R. Matrigel: Basement membrane matrix with biological activity. *Semin. Cancer Biol.* **2005,** 15, 378–386.

286. Kleinman, H. K.; McGarvey, M. L.; Liotta, L. A.; Robey, P. G.; Tryggvason, K.; Martin, G. R. Isolation and characterization of type IV procollagen, laminin, and heparan sulfate proteoglycan from the EHS sarcoma *Biochemistry* **1982,** 21, 6188-6193.

287. Wenzel, C.; Riefke, B.; Gründemann, S.; Krebs, A.; Christian, S.; Prinz, F.; Osterland, M.; Golfier, S.; Räse, S.; Ansari, N.; Esner, M.; Bickle, M.; Pampaloni, F.; Mattheyer, C.; Stelzer, E. H.; Parczyk, K.; Prechtl, S.; Steigemann, P. 3D high-content screening for the identification of compounds that target cells in dormant tumor spheroid regions. *Exp. Cell Res.* **2014,** 323, 131-143.

288. Seeley, E. H.; Caprioli, R. M. MALDI imaging mass spectrometry of human tissue: method challenges and clinical perspectives. *Trends Biotechnol.* **2011,** 29, 136-143.

289. Randall, E. C.; Emdal, K. B.; Laramy, J. K.; Kim, M.; Roos, A.; Calligaris, D.; Regan, M. S.; Gupta, S. K.; Mladek, A. C.; Carlson, B. L.; Johnson, A. J.; Lu, F.-K.; Xie, X. S.; Joughin, B. A.; Reddy, R. J.; Peng, S.; Abdelmoula, W. M.; Jackson, P. R.; Kolluri, A.; Kellersberger, K. A.; Agar, J. N.; Lauffenburger, D. A.; Swanson, K. R.; Tran, N. L.; Elmquist, W. F.; White, F. M.; Sarkaria, J. N.; Agar, N. Y. R. Integrated mapping of pharmacokinetics and pharmacodynamics in a patient-derived xenograft model of glioblastoma. *Nat. Commun.* **2018,** 9, 4904.

290. Atkinson, S. J.; Loadman, P. M.; Sutton, C.; Patterson, L. H.; Clench, M. R. Examination of the distribution of the bioreductive drug AQ4N and its active metabolite

AQ4 in solid tumours by imaging matrix-assisted laser desorption/ionisation mass spectrometry. *Rapid Commun. Mass Spectrom.* **2007,** 21, 1271–1276.

291. Weia, M.; Shi, L.; Shen, Y.; Zhao, Z.; Guzman, A.; Kaufman, L. J.; Wei, L.; Min, W. Volumetric chemical imaging by clearing-enhanced stimulated Raman scattering microscopy. *Proc. Natl. Acad. Sci. U.S.A.* **2019,** 116, 6608–6617.

292. Zhang, J.; Whitehead, J.; Liu, Y.; Yang, Q.; Leach, J. K.; Liu, G. Direct observation of tunneling nanotubes within human mesenchymal stem cell spheroids. *J. Phys. Chem. B* **2018,** 122, 9920-9926.

293. Jacques, S. L. Optical properties of biological tissues: a review. *Phys. Med. Biol.* **2013,** 58, R37.

294. Takasaki, K.; Abbasi-Asl, R.; Waters, J. Superficial bound of the depth limit of two-photon imaging in mouse brain. *eNeuro* **2020,** 7, 1-10.

295. Tischbirek, C.; Birkner, A.; Jia, H.; Sakmann, B.; Konnerth, A. Deep two-photon brain imaging with a red-shifted fluorometric Ca^{2+} indicator. *Proc. Natl. Acad. Sci.* **2015,** 112, 11377–11382.

296. Hill, A. H.; Manifold, B.; Fu, D. Tissue imaging depth limit of stimulated Raman scattering microscopy. *Biomed. Opt. Express* **2020,** 11, 762-774.

297. Li, J.; Lin, P.; Tan, Y.; Cheng, J.-X. Volumetric stimulated Raman scattering imaging of cleared tissues towards three-dimensional chemical histopathology. *Biomed. Opt. Express* **2019,** 10, 4329-4339.

298. Berto, P.; Andresen, E. R.; Rigneault, H. Background-free stimulated Raman spectroscopy and microscopy. *Phys. Rev. Lett.* **2014,** 112, 053905.

299. Lombardini, A.; Berto, P.; Duboisset, J.; Andresen, E. R.; Heuke, S.; Büttner, E.; Rimke, I.; Vergnole, S.; Shinkar, V.; Bettignies, P. d.; Rigneault, H. Background-suppressed SRS fingerprint imaging with a fully integrated system using a single optical parametric oscillator. *Opt. Express* **2020,** 28, 14490-14502.

300. Pavlovsky, C.; Chan, O.; Talati, C.; Pinilla-Ibarz, J. Ponatinib in the treatment of chronic myeloid leukemia and philadelphia chromosome positive acute lymphoblastic leukemia. *Future Oncol.* **2019,** 15, 257-269.

301. Zabriskie, M. S.; Eide, C. A.; Tantravahi, S. K.; Vellore, N. A.; Estrada, J.; Nicolini, F. E.; Khoury, H. J.; Larson, R. A.; Konopleva, M.; Cortes, J. E.; Kantarjian, H.; Jabbour, E. J.; Kornblau, S. M.; Lipton, J. H.; Rea, D.; Stenke, L.; Barbany, G.; Lange, T.; Hernández-Boluda, J.-C.; Ossenkoppele, G. J.; Press, R. D.; Chuah, C.; Goldberg, S. L.; Wetzler, M.; Mahon, F.-X.; Etienne, G.; Baccarani, M.; Soverini, S.; Rosti, G.; Rousselot, P.; Friedman, R.; Deininger, M.; Reynolds, K. R.; Heaton, W. L.; Eiring, A. M.; Pomicter, A. D.; Khorashad, J. S.; Kelley, T. W.; Baron, R.; Druker, B. J.; Deininger, M. W.; O'Hare, T. BCR-ABL1 compound mutations combining key

kinase domain positions confer clinical resistance to ponatinib in Ph chromosome-positive leukemia. *Cancer Cell* **2014,** 26, 428–442.

302. Deininger, M. W.; Hodgson, J. G.; Shah, N. P.; Cortes, J. E.; Kim, D.-W.; Nicolini, F. E.; Talpaz, M.; Baccarani, M.; Müller, M. C.; Li, J.; Parker, W. T.; Lustgarten, S.; Clackson, T.; Haluska, F. G.; Guilhot, F.; Kantarjian, H. M.; Soverini, S.; Hochhaus, A.; Hughes, T. P.; Rivera, V. M.; Branford, S. Compound mutations in BCR-ABL1 are not major drivers of primary or secondary resistance to ponatinib in CP-CML patients *Blood* **2016,** 127, 703-712.

303. Lu, L.; Kok, C. H.; McLean, A.; Saunders, V. A.; Hughes, T. P.; Wang, J.; White, D. L. Modelling ponatinib resistance in tyrosine kinase inhibitor-naïve and dasatinib resistant *BCR-ABL1*+ cell lines. *Oncotarget* **2018,** 9, 34735-34747.

304. Musumeci, F.; Greco, C.; Grossi, G.; Molinari, A.; Schenone, S. Recent studies on ponatinib in cancers other than chronic myeloid leukemia. *Cancers* **2018,** 10, 430.

305. Rzagalinski, I.; Kovačević, B.; Hainz, N.; Meier, C.; Tschernig, T.; Volmer, D. A. Toward higher sensitivity in quantitative MALDI imaging mass spectrometry of CNS drugs using a nonpolar matrix. *Anal. Chem.* **2018,** 90, 12592−12600.

306. Zong, C.; Premasiri, R.; Lin, H.; Huang, Y.; Zhang, C.; Yang, C.; Ren, B.; Ziegler, L. D.; Cheng, J.-X. Plasmon-enhanced stimulated Raman scattering microscopy with single-molecule detection sensitivity. *Nat. Commun.* **2019,** 10, 5318.

307. Sarri, B.; Chen, X.; Canonge, R.; Grégoire, S.; Formanek, F.; Galey, J.-B.; Potter, A.; Bornschlögl, T.; Rigneault, H. In vivo quantitative molecular absorption of glycerol in human skin usingcoherent anti-Stokes Raman scattering (CARS) and two-photon auto-fluorescence. *J. Control. Release* **2019,** 308, 190-196.

308. Chen, X.; Grégoire, S.; Formanek, F.; Galey, J.-B.; Rigneault, H. Quantitative 3D molecular cutaneous absorption in human skin using label free nonlinear microscopy. *J. Control. Release* **2015,** 200, 78-86.

Appendices

Appendix 1 Common abbreviations

2D	2-dimensional
3D	3-dimensional
A.U.	arbitrary units
ABC	ATP-binding cassette
ABCA3	ATP-binding cassette sub-family A member 3
abl	Ableson leukemia virus
AIQ	aminoisoquinoline
AM	acetoxymethylester
AML	acute myeloid leukaemia
AOM	acousto-optic modulator
AP	accelerated phase
AQ	aminoquinoline
ATG5	autophagy-related gene 5
ATG7	autophagy-related gene 7
ATP	adenosine triphosphate
BADY	bisaryldiyne
bcr	breakpoint cluster region
BP	blast phase
BSA	bovine serum albumin
Carbow	carbon rainbow
CARS	coherent anti-Stokes scattering
CLEAR	coordinated lysosomal expression and regulation
CML	chronic myeloid leukaemia

CNS	central nervous system
CQ	chloroquine
cRIE	calculated relative intensity to EdU
CYP	cytochrome P450
Da	Dalton
DFT	density functional theory
DMEM	Dulbecco's modified Eagle's medium
DMSO	dimethyl sulfoxide
ECM	extracellular matrix
EdU	5’-Ethynyl-2’-deoxyuridine
EGFR	epidermal growth factor receptor
EOM	electro-optic modulator
ER	endoplasmic reticulum
FACS	fluorescence assisted cell sorting
FDA	U.S. Food and Drug Administration
FGFR	fibroblast growth factor receptor
FM-SRS	frequency modulated SRS
GA	glutaraldehyde
GI50	growth inhibitory 50%
GPN	glycyl-*L*-phenylalanine 2-naphthylamide
GSH	glutathione
HCA	hierarchical cluster analysis
HCQ	hydroxychloroquine
HCS	high content screening
HDM	hanging droplet method

HER2	human epidermal growth factor receptor 2
hSRS	hyperspectral stimulated Raman scattering
IF	immunofluorescence
IR	infrared
IUR	intracellular uptake and retention
LAMP1	lysosomal-associated membrane protein 1
LC3	microtubule-associated protein 1 light chain 3
LC-MS	liquid chromatography mass spectrometry
LSC	leukemic stem cells
LSFM	light sheet fluorescence microscopy
LTR	lysotracker red
MALDI	matrix assisted laser desorption ionisation
MALDI-IMS	MALDI imaging mass spectrometry
MCOLN1	mucolipin-1
MCR	multivariate curve resolution
MFI	mean fluorescence intensity
MIP	maximum intensity projection
MRI	magnetic resonance imaging
MS	mass spectrometry
mTOR	mammalian target of rapamycin
mTORC1	mTOR complex 1
OCT1	organic cation transporter 1
PA	polylactic acid
PE	phosphatidylethanolamine
PESRS	plasmon enhanced SRS

PET	positron emission tomography
PFA	paraformaldehyde
PG	propylene glycol
PGA	polyglycolic acid
PGE	polyethylene glycol
P-gp	P-glycoprotein
Ph	Philadelphia chromosome
PhDY	phenyldiyne
PI	propidium iodide
PI3K	phosphoinositide 3-kinase
PKI	protein kinase inhibitor
poly-HEMA	poly(2-hydroxyethyl methacrylate)
QNC	quinacrine
R&D	research and development
R123	rhodamine 123
R6G	rhodamine 6G
RAF	rapidly accelerated fibrosarcoma
RIE	relative intensity to EdU
ROS	reactive oxygen species
RPMI	Roswell Park Memorial Institute medium
RT	room temperature
SD	standard deviation
SEM	standard error of the mean
SERS	surface enhanced Raman scattering
SIMS	secondary ion mass spectrometry

SRG	stimulated Raman gain
SRGOLD	stimulated Raman gain and opposite loss detection
SRL	stimulated Raman loss
SRS	stimulated Raman scattering
TFEB	transcription factor EB
TFI	total fluorescence intensity
TH	terbafine hydrochloride
TKI	tyrosine kinase inhibitor
TME	tumour microenvironment
TPF	two photon fluorescence
ULA	ultra-low attachment
ULK	Unc-51 like kinase
v-ATPase	vacuolar H^+ ATPase
WBA	whole-body autoradiography

Appendix 2 Supplementary figures

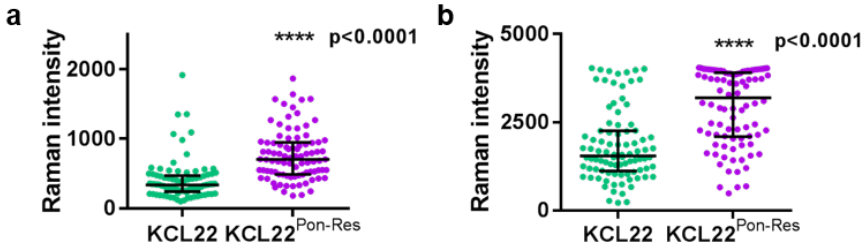

Figure S1 KCL22 and KCL22$^{Pon\text{-}Res}$ cells that were treated with 5 μM ponatinib (1 h) and labelled with Lysotracker Red (75 nM, 1 h) and imaged live. (a) Mean ponatinib Raman intensity, and; (b) Maximum ponatinib Raman intensity inside the vesicles of each individual cell were quantified for n=30 cells, 3 biological repeats. The Mann-Whitney test was used to compare ponatinib Raman intensity values.

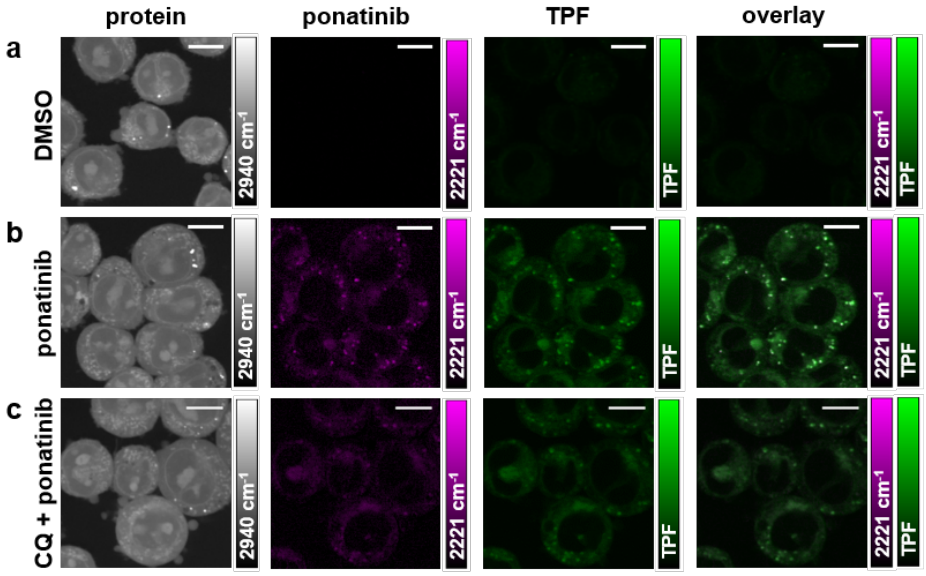

Figure S2 Multimodal imaging and quantitative assessment of ponatinib uptake in KCL22 cells following CQ combination treatment. KCL22 cells were treated with (a) DMSO (0.0003%, v/v), (b) ponatinib (5 μM, 1 h) or (c) chloroquine (20 μM, 2 h) followed by combination treatment of ponatinib (5 μM, 1 h) and chloroquine (20 μM, 1 h). All the samples were labelled with Lysotracker® Green (50 nM, 1 h). SRS images acquired at (from left to right) 2940 cm^{-1} (CH_3, proteins); 2221 cm^{-1} (C≡C, ponatinib); 2257 cm^{-1} (off-resonance), TPF image acquired at 861 nm (Lysotracker® Green); overlay of ponatinib and TPF. Images acquired at 1024 × 1024 pixels, 20 μs pixel dwell time, laser power p200 gain 1 with false colours applied to different detection wavenumbers. Scale bars: 10 μm.

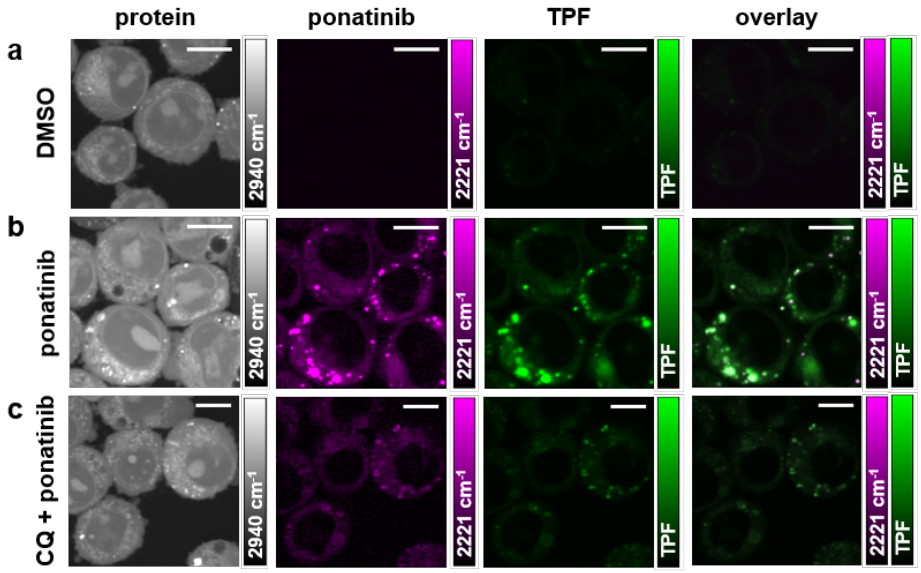

Figure S3 Multimodal imaging and quantitative assessment of ponatinib uptake in KCL22 cells following CQ combination treatment. KCL22 cells were treated with (a) DMSO (0.0003%, v/v), (b) ponatinib (5 μM, 1 h) or (c) chloroquine (20 μM, 2 h) followed by combination treatment of ponatinib (5 μM, 1 h) and chloroquine (20 μM, 1 h). All the samples were labelled with Lysotracker® Green (50 nM, 1 h). SRS images acquired at (from left to right) 2940 cm^{-1} (CH_3, proteins); 2221 cm^{-1} (C≡C, ponatinib); 2257 cm^{-1} (off-resonance), TPF image acquired at 861 nm (Lysotracker® Green); overlay of ponatinib and TPF. Images acquired at 1024 × 1024 pixels, 20 μs pixel dwell time, laser power p200 gain 1 with false colours applied to different detection wavenumbers. Scale bars: 10 μm.

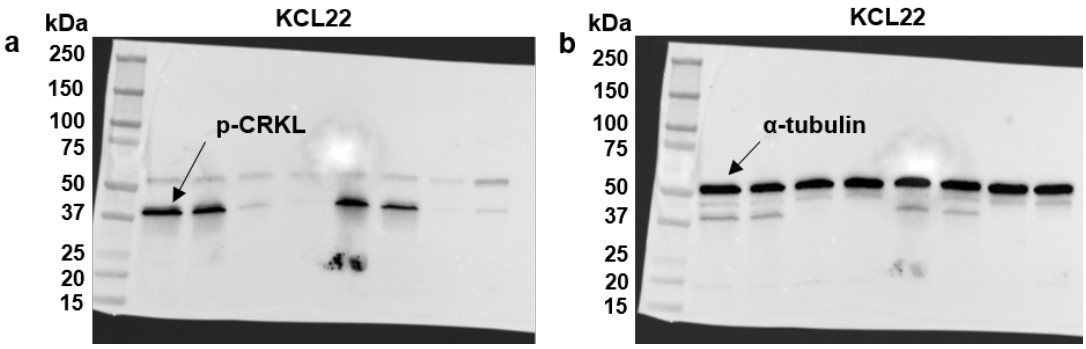

Figure S4 Full Western blots shown for KCL22 cell lysates that were probed for (a) p-CRKL (39 kDa) and (b) α-tubulin (50 kDa). Standard ladder has been annotated.

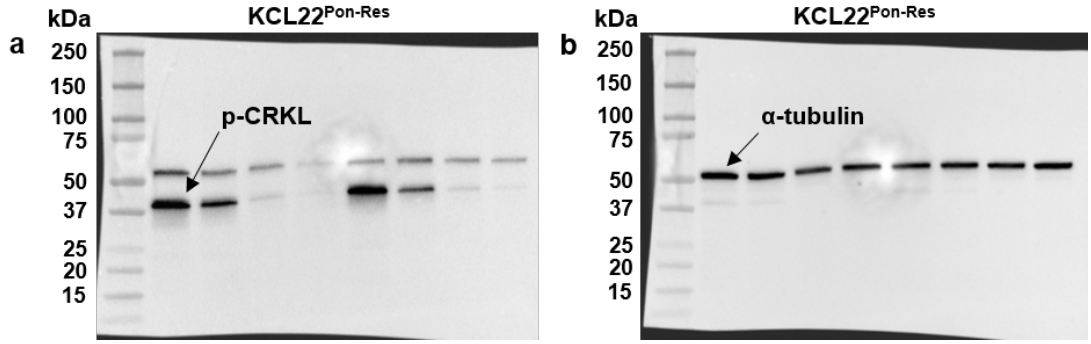

Figure S5 Full Western blots shown for KCL22$^{Pon-Res}$ cell lysates that were probed for (a) p-CRKL (39 kDa) and (b) α-tubulin (50 kDa). Standard ladder has been annotated.

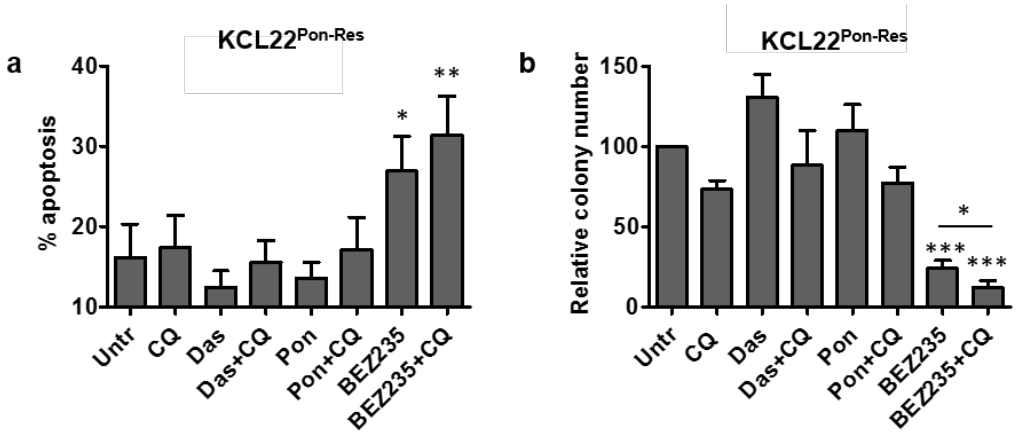

Figure S6. Measuring apoptosis and relative colony number in KCL22$^{Pon-Res}$ cells using various inhibitors.[***] KCL22$^{Pon-Res}$ cells were cultured with 10 μM CQ , 150 nM dasatinib (Das), 100 nM ponatinib (Pon), 100 nM NVP-BEZ235 (BEZ235) or a combination of two drugs for 72 h. (a) Apoptosis was measured by staining the cells with annexin V and 7-Amino-Actinomycin D and analysed by FACS. Error bars ± SD, n=3 biological repeats. (b) Number or colonies was measured following 72 h of drug treatment using colony formation assay. Statistical analysis was performed by using paired t-test. Annotation above a bar refers to statistical significance between the bar and the untreated control, *** ($p \leq 0.001$), ** ($p \leq 0.01$), * $p \leq 0.05$.

[***] Unpublished data acquired by the Helgason group, The University of Glasgow.

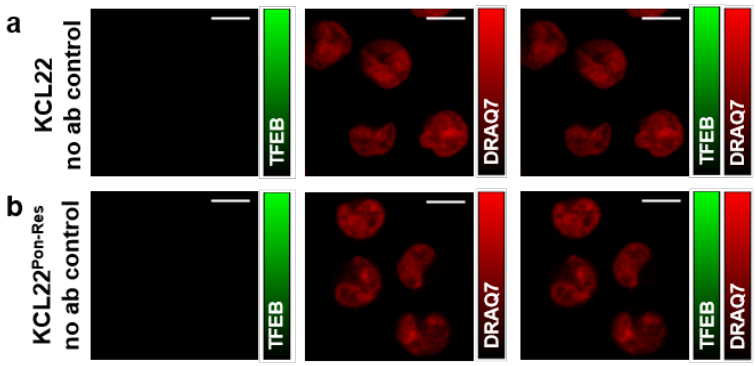

Figure S7 No antibody control images for IF imaging of nuclear TFEB in CML cells. (a) KCL22 and (b) KCL22$^{Pon\text{-}Res}$ no antibody control cells were treated with DMSO (0.0003%, v/v) for 1 h. Cell nuclei were stained with DRAQ7, but cells were not stained with TFEB. Images acquired at 1024 × 1024 pixels, 4 µs pixel dwell time, laser power p200 gain 1. Scale bars: 10 µm.

Journal of Medicinal Chemistry

Featured Article

Cite This: J. Med. Chem. 2020, 63, 2028−2034

pubs.acs.org/jmc

Utilizing Stimulated Raman Scattering Microscopy To Study Intracellular Distribution of Label-Free Ponatinib in Live Cells

Kristel Sepp,[†,‡] Martin Lee,[†] Marie T. J. Bluntzer,[‡] G. Vignir Helgason,[§] Alison N. Hulme,*[,‡] and Valerie G. Brunton*[,†]

[†]Edinburgh Cancer Research UK Centre, Institute of Genetics & Molecular Medicine, University of Edinburgh, Edinburgh EH4 2XR, U.K.

[‡]EaStCHEM School of Chemistry, University of Edinburgh, Joseph Black Building, David Brewster Road, Edinburgh EH9 3FJ, U.K.

[§]Wolfson Wohl Cancer Research Centre, Institute of Cancer Sciences, University of Glasgow, Garscube Estate, Glasgow G61 1QH, U.K.

Supporting Information

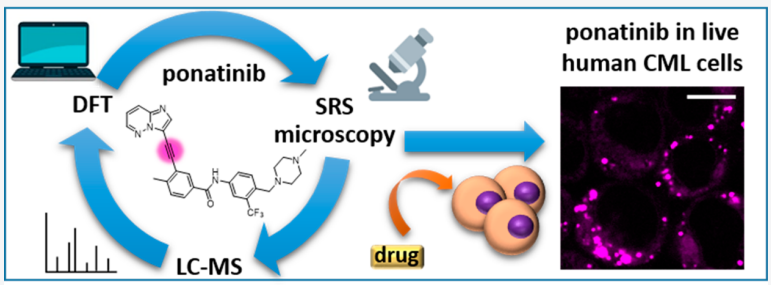

ABSTRACT: Stimulated Raman scattering (SRS) microscopy represents a powerful method for imaging label-free drug distribution with high resolution. SRS was applied to image label-free ponatinib with high sensitivity and specificity in live human chronic myeloid leukemia (CML) cell lines. This was achieved at biologically relevant, nanomolar concentrations, allowing determination of ponatinib uptake and sequestration into lysosomes during the development of acquired drug resistance and an improved understanding of target engagement.

INTRODUCTION

Despite the identification of an unprecedented number of potential new drug targets over the past two decades, and an accompanying intense investment in the generation of NCEs with improved potency and selectivity, currently only 1 in 10 clinical candidates progresses to regulatory approval.[1] This major loss in investment by drug developers can be analyzed from the viewpoint of the physicochemical properties of drug candidates,[2] but these studies do not provide clear indicators for how to reduce attrition rates.[3] Some of the highest pipeline attrition rates are seen in the development of chemotherapeutics.[4] As a plethora of new, targeted chemotherapeutics enter the clinic and, with the development of resistance to these agents, alternative approaches are urgently required to optimize their development and use. A shift toward determining critical information through the use of relevant cell-based assays at an earlier stage in the pipeline[5] could result in a much cheaper and more effective development process.[6]

Stimulated Raman scattering (SRS) microscopy generates image contrast using the Raman active vibrational frequency of a given chemical bond, providing information on the biochemical composition of tissues and allowing label-free visualization for a number of biomedical applications including drug interactions.[7,8] SRS is distinguished by a number of key features:

(1) Fast acquisition speeds (orders of magnitude faster than those achieved with spontaneous Raman), good photostability, and a lack of phototoxicity, which together allow real-time imaging.
(2) A linear relationship between signal intensity and chemical concentration, which enables quantitative imaging.
(3) Multiple acquisition wavelengths, which allows drug distribution within cells to be mapped onto subcellular features providing intracellular registration.
(4) Multimodal imaging (SRS and fluorescence), which allows image overlay with cell- or tissue-specific markers.[9,10]

Combined, these characteristics ensure that SRS imaging provides a unique platform to understand drug distribution within individual cells, thus distinguishing it from other technologies, such as whole-body autoradiography and liquid

Special Issue: Women in Medicinal Chemistry

Received: September 17, 2019
Published: December 12, 2019

chromatography−mass spectrometry (LC-MS), that are typically used to monitor drug distribution.[11,12]

Raman imaging was initially developed as a label-free technique for visualization of biomolecules including lipids and proteins, and more recently the development of alkynes (C≡C) as nonlinear vibrational tags for imaging small biomolecules using SRS microscopy has extended the applicability of this approach.[13,14] Alkynes are both chemically and Raman spectroscopically biorthogonal as they do not react with endogenous biomolecules and do not exist inside cells. The C≡C stretching motion can hence be detected in the Raman "cellular-silent" region (1800−2800 cm^{-1}). This also presents an optimal region for drug imaging, as there is minimal contribution from endogenous cellular biomolecules, thus improving detection sensitivity.[8,15] In this study, we utilize the advantages of an alkyne-based imaging approach to assess label-free drug uptake and distribution in cellular models of resistance using ponatinib (**1**),[16] a tyrosine kinase inhibitor with regulatory approval for the treatment of chronic myeloid leukemia.

RESULTS AND DISCUSSION

Ponatinib (**1**) has an inherent alkyne moiety in its structure providing the potential for imaging its cellular localization in the Raman "cellular-silent" region (Figure 1a,b), without the addition of bulky tags such as fluorophores, which can negatively impact on the biological activity of drugs. In SRS, two synchronized lasers, the pump and the Stokes beam are used to excite a specific molecular vibration (Figure 1c). To visualize a chemical bond of interest, the frequency difference between the pump beam and the Stokes beam is tuned to match the chosen vibration (ω_v), allowing stimulated Raman scattering to take place in addition to the inherently weak spontaneous Raman scattering.

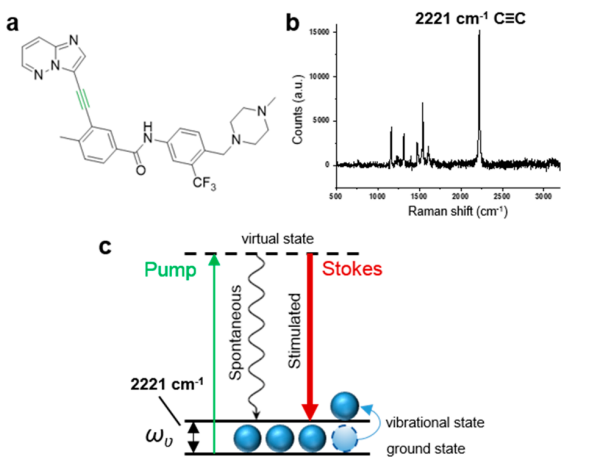

Figure 1. (a) Chemical structure of ponatinib; (b) Raman spectrum of solid ponatinib. The following peak has been annotated: 2221 cm^{-1} (C≡C, ponatinib). Raman spectra were acquired at λ_{ex} = 532 nm for 10 s using a 50× objective. (c) Energy level diagram showing the working principle of SRS microscopy.

Predicting the Intensity and Frequency of Raman Signals by DFT. Density functional theory (DFT) calculations have previously been used to predict theoretical Raman intensities (I_{Ram}),[8,15] while experimentally observed Raman intensities have been compared with the intensity of the alkyne resonance in the nucleoside analogue ethynyl deoxyuridine (EdU) to give relative intensity to EdU (RIE) values.[17] We have combined these two approaches to give a series of calculated RIE values (cRIE) to facilitate comparison of the predicted intensity values for signals in the "cellular-silent" region. DFT calculations have also, very recently been used to predict the changes in Raman vibrational frequencies that result from primary drug metabolism.[18] Thus, we have used a series of DFT calculations to establish whether the acquisition of SRS images at a single vibrational frequency for the alkyne (Figure 1b, C≡C, 2221 cm^{-1}) would provide an accurate assessment of the ponatinib concentration within a cell (Supporting Information (SI), Table S1).

The piperidine unit in ponatinib means that it is susceptible to lysosomal trapping through protonation.[19,20] However, in our DFT calculations, both the parent drug and its protonated counterpart were predicted to have very similar frequencies for the alkyne resonance, with a slight decrease in cRIE value upon protonation (SI, Table S1). Hence, it was determined that SRS imaging at a single wavenumber would allow assessment of ponatinib concentrations across the whole cell environment, independent of subcellular variations in pH. Previous studies have identified the primary metabolites of ponatinib as its *N*-oxide and *N*-desmethyl analogues, together with dihydroxylated forms.[21−23] As the chemical perturbations in these two major metabolites is distal to the alkyne vibrational motif, a large change in I_{Ram} is not expected. This conclusion was confirmed by DFT calculations (SI, Table S1), which show similar cRIE values to the parent drug, with only minimal shifts in the predicted Raman frequencies for the alkyne absorption. The formation of these metabolites has been shown to be catalyzed predominantly by the P450 enzyme CYP3A4.[23,24] Western blot analysis confirmed expression of CYP3A4 protein in both KCL22 and KCL22$^{Pon-Res}$ cells (Figure 2a). However, we identified ponatinib as the predominant peak by LC-MS analysis with only trace amounts of the *N*-desmethyl and

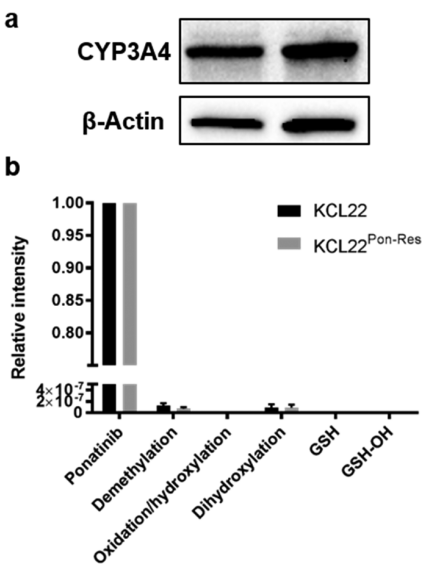

Figure 2. (a) Expression of CYP3A4 in lysates from KCL22 and KCL22$^{Pon-Res}$ cells. β-actin was used as a loading control. (b) Ponatinib and ponatinib metabolites identified by LC-MS. Cells were treated with ponatinib for 1 h prior to analysis. Mean values from five biological repeats expressed relative to ponatinib.

DOI: 10.1021/acs.jmedchem.9b01546
J. Med. Chem. 2020, 63, 2028−2034

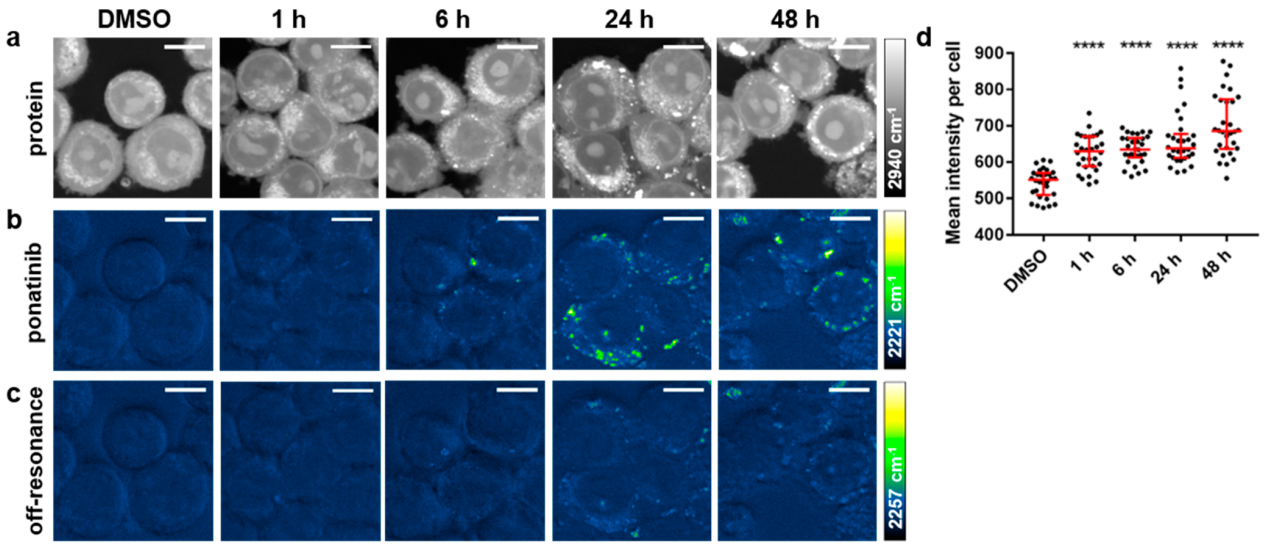

Figure 3. (a–c) Imaging ponatinib uptake in KCL22$^{Pon\text{-}Res}$ cells. KCL22$^{Pon\text{-}Res}$ cells were treated with DMSO (0.0003%, v/v) or ponatinib (500 nM) for 1, 6, 24, or 48 h (left to right). SRS images acquired at (a) 2940 cm^{-1} (CH_3, proteins); (b) 2221 cm^{-1} (C≡C, ponatinib); (c) 2257 cm^{-1} (off-resonance). Images acquired at 1024 × 1024 pixels, 20 μs pixel dwell time, laser power p300, gain 2 with false colors applied to different detection wavenumbers. Scale bars: 10 μm. (d) Mean ponatinib intensity per cell quantified from 2221 cm^{-1} in n = 30 cells, three biological repeats. The Mann–Whitney test was used to compare ponatinib Raman intensity values against the DMSO control.

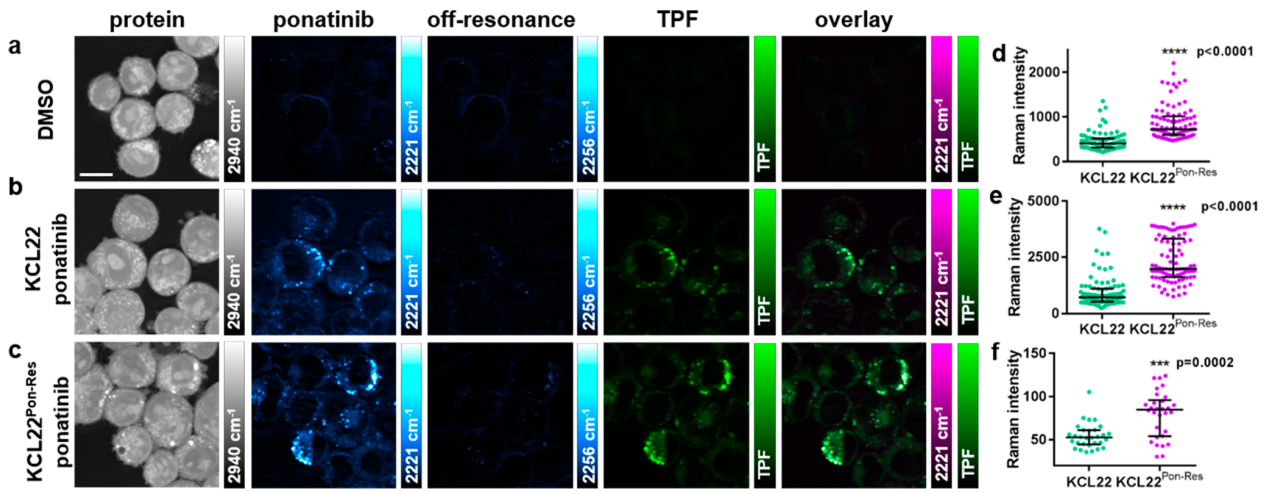

Figure 4. Multimodal imaging and quantitative assessment of ponatinib uptake in KCL22 and KCL22$^{Pon\text{-}Res}$ cell lines. KCL22 cells were treated with (a) DMSO (0.0003%, v/v) or (b) ponatinib (5 μM, 1 h). KCL22 $^{Pon\text{-}Res}$ cells were treated with (c) ponatinib (5 μM ponatinib, 1 h). SRS images acquired at (from left to right) 2940 cm^{-1} (CH_3, proteins), 2221 cm^{-1} (C≡C, ponatinib), 2257 cm^{-1} (off-resonance), TPF image acquired at 861 nm (Lysotracker Green), overlay of ponatinib and TPF. (d) Mean ponatinib Raman intensity. (e) Maximum ponatinib Raman intensity inside the vesicles of each individual cell quantified for KCL22 and KCL22$^{Pon\text{-}Res}$ cells that were treated with 5 μM ponatinib for 1 h, n = 30 cells, three biological repeats. (f) Mean ponatinib Raman intensity quantified outside of the vesicles of individual cells, n = 10, three biological repeats. Images acquired at 1024 × 1024 pixels, 20 μs pixel dwell time, laser power p200 gain 1 with false colors applied to different detection wavenumbers. Scale bars: 10 μm. The Mann–Whitney test was used to compare ponatinib Raman intensity values, ***$p < 0.0001$.

dihydroxylated metabolites present in the CML cells (Figure 2b).

Thus, given the relatively low concentrations of these metabolites in the CML cell lines, and the minimal shifts in their predicted Raman frequencies, their presence is not expected to affect SRS imaging of the intracellular distribution of ponatinib. This conclusion is in sharp contrast to recent imaging studies conducted on neratinib using Raman microscopy, where metabolism directly affects the Raman active motif in the drug and significant vibrational shifts are observed.[18]

Applications of SRS Imaging of Intracellular Drug Concentrations. With the validity of imaging the alkyne in ponatinib by Raman to assess its intracellular distribution established, we conducted a series of experiments to demonstrate the utility of this approach experimentally. CML results from expression of the constitutively active tyrosine kinase BCR-ABL and treatment with TKIs, such as ponatinib, which target BCR-ABL, have been successful in providing improved life expectancy, although resistance prevents long-term durable responses in many patients.[25] There is currently no information on the subcellular distribution and uptake of

DOI: 10.1021/acs.jmedchem.9b01546
J. Med. Chem. 2020, 63, 2028–2034

TKIs in the context of drug resistance, and here we demonstrate the utility of SRS for label-free live cell imaging of ponatinib in a model of ponatinib resistance.

1. Direct Imaging of Ponatinib at Biologically Relevant Doses. In a recent study, spontaneous Raman imaging of the intense fingerprint peak for the TKI neratinib (1386 cm^{-1}) allowed visualization of the drug following incubation at nanomolar concentrations; however, this process requires extended acquisition times (>30 min) using fixed cells.[18] In contrast, SRS microscopy enables up to video-rate imaging speed, allowing live cell imaging. Hyperspectral SRS imaging, which enables drug signals in the fingerprint region to be extracted from the cellular signals, can also been used to follow drug uptake into cells, although as yet this requires incubation with micromolar concentrations of analyte and successful imaging is dependent on 1000-fold enrichment of drugs into lysosomes.[9] The detection sensitivity is the major limitation of intracellular imaging using SRS, with the micromolar concentrations required to detect the molecule of interest often not being physiologically relevant.[9,10,13,14,26] To determine whether we could use SRS to visualize ponatinib at biologically active concentrations, we chose a concentration of ponatinib (500 nM), which is close to the GI_{50} for human $KCL22^{Pon\text{-}Res}$ CML cells (SI, Table S2). The $KCL22^{Pon\text{-}Res}$ cells are a ponatinib-resistant cell line that was generated to understand the drivers of resistance to ponatinib, as resistance to ponatinib is a recognized clinical problem.[27]

Cells were treated with ponatinib (500 nM) for up to 48 h prior to live cell imaging using a custom built SRS microscope,[28] where optimal setup resulted in acquisition speeds of around 45 s per image. Images were acquired by tuning the frequency difference between the pump and Stokes lasers to be resonant with ponatinib (C≡C, 2221 cm^{-1}, SI, Figure S1) or intracellular proteins (CH_3, 2940 cm^{-1}) to provide cellular registration (Figure 3a,b). SRS images can contain background signals from competing pump−probe processes such as cross-phase modulation, transient absorption, and photothermal effects.[29] When the signal-to-noise (S/N) ratio of the SRS image of the drug is low, these background artifacts can be subtracted to remove the unwanted processes from the image. This can be achieved by changing the pump wavelength by a few nanometers, which allows off-resonance images to be acquired (at a difference of 10−30 cm^{-1} from the on-resonance image). This difference image can be used to distinguish true SRS signals from these artifacts (Figure 3c).[30] When imaging with drug concentrations over 5 μM, the SRS S/N is sufficiently high that subtraction is not necessary to visualize ponatinib within the cell (see Figure 4a−c).

We analyzed the ponatinib Raman signal intensity (C≡C, 2221 cm^{-1}) per cell in a population (n = 30) at each time point and compared it to the values of DMSO treated control cells. At each time point, there was a significant increase in Raman signal compared to the control cells, indicating intracellular accumulation of ponatinib (Figure 3d). Ponatinib puncta formed in the cells from 6 h onward, with the largest number of puncta in cells at 24 and 48 h (Figure 3d). This demonstrates that SRS can be used to image live cells treated with biologically relevant doses without the need for any additional labeling or fixation. Many TKIs, including ponatinib (Figure 1b), have strong Raman bands in the cellular fingerprint region, and if one of these bands is sufficiently strong, it can also be used for visualization, as has been demonstrated for neratinib using spontaneous Raman.[18]

2. Determination of the Intracellular Localization of Ponatinib. As ponatinib was concentrated in puncta in the cytoplasm of the cells, it was important to consider which cellular organelles these were, as the known target of ponatinib is the cytoplasmic tyrosine kinase BCR-ABL. Knowing that ponatinib is a weakly basic drug with a pK_a value greater than eight (pK_{a1} = 11.4, pK_{a2} = 8.0)[31] and hence is likely to be protonated in acidic environments, we predicted that it would accumulate in lysosomes or related acidic organelles in the cell. A multimodal imaging approach was used to explore this. Cells were simultaneously incubated with ponatinib (5 μM, 1 h) or DMSO (vehicle control, 1 h) and Lysotracker Green (50 nM, 1 h), a cell-permeable fluorescent dye that stains acidic organelles in live cells (Figure 4). Cells treated with DMSO and stained with Lysotracker Green (Figure 4a) showed no SRS signal at 2221 cm^{-1} (C≡C, ponatinib on-resonance), indicating that the presence of the fluorophore does not give a background SRS signal. In cells treated with ponatinib (Figure 4b,c), we could see colocalization between the SRS signal at 2221 cm^{-1} and the two-photon fluorescence (TPF) signal shown in the merged images, with evidence of lower levels of ponatinib in the cytoplasm, which did not colocalize with the TPF signal. This demonstrates that the majority of ponatinib is trapped within acidic organelles, most likely lysosomes, upon protonation.

There is evidence that lysosomal trapping plays a role in resistance to TKIs by sequestering them away from their intracellular targets and thereby reducing target engagement.[32] Using the TPF signal as a map, the ponatinib Raman intensity was quantified in individual cells which showed an increased ponatinib Raman signal in the resistant $KCL22^{Pon\text{-}Res}$ cells compared to parental KCL22 cells (Figure 4d,e). The mean intensity of ponatinib was increased 1.9-fold in the $KCL22^{Pon\text{-}Res}$ cells compared to parental KCL22 cells (Figure 4d), and the maximum ponatinib signal had increased 2.5-fold (Figure 4e). There was also a significant increase in the ponatinib signal within the cytoplasm of the resistant cells (Figure 4f).

To determine whether differences in lysosomal pH in the cell lines could be contributing to the increased accumulation of ponatinib in the $KCL22^{Pon\text{-}Res}$ cells we used Lysosensor Green, a dye whose fluorescence increases in acidic environments. There was no significant difference in Lysosensor Green signal between the KCL22 and $KCL22^{Pon\text{-}Res}$ cells (SI, Figure S2a,b). However, we did see an increase in expression of the lysosomal marker LAMP1 in the $KCL22^{Pon\text{-}Res}$ cells (SI, Figure S2c,d), indicative of increased lysosome number or lysosome size. To establish whether lysosome biogenesis was differentially regulated in the resistant cells at a transcriptional level, we looked at nuclear transcription factor EB (TFEB), which is a master regulator of lysosome biogenesis.[33] There was a significant increase in nuclear TFEB in the $KCL22^{Pon\text{-}Res}$ cells (SI, Figure S2e,f), indicative of increased lysosome biogenesis in the resistant cells. This may reflect adaptation of the resistant cells to allow them to respond to lysosomal stress.

3. Using SRS Imaging to Enhance Target Engagement Studies. To investigate the importance of lysosomal trapping on ponatinib−target engagement, we used chloroquine (CQ), which is a nonspecific autophagy inhibitor that acts as a lysosomotropic agent, increasing lysosomal pH and ultimately preventing fusion of autophagosomes and lysosomes. It was hypothesized that chloroquine treatment could be used to prevent the increased lysosomal uptake of ponatinib. Pretreat-

DOI: 10.1021/acs.jmedchem.9b01546
J. Med. Chem. 2020, 63, 2028−2034

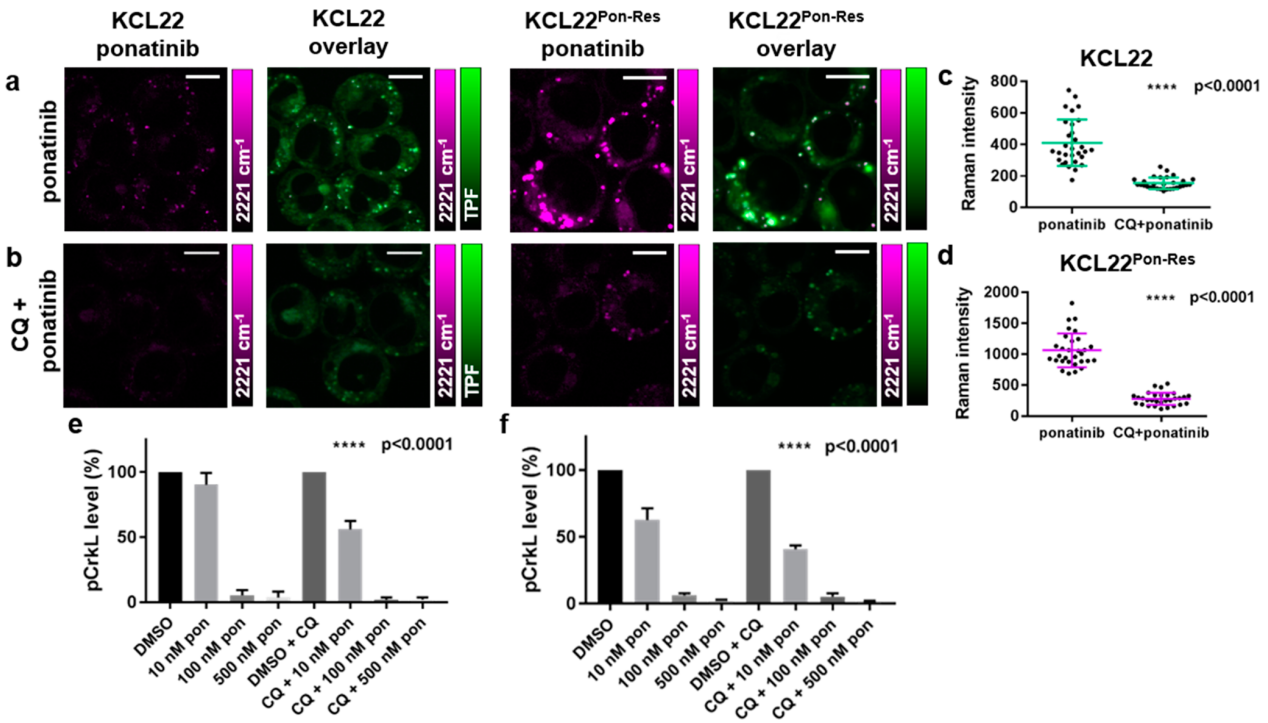

Figure 5. Multimodal imaging and quantitative assessment of the effect of chloroquine treatment on the vesicular uptake of ponatinib. KCL22 and KCL22$^{Pon\text{-}Res}$ cells were treated with (a) ponatinib (5 μM, 1 h), (b) chloroquine (20 μM, 2 h) followed by combination treatment of ponatinib (5 μM, 1 h) and chloroquine (20 μM, 1 h). Images shown (left to right) 2221 cm^{-1} (C≡C, ponatinib), overlay TPF image at 861 nm (Lysotracker Green) merged with 2221 cm^{-1}. (c,d) Mean ponatinib Raman intensity inside the vesicles of each individual cell quantified in (c) KCL22 and (d) KCL22$^{Pon\text{-}Res}$ cell line, n = 10 cells, three biological repeats. Images acquired at 1024 × 1024 pixels, 20 μs pixel dwell time with false colors applied to different detection wavenumbers. Scale bars: 10 μm. (e,f) p-CRKL level quantification from Western blots where KCL22 and KCL22$^{Pon\text{-}Res}$ cells were treated with (left to right) either DMSO (0.0003%, v/v), ponatinib (10, 100, 500 nM, 1 h), or a combination of chloroquine (20 μM, 2 h) pretreatment and ponatinib (10, 100, or 500 nM, 1 h). p-CRKL level was quantified against α-tubulin control and normalized to DMSO using Image Lab Software. One-Way ANOVA (Tukey's multiple comparisons test) was used to compare ponatinib (10 nM) alone vs CQ combination treatment.

ment of KCL22 and KCL22$^{Pon\text{-}Res}$ cells with CQ (20 μM, 2 h) prior to treatment with ponatinib (5 μM, 1 h) significantly reduced the ponatinib Raman signal in both cell lines (Figure 5b–e)

Quantification of ponatinib signal inside lysosomes demonstrated that CQ treatment reduced mean ponatinib concentration in the lysosomes 2.7- and 3.8-fold in the KCL22 and KCL22$^{Pon\text{-}Res}$ cells, respectively, compared to ponatinib alone (Figure 5c,d). To determine whether the inhibition of autophagy by CQ also contributed to the reduced lysosomal accumulation of ponatinib, we used KCL22$^{Pon\text{-}Res}$ CRISPR-*ATG7* knockout cells. ATG7 is a critical autophagy regulator and KCL22$^{Pon\text{-}Res}$ CRISPR-*ATG7* cells have a defect in the autophagy pathway. KCL22$^{Pon\text{-}Res}$ CRISPR-ATG7 and KCL22$^{Pon\text{-}Res}$ CRISPR-Control cells were simultaneously treated with ponatinib (5 μM, 1 h) and labeled with Lysotracker (50 nM, 1 h) before live imaging using SRS (SI, Figure S3). Quantification of relative concentrations of ponatinib by Raman intensity in individual cells of both cell lines demonstrated no significant difference between the cell lines, demonstrating that autophagy does not play a role in ponatinib accumulation in lysosomes. Therefore, reduction of ponatinib concentration in lysosomes upon CQ combination treatment was likely due to the lysosomotropic properties of CQ, which decreased the ability of ponatinib to accumulate in the lysosomes.

Having found that CQ treatment significantly decreased lysosomal trapping of ponatinib in both cell lines, we looked at how this affected BCR-ABL inhibition. BCR-ABL is a cytosolic tyrosine kinase and phosphorylation of CRKL (Tyr207), a direct BCR-ABL substrate, was used as a surrogate for BCR-ABL activity. Pretreatment with CQ significantly increased p-CRKL inhibition at the lowest 10 nM ponatinib dose (Figure 5e,f, and SI, Figure S4). Thus, the reduced lysosome trapping of ponatinib in the CQ treated cells increased BCR-ABL inhibition. Interestingly, we saw a greater inhibition of pCRKL phosphorylation in the KCL22$^{Pon\text{-}Res}$ cells than in KCL22 ponatinib sensitive cells which correlates with the increased cytoplasmic levels of ponatinib in the resistant cells (Figure 4f) and supports a BCR-ABL independent mechanism of ponatinib resistance.[26] This is in contrast to the BCR-ABL dependent resistance to other basic TKIs such as imatinib that are used in the treatment of CML, where CQ can increase target engagement with combined CQ and TKI treatments resulting in enhanced efficacy.[9,34]

■ CONCLUSIONS

This study demonstrates the benefits of SRS microscopy in providing real-time measurements of drug distribution in live cells with high sensitivity and resolution. Use of SRS microscopy has allowed label-free imaging of the TKI ponatinib at biologically relevant concentrations and provided

DOI: 10.1021/acs.jmedchem.9b01546
J. Med. Chem. 2020, 63, 2028–2034

insight into changes in uptake and sequestration of drug that has occurred during the development of acquired drug resistance. We show that tuning the pump wavelength to the alkyne stretch within ponatinib allows SRS imaging within the Raman cellular-silent region following treatment with nanomolar concentrations of ponatinib. Although imaging within the cell silent region increases sensitivity, the recent demonstration that Raman imaging of drugs may also be achieved in the fingerprint region when the drug is enriched in subcellular locales, opens up the possibility of label-free imaging for a wider number of drug candidates and metabolites.[9,16] Furthermore, the addition of small alkyne tags or deuterium substitutions to enable SRS imaging of drugs and small molecules in the cellular-silent region with increased sensitivity, further extends the potential for this technology to provide read-outs of drug kinetics and mechanism of action.[10,17,35,36] Combined with DFT calculations and LC-MS measurements, SRS imaging could be transformative to the drug discovery pipeline by providing important information on drug localization, mechanism of action, and target engagement.

■ ASSOCIATED CONTENT

Supporting Information

The Supporting Information is available free of charge at https://pubs.acs.org/doi/10.1021/acs.jmedchem.9b01546.

Materials and methods; DFT calculated wavenumbers and intensities (I_{Ram}); SRS ponatinib peak in cells; GI_{50} values; Lysosensor FACS; LAMP1 and TFEB immunofluorescence; SRS data for $KCL22^{Pon\text{-}Res}$ CRISPR-Ctrl and $KCL22^{Pon\text{-}Res}$ CRISPR-ATG7 cell lines; p-CRKL Western blots (PDF)

■ AUTHOR INFORMATION

Corresponding Authors

*For V.G.B.: phone, (0044)1316518702; E-mail, v.brunton@ed.ac.uk.

*For A.N.H.: E-mail, Alison.Hulme@ed.ac.uk.

ORCID

Alison N. Hulme: 0000-0002-4619-1506

Valerie G. Brunton: 0000-0002-7778-8794

Author Contributions

The manuscript was written through contributions of all authors.

Notes

The authors declare no competing financial interest.

■ ACKNOWLEDGMENTS

We thank EPSRC and MRC (OPTIMA CDT Studentship to K.S., EP/L016559/1), Cancer Research UK (grant ref: C157/A25140 and C157/A15703), and Prof. Colin Campbell for use of the spontaneous Raman microscope [UK Regenerative Medicine Platform Niche Hub, MRC grant ref MR/K026666/1].

■ ABBREVIATIONS USED

CML, chronic myeloid leukemia; CQ, chloroquine; DFT, density functional theory; EdU, ethynyl deoxyuridine; FACS, fluorescence assisted cell sorting; GI_{50}, growth inhibition by 50%; I_{Ram}, theoretical Raman intensity; LC-MS, liquid chromatography−mass spectrometry; NCE, new chemical entity; RIE, relative intensity to EdU; SRS, stimulated Raman scattering; TFEB, transcription factor EB; TKI, tyrosine kinase inhibitor; TPF, two-photon fluorescence

■ REFERENCES

(1) Hay, M.; Thomas, D. W.; Craighead, J. L.; Economides, C.; Rosenthal, J. Clinical development success rates for investigational drugs. *Nat. Biotechnol.* **2014**, *32*, 40−51.

(2) Shultz, M. D. Two decades under the influence of the rule of five and the changing properties of approved oral drugs. *J. Med. Chem.* **2019**, *62*, 1701−1714.

(3) Waring, M. J.; Arrowsmith, J.; Leach, A. R.; Leeson, P. D.; Mandrell, S.; Owen, R. M.; Pairaudeau, G.; Pennie, W. D.; Pickett, S. D.; Wang, J.; Wallace, O.; Weir, A. An analysis of the attrition of drug candidates from four major pharmaceutical companies. *Nat. Rev. Drug Discovery* **2015**, *14*, 475−486.

(4) Goodwin, R.; Giaccone, G.; Calvert, H.; Lobbezoo, M.; Eisenhauer, E. A. Targeted agents: how to select the winners in preclinical and early clinical studies? *Eur. J. Cancer* **2012**, *48*, 170−178.

(5) Horvath, P.; Aulner, N.; Bickle, M.; Davies, A. M.; Nery, E. D.; Ebner, D.; Montoya, M. C.; Ostling, P.; Pietiainen, V.; Price, L. S.; Shorte, S. L.; Turcatti, G.; von Schantz, C.; Carragher, N. O. Screening out irrelevant cell-based models of disease. *Nat. Rev. Drug Discovery* **2016**, *15*, 751−769.

(6) Paul, S. M.; Mytelka, D. S.; Dunwiddie, C. T.; Persinger, C. C.; Munos, B. H.; Lindborg, S. R.; Schacht, A. L. How to improve R&D productivity: the pharmaceutical industry's grand challenge. *Nat. Rev. Drug Discovery* **2010**, *9*, 203−214.

(7) Cheng, J. X.; Xie, X. S. Vibrational spectroscopic imaging of living systems: An emerging platform for biology and medicine. *Science* **2015**, *350*, No. aaa8870.

(8) Tipping, W. J.; Lee, M.; Serrels, A.; Brunton, V. G.; Hulme, A. N. Stimulated Raman scattering microscopy: an emerging tool for drug discovery. *Chem. Soc. Rev.* **2016**, *45*, 2075−2089.

(9) Fu, D.; Zhou, J.; Zhu, W. S.; Manley, P. W.; Wang, Y. K.; Hood, T.; Wylie, A.; Xie, X. S. Imaging the intracellular distribution of tyrosine kinase inhibitors in living cells with quantitative hyperspectral stimulated Raman scattering. *Nat. Chem.* **2014**, *6*, 614−622.

(10) Tipping, W. J.; Lee, M.; Serrels, A.; Brunton, V. G.; Hulme, A. N. Imaging drug uptake by bioorthogonalstimulated Raman scattering microscopy. *Chem. Sci.* **2017**, *8*, 5606−5615.

(11) Cobice, D. F.; Goodwin, R. J.; Andren, P. E.; Nilsson, A.; Mackay, C. L.; Andrew, R. Future technology insight: mass spectrometry imaging as a tool in drug research and development. *Br. J. Pharmacol.* **2015**, *172*, 3266−3283.

(12) McEwen, A.; Henson, C. Quantitative whole-body autoradiography: past, present and future. *Bioanalysis* **2015**, *7*, 557−568.

(13) Hong, S.; Chen, T.; Zhu, Y.; Li, A.; Huang, Y.; Chen, X. Live-cell stimulated Raman scattering imaging of alkyne-tagged biomolecules. *Angew. Chem., Int. Ed.* **2014**, *53*, 5827−5831.

(14) Wei, L.; Hu, F.; Shen, Y.; Chen, Z.; Yu, Y.; Lin, C.-C.; Wang, M. C.; Min, W. Live-cell imaging of alkyne-tagged small biomolecules by stimulated Raman scattering. *Nat. Methods* **2014**, *11*, 410−412.

(15) Zhao, Z.; Shen, Y.; Hu, F.; Min, W. Applications of vibrational tags in biological imaging by Raman microscopy. *Analyst* **2017**, *142*, 4018−4029.

(16) Pavlovsky, C.; Chan, O.; Talati, C.; Pinilla-Ibarz, J. Ponatinib in the treatment of chronic myeloid leukemia and philadelphia chromosome positive acute lymphoblastic leukemia. *Future Oncol.* **2019**, *15*, 257−269.

(17) Yamakoshi, H.; Dodo, K.; Palonpon, A.; Ando, J.; Fujita, K.; Kawata, S.; Sodeoka, M. Alkyne-tag Raman imaging for visualization of mobile small molecules in live cells. *J. Am. Chem. Soc.* **2012**, *134*, 20681−20689.

(18) Aljakouch, K.; Lechtonen, T.; Yosef, H. K.; Hammoud, M. K.; Alsaidi, W.; Kotting, C.; Mugge, C.; Kourist, R.; El-Mashtoly, S. F.; Gerwert, K. Raman microspectroscopicevidence for the metabolism of a tyrosine kinase inhibitor, neratinib, in cancer cells. *Angew. Chem., Int. Ed.* **2018**, *57*, 7250−7254.

DOI: 10.1021/acs.jmedchem.9b01546
J. Med. Chem. 2020, 63, 2028−2034

(19) Klein, T.; Vajpai, N.; Phillips, J. J.; Davies, G.; Holdgate, G. A.; Phillips, C.; Tucker, J. A.; Norman, R. A.; Scott, A. D.; Higazi, D. R.; Lowe, D.; Thompson, G. S.; Breeze, A. L. Structural and dynamic insights into the energetics of activation loop rearrangement in FGFR1 kinase. *Nat. Commun.* **2015**, *6*, 7877.
(20) Ye, Y. E.; Woodward, C. N.; Narasimhan, N. I. Absorption, metabolism, and excretion of [^{14}C]ponatinib after a single oral dose in humans. *Cancer Chemother. Pharmacol.* **2017**, *79*, 507−518.
(21) Attwa, M. W.; Kadi, A. A.; Darwish, H. W.; Amer, S. M.; AlRabiah, H. LC-ESI-MS/MS identification and characterization of ponatinib in vivo phase I and phase II metabolites. *Clin. Chim. Acta* **2018**, *485*, 144−151.
(22) Kadi, A. A.; Darwish, H. W.; Attwa, M. W.; Amer, S. M. Detection and characterization of ponatinib reactive metabolites by liquid chromatography tandem mass spectrometry and elucidation of bioactivation pathways. *RSC Adv.* **2016**, *6*, 72575−72585.
(23) Lin; Kostov, R.; Huang, J. T.; Henderson, C. J.; Wolf, C. R. Novel pathways of ponatinib disposition catalyzed by CYP1A1 involving generation of potentially toxic metabolites. *J. Pharmacol. Exp. Ther.* **2017**, *363*, 12−19.
(24) Narasimhan, N. I.; Dorer, D. J.; Niland, K.; Haluska, F.; Sonnichsen, D. Effects of Ketoconazole on the Pharmacokinetics of Ponatinib in Healthy Subjects. *J. Clin. Pharmacol.* **2013**, *53*, 974−981.
(25) Cortes, J. E.; Kim, D. W.; Pinilla-Ibarz, J.; le Coutre, P.; Paquette, R.; Chuah, C.; Nicolini, F. E.; Apperley, J. F.; Khoury, H. J.; Talpaz, M.; DiPersio, J.; DeAngelo, D. J.; Abruzzese, E.; Rea, D.; Baccarani, M.; Müller, M. C.; Gambacorti-Passerini, C.; Wong, S.; Lustgarten, S.; Rivera, V. M.; Clackson, T.; Turner, C. D.; Haluska, F. G.; Guilhot, F.; Deininger, M. W.; Hochhaus, A.; Hughes, T.; Goldman, J. M.; Shah, N. P.; Kantarjian, H. A phase 2 trial of ponatinib in Philadelphia chromosome-positive leukemias. *N. Engl. J. Med.* **2013**, *369*, 1783−1796.
(26) Lee, H. J.; Zhang, W.; Zhang, D.; Yang, Y.; Liu, B.; Barker, E. L.; Buhman, K. K.; Slipchenko, L. V.; Dai, M.; Cheng, J. X. Assessing cholesterol storage in live cells and *C. elegans* by stimulated Raman scattering imaging of phenyl-Diyne cholesterol. *Sci. Rep.* **2015**, *5*, 7930.
(27) Mitchell, R.; Hopcroft, L. E. M.; Baquero, P.; Allan, E. K.; Hewit, K.; James, D.; Hamilton, G.; Mukhopadhyay, A.; O'Prey, J.; Hair, A.; Melo, J. V.; Chan, E.; Ryan, K. M.; Maguer-Satta, V.; Druker, B. J.; Clark, R. E.; Mitra, S.; Herzyk, P.; Nicolini, F. E.; Salomoni, P.; Shanks, E.; Calabretta, B.; Holyoake, T. L.; Helgason, G. V. Targeting BCR-ABL-independent TKI resistance in chronic myeloid leukemia by mTOR and autophagy inhibition. *J. Natl. Cancer Inst.* **2018**, *110*, 467−478.
(28) Lee, M.; Downes, A.; Chau, Y.-Y.; Serrels, B.; Hastie, N.; Elfick, A.; Brunton, V. G.; Frame, M. C.; Serrels, A. In vivo imaging of the tumor and its associated microenvironment using combined CARS/2-photon microscopy. *IntraVital* **2015**, *4*, No. e1055430.
(29) Berto, P.; Andresen, E. R.; Rigneault, H. Background-free stimulated Raman spectroscopy and microscopy. *Phys. Rev. Lett.* **2014**, *112*, 053905.
(30) Zhang, D.; Slipchenko, M. N.; Leaird, D. E.; Weiner, A. M.; Cheng, J.-X. Spectrally modulated stimulated Raman scattering imaging with an angle-to-wavelength pulse shaper. *Opt. Express* **2013**, *21*, 13864−13874.
(31) Iclusig (Ponatinib) Tablets for Oral Use. *U.S. Food and Drug Administration Medication Guide*; U.S. Food and Drug Administration, 2016; https://www.accessdata.fda.gov/drugsatfda_docs/label/2016/203469s022lbl.pdf (accessed Sept 6th, 2019).
(32) Zhitomirsky, B.; Assaraf, Y. G. Lysosomes as mediators of drug resistance in cancer. *Drug Resist. Updates* **2016**, *24*, 23−33.
(33) Sardiello, M. Transcription factor EB: from master coordinator of lysosomal pathways to candidate therapeutic target in degenerative storage diseases. *Ann. N. Y. Acad. Sci.* **2016**, *1371*, 3−14.
(34) Bellodi, C.; Lidonnici, M. R.; Hamilton, A.; Helgason, G. V.; Soliera, A. R.; Ronchetti, M.; Galavotti, S.; Young, K. W.; Selmi, T.; Yacobi, R.; Van Etten, R.; Donato, N.; Hunter, A.; Dinsdale, D.; Tirro, E.; Vigneri, P.; Nicotera, P.; Dyer, M. J.; Holyoake, T.; Salomoni, P.; Calabretta, B. Targeting autophagy potentiates tyrosine kinase inhibitor-induced cell death in Philadelphia chromosome-positive cells, including primary CML stem cells. *J. Clin. Invest.* **2009**, *119*, 1109−1123.
(35) Chiu, W. S.; Belsey, N. A.; Garrett, N. L.; Moger, J.; Delgado-Charro, M. B.; Guy, R. H. Molecular diffusion in the human nail measured by stimulated Raman scattering microscopy. *Proc. Natl. Acad. Sci. U. S. A.* **2015**, *112*, 7725−7730.
(36) Gaschler, M. M.; Hu, F.; Feng, H.; Linkermann, A.; Min, W.; Stockwell, B. R. Determination of the subcellular localization and mechanism of action of ferrostatins in suppressing ferroptosis. *ACS Chem. Biol.* **2018**, *13*, 1013−1020.

DOI: 10.1021/acs.jmedchem.9b01546
J. Med. Chem. 2020, 63, 2028−2034

SPRINGER NATURE

Phase II and Phase III attrition rates 2011–2012

Author: John Arrowsmith et al
Publication: Nature Reviews Drug Discovery
Publisher: Springer Nature
Date: Aug 1, 2013

Order Completed

Thank you for your order.

This Agreement between Kristel Sepp ("You") and Springer Nature ("Springer Nature") consists of your license details and the terms and conditions provided by Springer Nature and Copyright Clearance Center.

Your confirmation email will contain your order number for future reference.

License Number	4896510806284
License date	Aug 26, 2020

Printable Details

Licensed Content

Licensed Content Publisher	Springer Nature
Licensed Content Publication	Nature Reviews Drug Discovery
Licensed Content Title	Phase II and Phase III attrition rates 2011–2012
Licensed Content Author	John Arrowsmith et al
Licensed Content Date	Aug 1, 2013

Order Details

Type of Use	Thesis/Dissertation
Requestor type	academic/university or research institute
Format	print and electronic
Portion	figures/tables/illustrations
Number of figures/tables/illustrations	1
High-res required	no
Will you be translating?	no
Circulation/distribution	1 - 29
Author of this Springer Nature content	no

About Your Work

Title	Utilising Stimulated Raman Scattering Microscopy To Study Intracellular Distribution of Label-Free Ponatinib in Live Cells
Institution name	University of Edinburgh
Expected presentation date	Nov 2020

Additional Data

Portions	Figure 1

Requestor Location

Requestor Location	Kristel Sepp 6 Allanfield Place Flat 3 Edinburgh, other EH7 5AJ United Kingdom Attn: Miss Kristel Sepp

Tax Details

Price

Total	0.00 GBP

Total: 0.00 GBP

CLOSE WINDOW ORDER MORE

SPRINGER NATURE

Live-cell imaging of alkyne-tagged small biomolecules by stimulated Raman scattering

Author: Lu Wei et al
Publication: Nature Methods
Publisher: Springer Nature
Date: Mar 2, 2014

Order Completed

Thank you for your order.

This Agreement between Kristel Sepp ("You") and Springer Nature ("Springer Nature") consists of your license details and the terms and conditions provided by Springer Nature and Copyright Clearance Center.

Your confirmation email will contain your order number for future reference.

License Number	4896520104676
License date	Aug 26, 2020

Printable Details

Licensed Content

Licensed Content Publisher	Springer Nature
Licensed Content Publication	Nature Methods
Licensed Content Title	Live-cell imaging of alkyne-tagged small biomolecules by stimulated Raman scattering
Licensed Content Author	Lu Wei et al
Licensed Content Date	Mar 2, 2014

Order Details

Type of Use	Thesis/Dissertation
Requestor type	academic/university or research institute
Format	print and electronic
Portion	figures/tables/illustrations
Number of figures/tables/illustrations	2
High-res required	no
Will you be translating?	no
Circulation/distribution	1 - 29
Author of this Springer Nature content	no

About Your Work

Title	Utilising Stimulated Raman Scattering Microscopy To Study Intracellular Distribution of Label-Free Ponatinib in Live Cells
Institution name	University of Edinburgh
Expected presentation date	Nov 2020

Additional Data

Portions	Figure 2a and SI Figure 7

Requestor Location

Requestor Location	Kristel Sepp 6 Allanfield Place Flat 3 Edinburgh, other EH7 5AJ United Kingdom Attn: Miss Kristel Sepp

Tax Details

Price

Total	0.00 GBP

Total: 0.00 GBP

CLOSE WINDOW ORDER MORE

Vibrational Imaging of Glucose Uptake Activity in Live Cells and Tissues by Stimulated Raman Scattering

Author: Fanghao Hu, Zhixing Chen, Luyuan Zhang, et al

Publication: Angewandte Chemie International Edition

Publisher: John Wiley and Sons

Date: Jul 16, 2015

Order Completed

Thank you for your order.

This Agreement between Kristel Sepp ("You") and John Wiley and Sons ("John Wiley and Sons") consists of your license details and the terms and conditions provided by John Wiley and Sons and Copyright Clearance Center.

Your confirmation email will contain your order number for future reference.

License Number	4896520457861
License date	Aug 26, 2020

Printable Details

Licensed Content

Licensed Content Publisher	John Wiley and Sons
Licensed Content Publication	Angewandte Chemie International Edition
Licensed Content Title	Vibrational Imaging of Glucose Uptake Activity in Live Cells and Tissues by Stimulated Raman Scattering
Licensed Content Author	Fanghao Hu, Zhixing Chen, Luyuan Zhang, et al
Licensed Content Date	Jul 16, 2015
Licensed Content Volume	54
Licensed Content Issue	34
Licensed Content Pages	5

Order Details

Type of use	Dissertation/Thesis
Requestor type	University/Academic
Format	Print and electronic
Portion	Figure/table
Number of figures/tables	1
Will you be translating?	No

About Your Work

Title	Utilising Stimulated Raman Scattering Microscopy To Study Intracellular Distribution of Label-Free Ponatinib in Live Cells
Institution name	University of Edinburgh
Expected presentation date	Nov 2020

Additional Data

Portions	Figure 5a

Requestor Location

Requestor Location	Kristel Sepp 6 Allanfield Place Flat 3 Edinburgh, other EH7 5AJ United Kingdom Attn: Miss Kristel Sepp

Tax Details

Publisher Tax ID	EU826007151

Price

Total	0.00 GBP

Would you like to purchase the full text of this article? If so, please continue on to the content ordering system located here: Purchase PDF
If you click on the buttons below or close this window, you will not be able to return to the content ordering system.

Total: 0.00 GBP

CLOSE WINDOW ORDER MORE

SPRINGER NATURE

Supermultiplexed optical imaging and barcoding with engineered polyynes

Author: Fanghao Hu et al
Publication: Nature Methods
Publisher: Springer Nature
Date: Jan 15, 2018

Order Completed

Thank you for your order.

This Agreement between Kristel Sepp ("You") and Springer Nature ("Springer Nature") consists of your license details and the terms and conditions provided by Springer Nature and Copyright Clearance Center.

Your confirmation email will contain your order number for future reference.

License Number	4896521244297
License date	Aug 26, 2020

Printable Details

Licensed Content

Licensed Content Publisher	Springer Nature
Licensed Content Publication	Nature Methods
Licensed Content Title	Supermultiplexed optical imaging and barcoding with engineered polyynes
Licensed Content Author	Fanghao Hu et al
Licensed Content Date	Jan 15, 2018

Order Details

Type of Use	Thesis/Dissertation
Requestor type	academic/university or research institute
Format	print and electronic
Portion	figures/tables/illustrations
Number of figures/tables/illustrations	2
High-res required	no
Will you be translating?	no
Circulation/distribution	1 - 29
Author of this Springer Nature content	no

About Your Work

Title	Utilising Stimulated Raman Scattering Microscopy To Study Intracellular Distribution of Label-Free Ponatinib in Live Cells
Institution name	University of Edinburgh
Expected presentation date	Nov 2020

Additional Data

Portions	Figure 2a, Figure 3

Requestor Location

Requestor Location	Kristel Sepp 6 Allanfield Place Flat 3 Edinburgh, other EH7 5AJ United Kingdom Attn: Miss Kristel Sepp

Tax Details

Price

Total	0.00 GBP

Total: 0.00 GBP

CLOSE WINDOW ORDER MORE

Assessing Cholesterol Storage in Live Cells and C. elegans by Stimulated Raman Scattering Imaging of Phenyl-Diyne Cholesterol

Author: Hyeon Jeong Lee et al

Publication: Scientific Reports

Publisher: Springer Nature

Date: Jan 22, 2015

Live-Cell Stimulated Raman Scattering Imaging of Alkyne-Tagged Biomolecules

Author: Senlian Hong, Tao Chen, Yuntao Zhu, et al
Publication: Angewandte Chemie International Edition
Publisher: John Wiley and Sons
Date: Apr 17, 2014

Order Completed

Thank you for your order.

This Agreement between Kristel Sepp ("You") and John Wiley and Sons ("John Wiley and Sons") consists of your license details and the terms and conditions provided by John Wiley and Sons and Copyright Clearance Center.

Your confirmation email will contain your order number for future reference.

License Number	4896530373410
License date	Aug 26, 2020

Printable Details

Licensed Content

Licensed Content Publisher	John Wiley and Sons
Licensed Content Publication	Angewandte Chemie International Edition
Licensed Content Title	Live-Cell Stimulated Raman Scattering Imaging of Alkyne-Tagged Biomolecules
Licensed Content Author	Senlian Hong, Tao Chen, Yuntao Zhu, et al
Licensed Content Date	Apr 17, 2014
Licensed Content Volume	53
Licensed Content Issue	23
Licensed Content Pages	5

Order Details

Type of use	Dissertation/Thesis
Requestor type	University/Academic
Format	Print and electronic
Portion	Figure/table
Number of figures/tables	1
Will you be translating?	No

About Your Work

Title	Utilising Stimulated Raman Scattering Microscopy To Study Intracellular Distribution of Label-Free Ponatinib in Live Cells
Institution name	University of Edinburgh
Expected presentation date	Nov 2020

Additional Data

Portions	Figure S2

Requestor Location

Requestor Location	Kristel Sepp 6 Allanfield Place Flat 3 Edinburgh, other EH7 5AJ United Kingdom Attn: Miss Kristel Sepp

Tax Details

Publisher Tax ID	EU826007151

Price

Total	0.00 GBP

Would you like to purchase the full text of this article? If so, please continue on to the content ordering system located here: Purchase PDF
If you click on the buttons below or close this window, you will not be able to return to the content ordering system.

Total: 0.00 GBP

CLOSE WINDOW ORDER MORE

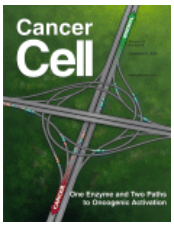

AP24534, a Pan-BCR-ABL Inhibitor for Chronic Myeloid Leukemia, Potently Inhibits the T315I Mutant and Overcomes Mutation-Based Resistance

Author:
Thomas O'Hare,William C. Shakespeare,Xiaotian Zhu,Christopher A. Eide,Victor M. Rivera,Frank Wang,Lauren T. Adrian,Tianjun Zhou,Wei-Sheng Huang,Qihong Xu,Chester A. Metcalf,Jeffrey W. Tyner,Marc M. Loriaux,Amie S. Corbin,Scott Wardwell,Yaoyu Ning et al.

Publication: Cancer Cell

Publisher: Elsevier

Date: 3 November 2009

Order Completed

Thank you for your order.

This Agreement between Kristel Sepp ("You") and Elsevier ("Elsevier") consists of your license details and the terms and conditions provided by Elsevier and Copyright Clearance Center.

Your confirmation email will contain your order number for future reference.

License Number	4896600203228
License date	Aug 26, 2020

Printable Details

Licensed Content

Licensed Content Publisher	Elsevier
Licensed Content Publication	Cancer Cell
Licensed Content Title	AP24534, a Pan-BCR-ABL Inhibitor for Chronic Myeloid Leukemia, Potently Inhibits the T315I Mutant and Overcomes Mutation-Based Resistance
Licensed Content Author	Thomas O'Hare,William C. Shakespeare,Xiaotian Zhu,Christopher A. Eide,Victor M. Rivera,Frank Wang,Lauren T. Adrian,Tianjun Zhou,Wei-Sheng Huang,Qihong Xu,Chester A. Metcalf,Jeffrey W. Tyner,Marc M. Loriaux,Amie S. Corbin,Scott Wardwell,Yaoyu Ning et al.
Licensed Content Date	Nov 3, 2009
Licensed Content Volume	16
Licensed Content Issue	5
Licensed Content Pages	12
Journal Type	S&T

Order Details

Type of Use	reuse in a thesis/dissertation
Portion	figures/tables/illustrations
Number of figures/tables/illustrations	1
Format	both print and electronic
Are you the author of this Elsevier article?	No
Will you be translating?	No

About Your Work

Title	Utilising Stimulated Raman Scattering Microscopy To Study Intracellular Distribution of Label-Free Ponatinib in Live Cells
Institution name	University of Edinburgh
Expected presentation date	Nov 2020

Additional Data

Portions	Figure 1C

Requestor Location

Requestor Location	Kristel Sepp 6 Allanfield Place Flat 3 Edinburgh, other EH7 5AJ United Kingdom Attn: Miss Kristel Sepp

Tax Details

Publisher Tax ID	GB 494 6272 12

Price

Total	0.00 GBP

Total: 0.00 GBP

CLOSE WINDOW ORDER MORE

Copyright Clearance Center Marketplace™

Royal Society of Chemistry - License Terms and Conditions

This is a License Agreement between Kristel Sepp ("You") and Royal Society of Chemistry ("Publisher") provided by Copyright Clearance Center ("CCC"). The license consists of your order details, the terms and conditions provided by Royal Society of Chemistry, and the CCC terms and conditions.

All payments must be made in full to CCC.

Order Date	11-Jul-2020	**Type of Use**	Republish in a thesis/dissertation
Order license ID	1047739-1		
ISSN	1364-5528	**Publisher**	Royal Society of Chemistry
		Portion	Image/photo/illustration

LICENSED CONTENT

Publication Title	The analyst online	**Country**	United Kingdom of Great Britain and Northern Ireland
Author/Editor	Society of Public Analysts (Great Britain), Chemical Society (Great Britain), Society for Analytical Chemistry, Society of Public Analysts (Great Britain), Royal Society of Chemistry (Great Britain)	**Rightsholder**	Royal Society of Chemistry
		Publication Type	e-Journal
		URL	http://www.rsc.org/is/journals/current/analyst/anlcon.htm
Date	01/01/1876		
Language	English		

REQUEST DETAILS

Portion Type	Image/photo/illustration	**Distribution**	Worldwide
Number of images / photos / illustrations	1	**Translation**	Original language of publication
Format (select all that apply)	Electronic	**Copies for the disabled?**	No
		Minor editing privileges?	No
Who will republish the content?	Academic institution	**Incidental promotional use?**	No
Duration of Use	Life of current edition	**Currency**	GBP
Lifetime Unit Quantity	Up to 499		
Rights Requested	Main product		

NEW WORK DETAILS

Title	Utilising Stimulated Raman Scattering Microscopy To Study Intracellular Distribution of Label-Free Ponatinib in Live Cells	**Institution name**	University of Edinburgh
		Expected presentation date	2020-11-30
Instructor name	Prof Alison N Hulme		

ADDITIONAL DETAILS

Order reference number	N/A

The requesting person / organization to appear on the license	Kristel Sepp

REUSE CONTENT DETAILS

Title, description or numeric reference of the portion(s)	Figure 1	**Title of the article/chapter the portion is from**	Label-free imaging of drug distribution and metabolism in colon cancer cells by Raman microscopy
Editor of portion(s)	N/A	**Author of portion(s)**	Society of Public Analysts (Great Britain); Chemical Society (Great Britain); Society for Analytical Chemistry; Society of Public Analysts (Great Britain); Royal Society of Chemistry (Great Britain)
Volume of serial or monograph	N/A	**Issue, if republishing an article from a serial**	N/A
Page or page range of portion	1157	**Publication date of portion**	2013-12-20

CCC Republication Terms and Conditions

1. Description of Service; Defined Terms. This Republication License enables the User to obtain licenses for republication of one or more copyrighted works as described in detail on the relevant Order Confirmation (the "Work(s)"). Copyright Clearance Center, Inc. ("CCC") grants licenses through the Service on behalf of the rightsholder identified on the Order Confirmation (the "Rightsholder"). "Republication", as used herein, generally means the inclusion of a Work, in whole or in part, in a new work or works, also as described on the Order Confirmation. "User", as used herein, means the person or entity making such republication.

2. The terms set forth in the relevant Order Confirmation, and any terms set by the Rightsholder with respect to a particular Work, govern the terms of use of Works in connection with the Service. By using the Service, the person transacting for a republication license on behalf of the User represents and warrants that he/she/it (a) has been duly authorized by the User to accept, and hereby does accept, all such terms and conditions on behalf of User, and (b) shall inform User of all such terms and conditions. In the event such person is a "freelancer" or other third party independent of User and CCC, such party shall be deemed jointly a "User" for purposes of these terms and conditions. In any event, User shall be deemed to have accepted and agreed to all such terms and conditions if User republishes the Work in any fashion.

3. Scope of License; Limitations and Obligations.

    3.1. All Works and all rights therein, including copyright rights, remain the sole and exclusive property of the Rightsholder. The license created by the exchange of an Order Confirmation (and/or any invoice) and payment by User of the full amount set forth on that document includes only those rights expressly set forth in the Order Confirmation and in these terms and conditions, and conveys no other rights in the Work(s) to User. All rights not expressly granted are hereby reserved.

    3.2. General Payment Terms: You may pay by credit card or through an account with us payable at the end of the month. If you and we agree that you may establish a standing account with CCC, then the following terms apply: Remit Payment to: Copyright Clearance Center, 29118 Network Place, Chicago, IL 60673-1291. Payments Due: Invoices are payable upon their delivery to you (or upon our notice to you that they are available to you for downloading). After 30 days, outstanding amounts will be subject to a service charge of 1-1/2% per month or, if less, the maximum rate allowed by applicable law. Unless otherwise specifically set forth in the Order Confirmation or in a separate written agreement signed by CCC, invoices are due and payable on "net 30" terms. While User may exercise the rights licensed immediately upon issuance of the Order Confirmation, the license is automatically revoked and is null and void, as if it had never been issued, if complete payment for the license is not received on a timely basis either from User directly or through a payment agent, such as a credit card company.

3.3. Unless otherwise provided in the Order Confirmation, any grant of rights to User (i) is "one-time" (including the editions and product family specified in the license), (ii) is non-exclusive and non-transferable and (iii) is subject to any and all limitations and restrictions (such as, but not limited to, limitations on duration of use or circulation) included in the Order Confirmation or invoice and/or in these terms and conditions. Upon completion of the licensed use, User shall either secure a new permission for further use of the Work(s) or immediately cease any new use of the Work(s) and shall render inaccessible (such as by deleting or by removing or severing links or other locators) any further copies of the Work (except for copies printed on paper in accordance with this license and still in User's stock at the end of such period).

3.4. In the event that the material for which a republication license is sought includes third party materials (such as photographs, illustrations, graphs, inserts and similar materials) which are identified in such material as having been used by permission, User is responsible for identifying, and seeking separate licenses (under this Service or otherwise) for, any of such third party materials; without a separate license, such third party materials may not be used.

3.5. Use of proper copyright notice for a Work is required as a condition of any license granted under the Service. Unless otherwise provided in the Order Confirmation, a proper copyright notice will read substantially as follows: "Republished with permission of [Rightsholder's name], from [Work's title, author, volume, edition number and year of copyright]; permission conveyed through Copyright Clearance Center, Inc. " Such notice must be provided in a reasonably legible font size and must be placed either immediately adjacent to the Work as used (for example, as part of a by-line or footnote but not as a separate electronic link) or in the place where substantially all other credits or notices for the new work containing the republished Work are located. Failure to include the required notice results in loss to the Rightsholder and CCC, and the User shall be liable to pay liquidated damages for each such failure equal to twice the use fee specified in the Order Confirmation, in addition to the use fee itself and any other fees and charges specified.

3.6. User may only make alterations to the Work if and as expressly set forth in the Order Confirmation. No Work may be used in any way that is defamatory, violates the rights of third parties (including such third parties' rights of copyright, privacy, publicity, or other tangible or intangible property), or is otherwise illegal, sexually explicit or obscene. In addition, User may not conjoin a Work with any other material that may result in damage to the reputation of the Rightsholder. User agrees to inform CCC if it becomes aware of any infringement of any rights in a Work and to cooperate with any reasonable request of CCC or the Rightsholder in connection therewith.

4. Indemnity. User hereby indemnifies and agrees to defend the Rightsholder and CCC, and their respective employees and directors, against all claims, liability, damages, costs and expenses, including legal fees and expenses, arising out of any use of a Work beyond the scope of the rights granted herein, or any use of a Work which has been altered in any unauthorized way by User, including claims of defamation or infringement of rights of copyright, publicity, privacy or other tangible or intangible property.

5. Limitation of Liability. UNDER NO CIRCUMSTANCES WILL CCC OR THE RIGHTSHOLDER BE LIABLE FOR ANY DIRECT, INDIRECT, CONSEQUENTIAL OR INCIDENTAL DAMAGES (INCLUDING WITHOUT LIMITATION DAMAGES FOR LOSS OF BUSINESS PROFITS OR INFORMATION, OR FOR BUSINESS INTERRUPTION) ARISING OUT OF THE USE OR INABILITY TO USE A WORK, EVEN IF ONE OF THEM HAS BEEN ADVISED OF THE POSSIBILITY OF SUCH DAMAGES. In any event, the total liability of the Rightsholder and CCC (including their respective employees and directors) shall not exceed the total amount actually paid by User for this license. User assumes full liability for the actions and omissions of its principals, employees, agents, affiliates, successors and assigns.

6. Limited Warranties. THE WORK(S) AND RIGHT(S) ARE PROVIDED "AS IS". CCC HAS THE RIGHT TO GRANT TO USER THE RIGHTS GRANTED IN THE ORDER CONFIRMATION DOCUMENT. CCC AND THE RIGHTSHOLDER DISCLAIM ALL OTHER WARRANTIES RELATING TO THE WORK(S) AND RIGHT(S), EITHER EXPRESS OR IMPLIED, INCLUDING WITHOUT LIMITATION IMPLIED WARRANTIES OF MERCHANTABILITY OR FITNESS FOR A PARTICULAR PURPOSE. ADDITIONAL RIGHTS MAY BE REQUIRED TO USE ILLUSTRATIONS, GRAPHS, PHOTOGRAPHS, ABSTRACTS, INSERTS OR OTHER PORTIONS OF THE WORK (AS OPPOSED TO THE ENTIRE WORK) IN A MANNER CONTEMPLATED BY USER; USER UNDERSTANDS AND AGREES THAT NEITHER CCC NOR THE RIGHTSHOLDER MAY HAVE SUCH ADDITIONAL RIGHTS TO GRANT.

7. Effect of Breach. Any failure by User to pay any amount when due, or any use by User of a Work beyond the scope of the license set forth in the Order Confirmation and/or these terms and conditions, shall be a material breach of

the license created by the Order Confirmation and these terms and conditions. Any breach not cured within 30 days of written notice thereof shall result in immediate termination of such license without further notice. Any unauthorized (but licensable) use of a Work that is terminated immediately upon notice thereof may be liquidated by payment of the Rightsholder's ordinary license price therefor; any unauthorized (and unlicensable) use that is not terminated immediately for any reason (including, for example, because materials containing the Work cannot reasonably be recalled) will be subject to all remedies available at law or in equity, but in no event to a payment of less than three times the Rightsholder's ordinary license price for the most closely analogous licensable use plus Rightsholder's and/or CCC's costs and expenses incurred in collecting such payment.

8. Miscellaneous.

    8.1. User acknowledges that CCC may, from time to time, make changes or additions to the Service or to these terms and conditions, and CCC reserves the right to send notice to the User by electronic mail or otherwise for the purposes of notifying User of such changes or additions; provided that any such changes or additions shall not apply to permissions already secured and paid for.

    8.2. Use of User-related information collected through the Service is governed by CCC's privacy policy, available online here:https://marketplace.copyright.com/rs-ui-web/mp/privacy-policy

    8.3. The licensing transaction described in the Order Confirmation is personal to User. Therefore, User may not assign or transfer to any other person (whether a natural person or an organization of any kind) the license created by the Order Confirmation and these terms and conditions or any rights granted hereunder; provided, however, that User may assign such license in its entirety on written notice to CCC in the event of a transfer of all or substantially all of User's rights in the new material which includes the Work(s) licensed under this Service.

    8.4. No amendment or waiver of any terms is binding unless set forth in writing and signed by the parties. The Rightsholder and CCC hereby object to any terms contained in any writing prepared by the User or its principals, employees, agents or affiliates and purporting to govern or otherwise relate to the licensing transaction described in the Order Confirmation, which terms are in any way inconsistent with any terms set forth in the Order Confirmation and/or in these terms and conditions or CCC's standard operating procedures, whether such writing is prepared prior to, simultaneously with or subsequent to the Order Confirmation, and whether such writing appears on a copy of the Order Confirmation or in a separate instrument.

    8.5. The licensing transaction described in the Order Confirmation document shall be governed by and construed under the law of the State of New York, USA, without regard to the principles thereof of conflicts of law. Any case, controversy, suit, action, or proceeding arising out of, in connection with, or related to such licensing transaction shall be brought, at CCC's sole discretion, in any federal or state court located in the County of New York, State of New York, USA, or in any federal or state court whose geographical jurisdiction covers the location of the Rightsholder set forth in the Order Confirmation. The parties expressly submit to the personal jurisdiction and venue of each such federal or state court.If you have any comments or questions about the Service or Copyright Clearance Center, please contact us at 978-750-8400 or send an e-mail to support@copyright.com.

v 1.1

License Details

This Agreement between Kristel Sepp ("You") and Springer Nature ("Springer Nature") consists of your license details and the terms and conditions provided by Springer Nature and Copyright Clearance Center.

Print Copy

License Number	4865870337130
License date	Jul 11, 2020
Licensed Content Publisher	Springer Nature
Licensed Content Publication	Nature Chemistry
Licensed Content Title	Imaging the intracellular distribution of tyrosine kinase inhibitors in living cells with quantitative hyperspectral stimulated Raman scattering
Licensed Content Author	Dan Fu et al
Licensed Content Date	May 25, 2014
Type of Use	Thesis/Dissertation
Requestor type	academic/university or research institute
Format	print and electronic
Portion	figures/tables/illustrations
Number of figures/tables/illustrations	2
High-res required	no
Will you be translating?	no
Circulation/distribution	1 - 29
Author of this Springer Nature content	no
Title	Utilising Stimulated Raman Scattering Microscopy To Study Intracellular Distribution of Label-Free Ponatinib in Live Cells
Institution name	University of Edinburgh
Expected presentation date	Nov 2020
Portions	Figure 1b on page 615, Figure 3 (a-i) on page 617
Requestor Location	Kristel Sepp 6 Allanfield Place Flat 3 Edinburgh, other EH7 5AJ United Kingdom Attn: Miss Kristel Sepp
Total	**0.00 USD**

BACK

License Details

This Agreement between Kristel Sepp ("You") and John Wiley and Sons ("John Wiley and Sons") consists of your license details and the terms and conditions provided by John Wiley and Sons and Copyright Clearance Center.

Print Copy

License Number	4865860422390
License date	Jul 11, 2020
Licensed Content Publisher	John Wiley and Sons
Licensed Content Publication	Angewandte Chemie International Edition
Licensed Content Title	Raman Microspectroscopic Evidence for the Metabolism of a Tyrosine Kinase Inhibitor, Neratinib, in Cancer Cells
Licensed Content Author	Klaus Gerwert, Samir F. El-Mashtoly, Robert Kourist, et al
Licensed Content Date	May 16, 2018
Licensed Content Volume	57
Licensed Content Issue	24
Licensed Content Pages	5
Type of Use	Dissertation/Thesis
Requestor type	University/Academic
Format	Print and electronic
Portion	Figure/table
Number of figures/tables	2
Will you be translating?	No
Title	Utilising Stimulated Raman Scattering Microscopy To Study Intracellular Distribution of Label-Free Ponatinib in Live Cells
Institution name	University of Edinburgh
Expected presentation date	Nov 2020
Portions	Figure 2a on Page 7251 and Figure S12 (A-C,F-G) on Page 23 of SI
Requestor Location	Kristel Sepp 6 Allanfield Place Flat 3 Edinburgh, other EH7 5AJ United Kingdom Attn: Miss Kristel Sepp
Publisher Tax ID	EU826007151
Total	**0.00 GBP**

BACK

Copyright Clearance Center Marketplace™

Royal Society of Chemistry - License Terms and Conditions

This is a License Agreement between Kristel Sepp ("You") and Royal Society of Chemistry ("Publisher") provided by Copyright Clearance Center ("CCC"). The license consists of your order details, the terms and conditions provided by Royal Society of Chemistry, and the CCC terms and conditions.

All payments must be made in full to CCC.

Order Date	11-Jul-2020	**Type of Use**	Republish in a thesis/dissertation
Order license ID	1047741-1		
ISSN	1364-5528	**Publisher**	Royal Society of Chemistry
		Portion	Image/photo/illustration

LICENSED CONTENT

Publication Title	The analyst online	**Country**	United Kingdom of Great Britain and Northern Ireland
Author/Editor	Society of Public Analysts (Great Britain), Chemical Society (Great Britain), Society for Analytical Chemistry, Society of Public Analysts (Great Britain), Royal Society of Chemistry (Great Britain)	**Rightsholder**	Royal Society of Chemistry
		Publication Type	e-Journal
		URL	http://www.rsc.org/is/journals/current/analyst/anlcon.htm
Date	01/01/1876		
Language	English		

REQUEST DETAILS

Portion Type	Image/photo/illustration	**Distribution**	Worldwide
Number of images / photos / illustrations	2	**Translation**	Original language of publication
Format (select all that apply)	Electronic	**Copies for the disabled?**	No
		Minor editing privileges?	No
Who will republish the content?	Academic institution	**Incidental promotional use?**	No
Duration of Use	Life of current edition	**Currency**	GBP
Lifetime Unit Quantity	Up to 499		
Rights Requested	Main product		

NEW WORK DETAILS

Title	Utilising Stimulated Raman Scattering Microscopy To Study Intracellular Distribution of Label-Free Ponatinib in Live Cells	**Institution name**	University of Edinburgh
		Expected presentation date	2020-11-30
Instructor name	Prof Alison N Hulme		

ADDITIONAL DETAILS

Order reference number	N/A

The requesting person / organization to appear on the license	Kristel Sepp

REUSE CONTENT DETAILS

Title, description or numeric reference of the portion(s)	Figure 6, Figure 7	**Title of the article/chapter the portion is from**	Exploring the efficacy and cellular uptake of sorafenib in colon cancer cells by Raman micro-spectroscopy
Editor of portion(s)	N/A	**Author of portion(s)**	Society of Public Analysts (Great Britain); Chemical Society (Great Britain); Society for Analytical Chemistry; Society of Public Analysts (Great Britain); Royal Society of Chemistry (Great Britain)
Volume of serial or monograph	N/A	**Issue, if republishing an article from a serial**	N/A
Page or page range of portion	6075-6076	**Publication date of portion**	2018-11-07

CCC Republication Terms and Conditions

1. Description of Service; Defined Terms. This Republication License enables the User to obtain licenses for republication of one or more copyrighted works as described in detail on the relevant Order Confirmation (the "Work(s)"). Copyright Clearance Center, Inc. ("CCC") grants licenses through the Service on behalf of the rightsholder identified on the Order Confirmation (the "Rightsholder"). "Republication", as used herein, generally means the inclusion of a Work, in whole or in part, in a new work or works, also as described on the Order Confirmation. "User", as used herein, means the person or entity making such republication.

2. The terms set forth in the relevant Order Confirmation, and any terms set by the Rightsholder with respect to a particular Work, govern the terms of use of Works in connection with the Service. By using the Service, the person transacting for a republication license on behalf of the User represents and warrants that he/she/it (a) has been duly authorized by the User to accept, and hereby does accept, all such terms and conditions on behalf of User, and (b) shall inform User of all such terms and conditions. In the event such person is a "freelancer" or other third party independent of User and CCC, such party shall be deemed jointly a "User" for purposes of these terms and conditions. In any event, User shall be deemed to have accepted and agreed to all such terms and conditions if User republishes the Work in any fashion.

3. Scope of License; Limitations and Obligations.

    3.1. All Works and all rights therein, including copyright rights, remain the sole and exclusive property of the Rightsholder. The license created by the exchange of an Order Confirmation (and/or any invoice) and payment by User of the full amount set forth on that document includes only those rights expressly set forth in the Order Confirmation and in these terms and conditions, and conveys no other rights in the Work(s) to User. All rights not expressly granted are hereby reserved.

    3.2. General Payment Terms: You may pay by credit card or through an account with us payable at the end of the month. If you and we agree that you may establish a standing account with CCC, then the following terms apply: Remit Payment to: Copyright Clearance Center, 29118 Network Place, Chicago, IL 60673-1291. Payments Due: Invoices are payable upon their delivery to you (or upon our notice to you that they are available to you for downloading). After 30 days, outstanding amounts will be subject to a service charge of 1-1/2% per month or, if less, the maximum rate allowed by applicable law. Unless otherwise specifically set forth in the Order Confirmation or in a separate written agreement signed by CCC, invoices are due and payable on "net 30" terms. While User may exercise the rights licensed immediately upon issuance of the Order Confirmation, the license is automatically revoked and is null and void, as if it had never been issued, if complete payment for the license is not received on a timely basis either from User directly or through a payment agent, such as a credit card company.

3.3. Unless otherwise provided in the Order Confirmation, any grant of rights to User (i) is "one-time" (including the editions and product family specified in the license), (ii) is non-exclusive and non-transferable and (iii) is subject to any and all limitations and restrictions (such as, but not limited to, limitations on duration of use or circulation) included in the Order Confirmation or invoice and/or in these terms and conditions. Upon completion of the licensed use, User shall either secure a new permission for further use of the Work(s) or immediately cease any new use of the Work(s) and shall render inaccessible (such as by deleting or by removing or severing links or other locators) any further copies of the Work (except for copies printed on paper in accordance with this license and still in User's stock at the end of such period).

3.4. In the event that the material for which a republication license is sought includes third party materials (such as photographs, illustrations, graphs, inserts and similar materials) which are identified in such material as having been used by permission, User is responsible for identifying, and seeking separate licenses (under this Service or otherwise) for, any of such third party materials; without a separate license, such third party materials may not be used.

3.5. Use of proper copyright notice for a Work is required as a condition of any license granted under the Service. Unless otherwise provided in the Order Confirmation, a proper copyright notice will read substantially as follows: "Republished with permission of [Rightsholder's name], from [Work's title, author, volume, edition number and year of copyright]; permission conveyed through Copyright Clearance Center, Inc. " Such notice must be provided in a reasonably legible font size and must be placed either immediately adjacent to the Work as used (for example, as part of a by-line or footnote but not as a separate electronic link) or in the place where substantially all other credits or notices for the new work containing the republished Work are located. Failure to include the required notice results in loss to the Rightsholder and CCC, and the User shall be liable to pay liquidated damages for each such failure equal to twice the use fee specified in the Order Confirmation, in addition to the use fee itself and any other fees and charges specified.

3.6. User may only make alterations to the Work if and as expressly set forth in the Order Confirmation. No Work may be used in any way that is defamatory, violates the rights of third parties (including such third parties' rights of copyright, privacy, publicity, or other tangible or intangible property), or is otherwise illegal, sexually explicit or obscene. In addition, User may not conjoin a Work with any other material that may result in damage to the reputation of the Rightsholder. User agrees to inform CCC if it becomes aware of any infringement of any rights in a Work and to cooperate with any reasonable request of CCC or the Rightsholder in connection therewith.

4. Indemnity. User hereby indemnifies and agrees to defend the Rightsholder and CCC, and their respective employees and directors, against all claims, liability, damages, costs and expenses, including legal fees and expenses, arising out of any use of a Work beyond the scope of the rights granted herein, or any use of a Work which has been altered in any unauthorized way by User, including claims of defamation or infringement of rights of copyright, publicity, privacy or other tangible or intangible property.

5. Limitation of Liability. UNDER NO CIRCUMSTANCES WILL CCC OR THE RIGHTSHOLDER BE LIABLE FOR ANY DIRECT, INDIRECT, CONSEQUENTIAL OR INCIDENTAL DAMAGES (INCLUDING WITHOUT LIMITATION DAMAGES FOR LOSS OF BUSINESS PROFITS OR INFORMATION, OR FOR BUSINESS INTERRUPTION) ARISING OUT OF THE USE OR INABILITY TO USE A WORK, EVEN IF ONE OF THEM HAS BEEN ADVISED OF THE POSSIBILITY OF SUCH DAMAGES. In any event, the total liability of the Rightsholder and CCC (including their respective employees and directors) shall not exceed the total amount actually paid by User for this license. User assumes full liability for the actions and omissions of its principals, employees, agents, affiliates, successors and assigns.

6. Limited Warranties. THE WORK(S) AND RIGHT(S) ARE PROVIDED "AS IS". CCC HAS THE RIGHT TO GRANT TO USER THE RIGHTS GRANTED IN THE ORDER CONFIRMATION DOCUMENT. CCC AND THE RIGHTSHOLDER DISCLAIM ALL OTHER WARRANTIES RELATING TO THE WORK(S) AND RIGHT(S), EITHER EXPRESS OR IMPLIED, INCLUDING WITHOUT LIMITATION IMPLIED WARRANTIES OF MERCHANTABILITY OR FITNESS FOR A PARTICULAR PURPOSE. ADDITIONAL RIGHTS MAY BE REQUIRED TO USE ILLUSTRATIONS, GRAPHS, PHOTOGRAPHS, ABSTRACTS, INSERTS OR OTHER PORTIONS OF THE WORK (AS OPPOSED TO THE ENTIRE WORK) IN A MANNER CONTEMPLATED BY USER; USER UNDERSTANDS AND AGREES THAT NEITHER CCC NOR THE RIGHTSHOLDER MAY HAVE SUCH ADDITIONAL RIGHTS TO GRANT.

7. Effect of Breach. Any failure by User to pay any amount when due, or any use by User of a Work beyond the scope of the license set forth in the Order Confirmation and/or these terms and conditions, shall be a material breach of

the license created by the Order Confirmation and these terms and conditions. Any breach not cured within 30 days of written notice thereof shall result in immediate termination of such license without further notice. Any unauthorized (but licensable) use of a Work that is terminated immediately upon notice thereof may be liquidated by payment of the Rightsholder's ordinary license price therefor; any unauthorized (and unlicensable) use that is not terminated immediately for any reason (including, for example, because materials containing the Work cannot reasonably be recalled) will be subject to all remedies available at law or in equity, but in no event to a payment of less than three times the Rightsholder's ordinary license price for the most closely analogous licensable use plus Rightsholder's and/or CCC's costs and expenses incurred in collecting such payment.

8. Miscellaneous.

    8.1. User acknowledges that CCC may, from time to time, make changes or additions to the Service or to these terms and conditions, and CCC reserves the right to send notice to the User by electronic mail or otherwise for the purposes of notifying User of such changes or additions; provided that any such changes or additions shall not apply to permissions already secured and paid for.

    8.2. Use of User-related information collected through the Service is governed by CCC's privacy policy, available online here:https://marketplace.copyright.com/rs-ui-web/mp/privacy-policy

    8.3. The licensing transaction described in the Order Confirmation is personal to User. Therefore, User may not assign or transfer to any other person (whether a natural person or an organization of any kind) the license created by the Order Confirmation and these terms and conditions or any rights granted hereunder; provided, however, that User may assign such license in its entirety on written notice to CCC in the event of a transfer of all or substantially all of User's rights in the new material which includes the Work(s) licensed under this Service.

    8.4. No amendment or waiver of any terms is binding unless set forth in writing and signed by the parties. The Rightsholder and CCC hereby object to any terms contained in any writing prepared by the User or its principals, employees, agents or affiliates and purporting to govern or otherwise relate to the licensing transaction described in the Order Confirmation, which terms are in any way inconsistent with any terms set forth in the Order Confirmation and/or in these terms and conditions or CCC's standard operating procedures, whether such writing is prepared prior to, simultaneously with or subsequent to the Order Confirmation, and whether such writing appears on a copy of the Order Confirmation or in a separate instrument.

    8.5. The licensing transaction described in the Order Confirmation document shall be governed by and construed under the law of the State of New York, USA, without regard to the principles thereof of conflicts of law. Any case, controversy, suit, action, or proceeding arising out of, in connection with, or related to such licensing transaction shall be brought, at CCC's sole discretion, in any federal or state court located in the County of New York, State of New York, USA, or in any federal or state court whose geographical jurisdiction covers the location of the Rightsholder set forth in the Order Confirmation. The parties expressly submit to the personal jurisdiction and venue of each such federal or state court.If you have any comments or questions about the Service or Copyright Clearance Center, please contact us at 978-750-8400 or send an e-mail to support@copyright.com.

v 1.1

SEPP Kristel

From: support@services.acs.org
Sent: 12 July 2020 18:35
To: SEPP Kristel
Subject: Regarding Incident 3668846 Permission to republish within thesis -- DOI: 10.1021/acs.jmedchem.9b01546

Importance: High

Follow Up Flag: Flag for follow up
Flag Status: Flagged

Dear Kristel Sepp,

Your permission requested is granted and there is no fee for this reuse. In your planned reuse, you must cite th article as the source, add this direct link https://pubs.acs.org/doi/full/10.1021/acs.jmedchem.9b01546, and inclu notice to readers that further permissions related to the material excerpted should be directed to the ACS.

If you need further assistance, please let me know.

Sincerely,

Raquel Picar-Simpson
ACS Publications Support
Customer Services & Information
Website: https://help.acs.org/

Incident Information:

Incident #: 3668846
Date Created: 2020-07-11T08:30:25
Priority: 3
Customer: Kristel Sepp
Title: Permission to republish within thesis -- DOI: 10.1021/acs.jmedchem.9b01546
Description: Dear ACS publisher,

I am contacting you to get permission to use the following article in my thesis:

https://pubs.acs.org/doi/abs/10.1021/acs.jmedchem.9b01546

I am the first author of the article and need to use the entire published article in my PhD Th However, the content and figures are spread out to different chapters within my thesis.

Thanks in advance for your help.

Best wishes,

A Chemical Strategy To Manipulate the Intracellular Localization of Drugs in Resistant Cancer Cells

Author: Muralikrishna Duvvuri, Samidha Konkar, Ryan S. Funk, et al

Publication: Biochemistry

Publisher: American Chemical Society

Date: Dec 1, 2005

PERMISSION/LICENSE IS GRANTED FOR YOUR ORDER AT NO CHARGE

This type of permission/license, instead of the standard Terms & Conditions, is sent to you because no fee is being charged for your order. Please note the following:

- Permission is granted for your request in both print and electronic formats, and translations.
- If figures and/or tables were requested, they may be adapted or used in part.
- Please print this page for your records and send a copy of it to your publisher/graduate school.
- Appropriate credit for the requested material should be given as follows: "Reprinted (adapted) with permission from (COMPLETE REFERENCE CITATION). Copyright (YEAR) American Chemical Society." Insert appropriate information in place of the capitalized words.
- One-time permission is granted only for the use specified in your request. No additional uses are granted (such as derivative works or other editions). For any other uses, please submit a new request.

If credit is given to another source for the material you requested, permission must be obtained from that source.

BACK CLOSE WINDOW

License Details

This Agreement between Kristel Sepp ("You") and American Association for Cancer Research ("American Association for Cancer Research") consists of your license details and the terms and conditions provided by American Association for Cancer Research and Copyright Clearance Center.

Print Copy

License Number	4865900686483
License date	Jul 11, 2020
Requestor Location	Kristel Sepp 6 Allanfield Place Flat 3 Edinburgh, other EH7 5AJ United Kingdom Attn: Miss Kristel Sepp
Licensed Content Publisher	American Association for Cancer Research
Licensed Content Publication	Clinical Cancer Research
Licensed Content Title	Lysosomal Sequestration of Sunitinib: A Novel Mechanism of Drug Resistance
Licensed Content Author	Kristy J. Gotink,Henk J. Broxterman,Mariette Labots,Richard R. de Haas,Henk Dekker,Richard J. Honeywell,Michelle A. Rudek,Laurens V. Beerepoot,René J. Musters,Gerrit Jansen,Arjan W. Griffioen,Yehuda G. Assaraf,Roberto Pili,Godefridus J. Peters,Henk M.W. Verheul
Licensed Content Date	Dec 1, 2011
Licensed Content Volume	17
Licensed Content Issue	23
Total	**0.00 GBP**
Type of Use	Thesis/Dissertation
Requestor type	academic/educational
Format	print and electronic
Portion	figures/tables/illustrations
Number of figures/tables/illustrations	1
Will you be translating?	no
Circulation	10
Territory of distribution	Worldwide

BACK

newWorkDetailsTitleLabel1	Utilising Stimulated Raman Scattering Microscopy To Study Intracellular Distribution of Label-Free Ponatinib in Live Cells
newWorkDetailsPublisherLabel5	University of Edinburgh
newWorkDetailsExpectedPublicationDateLabel4	Nov 2020
Portions	Figure 4 (A,C,E) on page 7343
Requestor Location	Kristel Sepp 6 Allanfield Place Flat 3 Edinburgh, other EH7 5AJ United Kingdom Attn: Miss Kristel Sepp
Total	**0.00 GBP**

BACK

Copyright Clearance Center Marketplace™

American Soc for Biochemistry & Molecular Biology - License Terms and Conditions

This is a License Agreement between Kristel Sepp ("You") and American Soc for Biochemistry & Molecular Biology ("Publisher") provided by Copyright Clearance Center ("CCC"). The license consists of your order details, the terms and conditions provided by American Soc for Biochemistry & Molecular Biology, and the CCC terms and conditions.

All payments must be made in full to CCC.

Order Date	11-Jul-2020	**Type of Use**	Republish in a thesis/dissertation
Order license ID	1047755-1		
ISSN	1083-351X	**Publisher**	AMERICAN SOCIETY FOR BIOCHEMISTRY AND MOLECULAR BI
		Portion	Chart/graph/table/figure

LICENSED CONTENT

Publication Title	Journal of biological chemistry	**Country**	United States of America
Author/Editor	AMERICAN SOCIETY FOR BIOCHEMISTRY & MOLECULAR BIOL	**Rightsholder**	American Soc for Biochemistry & Molecular Biology
Date	01/01/1905	**Publication Type**	e-Journal
Language	English	**URL**	http://www.jbc.org/

REQUEST DETAILS

Portion Type	Chart/graph/table/figure	**Distribution**	Worldwide
Number of charts / graphs / tables / figures requested	1	**Translation**	Original language of publication
Format (select all that apply)	Electronic	**Copies for the disabled?**	No
		Minor editing privileges?	No
Who will republish the content?	Academic institution	**Incidental promotional use?**	No
Duration of Use	Life of current edition	**Currency**	GBP
Lifetime Unit Quantity	Up to 499		
Rights Requested	Main product		

NEW WORK DETAILS

Title	Utilising Stimulated Raman Scattering Microscopy To Study Intracellular Distribution of Label-Free Ponatinib in Live Cells	**Institution name**	University of Edinburgh
		Expected presentation date	2020-11-30
Instructor name	Prof Alison N Hulme		

ADDITIONAL DETAILS

Order reference number	N/A

The requesting person / organization to appear on the license	Kristel Sepp

REUSE CONTENT DETAILS

Title, description or numeric reference of the portion(s)	Figure 4	**Title of the article/chapter the portion is from**	Weak Base Permeability Characteristics Influence the Intracellular Sequestration Site in the Multidrug-resistant Human Leukemic Cell Line HL-60
Editor of portion(s)	N/A		
Volume of serial or monograph	N/A	**Author of portion(s)**	AMERICAN SOCIETY FOR BIOCHEMISTRY & MOLECULAR BIOL
Page or page range of portion	32371	**Issue, if republishing an article from a serial**	N/A
		Publication date of portion	2004-06-03

PUBLISHER TERMS AND CONDITIONS

Journal of Biological Chemistry permissions policies: • If you are an author of the content for which you are seeking permission, or if you are not an author but are requesting permission to copy, distribute, transmit and adapt the work for noncommercial purposes (e.g. reproduction of a figure for educational purposes such as schoolwork, or appending a reprinted article to a PhD dissertation), you do not need to seek permission using the options listed below, as long as any reuse includes the credit line in the reuse policies listed above. • Parties who are not authors on the article who wish to reuse content for commercial purposes such as reproducing a figure in a book, journal, or coursepack published by a commercial publisher, do need permission and should request permission by completing the form below. For more information please see Journal of Biological Chemistry: http://www.jbc.org/site/misc/edpolicy.xhtml#copyright

CCC Republication Terms and Conditions

1. Description of Service; Defined Terms. This Republication License enables the User to obtain licenses for republication of one or more copyrighted works as described in detail on the relevant Order Confirmation (the "Work(s)"). Copyright Clearance Center, Inc. ("CCC") grants licenses through the Service on behalf of the rightsholder identified on the Order Confirmation (the "Rightsholder"). "Republication", as used herein, generally means the inclusion of a Work, in whole or in part, in a new work or works, also as described on the Order Confirmation. "User", as used herein, means the person or entity making such republication.

2. The terms set forth in the relevant Order Confirmation, and any terms set by the Rightsholder with respect to a particular Work, govern the terms of use of Works in connection with the Service. By using the Service, the person transacting for a republication license on behalf of the User represents and warrants that he/she/it (a) has been duly authorized by the User to accept, and hereby does accept, all such terms and conditions on behalf of User, and (b) shall inform User of all such terms and conditions. In the event such person is a "freelancer" or other third party independent of User and CCC, such party shall be deemed jointly a "User" for purposes of these terms and conditions. In any event, User shall be deemed to have accepted and agreed to all such terms and conditions if User republishes the Work in any fashion.

3. Scope of License; Limitations and Obligations.

    3.1. All Works and all rights therein, including copyright rights, remain the sole and exclusive property of the Rightsholder. The license created by the exchange of an Order Confirmation (and/or any invoice) and payment by User of the full amount set forth on that document includes only those rights expressly set forth in the Order Confirmation and in these terms and conditions, and conveys no other rights in the Work(s) to User. All rights not expressly granted are hereby reserved.

    3.2. General Payment Terms: You may pay by credit card or through an account with us payable at the end of the month. If you and we agree that you may establish a standing account with CCC, then the following terms apply: Remit Payment to: Copyright Clearance Center, 29118 Network Place, Chicago, IL 60673-1291. Payments Due: Invoices are payable upon their delivery to you (or upon our notice to you that they are

available to you for downloading). After 30 days, outstanding amounts will be subject to a service charge of 1-1/2% per month or, if less, the maximum rate allowed by applicable law. Unless otherwise specifically set forth in the Order Confirmation or in a separate written agreement signed by CCC, invoices are due and payable on "net 30" terms. While User may exercise the rights licensed immediately upon issuance of the Order Confirmation, the license is automatically revoked and is null and void, as if it had never been issued, if complete payment for the license is not received on a timely basis either from User directly or through a payment agent, such as a credit card company.

3.3. Unless otherwise provided in the Order Confirmation, any grant of rights to User (i) is "one-time" (including the editions and product family specified in the license), (ii) is non-exclusive and non-transferable and (iii) is subject to any and all limitations and restrictions (such as, but not limited to, limitations on duration of use or circulation) included in the Order Confirmation or invoice and/or in these terms and conditions. Upon completion of the licensed use, User shall either secure a new permission for further use of the Work(s) or immediately cease any new use of the Work(s) and shall render inaccessible (such as by deleting or by removing or severing links or other locators) any further copies of the Work (except for copies printed on paper in accordance with this license and still in User's stock at the end of such period).

3.4. In the event that the material for which a republication license is sought includes third party materials (such as photographs, illustrations, graphs, inserts and similar materials) which are identified in such material as having been used by permission, User is responsible for identifying, and seeking separate licenses (under this Service or otherwise) for, any of such third party materials; without a separate license, such third party materials may not be used.

3.5. Use of proper copyright notice for a Work is required as a condition of any license granted under the Service. Unless otherwise provided in the Order Confirmation, a proper copyright notice will read substantially as follows: "Republished with permission of [Rightsholder's name], from [Work's title, author, volume, edition number and year of copyright]; permission conveyed through Copyright Clearance Center, Inc. " Such notice must be provided in a reasonably legible font size and must be placed either immediately adjacent to the Work as used (for example, as part of a by-line or footnote but not as a separate electronic link) or in the place where substantially all other credits or notices for the new work containing the republished Work are located. Failure to include the required notice results in loss to the Rightsholder and CCC, and the User shall be liable to pay liquidated damages for each such failure equal to twice the use fee specified in the Order Confirmation, in addition to the use fee itself and any other fees and charges specified.

3.6. User may only make alterations to the Work if and as expressly set forth in the Order Confirmation. No Work may be used in any way that is defamatory, violates the rights of third parties (including such third parties' rights of copyright, privacy, publicity, or other tangible or intangible property), or is otherwise illegal, sexually explicit or obscene. In addition, User may not conjoin a Work with any other material that may result in damage to the reputation of the Rightsholder. User agrees to inform CCC if it becomes aware of any infringement of any rights in a Work and to cooperate with any reasonable request of CCC or the Rightsholder in connection therewith.

4. Indemnity. User hereby indemnifies and agrees to defend the Rightsholder and CCC, and their respective employees and directors, against all claims, liability, damages, costs and expenses, including legal fees and expenses, arising out of any use of a Work beyond the scope of the rights granted herein, or any use of a Work which has been altered in any unauthorized way by User, including claims of defamation or infringement of rights of copyright, publicity, privacy or other tangible or intangible property.

5. Limitation of Liability. UNDER NO CIRCUMSTANCES WILL CCC OR THE RIGHTSHOLDER BE LIABLE FOR ANY DIRECT, INDIRECT, CONSEQUENTIAL OR INCIDENTAL DAMAGES (INCLUDING WITHOUT LIMITATION DAMAGES FOR LOSS OF BUSINESS PROFITS OR INFORMATION, OR FOR BUSINESS INTERRUPTION) ARISING OUT OF THE USE OR INABILITY TO USE A WORK, EVEN IF ONE OF THEM HAS BEEN ADVISED OF THE POSSIBILITY OF SUCH DAMAGES. In any event, the total liability of the Rightsholder and CCC (including their respective employees and directors) shall not exceed the total amount actually paid by User for this license. User assumes full liability for the actions and omissions of its principals, employees, agents, affiliates, successors and assigns.

6. Limited Warranties. THE WORK(S) AND RIGHT(S) ARE PROVIDED "AS IS". CCC HAS THE RIGHT TO GRANT TO USER THE RIGHTS GRANTED IN THE ORDER CONFIRMATION DOCUMENT. CCC AND THE RIGHTSHOLDER DISCLAIM ALL OTHER WARRANTIES RELATING TO THE WORK(S) AND RIGHT(S), EITHER EXPRESS OR IMPLIED, INCLUDING WITHOUT LIMITATION IMPLIED WARRANTIES OF MERCHANTABILITY OR FITNESS FOR A PARTICULAR PURPOSE.

ADDITIONAL RIGHTS MAY BE REQUIRED TO USE ILLUSTRATIONS, GRAPHS, PHOTOGRAPHS, ABSTRACTS, INSERTS OR OTHER PORTIONS OF THE WORK (AS OPPOSED TO THE ENTIRE WORK) IN A MANNER CONTEMPLATED BY USER; USER UNDERSTANDS AND AGREES THAT NEITHER CCC NOR THE RIGHTSHOLDER MAY HAVE SUCH ADDITIONAL RIGHTS TO GRANT.

7. Effect of Breach. Any failure by User to pay any amount when due, or any use by User of a Work beyond the scope of the license set forth in the Order Confirmation and/or these terms and conditions, shall be a material breach of the license created by the Order Confirmation and these terms and conditions. Any breach not cured within 30 days of written notice thereof shall result in immediate termination of such license without further notice. Any unauthorized (but licensable) use of a Work that is terminated immediately upon notice thereof may be liquidated by payment of the Rightsholder's ordinary license price therefor; any unauthorized (and unlicensable) use that is not terminated immediately for any reason (including, for example, because materials containing the Work cannot reasonably be recalled) will be subject to all remedies available at law or in equity, but in no event to a payment of less than three times the Rightsholder's ordinary license price for the most closely analogous licensable use plus Rightsholder's and/or CCC's costs and expenses incurred in collecting such payment.

8. Miscellaneous.

    8.1. User acknowledges that CCC may, from time to time, make changes or additions to the Service or to these terms and conditions, and CCC reserves the right to send notice to the User by electronic mail or otherwise for the purposes of notifying User of such changes or additions; provided that any such changes or additions shall not apply to permissions already secured and paid for.

    8.2. Use of User-related information collected through the Service is governed by CCC's privacy policy, available online here:https://marketplace.copyright.com/rs-ui-web/mp/privacy-policy

    8.3. The licensing transaction described in the Order Confirmation is personal to User. Therefore, User may not assign or transfer to any other person (whether a natural person or an organization of any kind) the license created by the Order Confirmation and these terms and conditions or any rights granted hereunder; provided, however, that User may assign such license in its entirety on written notice to CCC in the event of a transfer of all or substantially all of User's rights in the new material which includes the Work(s) licensed under this Service.

    8.4. No amendment or waiver of any terms is binding unless set forth in writing and signed by the parties. The Rightsholder and CCC hereby object to any terms contained in any writing prepared by the User or its principals, employees, agents or affiliates and purporting to govern or otherwise relate to the licensing transaction described in the Order Confirmation, which terms are in any way inconsistent with any terms set forth in the Order Confirmation and/or in these terms and conditions or CCC's standard operating procedures, whether such writing is prepared prior to, simultaneously with or subsequent to the Order Confirmation, and whether such writing appears on a copy of the Order Confirmation or in a separate instrument.

    8.5. The licensing transaction described in the Order Confirmation document shall be governed by and construed under the law of the State of New York, USA, without regard to the principles thereof of conflicts of law. Any case, controversy, suit, action, or proceeding arising out of, in connection with, or related to such licensing transaction shall be brought, at CCC's sole discretion, in any federal or state court located in the County of New York, State of New York, USA, or in any federal or state court whose geographical jurisdiction covers the location of the Rightsholder set forth in the Order Confirmation. The parties expressly submit to the personal jurisdiction and venue of each such federal or state court.If you have any comments or questions about the Service or Copyright Clearance Center, please contact us at 978-750-8400 or send an e-mail to support@copyright.com.

v 1.1

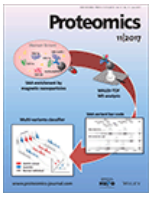

Drug penetration and metabolism in 3D cell cultures treated in a 3D printed fluidic device: assessment of irinotecan via MALDI imaging mass spectrometry

Author: Gabriel J. LaBonia, Sarah Y. Lockwood, Andrew A. Heller, et al

Publication: Proteomics

Publisher: John Wiley and Sons

Date: Jun 15, 2016

Order Completed

Thank you for your order.

This Agreement between Kristel Sepp ("You") and John Wiley and Sons ("John Wiley and Sons") consists of your license details and the terms and conditions provided by John Wiley and Sons and Copyright Clearance Center.

Your confirmation email will contain your order number for future reference.

License Number	4884880742006
License date	Aug 09, 2020

Printable Details

Licensed Content

Licensed Content Publisher	John Wiley and Sons
Licensed Content Publication	Proteomics
Licensed Content Title	Drug penetration and metabolism in 3D cell cultures treated in a 3D printed fluidic device: assessment of irinotecan via MALDI imaging mass spectrometry
Licensed Content Author	Gabriel J. LaBonia, Sarah Y. Lockwood, Andrew A. Heller, et al
Licensed Content Date	Jun 15, 2016
Licensed Content Volume	16
Licensed Content Issue	11-12
Licensed Content Pages	8

Order Details

Type of use	Dissertation/Thesis
Requestor type	University/Academic
Format	Print and electronic
Portion	Figure/table
Number of figures/tables	1
Will you be translating?	No

About Your Work

Title	Utilising Stimulated Raman Scattering Microscopy To Study Intracellular Distribution of Label-Free Ponatinib in Live Cells
Institution name	University of Edinburgh
Expected presentation date	Nov 2020

Additional Data

Portions	Figure 5

Requestor Location

Requestor Location	Kristel Sepp 6 Allanfield Place Flat 3 Edinburgh, other EH7 5AJ United Kingdom Attn: Miss Kristel Sepp

Tax Details

Publisher Tax ID	EU826007151

Price

Total	0.00 GBP

Would you like to purchase the full text of this article? If so, please continue on to the content ordering system located here: Purchase PDF
If you click on the buttons below or close this window, you will not be able to return to the content ordering system.

Total: 0.00 GBP

CLOSE WINDOW ORDER MORE

Three-dimensional culture systems in cancer research: Focus on tumor spheroid model

Author: Sritama Nath,Gayathri R. Devi
Publication: Pharmacology & Therapeutics
Publisher: Elsevier
Date: July 2016

Order Completed

Thank you for your order.

This Agreement between Kristel Sepp ("You") and Elsevier ("Elsevier") consists of your license details and the terms and conditions provided by Elsevier and Copyright Clearance Center.

Your confirmation email will contain your order number for future reference.

License Number	4884870732203
License date	Aug 09, 2020

Printable Details

Licensed Content

Licensed Content Publisher	Elsevier
Licensed Content Publication	Pharmacology & Therapeutics
Licensed Content Title	Three-dimensional culture systems in cancer research: Focus on tumor spheroid model
Licensed Content Author	Sritama Nath,Gayathri R. Devi
Licensed Content Date	Jul 1, 2016
Licensed Content Volume	163
Licensed Content Issue	n/a
Licensed Content Pages	15
Journal Type	S&T

Order Details

Type of Use	reuse in a thesis/dissertation
Portion	figures/tables/illustrations
Number of figures/tables/illustrations	1
Format	both print and electronic
Are you the author of this Elsevier article?	No
Will you be translating?	No

About Your Work

Title	Utilising Stimulated Raman Scattering Microscopy To Study Intracellular Distribution of Label-Free Ponatinib in Live Cells
Institution name	University of Edinburgh
Expected presentation date	Nov 2020

Additional Data

Portions	Adapted Table 2

Requestor Location

Requestor Location	Kristel Sepp 6 Allanfield Place Flat 3 Edinburgh, other EH7 5AJ United Kingdom Attn: Miss Kristel Sepp

Price

Total	0.00 GBP

Tax Details

Publisher Tax ID	GB 494 6272 12

Total: 0.00 GBP

CLOSE WINDOW ORDER MORE